Université d'Ottawa · University of Ottawa

## Abstract

This thesis describes the mechanism of the electrodeposition and dissolution of aluminum (Al) from a non-aqueous, aprotic bath. Due to its highly negative electrochemical potential, Al cannot be electrodeposited from aqueous solution. Al metal does, however, possess many desirable characteristics promoting its application for coating other, perhaps less corrosion-resistant materials, and as a portable energy source. The present work arose from earlier research on Al dissolution in acetonitrile solution which, itself, attempted to minimize limitations of the electrodissolution reaction in aqueous media in connection with Al battery development. Efforts to electrodeposit the metal, which would be interesting for coating applications as well as possible secondary battery development, from an acetonitrile bath gave, however, disappointing results. Herein was to lie the focus for the present author's research project, to examine media for the electrodeposition of Al and elucidate the mechanisms involved.

In order to electrodeposit Al, however, media which are aprotic are required, but additionally Al complexes that are reactive. One system for such a purpose, based upon mixtures of $AlCl_3$ and $LiAlH_4$ dissolved in etheric solvents, was examined as a starting point for further exploration. Considering the generally low dielectric constants of etheric solvents, it is actually quite remarkable that these so-called *hydride-baths* perform so well for the purpose of depositing (and stripping) Al. A limitation in the use of these baths is the necessity to accommodate the reactive $H^-$ species.

Baths based on tetrahydrofuran (thf) have been investigated since 1970 and have received attention in the literature, but, as discovered in the present research, they had not been at all properly characterized. These difficulties led to a critical examination of the published mechanisms of deposition of Al (Chapter 3), but, more fundamentally, an exploration, in careful detail, of the means by which such mechanisms can be determined from electrochemical measurements. This latter development, given in Chapter 2, highlighted a number of limitations to the theory that seemed to be responsible for the previously published, but incorrect conclusions on the mechanism of Al deposition from the hydride-bath.

With the above critique in mind and in light of the kinetic development given in Chapter 2, electrochemical results derived from cyclic-voltammetry, steady-state polarization and *a.c.* impedance applied in experiments on hydride-baths were carefully examined in order to establish the mechanism of Al electrodeposition and dissolution. It was established that the mechanism was dependent upon the composition of the hydride-bath, for which, in fact, the symmetry factor, $\beta$, in the electrode-kinetics varied between the compositional extremes.

Interestingly, from neither of the two compounds composing the baths could Al be deposited when examined separately in thf, but baths of nearly all proportions of the two combined gave good quality Al electrodeposits at high rates. The success of the latter baths has been found to lie in the ligand mixing, catalyzed by $H^-$, which gives a distribution of aluminate complexes of varying ligation in solution.

The speciation of the plating bath, which was found to contain up to nine different aluminate complexes, was examined by $^{27}$Al-NMR over a wide range of bath compositions. Additionally, a comparative examination of relative chemical shifts, linewidths and concentration dependences was conducted in an effort to characterize the reactivity of the individual chloro-hydrido-aluminates that were found to be responsible for the composition-dependent behaviours observed for these baths.

The Al deposit from the hydride-bath was generally of very good quality. The morphology of deposits from the hydride-bath was characterized by electron microscopy and the mechanism of initial phase formation examined in terms of nucleation and growth theories and was also found to depend upon the composition of the plating bath.

The results of this work either have already formed or soon will form the bases of a number of publications. One, on the content of Chapter 5, the NMR investigation into the reactivity of aluminate complexes composing the hydride-baths, has just (at time of thesis submission, January, 1997) received acceptance for publication by the Journal of Electroanalytical Chemistry. The contents of Chapter 2, specifically the effect of a stoichiometric number on multi-step electrode reaction kinetics, will shortly be submitted

as a Chapter in an electrochemical review series. A further publication will describe how the mechanism of the Al deposition reaction from the hydride-bath can be determined based upon the electrochemical experimental data recorded in Chapter 6 and with due consideration of the results that have been previously reported elsewhere in the literature as reviewed in Chapter 3.

## Acknowledgements

I wish to thank the following people for their assistance over the course of my work, here at the University of Ottawa:

My supervisor, **Professor Brain E. Conway**, for providing the means and much guidance to pursue this work.

The support staff in the Chemistry and Physics Departments at the University of Ottawa for their assistance with fabrication / repair of equipment.

**Raj Capoor** for assistance with running samples on the 300 MHz NMR spectrometer.

**John McCaffery**, (from NRC) for his assistance with running the SEM.

My colleagues in Professor Conway's electrochemistry group for providing such a stimulating environment in which to work in recent years.

My wife, **Marie**, and daughter, **Sydney**, for their unfailing support and love.

The following for financial assistance:

The Fonds **FCAR** of the government of Québec for a Doctoral Scholarship and the University of Ottawa for Entrance and Supplementary Scholarships. The Natural Sciences and Engineering Research Council for support to the Electrochemistry Group of Professor Conway through the Alcan - NSERC Chair through which the present project was funded.

# Table of Contents

Page

Page

Page

Page

# List of Figures

Page

Page

# List of Tables

# List of Schemes

# List of Symbols and Abbreviations

| Symbol | Description | Units |
|---|---|---|
| $a_i$ | activity of species *i* (an effective mole fraction) | |
| $a^s_{Ii}$ | surface activity (effective concentration) of an unstable intermediate | |
| A | electrode area | $cm^2$ |
| A-1 | first anodic aluminum feature (Chapter 6) | |
| A-2 | second anodic aluminum feature | |
| $A_{gross}$ | hypothetical substrate area covered by growing deposit ignoring the possibility of overlap | $cm^2$ |
| $A_i$ | a hypothetical stable solution species participating in a multi-step electrode reaction | |
| $A_{act}$ | actual substrate area covered by a growing deposit | $cm^2$ |
| B | flux density of a magnetic field | $T(kg\,s^{-2}\,A^{-1})$ |
| $B_{env}$ | magnetic field of a particular chemical environment | $T(kg\,s^{-2}\,A^{-1})$ |
| $B_{inst}$ | magnetic field of instrument | $T(kg\,s^{-2}\,A^{-1})$ |
| B&R | refers to monograph of Bockris & Reddy | |
| BV | refers to Bulter-Volmer equation of electrochemical rate | |
| $c_{el}$ | concentration of reacting species at electrode surface at time *t* | $mol\,cm^{-3}$ |
| $c_{(x,t)}$ | concentration at position *x* at time *t* | $mol\,cm^{-3}$ |
| $c_\infty$ | concentration of reacting species in the bulk of solution | $mol\,cm^{-3}$ |
| C | differential capacitance | $F\,cm^{-2}$ |
| C′ | (absolute) differential capacitance | F (C/V) |
| $C_{DL}$ | double-layer capacitance | $F\,cm^{-2}$ |
| $C_G$ | geometric (solution) capacitance | $F\,cm^{-2}$ |
| $C_{LF}$ | pseudo-capacitance of low frequency element | $F\,cm^{-2}$ |
| $C_P$ | pseudo-capacitance of an adsorbed intermediate | $F\,cm^{-2}$ |
| d | distance | cm |
| D | diffusion coefficient of a solution species | $cm^{-2}\,s^{-1}$ |
| $D_{Cottr}$ | diffusion coefficient calculated via Cottrell equation | $cm^{-2}\,s^{-1}$ |

| Symbol | Description | Units |
|---|---|---|
| $D_{Max}$ | diffusion coefficient calculated from transient maximum | $cm^{-2}\ s^{-1}$ |
| $e^-$ | an electron | |
| $e_o$ | charge of an electron / $1.609 \times 10^{-19}$ C | |
| E | applied potential difference between working and reference electrodes | V |
| $E_{nuc}$ | energy of nuclear spin | J |
| $E^\circ_e$ | equilibrium potential of a given reversible reaction under standard conditions ($a_i = 1$) | V |
| $E_i$ | instantaneous potential of a sinusoidally oscillating signal | V |
| $E_{max}$ | maximum potential of a sinusoidally oscillating signal | V |
| $E_r$ | thermodynamic reversible potential of an electrode reaction | V |
| $f$ | constant equal to F / RT | $V^{-1}$ |
| F | Faraday's constant / 96485 C $mol^{-1}$ (of electrons) | |
| $F_{ex}$ | extended fractional area ($A_{gross}$ / A) | |
| $F_\theta$ | actual fractional area ($A_{act}$ / A) | |
| FID | free induction decay | |
| FT | Fourier transform | |
| $g_I$ | empirical nuclear spin factor (Chapter 5) | |
| $g_i$ | Frumkin empirical interaction factor | |
| $\Delta G^{\circ\ddagger}_{\rightarrow}$ | chemical activation energy in the "→" reaction direction | J $mol^{-1}$ |
| $\Delta G^{\circ\ddagger}_{\leftarrow}$ | chemical activation energy in the "←" direction | J $mol^{-1}$ |
| $\Delta \bar{G}^{\circ\ddagger}_{\rightarrow}$ | electrochemical activation energy in the "→" (cathodic) reaction direction | J $mol^{-1}$ |
| $\Delta_\gamma \Delta \bar{G}^{\circ\ddagger}_{\rightarrow}$ | change of cathodic activation barrier height as the result of an applied overpotential | J $mol^{-1}$ |
| h | height of a deposit growing two-dimensionally (Chapter 8) | cm |
| h | Planck constant / $6.626 \times 10^{-34}$ J s | |
| $i_{max}$ | current-density at the maximum of a diffusion controlled current transient | A $cm^{-2}$ |

| Symbol | Description | Units |
|---|---|---|
| $i_{nucl}$ | steady-state nucleation rate equal to the product: $N_o W$ | $cm^{-2} s^{-1}$ |
| $i_o$ | exchange-current density | $A\,cm^{-2}$ |
| $i_{ss}$ | steady-state current-density (Chapter 8) | $A\,cm^{-2}$ |
| $i_{(t)}$ | current-density at time $t$ | $A\,cm^{-2}$ |
| $i_{(t)\ gross}$ | current-density at time $t$ if possibility of grain overlap is ignored | $A\,cm^{-2}$ |
| $i_{(t)\ act}$ | current-density at time $t$ considering grain overlap | $A\,cm^{-2}$ |
| I | nuclear spin quantum numbers (Chapter 5) | |
| \|I\| | ionic strength | $mol\,cm^{-3}$ |
| $I_i$ | a hypothetical unstable intermediate species participating in a multi-step electrode reaction (Chapter 2) | |
| $I_i$ | instantaneous current of a sinusoidally oscillating signal | A |
| $I_{(t)}$ | current at time $t$ | A |
| $I_{\rightarrow}$ | current for "→", forward reaction direction | A |
| $J_{(x,t)}$ | flux | $mol\,s^{-1}\,cm^{-2}$ |
| k | rate constant | $mol\,cm^{-2}\,s^{-1}$ |
| $k_B$ | Boltzmann constant / $1.381 \times 10^{-23}$ J $K^{-1}$ | |
| $k_{r,p}$ | vibration force constants of reactant and product | $kg\,s^{-2}$ |
| $k_{\rightarrow}$ | rate constant for the "→" reaction direction | $s^{-1}$ |
| $\bar{k}_{\rightarrow}$ | electrochemical rate constant for "→" reaction direction | $s^{-1}$ |
| $K_i$ | quasi-equilibrium constant for step $i$; assuming rates of forward and reverse rates of step $i$ being equal | |
| $K^{\ddagger}_{\rightarrow}$ | pseudo-equilibrium constant for the hypothetical equilibrium of formation of the transition-state complex from reactants | |
| L | Nernst layer (concentration gradient) thickness | $cm^2$ |
| m | moles | moles |
| M | molecular weight | $g\,mol^{-1}$ |
| $n_{cr}$ | number of atoms in the critical nucleus | |

| Symbol | Description | Units |
|---|---|---|
| $N_{sat}$ | total number of nucleation sites when site blocking is considered | $cm^{-2}$ |
| $N_{(t)}$ | number of nuclei at time t | $cm^{-2}$ |
| $N_{\infty}$ | total number of nucleation active sites per unit area | $cm^{-2}$ |
| pzc | potential of zero charge; potential where charge on metal is zero | |
| PE | potential-energy | |
| $q_{grow}$ | charge corresponding to a growing nuclei ignoring the possibility of overlap | $C\,cm^{-2}$ |
| $q_i$ | electric charge on species *i* | $C\,cm^{-2}$ |
| $q_{mon}$ | charge corresponding to deposition of a complete monolayer on a substrate electrode | $C\,cm^{-2}$ |
| $Q_i$ | instantaneous charge for an oscillating signal | C |
| *r* | compositional ratio describing the hydride-bath $[AlCl_3]/[LiAlH_4]$ | |
| $r_{(t)}$ | time-dependent radius | cm |
| $r_{(t)\,d}$ | time-dependent radius of a spherical *diffusion* zone | cm |
| $r_{(t)\,el}$ | time-dependent radius of a spherical electrode | cm |
| rds | rate-determining step | |
| R | gas constant / 8.314 $J\,mol^{-1}\,K^{-1}$ | |
| R | resistance | Ω |
| $R_{CT}$ | charge transfer resistance | Ω |
| $R_D$ | diffusional resistance | Ω |
| $R_F$ | resistance of a film | Ω |
| $R_{LF}$ | resistance associate with low frequency element | Ω |
| $R_P$ | resistance associated with adsorption process | Ω |
| $R_S$ | solution resistance | Ω |
| t | time | s |
| $t_o$ | time zero (for growth-transients in Chapter 8) | s |
| $t_{oj}$ | time of birth of the *j*th grain | s |
| $t_{max}$ | time of the maximum of a diffusion controlled | s |

| Symbol | Description | Units |
|---|---|---|
| | current-transient | |
| $T$ | temperature | K |
| $u_j$ | age of the *j*th grain | s |
| $U$ | integration constant for indefinite integrals or dummy variable | |
| $U_{p,i}$ | dummy constants (Chapter 8) | |
| $V$ | volume | $cm^3$ |
| $W$ | rate constant for formation for conversion of nucleation sites into growing grains | $s^{-1}$ |
| $W_{cn}$ | work to form the critical nucleus | $J\,mol^{-1}$ |
| $x$ | position | cm |
| $X_c$ | capacitive reactance | Ω |
| $Y$ | dummy variable (Chapter 8) | |
| $z$ | total number of electrons transferred in one turnover of the entire reaction | |
| $z_i$ | number of electrons transferred in step *i* of a multi-step electrode reaction | |
| $z_{rds}$ | number of electrons transferred in the rds | |
| $Z$ | total impedance | Ω |
| $Z_C$ | capacitive impedance | Ω |
| $Z_D$ | diffusional impedance | Ω |
| $Z_R$ | resistive impedance | Ω |
| $Z'$ | real impedance | Ω |
| $Z''$ | imaginary ("capacitive") impedance | Ω |
| $[i]$ | concentration of species *i* | $mol\,cm^{-3}$ |
| $\alpha_a$ | anodic transfer coefficient | |
| $\alpha_c$ | cathodic transfer coefficient | |
| $\beta$ | symmetry factor for the rate-limiting transition-state | |
| $\beta_a$ | symmetry factor for anodic reaction transition-state | |
| $\beta_c$ | symmetry factor for cathodic reaction transition-state | |

| Symbol | Description | Units |
|---|---|---|
| $\gamma$ | magnetogyric ratio | |
| $\gamma_t$ | electron number coefficients indicating the total number of electrons transferred in steps following the rds, speaking reductively | |
| $\gamma_p$ | total number of electrons transferred prior to the rds, speaking reductively | |
| $\gamma_{E\text{-}F}$ | number of electrons transferred in *elementary* steps following the rds, speaking reductively | |
| $\gamma_{E\text{-}P}$ | number of electrons transferred in *elementary* steps prior to the rds, speaking reductively | |
| $\gamma_{E\text{-}S}$ | number of electrons transferred in *elementary* steps between the rds and a *stoichiometry-determining* step | |
| $\delta$ | chemical shift | ppm |
| $\varepsilon_0$ | permittivity of vacuum / $8.854 \times 10^{-12}$ $C^2 N^{-1} m^{-2}$ | |
| $\varepsilon$ | dielectric constant | |
| $\eta$ | overpotential, potential versus the reversible potential of an electrode process | V or mV |
| $\theta_i$ | surface coverage fraction | |
| $\mu_i$ | chemical potential of species *i* | $J\,mol^{-1}$ |
| $\bar{\mu}$ | electrochemical potential of species *i* | $J\,mol^{-1}$ |
| $\mu^\circ_i$ | standard chemical potential of species *i* | $J\,mol^{-1}$ |
| $\mu_z$ | magnetic moment along axis of applied field | $A\,m^2$ |
| $\mu_N$ | nuclear magneton / $2.051 \times 10^{-27}$ $JT^{-1}$ | |
| $\nu$ | stoichiometric number, the number of times the rds must occur for one turnover of the entire reaction | |
| $\nu$ | frequency of NMR transitions | $s^{-1}$ |
| $\nu_{ref}$ | frequency of NMR transition of reference species | $s^{-1}$ |
| $\rho$ | density | $g\,cm^{-3}$ |
| $\rho$ | correlation coefficient (Chapter 6) | |
| $\psi_1$ | potential at the OHP | V |

| Symbol | Description | Units |
|---|---|---|
| $v_{\rightarrow}$ | reaction rate in "→" direction | $s^{-1}$ |
| $\phi_i$ | inner electric potential, or work function of phase $i$ | V |
| $\phi_{i,rev}$ | inner electric potential at equilibrium (as part of an interface) | V |
| $\phi$ | phase angle between current and potential (Chapter 6) | |
| $\omega$ | stoichiometric coefficient for a combination or dissociation step (Chapter 2) | |
| $\omega$ | angular frequency (Chapter 6) | $rad\,s^{-1}$ |
| $\omega_{max}$ | angular frequency at top of a Nyquist plot semicircle | $rad\,s^{-1}$ |

# Chapter 1 Introduction

## 1.1. Preamble

The present thesis is concerned with the electrodeposition of aluminum (Al). The reduction potential of Al is too *negative* to permit electroplating from aqueous solution, hydrogen evolution via solvent decomposition being the preferred electrochemical reaction. This fact necessitates the use of non-aqueous aprotic media or melts. This chapter will cover the principal properties of Al, outline its aqueous and non-aqueous electrochemistry, demonstrating the reactivity of aluminum species in various media, and will also describe the few practical plating baths that are available.

A description of the scope and structure of the present thesis work will be given at the end of this chapter which is more appropriate for presenting the scope of the new research since its motivation will be more easily understood after appropriate introduction.

## 1.2. Aluminum: Properties and Production Background

Aluminum is the most abundant metal found in the earth's crust, composing 8.1% of its weight by one estimate. Pure aluminum, which is a silvery-white metal, possesses many desirable characteristics. It is abundant and widely distributed, is one of the lightest metals and is nontoxic. It can be easily formed, machined or cast, is malleable (2$^{nd}$ among metals), ductile (6$^{th}$) and has good corrosion resistance due to a protective oxide film. It is nonmagnetic, nonsparking, has high thermal conductivity, while its good electrical conductivity is 60% that of copper per area of cross section and being a third less dense, its conductivity by mass is therefore twice that of copper. Pure aluminum is, however, soft and lacks strength, but it can be alloyed with many metals such as copper, magnesium, silicon, manganese to increase its strength [1:p.B7].

Aluminum is never found free in nature. The most important aluminum-containing minerals are the *feldspars* in which aluminum is found in combination with silica. Alumina occurs naturally as the minerals boehmite ($\alpha$-$Al_2O_3 \cdot H_2O$), diaspore ($\beta$-$Al_2O_3 \cdot H_2O$), gibbsite ($\alpha$-$Al_2O_3 \cdot 3H_2O$), bayerite ($\beta$-$Al_2O_3 \cdot 3H_2O$), corundum ($Al_2O_3$) and bauxite (a mixture of hydrated oxides the composition of which is known to vary consid-

erably from source to source) [2]. The latter is so named because it was first found at Les Baux, Provence, France and is now the major industrial feedstock. Bauxite is the most common Al ore and is found in large deposits around the world in Jamaica, Australia, Surinam, Guyana, etc. Metallic aluminum was first obtained and positively identified as an impure metal in 1825 by Oersted. An interesting condensed version of the history of the development of its refining process and its strikingly slow commercial application is given by Williams [3].

The most commonly used method for obtaining aluminum metal is by electrolysis of alumina dissolved in molten cryolite ($Na_3AlF_6$), the so-called Hall-Heroult process named for the workers who in the US and France developed it separately, but very nearly simultaneously in 1886. Cryolite is a natural ore found in Greenland, but is no longer widely used in commercial production, having been replaced by an artificial mixture of sodium, aluminum and calcium fluorides. Bauxite is refined in the Bayer process by dissolving the impure ore in sodium hydroxide, filtering and reprecipitating the aluminum as $Al_2O_3 \cdot 3H_2O$ with $CO_2$, then heating to drive off the hydrate water [4]. The alumina thus prepared can then be used directly in the Hall-Heroult refining process which, in Canada, is practiced at Arvida Québec.

Aluminum production represents one of the major products of the electrochemical industry, using fully 60% of the consumed electrical energy [1:p.B7]. Global primary production is about 25 million metric tons (estimated from 20 years of data up to 1990 from [5]). Canada, as one of the world's largest electrical energy producers, is also one of the principal refiners of aluminum and the largest exporter of aluminum. It may be remarked that the electrochemical smelting technology involves consumption of electrons on the order of 125 metric tons per month globally!

Aluminum has many useful properties which have led to various industrial applications that may be separated into two general categories: use in structure and corrosion protection (automobile parts, toasters, beverage cans, etc.), this being by far its major application; and in portable energy production applications (for instance the aluminum-air mechanically rechargeable battery [6,7]). The metal and its alloys can be formed, cast or extruded for structural and decorative applications, vapour deposited for cladding as used

in the electronics industry; also it has found specific application as a highly reflective coating for visible and infrared radiation (in fact, only gold and silver reflect infrared radiation better than does Al and these only slightly so) and can also be electro-dissolved in applications involving batteries or electrodeposited for cladding. These latter uses are the focus of the present thesis.

## 1.3. Aluminum Hydride and Chlorides: Chemical and Electrochemical Reactivity

The aluminum compounds of major interest in the present work are those that have hydrogen and chlorine as ligands, specifically $LiAlH_4$ and $AlCl_3$. The electronic configuration of atomic aluminum is $3s^23p^1$ and $Al^{3+}$ is its only stable oxidation state. It usually tends to form compounds with only three covalent bonds, although a coordination compound such as $Al(H_2O)_6^{3+}$ is known. There is, however, spectroscopic evidence confirming the existence of short-lived $Al^{1+}$ compounds in the gas phase at elevated temperatures [2:p.1011] while there is no such evidence for an $Al^{2+}$ species. Al compounds are coordinatively unsaturated in their octet and, as a result, they are usually strong Lewis acids which accounts for their chemical reactivity. There is a tendency for Al compounds to form bridged dimeric species to complete their octets and, for the same reason to favour coordination with solvent donor moieties which drives the solubilization of Al compounds in many solvents. This process is dependent upon the donor number [8] of the solvent in question; for instance in benzene, $D_n = 0.1$, $AlX_3$ (X = halide) exists as dimers, but in tetrahydrofuran (thf), $D_n = 20.0$, it exists as monomers. Indeed $AlCl_3 \cdot 2thf$ can undergo auto-ionization as:

$$2AlX_3 \cdot 2thf \rightleftharpoons AlX_2^+ \cdot 4thf + AlX_4^- \qquad (1)$$

to an extent that depends on the particular solvent's dielectric constant or donor number. Addition of agents which promote ionization, usually LiH or $LiAlH_4$, can improve conductivity in solvents of low dielectric constant.

Aluminum has a large negative standard electrochemical potential under nearly all conditions (see Fig. 1.1). Its electrochemical energy characteristics are amongst the best of all metals given its small atomic weight and its three valence electrons, i.e. close in

equivalent energy terms to that of Li. Its theoretical charge capacity by weight is 2.98 A h $g^{-1}$ (note 1 A h = 3600 C) which is second only to that of lithium and, by volume at 8.05 A h $cm^{-3}$, is the highest among anode materials. Table 1.1 is from reference [9] and compares the properties of Al, including theoretical capacities, with those of other possible anode materials in acidic electrolytes. The oxidation of aluminum metal to its most common hydrated oxide, $Al_2O_3 \cdot 3H_2O$, in aqueous solution is accompanied by a standard Gibbs energy change of 11.7 kW h $kg^{-1}$. Only hydrogen and a few other elements (lithium, beryllium and boron) have better characteristics, but Al has the advantage of being easier to handle (particularly over hydrogen) and being of much greater availability and lower price that the other elements.

Table 1.1. Characteristics of Electrode Materials in Lewis Acidic Electrolytes.

| Material | Weight g $mol^{-1}$ | Std Potl V | Charge | Density g $cm^{-3}$ | Capacity A h $g^{-1}$ | Capacity A h $cm^{-3}$ |
|---|---|---|---|---|---|---|
| $H_2$ | 2.0 | 0.0 | 2 | | 26.59 | |
| Li | 6.9 | -3.01 | 1 | 0.54 | 3.86 | 2.06 |
| Na | 23.0 | -2.71 | 1 | 0.97 | 1.16 | 1.14 |
| Mg | 24.3 | -2.38 | 2 | 1.74 | 2.20 | 3.80 |
| **Al** | **26.9** | **-1.66** | **3** | **2.69** | **2.98** | **8.10** |
| Ca | 40.1 | -2.84 | 2 | 1.54 | 1.34 | 2.06 |
| Fe | 55.8 | -0.44 | 2 | 7.85 | 0.96 | 7.50 |
| Cd | 112.4 | -0.40 | 2 | 8.65 | 0.48 | 4.10 |
| Pb | 207.2 | -0.13 | 2 | 11.34 | 0.26 | 2.90 |

As was noted earlier, the electronic configuration of ground-state atomic aluminum is $3s^2 3p^1$ and thus not all of its valence electrons are degenerate. Its electrochemistry can, therefore, be expected to be complex, involving multistep reaction mechanisms with sequential transfer of three electrons. $Al^{1+}$ has a complete 3s orbital, hence is a more probable intermediate than $Al^{2+}$ and the former of these, as stated above, has been confirmed spectroscopically. However, either the $Al^{1+}$ or $Al^{2+}$ would be expected to disproportionate quickly as follows:

$$3Al(I) \rightarrow 2Al + Al(III) \quad \text{or} \quad 3Al(II) \rightarrow Al + 2Al(III) \qquad (2)$$

## 1.4. Aluminum Electrochemistry

### 1.4.1. Aqueous Electrochemistry

The majority of studies of the aqueous electrochemistry of Al have concentrated on the growth, structure and stability of its oxide film [10]. The practical electrochemical and mechanical properties of aluminum are both determined by this surface oxide and in order to exploit the electroactivity of Al this oxide must be discouraged from being formed or be easily breached. A detailed description of aqueous Al systems will not be given here, but some general characteristics of aluminum's oxide film will be presented in order to emphasize the difficulty of accessing the actual electroactivity of bare Al. These points will serve to highlight the necessity for studying the behaviour of Al in non-aqueous aprotic solvents.

Most of the work on anodic dissolution of Al is closely related to development of the Al-air battery. Serious impediments to the application of Al as an electroactive material in water exist. The product of its anodic dissolution is its oxide (or hydroxide) which is highly resistive and under certain conditions insoluble (aluminum's oxides are dissolved by acid, base and a specific complexing affinity is exhibited with chloride). The oxide film can be a barrier to electronic and, depending on its structure, ionic conduction and these prevent high reaction rates rendering the Al passive.

The thermodynamic region of stability of water is bounded by (anodic) oxygen evolution on the positive side and (cathodic) hydrogen evolution on the negative side and is potential-dependent. It is usual to represent the pH and potential regions of stability of the solvent and those of any possible compounds (solution species and precipitates; e.g. oxides) and phases in so-called Pourbaix diagrams. Such a diagram for aluminum is given in Fig. 1.1 (from [11]). The electrochemical potential of bare aluminum metal is significantly negative of the cathodic stability limit of water (lower dashed line in Fig. 1.1) at all pH, but note also that only at low ($< 4$) and high ($> 12$) pH are aluminum solution species stable (see Fig. 1.1). In the case of the anodic dissolution of Al, hydrogen evolution will occur simultaneously on the bare, dissolving aluminum reducing the

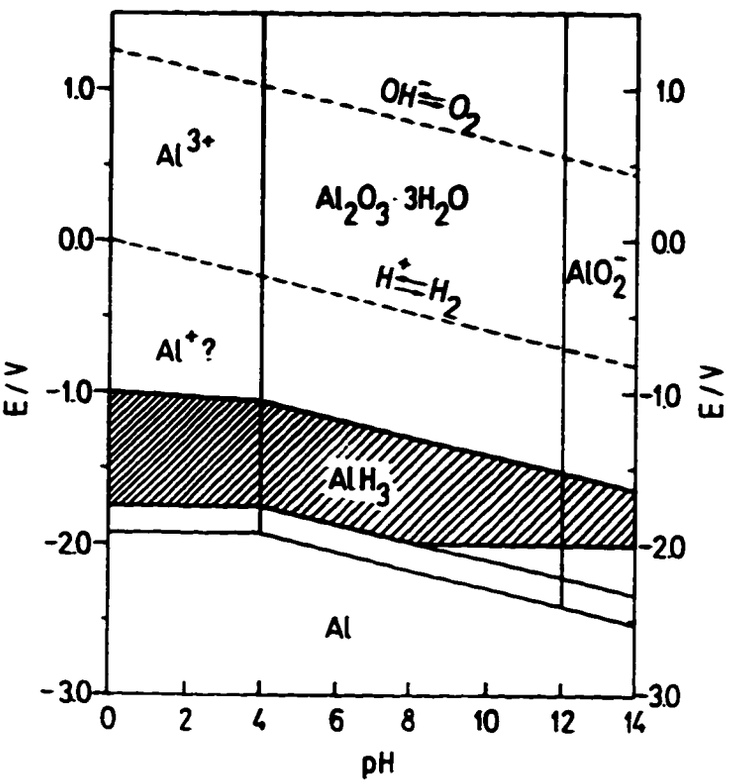


**Fig. 1.1.** Pourbaix diagram for aluminum in water defining potential and pH regions of species that are thermodynamically stable (from [11]).

efficiency of the Al anode as a battery material which assumes a potential lower than its theoretical thermodynamic value in aqueous solution. The rate of the simultaneous $H_2$ formation is known to increase with Al dissolution current-density, and thus the percentage of aluminum lost to corrosion involving hydrogen formation increases up to high current-densities (and this phenomenon is termed the "negative difference effect" [10:p.444]) which is a serious disadvantage to its practical utilization as an electrochemical energy source. Alloying Al with a small percent of a number of less base metals has been shown to suppress hydrogen evolution while remarkably also activating aluminum dissolution [12], specifically with gallium, indium or thallium.

In the case of cathodic electrodeposition of Al, the stability of solution species such as $[Al(H_2O)_6]^{3+}$ relative to solvent decomposition makes it impossible to electroplate Al from protic media due to the preferred reduction of protons.

### 1.4.2. The Oxide of Aluminum

Oxides of aluminum are expected to be present on the surface of the metal under all conditions, even in dry non-aqueous aprotic solvents, due, of course, to the nearly impossible task of completely removing all air and water from them. Indeed the oxide has been observed to reform quickly on fresh Al surfaces produced by scratching or guillotining Al rod electrodes [13,14], even in rigorously dried non-aqueous solvents. The Gibbs energy for the formation of aluminum oxide by hydrolysis from metallic aluminum and water (i.e. $2Al^{3+} + 3H_2O \rightarrow Al_2O_3 + 3H_2$; $\Delta G^\circ_{form} = -864.6$ kJ mol$^{-1}$) is very large and negative under standard conditions and therefore this reaction should occur spontaneously, but usually does so only until a compact layer of the insoluble oxide has formed since Al's oxide is an excellent electronic insulator (its electrical band-gap energy, $E_g$, is *ca.* 8 eV[a] [10]).

The nature of the oxide on Al can be quite complex [10]. Aspects that may contribute to its complexity are: 1) the structure of the oxide which can vary from being entirely amorphous, to highly ordered; 2) this structure can, in turn, affect the *ionic*

---

[a] Compare to a narrow band-gap semiconductor, Si, $E_g = 1.1$ eV and an insulator, diamond, $E_g = 5.4$ eV.

conductivity through it (even though it is an *electronic* insulator) and; 3) the composition of the film can vary; although the anhydrous oxide is the most stable, hydrates up to $Al_2O_3 \cdot 3H_2O$ (or $Al(OH)_3$) can form. The result is that the oxide film on Al can be nonuniform and possess a great deal of microheterogeneity [10].

### 1.4.3. Aluminum: Its Non-aqueous Electrochemistry

The restrictions imposed by the thermodynamics of reactions of aluminum and its compounds in water necessitate utilization of aprotic solvents for studies of its practical electrochemistry. While, in many cases, shifting the working potential window into the region of stability of many Al compounds, use of these solvents presents fundamental technical problems in that the conductivities realizable are lower in these solvents since they often have a much lower dielectric constant than water.

The reduction of a number of Al compounds in organic solvents at mercury has been reported in the literature [15,16] and several examples are listed in Table 1.2.

Table 1.2. Polarographic Results for $AlCl_3$ in Various Organic Solvents

| Solvent | Potential[a] / V vs SCE | | Donor Number[b] |
|---|---|---|---|
| | $AlCl_3$ | $AlBr_3$ | |
| Acetonitrile* | -0.96 | -0.73 | 14.1 |
| | | -1.07 | |
| Propylene carbonate | -1.08 | | 15.1 |
| Tetrahydrofuran* | -1.68 | -1.48 | 20.0 |
| | -1.83 | -1.58 | |
| Dimethylformamide | -1.92 | | 26.6 |
| | -2.05 | | |
| Dimethylsulfoxide | -2.08[c] | | 29.8 |

a Values from [15] except * from [16].
b From [17] and which gives a relative measure of solvent coordinating ability.
c Estimated from a value cited against an Hg-pool reference.

Although the reduction of the aluminum species showed multiple polarographic waves for a number of solvents, these waves were usually ill-defined, the ratio of their wave-heights not being proportional to electron charges (and thence corresponding to separate electron

transfers). The variation of the reduction potentials of $AlCl_3$ listed in Table 1.2 seem, however, to have a rough correlation with solvent donor number [8,17]. The aluminum species are reduced with increasing difficulty, i.e. at increasing negative potentials when they are coordinated by a more strongly ligating or donative solvent. Table 1.2 also includes polarographic $E_{1/2}$ values for $AlBr_3$ in two solvents [16]. Compared to $AlCl_3$, $AlBr_3$ is reduced more easily, thus demonstrating the decreasing trend in stability with increasing size and decreasing basicity of ligand (which has also been shown to extend to $AlI_3$ in the few solvents in which it was studied).

There is a paucity of work on the dissolution of aluminum and aluminum alloys in non-aqueous solvents, studies on the latter being dwarfed by the work in aqueous media. The low dielectric constant of many non-aqueous solvents makes them less interesting for technical applications but, beyond this, due to the extreme difficulty of excluding water from such solvents, the same problems with regard to maintaining an oxide-free Al surface arise in non-aqueous as in aqueous media. Aluminum and its alloys have been studied in acetonitrile [13,18-20], dimethylformamide [21], tetrahydrofuran [22]. Table 1.3 lists some physical properties for solvents of significance in aluminum electrochemistry and will be referred to throughout the present thesis.

Table 1.3. Physical Properties of Selected Solvents: Formula Weight, Melting and Boiling Points, Density ($\rho$), Viscosity ($\eta$), Donor ($D_n$) and Acceptor ($A_n$) Numbers [17] and Dielectric Constant. Compiled from [1:pp.E51 & F41,23,24].

| Solvent | Formula Weight | mp °C | bp °C | $\rho$ g cm$^{-3}$ | $\eta$ cP | $D_n$ | $A_n$ | Dielectric Constant |
|---|---|---|---|---|---|---|---|---|
| Acetonitrile | 41.1 | -48 | 81 | 0.79 | 0.35 | 14.1 | 18.9 | 38.0 |
| Dimethylformamide | 73.1 | -61 | 153 | 0.94 | 0.79 | 26.6 | 16.0 | 36.1 |
| Dimethylsulfoxide | 78.1 | +18 | 189 | 1.10 | 1.96 | 29.8 | 19.3 | 45.0 |
| Tetrahydrofuran | 72.1 | -108 | 65 | 0.89 | 0.46 | 20.0 | 8.0 | 7.8 |
| Toluene | 92.1 | -93 | 111 | 0.87 | 0.59 | 0.5 | 8.5 | 2.4 |
| Water | 18.0 | 0 | 100 | 1.00 | 0.89 | 33.0 | 54.8 | 81.0 |

## 1.5. Aluminum Plating

The aqueous solution species of Al are all very stable and hence their reduction in water is beyond the window of this latter's stability due to the preferred deposition of hydrogen. Thus any practical aluminum plating bath must start from an aprotic solvent or molten salt. Due to the low dielectric constants of most organic solvents, such solutions usually have poor conductivities, whereas these should be at least 1 $mS\,cm^{-1}$ for practical purposes. A strategy to accomplish this is to exploit the Lewis acid properties of octet-deficient aluminum species such as $AlCl_3$ and the Lewis base properties of a donative solvent or an added ionization agent. Dissolution and ion formation should result from the specific acid-base interaction. The coordination energies between the solvent and solute must not, however, be so strong as to prevent release of aluminum during electrolysis. Coordination centres such as oxygen atoms in ethers or conjugated double bonds in aromatic hydrocarbons have been used in selecting organic plating baths. All Al plating baths are extremely water sensitive and must be operated in moisture-free environments, although a certain amount of moisture is permissible since the components of the baths will usually exhibit water-consuming properties.

Electroplating of aluminum has generated much attention since the first report of successful electroplating of Al in 1950 by Couch and Brenner [25]. Their bath was based upon mixtures of $AlCl_3$ and $LiAlH_4$ in diethyl ether and since they were working at the National Bureau of Standards at the time, it has been subsequently referred to as the NBS bath. This bath was even upscaled during the 50's for application to electro-forming of mirrors [26] and electro-cladding of uranium rods [27]. The bath was limited in the amount of Al it could deposit by the amount of $AlCl_3$ that was initially and subsequently added to the bath. An improvement to this was introduced in 1968 by using $AlCl_3$, LiH and a quaternary ammonium salt, 2-ethoxyethyl trimethylammonium chloride in diethyl ether [28] which permitted continuous Al plating (and commensurate sacrificial-anode dissolution) not limited by the amount of Al species in solution. However, this procedure did not seem to attract attention and in the same year a much simpler improvement was employed where the diethyl ether was replaced by tetrahydrofuran (thf). The difference seemed to lie in the improved solubility of LiCl in thf. The use of thf has been the

standard ever since for the *hydride-type* baths. One group has termed this bath the REAL (Room temperature Electrodeposition of ALuminum) and has applied it for coating steel wire in a continuous process [29].

Most published work on the ether hydride-bath has been of a technical nature [25-28,30,31], the electrode processes involved in plating from this abandoned bath being still in doubt [32,33]. Work on the thf-based hydride-bath started in the 70's and over the next twenty years a number of scientific papers have characterized the conductivity [34-37] as well the kinetics and mechanism of Al deposition [32,38-41] from thf and mixed solvents. There was, however no concensus of mechanism amongst the above reports. Herein was to lie the motivation for the present thesis work. A detailed discussion of the results in these papers will be presented in Chapter 3.

Another type of organic bath for plating aluminum that has received a significant amount of attention is that based on mixtures of $AlBr_3$ and an alkali metal bromide or HBr in aromatic hydrocarbon solvents. In fact, baths of this type were the first to be tried for Al deposition from organic solvents as early as 1899 ([33] and references therein). Gileadi and his group studied the alkali metal halide, often in a mixture of alkyl benzenes [42-45]. Capuano and co-workers studied the HBr bath which was reported to have an excellent operational lifetime [13,46-49]. In these aromatic hydrocarbon solvent baths Al exists as the bulky anionic dimer $Al_2Br_7^-$ and the role of HBr or MBr was as an ionizing agent to promote formation of the dimer in these solvents of poor dielectric constant. Low bath conductivities, meagre practical current-densities and a comparably low reported purity of deposited Al seem to have precluded applications of this bath.

Extremely high-purity deposits have been reported for baths based on solutions of $Al(C_2H_5)_3$ and an alkali metal hydride, sodium flouride or quaternary ammonium salts in toluene. The bath operates above 80°C and has been applied industrially to coating mirrors [50-52]. Table 1.4 compares the properties of these most promising of the baths based on organic solvents.

Molten salts arise from Lewis acid-base interactions with, for instance, $AlCl_3$ and can provide very interesting environments in which to conduct electrochemical investigations (e.g. [53-58]) since they are highly conductive and have variable basicity and

Table 1.4. Characteristics of Popular Aluminum Plating Baths

| System | Bath Components | Solvent | Operation Temp. °C | Cond. $mS\,cm^{-1}$ | CD $mA\,cm^{-2}$ | Purity |
|---|---|---|---|---|---|---|
| Bromide | $AlBr_3$ MBr or HBr M = alkali | Alkyl benzenes | 10-25 | 10 | 1-10 | 99.5% |
| Hydride | $AlCl_3$ $LiAlH_4$ | thf | 10-40 | 10 | 1-50 | 99.99% |
| Organo-Aluminum | $Al(Et)_3$ MH; NaF; $N(R)_4^+$ M = alkali | toluene | 80-100 | 20 | 1-5 | 99.9999%* |

Compiled from [33,52] * claimed in [33]

melting point depending upon the ratio of acid ($AlCl_3$) to base. Inorganic molten salts are usually operated at temperatures above 150°C and have had application in Al electrodeposition [59-62]. The driving force for formation of these ionic liquids is the significantly reduced lattice energy, as compared to that of the separate components involved, of the [$AlCl_3$-organic salt anion] *acid-base* adduct that preferentially forms when the components are mixed. If the salt serving as the Lewis base is sufficiently bulky, as is the case for quaternary alkyl-ammonium halides, the melting point of mixtures with $AlCl_3$ may drop below room temperature, but if it is too bulky the liquids may be too viscous.

Aluminum can be electroplated from organic molten salts when these are acidic in character, i.e. where $AlCl_3$ is in greater proportion than the organic salt. A ratio of 2:1 is usually used since it has been found that $Al_2Cl_7^-$ is the only species from which aluminum can be reduced [63]. Plating aluminum from molten electrolytes based upon butylpyridinium salts [55,64-69], substituted imidazolium salts [70-73], trimethyl-phenyl-ammonium chloride [74] or trimethyl-sulfonium chloride [75], has been studied near ambient temperatures and in dimethylsulfone [76-78], at higher temperatures. Problems with these molten salts, apart from their intrinsically high viscosity, arise from the fact that the deposition process produces local compositional changes that can significantly

alter the conductivity and melting point of the melts near the surfaces of the electrodes since both these properties are extremely composition sensitive. Other solvents have been examined seemingly for the purpose of electroplating aluminum, for instance aniline and substituted anilines [79,80], and also dimethylsulfoxide [81], but results in these were poor.

## 1.6. Motivation and Scope of the Thesis Work

### 1.6.1. Origins of the Work

The present work arose from earlier research in our laboratory on the dissolution of Al and Al alloys in acetonitrile solutions of $AlCl_3$ as electrolyte [13,20] in connection with examination of new systems for Al battery development. In that work excellent dissolution rates and active Al potentials were realized. Putting aside its potential toxicity under certain conditions (e.g. it can decompose to release HCN), acetonitrile has excellent electrochemical properties, a large dielectric constant and moderate donor and acceptor numbers [8,17,82]; however, a preliminary investigation into the cathodic side of the Al reaction in this medium gave disappointing results [83]. Following this, a number of solvent systems such as sulpholane and hexamethyl-phosphoramide, and mixtures of these with acetonitrile, were cursorily explored, but with no success.

Attention was then turned to the literature of Al electrodeposition to find a more suitable starting point for further study and development. Examination of the characteristics of the major baths in the field listed in Table 1.4 pointed to the *hydride-bath* as the one that offered the highest purity deposit, the cheapest ingredients and the most practical of operating conditions to study the electrochemical reactivity of electro-depositable Al species. Even though the thf hydride-bath has received attention in the literature (see above), it had not been, as we discovered during the course of our work on the bath, at all completely or properly characterized. This was the motivation for the careful investigation given here in the present work of the interesting behaviour and reactivity of this aluminum plating bath.

The hydride-bath is actually a complicated mixture of aluminate species produced from the mixing of $AlCl_3$ with $LiAlH_4$ in thf, where $H^-$ (as LiH) might initially have been

added as an ionizing agent. Auto-ionization of $AlCl_3$ is expected to be low in thf, given this solvent's dielectric constant, and the role of $H^-$ as an ionizing agent is significant, but through the course of the present thesis work the participation and importance of the $H^-$ ligand in the Al electrodeposition reaction, beyond simply promoting ionization, became very clear.

### 1.6.2. Structure of the Thesis

The structure of the thesis describing this work is as follows. In Chapter 3 a critical review of published literature on the kinetics and mechanism of Al electrodeposition [32,38-41] from the thf hydride-baths is given. The mechanisms derived in these works were all based on the results of Tafel polarization experiments, and all were consistent with those deduced in the present work, but their derived conclusions were disparate. Their experimental works were, however, incomplete and their diverse conclusions based especially on measured *transfer coefficients* evaluated from experimental steady-state or *Tafel* plots, demonstrated a lack of thorough understanding of the basis on which these experimental electrochemical observables are related to critical aspects of reaction mechanism when an overall multistep reaction is involved.

For the purpose of avoiding the apparent ambiguities in the above mentioned publications and in order to establish a firm link between experimental transfer coefficients and the mechanisms of potentially complicated multistep electrode processes, a thorough development of the concept and significance of transfer coefficients from generalized reaction schemes in which a single step controls the rate of the reaction is given in Chapter 2. Of specific importance is the inclusion amongst the generalized schemes of the possible role of a *stoichiometric number*[b]. This development is presented before the above mentioned literature critique in order to establish some common ground, so to speak, which will facilitate discussion in Chapter 3 of the mechanistic particulars of the Al deposition and dissolution reactions that have been previously reported but incompletely analyzed.

---

[b] This discussion is being prepared for inclusion as a chapter in an electrochemical review series [84].

The experimental equipment and methods employed in the research will be described in Chapter 4, although subsequent chapters may also include such subsections where deemed appropriate. Chapter 5 presents the results of NMR experiments on the hydride-bath for the nuclei $^{27}Al$, $^{13}C$ and $^{7}Li$, conducted in order to elucidate speciation in the baths and characterize the chemical reactivity of the component aluminates[c].

Results of the electrochemical experiments are presented in Chapter 6 which include the cyclic-voltammetric behaviour, Tafel relation measurements, *a.c.* impedance results, etc. for the Al deposition reaction from hydride-baths having varying ratios of starting components[d]. Theoretical aspects of the more obscure techniques and theories involved in the discussed mechanisms are also presented. Chapter 7 describes and discusses the relevance of $\beta$, the electrochemical *symmetry factor*, (a parameter central to electrochemical mechanistic analysis) to the Al electrodeposition mechanism.

Apart from fundamental electron-transfer and chemical reaction steps, deposition reactions involve the incorporation of depositing atoms into a continuously growing lattice resulting in a continuously changing reaction interface. Chapter 8 examines aspects of the electrocrystallization or the initiation of an Al phase onto foreign substrates as well as the macroscopic morphology of deposits from the hydride-bath while Chapter 9 summarizes and concludes the thesis.

---

[c] The results in that chapter have been submitted for consideration for publication [85].

[d] The electrochemical results will be prepared and submitted for publication.

# Chapter 2 Development of Kinetic Equations

## 2.1. Foreword

The theory necessary for evaluation of the kinetics of an electrochemical reaction which proceeds in several consecutive steps, one of which is rate-determining, is presented here in order to demonstrate how potential vs current relations can be employed for mechanism elucidation. The impetus for the material presented in this chapter originates from work we have been conducting on the cathodic plating reaction of aluminum in non-aqueous solvents. A particular bath for this is the well known "etheric hydride-bath" [25] and a number of publications have appeared discussing the kinetics and mechanism of aluminum deposition from this bath [38-41] when the ether is tetrahydrofuran (thf). Aluminum is electroplated from the hydride-bath via a multistep reaction, but there has been no concensus of derived conclusions on mechanism amongst the above mentioned works although all of them are based on essentially the same experimental results (these will be presented and discussed thoroughly in Chapter 3). This problem prompted a closer examination and ultimately a re-derivation of the theory upon which the above conclusions were made.

The aims of mechanistic studies of chemical reactions may be summarized as:

1) determination of the reaction pathway(s);
2) characterization of the species involved and the reaction order in various respective species;
3) identification of the rate-determining step and species involved in it;
4) evaluation of the reaction order in various of the participating reactions;
5) the type of rate-control.

Central to mechanism determination in electrochemical kinetics is the use of steady-state potential versus logarithmic current relations (known as Tafel plots). In the electrochemical benchmark monograph of Bockris and Reddy [86:pp.1001-1007] these authors have developed *transfer coefficients*, $\alpha$'s, in terms of mechanistic parameters. Their analysis demonstrated how such $\alpha$'s, obtained from experimental polarization curves, can give information directly enabling elucidation of reaction mechanisms. The

pertinent quantities are the number of electrons transferred *prior to*, *during* and *following* a rate-determining step (rds) which are given the symbols $\gamma_p$, $z_{rds}$ and $\gamma_f$, respectively, and the number of times the rds occurs, i.e. the so-called *stoichiometric number*, $\nu$, for one overall act of the process. Their transfer coefficients are written as:

$$\alpha_c = \frac{\gamma_p}{\nu} + z_{rds}\beta \tag{1i}$$

$$\alpha_a = \frac{\gamma_f}{\nu} + z_{rds}(1-\beta) \tag{1ii}$$

where $\beta$ is the rate-limiting transition-state barrier symmetry factor (see Chapter 7).

These coefficients are obtainable experimentally, and since there appears to be a straightforward relation to the important mechanistic parameters (via Eqns. 2.1i and 2.1ii) these coefficients have been cited in many experimental works, including those mentioned in relation to the mechanism of aluminum reduction in the hydride-bath [38-41]. The coefficients have been determined and discussed in these works, but seemingly without regard to the limitations of their application. This confusion is due, in the present author's opinion, to an incomplete understanding of how the transfer coefficients and rate-determining steps to which they refer, link particulars of electrochemical reaction mechanisms to the experimentally observable *Tafel slopes*, specifically for cases of mechanisms involving a stoichiometric number greater than one.

It is on account of this confusing literature that we endeavour here to develop clearly and concisely the link between general mechanistic features and values of transfer coefficients that may be obtained experimentally, and thence justify their significance in relation to reaction mechanism determination.

## 2.2. Structure of the Present Chapter, and Apologia

The approach to the kinetic formulations to be developed here will start from the Transition-State Theory of chemical kinetics, followed by analysis of the effect of an applied potential on electrochemical kinetics built up through the well-known Butler-Volmer (BV) equation originally written for a one-electron reaction. For multi-step

electrochemical mechanisms, it is necessary to assume a rate-limiting step (**rds**) within the scheme and make a *quasi-equilibrium approximation* to define an exact potential-dependence of rates involving electrons transferred before, during and after this rds. Thus the BV equation is extended to simple multi-step cases including, importantly, the case of an overall reaction limited by a step having a stoichiometric number greater than one. The circumstances under which $\nu > 1$ can arise are described in detail.

The author apologies for the fact that the following derivations are potentially confusing, but the thorough and formal approach here, based on fundamental principles, will clearly illustrate how the potential-dependence of electrochemical reaction rates, characterized by experimentally determinable transfer coefficients, arises in generalized reaction schemes, and what constraints the required limiting assumptions impose upon this potential-dependence. This approach was called for because the simple transfer coefficients of B&R are really only of use if applied properly; this is actually not so trivial a point given the above mentioned confusion that has arisen in the kinetic analysis of the Al electrodeposition reaction. Hence, attention has to be given in the following material to completeness.

It is possible that confusion can arise in the kinetic developments that follow because both reduction and oxidation reaction directions are treated simultaneously in some cases (e.g. in relation to the Butler-Volmer equation and to overall reversibility of the reaction) but, for clarity, the reaction schemes are all (and only) written for the reduction directions and thus oxidations (or the anodic reaction branch) are simply the reverse of these and involve reaction products as reactants.

## 2.3. Chemical Kinetics

The kinetic treatment of electrochemical reactions is based on that for regular chemical reactions but with the inclusion of electrical energy terms (see §2.4). We first consider the progress of a simple chemical transformation:

$$\mathbf{A\text{-}B + C \rightleftarrows A + B\text{-}C} \qquad (2)$$

which is usually regarded as involving a transition-state defined by an activated complex

of high energy, having a configuration intermediate between that of the reactant and the product, and is written as:

$$\mathbf{A\text{-}B + C \rightleftarrows A\cdot B\cdot C^{\ddagger} \rightleftarrows A + B\text{-}C} \tag{3}$$

It is generally assumed that the same transition-state describes the reaction in the reverse direction, although exceptions will be examined later in §6.6.5.

The energy required to attain the transition-state is the energy difference between the activated complex, $\mathbf{A\cdot B\cdot C^{\ddagger}}$ and the minima (zero point energies) of the reactants for the forward reaction direction or of the products for the reverse direction where the Gibbs energies of these are described by their respective standard chemical potentials ($\mu^{o}_{i}$). The standard forward *activation energy* or *energy barrier*, $\Delta G^{o}_{\rightarrow}{}^{\ddagger}$ is then:

$$\mu^{o}_{A\cdot B\cdot C^{\ddagger}} - \left(\mu^{o}_{A\text{-}B} + \mu^{o}_{C}\right) = \Delta G^{o\ddagger}_{\rightarrow} \tag{4}$$

From the Transition-State (or Activated Complex) Theory of chemical reaction rates [87], the forward rate constant, $k_{\rightarrow}$, for a reaction, the rate of which is determined by a potential barrier $\Delta G^{o}_{\rightarrow}{}^{\ddagger}$, will be given by Eqn. 2.5:

$$k_{\rightarrow} = \frac{k_B T}{h} \exp\left[-\frac{\Delta G^{o\ddagger}_{\rightarrow}}{RT}\right] \tag{5}$$

where $k_B$ is the Boltzmann constant, $h$ Planck's constant, T the temperature (in K) and R the gas constant.

The rate of the reaction (in mol $s^{-1}$) in the cathodic direction, $v_{\rightarrow}$, depends upon the number of molecules entering the transition-state per second, defined by molarity for such ephemeral species, and thus:

$$v_{\rightarrow} = [A\cdot B\cdot C^{\ddagger}]k_{\rightarrow} \tag{6}$$

It is usually not convenient to measure this species' concentration, but if the passage of the $A\cdot B\cdot C^{\ddagger}$ complex over the barrier determines the rate, the formation of the complex from either reactants or products can be considered to be a "quasi"-equilibrium process which, for the case of the forward reaction, would have a quasi-equilibrium constant:

$$K^{\ddagger}_{\rightarrow} = \frac{[A\cdot B\cdot C^{\ddagger}]}{a_{A\text{-}B}\cdot a_{C}} \tag{7}$$

where the *a*'s are activities of the solution species.

Substituting for the activitated complex concentration in the rate equation (Eqn. 2.6) by a rearranged Eqn. 2.7 gives Eqn. 2.8 for the rate of the forward reaction:

$$\upsilon_{\rightarrow} = a_{A\text{-}B} a_C K^{\ddagger}_{\rightarrow} k_{\rightarrow} \tag{8}$$

where the *a*'s are the activities of the reactants, $k_{\rightarrow}$ the rate constant from Eqn. 2.5 and $K^{\ddagger}_{\rightarrow}$ the forward quasi-equilibrium constant from Eqn. 2.7. For simplicity, $K^{\ddagger}_{\rightarrow}$ will be subsequently dropped and assumed to be part of $k_{\rightarrow}$.

## 2.4. Simple One-Step, One-Electron Electrochemical Kinetics

The above activated complex theory is easily applied to the kinetics of electrochemical reactions which involve electrons as reactants, supplied from the Fermi level of a substrate electrode. An illustrative example of an electrochemical reaction is say, the electrodeposition of a species A from a solution complex $A^+$-$L^-$, onto a conductive electrode substrate M:

$$M(e^-) + A^+\text{-}L^- \rightleftarrows M\text{-}A + L^- \tag{9}$$

### 2.4.1. Energetics of the Electrochemical Transition-State

In order to describe the energetic course of such a reaction it is useful to introduce the potential-energy (PE) representation of the reaction coordinate [88], shown in Fig. 2.1 which is the single axis along which both the reactant, $A^+$-$L^-$, and product, M-A, vibrate. The transition-state for the reaction is defined by that region where the reactant and product PE surfaces intersect which usually involves stretching (or activation) of both reactant and product bonds. The positions of the substrate (M) and ligand ($L^-$) of the complex ion $A^+$-$L^-$ along the reaction coordinate (see Fig. 2.1) are considered to be frozen in place, the latter just outside the outer Helmholtz plane (OHP) of the substrate and the course of the reaction is described by the movement of A or $A^+$. This figure will be discussed in more detail later.

The energy of such a system may be described by the *electrochemical* potentials,

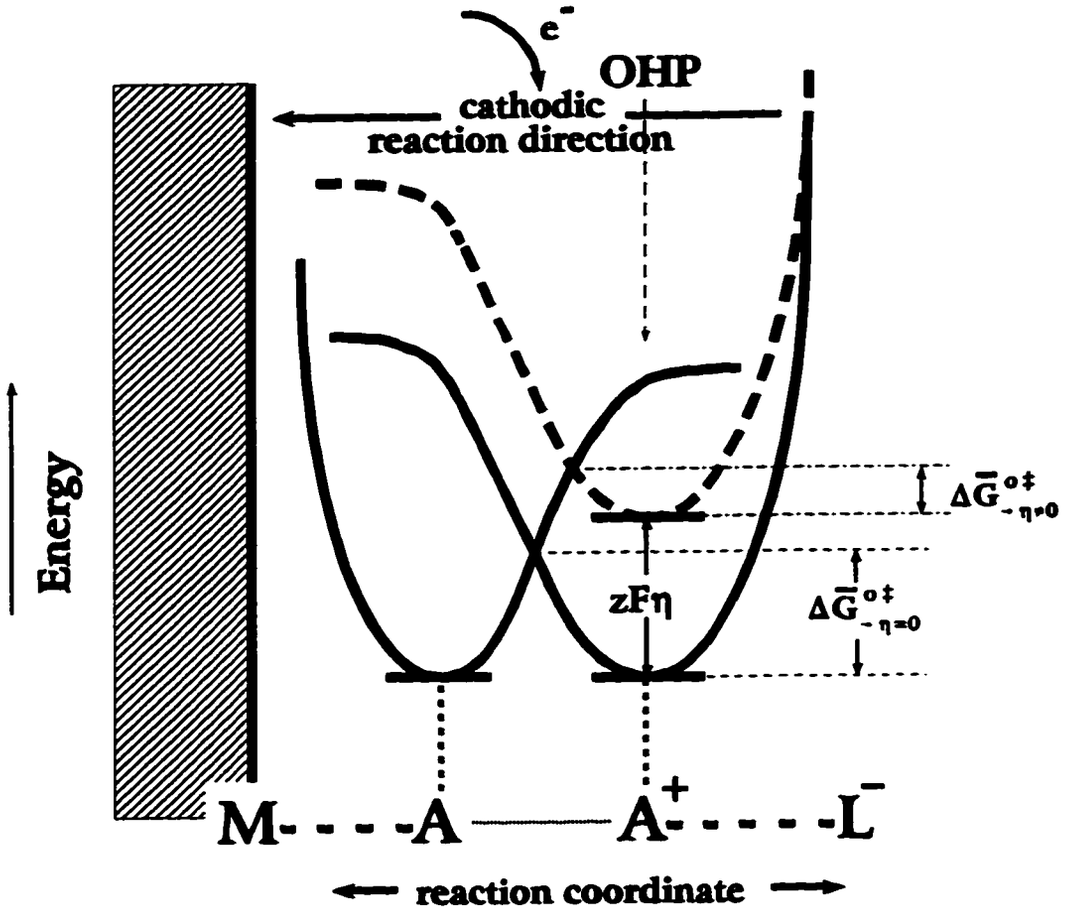


**Fig. 2.1.** Potential-energy diagram showing the course of an electrochemical reaction and the effect of an applied overpotential (solid curve [$\eta = 0$], dashed curve [$\eta \neq 0$]). The magnitude of the *cathodic* activation barriers in the presence, $\Delta\bar{G}^{\circ}_{\eta\neq 0}{}^{\ddagger}$, and absence, $\Delta\bar{G}^{\circ}_{\eta=0}{}^{\ddagger}$, of the applied $\eta$ are drawn as is the magnitude of the applied $zF\eta$.

$\bar{\mu}$'s, of the component species (note that the overbars "$^-$" indicate the so-called "electrochemical" quantities), i.e.:

$$\bar{\mu}_i = \mu_i^o + RT\ln[a_i] + z_iF\phi_i \qquad (10)$$

which includes the species' chemical potential, an activity term and an electrical energy term, which is the electrical work required to bring a charge $z_iF$ (or equivalently $-q_i$ for electron charges) from infinity into the species' phase. $z_iF$ is the molar charge on a given ionic species and $\phi_i$ is the standard inner potential or work function [89:p.20] of the phase in question, e.g. that of the metal, $\phi_M$, or of a particular ion in solution, $\phi_s$.

When considering the electrochemical reaction and interface as a whole, the charges on individual species, $z_i$'s, are less important than the number of electrons *transferred* in the step, i.e. $z$, which is assumed, in the usual way, to be equal to one[a].

In order to describe the rate or rate constant for either reaction direction we require an expression for the energy barrier or the energy of the transition-state in terms of either reactants, for the forward rate constant, $\Delta\bar{G}^{o\ddagger}_{\rightarrow}$, or products, for the reverse reaction rate constant, $\Delta\bar{G}^{o\ddagger}_{\leftarrow}$. For the forward, reductive direction of reaction 2.9 such an expression is:

$$\Delta\bar{G}^{o\ddagger}_{\rightarrow} = \bar{\mu}^o_{[M\cdot A\cdot L^-]^\ddagger} - \left(\bar{\mu}^o_{A^\bullet\text{-}L^-} + \bar{\mu}^o_{M(e^-)}\right) \qquad (11)$$

The great advantage of studying electrochemical over chemical kinetics is that the electrical component of the $\bar{\mu}$ of reacting electrons can be modified with an electric field, the result of an applied potential difference, E, at the electrode/solution interface which ultimately results in changes of electrical energy experienced by ions in their progress along the reaction coordinate. Additionally, these potentials can be controlled, with even the simplest instrumentation, to an accuracy of about 1 mV (96 J mol$^{-1}$).

---

[a] It is usually assumed that in multi-step electron-transfer processes (i.e. where $z > 1$), not more than *one* electron at a time is transferred. In the absolute rate theory of electron-transfer of Marcus ([90] and references therein) the energy requirements for medium reorganization associated with electron-transfer would seem to favour incremental transfer of charge.

The potential difference across the reaction interface, i.e. $\phi_M - \phi_S$, is the total electrical driving force, which can be defined as $\phi_{M,rev} - \phi_{S,rev}$ for the condition of equilibrium. The fact is, however, that the transition-state complex exists at some unknown position between the substrate and the bulk of solution and its inner potential is $\phi_\ddagger$. It is convenient to assume that the potential difference at this point, $\phi_{\ddagger,rev} - \phi_{S,rev}$, is some constant fraction, $\beta$, of the total interfacial potential difference, i.e. $\beta(\phi_{M,rev} - \phi_{S,rev})$, where $\beta zF(\phi_{M,rev} - \phi_{S,rev})$ would be the energy (in J mol$^{-1}$) associated with transfer of zF coulombs across the metal/solution interface under standard conditions.

We have considered up to this point potentials associated with a *single* metal-solution interface, i.e. $\phi_M$, $\phi_S$ and $\phi_\ddagger$. It is not possible, however, to measure these absolute potentials or differences between them directly. Potential is only experimentally measurable or controllable relative to another electrode of defined, invariant potential (i.e. a so-called nonpolarizable *reference* electrode) connected either directly or indirectly to both sides of the reaction interface. Apart from defining the applied potential, a reference electrode is required in order to complete the circuit and maintain electrical neutrality throughout the cell.

In order to develop a *kinetic* relation for the effect of an applied potential on the activation barriers, it is necessary to define that applied potential difference in terms of that of the reaction interface at *equilibrium*. For simplicity the symbol $E^o_e$, the *standard equilibrium potential*, now replaces $\phi_{M,rev} - \phi_{S,rev}$, indicating that it is measured against an appropriate reference electrode and where the activities of all involved species are equal to one (i.e. standard conditions). Practical electrochemical cells are, however, usually *non-standard* and this requires the introduction of the *Nernstian reversible potential*, $E_r$, which is related to $E^o_e$ by the well known Nernst equation [91:p.51]:

$$E_r = E_e^o + \frac{RT}{zF} \ln\left[\frac{a_O}{a_R}\right] \qquad (12)$$

where in the case of reaction 2.9, $a_O$ is the activity of $A^+$-$L^-$ and $a_R$ is that of M-A.

Thus a forward equilibrium rate constant for the electrodeposition reaction (written in Eqn. 2.9) is (cf. Eqn. 2.5):

$$\bar{k}_{-} = \frac{k_B T}{h} \exp\left[-\frac{\Delta G_{-}^{o\ddagger}}{RT}\right] \exp\left[-\frac{\beta z F E_r}{RT}\right] \tag{13}$$

in which the chemical and electrical terms are separated, but when combined are $\Delta\bar{G}^{o}_{-}{}^{\ddagger}$.

It is useful to describe the driving force of an applied potential, E, relative to that of the reversible potential, $E_r$, of the interfacial reaction. Overpotential, $\eta$, is the difference between these two, i.e. $\eta = E - E_r$. It must be assumed that the applied potentials do not influence either directly or indirectly the values of $E_r$ (i.e. $E^{o}_{e}$ or $a_O / a_R$) or the chemical potentials of reactants, products or the transition-state complex, and thus applied potentials are assumed to add linearly across the electrochemical interface. At the electronic mechanistic level, it is the change of Fermi-level energy of electrons by change of electrode potential that is the principal origin of effects of electrode potential on electron charge-transfer rates in electrochemical reactions. Since the potential of the transition-state complex is defined by a fraction of $E_r$, that *same* fraction of $(E - E_r)$ will modify the energy of the transition-state, i.e. $\beta zF(E - E_r)$ and influence the reaction rate.

An applied potential, E, equal to $E_r$ corresponds to a situation where the overpotential, $\eta$, is equal to zero and hence to equilibrium conditions, i.e. where the rates of forward and reverse reactions are equal. When we consider the PE surface representation of the reaction coordinate in Fig. 2.1, equilibrium corresponds to the PE surface consisting of the two solid curves ($\eta = 0$) where the barrier height is the same in both reaction directions. The situation of E being less than $E_r$ (i.e. of higher electrical energy) corresponds to a negative overpotential[b] and an excess of negative charge is built up on the electrode.

This excess negative charge will shift up (perfectly vertically, it is assumed) the

---

[b] As a point of clarification, IUPAC convention is followed here where a *negative* applied potential *raises* the energy of the electrons in the electrode and drives *reduction* in the forward direction [92]. Correspondingly, resulting currents are written negatively.

zero point energy of the reactant PE surface [93], i.e., for reaction 2.9 that of $A^+$-$L^-$, by $zF\eta$. This shift is shown in Fig. 2.1 where the dashed curve is that for the reactant when $\eta < 0$. Note that it is the $A^+$-$L^-$ curve that shifts since it is on the same side of the electrochemical reaction 2.9 as the electrons, written as $M_{(e^-)}$. Although the reactant curve in Fig. 2.1 was shifted by $zF\eta$, the cathodic barrier height, $\Delta\bar{G}^{o}_{-}{}^{\ddagger}$, changed by only a fraction, $\beta$, of that. This introduces a physical interpretation of $\beta$ conceptually different from a consideration of the electrical characteristics of the transition-state complex, i.e. $\phi_{\ddagger}-\phi_s = \beta(\phi_M-\phi_s)$. $\beta$, which is termed the *symmetry factor*, is a parameter central in electrochemical kinetics and models of its physical significance will be discussed further, with regard to the experimental results of the present thesis work, in Chapter 7. For the purpose of the present discussion $\beta$ is assumed potential-independent and symmetric, i.e. equal to 1/2, which has been noted for many reactions.

The amount by which an applied (negative) $\eta$ decreases the cathodic energy barrier is $zF\beta\eta$ giving a potential-dependent cathodic rate constant of:

$$\bar{k}_{-} = \frac{k_B T}{h}\exp\left[-\frac{\Delta G^{o\ddagger}_{-}}{RT}\right]\exp\left[-\frac{\beta z F(E-E_r)}{RT}\right] \tag{14}$$

Whereas a negative $\eta$ decreases the *cathodic* energy barrier, increasing the cathodic reaction rate, it simultaneously has the opposite effect (note the now positive argument for the second exponential in Eqn. 2.15) on the rate constant for the reverse, anodic, electrodissolution reaction, $\Delta\bar{G}^{o}_{-}{}^{\ddagger}$, thus the potential-dependent anodic rate constant, $\bar{k}_{-}$, is:

$$\bar{k}_{-} = \frac{k_B T}{h}\exp\left[-\frac{\Delta G^{o\ddagger}_{-}}{RT}\right]\exp\left[\frac{(1-\beta) z F(E-E_r)}{RT}\right] \tag{15}$$

Note that where $\beta$ refers to the height of the energy barrier of the *reduction* reaction, the rest of the fraction, $(1-\beta)$, refers to that of the reverse, *oxidation* reaction.

### 2.4.2. Double-Layer Considerations

If we consider the structure of the double-layer at an electrode/solution interface, the potential difference between the electrode and the bulk value of the solution is "dropped" by the accumulation of ions of opposite charge in the solution immediately adjacent to the electrode surface. The spatial distribution of ions gives a potential profile across the double-layer into solution over a distance that is dependent upon the electrolyte concentration. Given this position-dependent potential-profile, it is possible that species undergoing electrochemical reaction, assumed to reside in the OHP of the electrical double-layer adjacent to the substrate electrode (otherwise known as the plane of closest approach of nonspecifically adsorbed ions) may not actually be at $\phi_S$ and hence would not experience the full electrical field of the electrode/solution potential difference. The result of this is that only a part of the applied $\eta$ would affect the electronic energy of the reactant species. The potential at the OHP with respect to solution, $\phi_S$, is denoted $\psi_1$ [c] and is known as the potential of the diffuse-layer and is actually the part of the applied potential that *does not* affect the reactant in the OHP. Thus the ultimate electrical driving force of an applied overpotential $\eta$ at the OHP would be modified as $\beta(\eta - \psi_1)$. However, as long as $\psi_1$ is small, usually the case when solutions contain an inactive supporting electrolyte, or remains constant, it does not affect the actual potential-dependence of the interfacial reaction and $\eta$ can then be used in the kinetic equations without alteration.

### 2.4.3. Rate Equation

The potential-dependent rate of the forward, reductive direction of reaction 2.9 is the product of the rate constant of Eqn. 2.14, containing, as it does, the potential-dependent term and the concentration of the activated complex, $[M{\cdot}A{\cdot}L^-]^{\ddagger}$. This latter is substituted for, as was done in the strictly chemical case (Eqns. 2.6 to 2.8), by a quasi-equilibrium expression in terms of the activities of the reactants at the substrate electrode surface and therefore the rate, $v_{-}$, of the deposition reaction having units of mol $s^{-1}cm^{-2}$

[c] This is the symbol used in the Russian literature [89:p.26], $\phi_d$ or $\phi_2$ have been employed elsewhere [91].

(reaction cross-section area [of the substrate electrode]) is:

$$\upsilon_{-} = a_{A^{+}\text{-}L^{-}}\, k_{-} \exp\left[-\frac{zF\beta\eta}{RT}\right] = \frac{I_{-}}{zFA} \qquad (16)$$

where $a_{A+L^-}$ is the activity of $A^+$-$L^-$ in solution (diffusion is assumed not to be limiting), $k_-$ the heterogeneous rate constant, $I_-$ the current for the reduction and $A$ the accessible electrode area since electrochemical rates are measured as current-densities.

The reaction rate in the reverse direction is given analogously by Eqn. 2.17:

$$\upsilon_{-} = a_{M\text{-}A}\, a_{L^{-}}\, k_{-} \exp\left[\frac{zF(1-\beta)\eta}{RT}\right] = \frac{I_{-}}{zFA} \qquad (17)$$

Note that $(1-\beta)$ is the fraction of the applied overpotential affecting the reverse reaction.

Combining the forward and reverse rates (Eqns. 2.16 and 2.17) gives Eqn. 2.18 for the net current:

$$\begin{aligned} I_{net} &= -I_{-} + I_{-} \\ &= zFA\left(-a_{A^{+}\text{-}L^{-}}\, k_{-} \exp\left[-\frac{zF\beta\eta}{RT}\right] + a_{M\text{-}A}\, a_{L^{-}}\, k_{-} \exp\left[\frac{zF(1-\beta)\eta}{RT}\right]\right) \end{aligned} \qquad (18)$$

Notice that this equation is constructed so that the cathodic reaction contributes a negative current which follows the usual electrochemical convention [see footnote b]).

At equilibrium ($\eta = 0$), $I_{net} = 0$, but a so-called exchange current continues to pass. The exchange current-density is a direct measure of the kinetic facility of an electrochemical reaction through a particular transition-state and is given by:

$$i_o = zFa_{A^{+}\text{-}L^{-}}\, k_{-} = zFa_{M\text{-}A}\, a_{L^{-}}\, k_{-} \qquad (19)$$

writing $i$ for I/A. This $i_o$ may be introduced into Eqn. 2.18 to give the simplified Eqn. 2.20, which is the well known Butler-Volmer (BV) relation [94,95].

$$i_{net} = i_o \left(\exp\left[\frac{zF(1-\beta)\eta}{RT}\right] - \exp\left[-\frac{zF\beta\eta}{RT}\right]\right) \qquad (20)$$

Eqn. 2.20 essentially states that the cathodic and anodic slopes of log i vs $\eta$ curves (when the current is controlled by the reaction kinetics and not diffusion) in potential

regions where one or other of the reaction branches is negligible, is going to be proportional to $z\beta$ and $z(1-\beta)$, respectively, for a single-step, z-electron reaction. These factors are called the *transfer coefficients* and are essential tools for deriving reaction mechanism as will be demonstrated in what follows.

## 2.5. Sequence of Consecutive Electrochemical Reactions Involving a Single Rate-Determining Step

We now examine the situation for an electrochemical reaction that involves *multiple* consecutive electron-transfer steps since this particularly applies in the electrodeposition of Al, the basis of the present work. Usually the rate of such a reaction is limited by a single step, the rate-determining step (rds).

A hypothetical reaction sequence involving $n$ consecutive electron-transfer reduction steps is given below in Scheme 2.1. For Al deposition, $n$ is obviously 3. The $A_i$'s are stable species that can be reactants or products and the $I_i$'s are reaction intermediates of lower stability. The $z_i$'s indicate the number of electrons transferred in each step which can have values of 0, 1, 2, etc., and are used as a means of including in the general mechanisms (e.g. Scheme 2.1) the possibility of chemical steps, and single and multi-electron steps, respectively, as discrete reaction steps. However, steps in which more than one electron is transferred in a single act of the process are considered unlikely (see footnote a). $z$, used in the previous rate equation for a single step reaction (Eqn. 2.20) for the number of electrons transferred in the rds is now the sum total of all electrons

Scheme 2.1. Consecutive Electrochemical Reaction Scheme

| | | | | | | |
|---|---|---|---|---|---|---|
| Step | 1. | $A_1$ | + | $z_1e^-$ | $\rightleftarrows$ | $I_2$ |
| | 2. | $I_2$ | + | $z_2e^-$ | $\rightleftarrows$ | $I_3$ |
| | . | . . . . . | | | | |
| | rds-1. | $I_{rds-1}$ | + | $z_{rds-1}e^-$ | $\rightleftarrows$ | $I_{rds}$ |
| | **rds.** | $I_{rds}$ | + | $z_{rds}e^-$ | $\rightleftarrows$ | $I_{rds+1}$ |
| | rds+1. | $I_{rds+1}$ | + | $z_{rds+1}e^-$ | $\rightleftarrows$ | $I_{rds+2}$ |
| | . | . . . . . | | | | |
| | n. | $I_n$ | + | $z_ne^-$ | $\rightleftarrows$ | $A_{n+1}$ |

transferred for a single turnover of the entire reaction while $z_{rds}$ is the number specifically transferred in the rds. The "location" of the rds within the overall reaction of Scheme 2.1 is identified by an underline. The $\mathbf{A}_i$'s and $\mathbf{I}_i$'s can be uncharged, or be positively or negatively charged (the charge balance amongst these is omitted in Scheme 2.1 for simplicity) Although, there are limits to the charge these species can have, the n-step scheme will illustrate the origins of the potential-dependency that is relevant to mechanism determination in the present work.

Each of the steps will have individual rate constants for its forward and reverse reaction directions; for instance, for step $i$, these will be $\vec{k}_i$ and $\vec{k}_{-i}$, respectively. The activities of the reactants and products of the reaction may be defined in terms of their *solution* activities, $a_{Ai}$'s. The reaction *intermediates* will remain, however, in the immediate vicinity of the electrode substrate surface and do not possess "solution" activities, per se, since they are often unstable and ephemeral so are normally defined by *surface* activities, $a^s_{Ii}$'s (mol cm$^{-3}$)[d]. The volume that serves to describe the surface activity is defined by a solution thickness on the order of that of the double-layer itself and a particular species' bulk solubility would define the upper limit of its concentration (if that were estimable). This will account for the activities of intermediates if they reside somewhere in the double-layer or are *adsorbed* on the electrode surface. In the latter case only low coverages permit simplified treatment otherwise additional potential-dependent surface coverage terms, $\theta_i$'s are required (see the next section [§2.6] for further discussion).

In order to derive rate expressions for such complex mechanisms the following assumptions are usually made: 1) that only one of the steps is rate-limiting (the rds) which generally requires the rate constant of this reaction step be at least 100 times smaller than those of all other prior steps; 2) that the same step is also rate-limiting in the reverse direction; 3) that intermediates, if adsorbed on the surface of the electrode substrate, are at low coverages; 4) that the kinetics of all the other steps do not deviate

[d] The activities of intermediates will be designated by a superscript "s", while those of reactants contained in solution by omitting the "s".

significantly from either steady-state or quasi-equilibrium conditions (see below); 5) and that the nature of the mechanistic scheme does not change with potential. In reality this last point often does not hold since the PE surfaces for initial reactant, final product and all the intermediates will shift relative to one another; then some other step in the scheme could become rate-limiting, not to mention the possibility of emergence of alternate parallel steps that could change the mechanism.

If the above assumptions do hold, however, as they often will near to the reversible potential, the net rate of the overall reaction (measured as current-density) will be determined by the rate of the rds. The equation for the net rate of the overall reaction is:

$$i_{net} = -zFk_{rds}a^{s}_{I_{rds}}\exp\left[-z_{rds}\beta f\eta\right] + zFk_{-rds}a^{s}_{I_{rds+1}}\exp\left[z_{rds}(1-\beta)f\eta\right] \qquad (21)$$

where $k_{-rds}$ and $k_{rds}$ are the heterogeneous rate constants corresponding to the PE barrier of the rds at equilibrium ($\eta = 0$), $z_{rds}$ the number of electrons transferred in the rds, $a^{s}_{I_{rds+1}}$ and $a^{s}_{I_{rds}}$ are the surface activities of the species involved in this step and for simplicity, the constants F/(RT) have been replaced by $f$. Note that for the current-density for the *overall* reaction, the *total* number of electrons transferred per turnover of the overall reaction, z, and *not* only $z_{rds}$ is used in the pre-exponential.

The potential-dependence of $i_{net}$ in this expression (Eqn. 2.21) might initially appear to be defined solely by the exponential terms in either branch, but if, in fact, $I_{rds}$ and $I_{rds+1}$ are reaction intermediates, their surface activities are also usually potential-dependent.

The standard method for evaluating the potential-dependence of activities of reaction intermediates in electrochemical kinetics is to use the *steady-state* assumption, where, at a given overpotential, the surface activities of the intermediates are considered to remain constant in time and therefore be in a steady-state. The rates of their formation and disappearance will hence be equal with the result that the rates of their changes will be zero. If we evaluate this for say, $a^{s}_{I_2}$, the first intermediate of Scheme 2.1, we have:

$$\frac{da^{s}_{I_2}}{dt} = k_1 a_{A_1}\exp\left[-z_1\beta f\eta\right] + k_{-2}a^{s}_{I_2}\exp\left[z_2(1-\beta)f\eta\right] - k_{-1}a^{s}_{I_2}\exp\left[z_1(1-\beta)f\eta\right] - k_2 a^{s}_{I_2}\exp\left[-z_2\beta f\eta\right] = 0 \qquad (22)$$

which, upon solving for the surface activity of $I_2$, would give Eqn. 2.23:

$$a_{I_2}^s = \frac{k_1 a_{A_1} \exp[-z_1 \beta f\eta] + k_{-2} a_{I_2}^s \exp[z_2(1-\beta) f\eta]}{k_{-1} \exp[z_1(1-\beta) f\eta] + k_2 \exp[-z_2 \beta f\eta]} \qquad (23)$$

This is clearly a complicated expression that will become simplified only upon making (in some cases, arbitrary) assumptions about the relative magnitudes of some of the rate constants and thence neglecting some terms*. Such expressions could be written for the surface activities of all intermediates involved in the reaction scheme which, if they are substituted one into the other, could lead progressively to an expression, albeit quite complicated, defining the complete potential-dependence of the surface activity of $I_{ads}$.

In order to avoid such complicated expressions the *quasi-equilibrium* method is used, although the above steady-state approach can become reduced to the same result if various limiting assumptions are introduced. This approach assumes a rate-limiting step so that all other steps have much larger rate constants (in both directions) and hence are all in virtual or "quasi"-equilibrium. With application of a negative overpotential which drives the forward, reductive direction of the reaction, each of the steps *prior to* the rds (which are thence limited by it) will be at quasi-equilibrium, while those after will not be limited by the rds and will hence simply run to products without influencing the rate in that direction.

These steps *after* the rds (as they are written in Scheme 2.1, i.e. as reductions) will be rate-limited by the rds only in the *reverse*, oxidative reaction direction. The effect of these steps following the rds will be observed for applied positive overpotentials in which case those steps will be in quasi-equilibrium and those before will now run (backward) to reactants without influencing the rate in the reverse direction.

The potential-dependence of the surface activities of the "reactant" and "product" intermediates of the rds in the rate equation (Eqn. 2.21) can be evaluated by the quasi-equilibrium method. For the cathodic, forward direction this potential-dependence may

---

* See reference [96] for an example of this worked out fully.

be built up progressively in terms of the initial reactant of the reaction scheme which itself has a bulk solution activity $A_1$. Thus the rate of step *1* (in Scheme 2.1) is limited by the rds and, according to the above assumptions, is considered to be in quasi-equilibrium and therefore the rates (as current density) of this individual step's forward and reverse reactions may be equated as:

$$z_1 F k_1 a_{A_1} \exp[-z_1 \beta f\eta] = i_1 = z_1 F k_{-1} a^s_{I_2} \exp[z_1(1-\beta) f\eta] \qquad (24)$$

This is rearranged to extract the surface activity of the intermediate $I_2$ in terms of the bulk solution activity of $A_1$ and for simplicity $K_1$ substituted for $k_1 / k_{-1}$. This gives Eqn. 2.25, a Nernst equation-like expression for the quasi-equilibrium:

$$a^s_{I_2} = a_{A_1} K_1 \exp[-z_1 f\eta] \qquad (25)$$

in which $\beta$ has become cancelled in the rearrangement.

Next, the rates of the forward and reverse reactions in step *2* may be similarly equated and the activity of the next intermediate, $I_3$, solved for, as in Eqn. 2.26:

$$a^s_{I_3} = a^s_{I_2} K_2 \exp[-z_2 f\eta] \qquad (26)$$

into which the surface activity for $I_2$ may be substituted from Eqn. 2.25 giving:

$$a^s_{I_3} = a_{A_1} K_1 K_2 \exp[-(z_1+z_2) f\eta] \qquad (27)$$

which is an expression for the surface activity of the intermediate $I_3$ in terms of the (known) bulk solution activity of the overall reaction's initial reactant, the effective concentration of which is *not* potential-dependent.

This procedure may be carried through stepwise for all reaction steps which are in quasi-equilibrium up to the rds, and this then gives the general expression, Eqn. 2.28:

$$a^s_{I_{rds}} = a_{A_1} \left[\prod_{k=1}^{rds-1} K_k\right] \exp\left[-\left[\sum_{k=1}^{rds-1} z_k\right] f\eta\right] \qquad (28)$$

which shows the overall potential-dependence (in the exponential term of Eqn. 2.28) of the cathodic reaction rate that arises from quasi-equilibrium electron-transfers occurring

prior to the rds. The $z_i$'s must all be *integers* and thus each previously transferred electron adds "one" to the $\eta$-dependence factor.

In a similar fashion for the reverse, anodic reaction, a general equation for the surface activity of the intermediate that is the product of the rds can be developed.

### 2.5.1. Adsorption of Intermediates

With the special situation where the reaction intermediates are *adsorbed* onto the surface of the electrode substrate[f], the surface activities of the intermediates, as they are used in the present derivation, would have to be replaced with surface coverage fractions, $\theta$'s, since in this case the available electrode substrate area represents a limit to the extent of reaction. As the electrode becomes completely covered by one or more of the intermediates, the application of larger driving force ($\eta$) will no longer increase the rate of reaction as previously expected.

The quasi-equilibrium expression for step *1* of Scheme 2.1 would, in this case, be (cf. Eqn. 2.24) modified to:

$$z_1 F k_1 a_{4_1} \left(1-\left(\theta_{I_2}+\theta_{I_3}+\cdots\right)\right) \exp\left[-z_1 \beta f \eta\right] = z_1 F k_{-1} \theta_{I_2} \exp\left[z_1 (1-\beta) f \eta\right] \qquad (29)$$

where rearrangement would give:

$$\theta_{I_2} = a_{4_1} \left(1-\left(\theta_{I_2}+\theta_{I_3}+\cdots\right)\right) K_1 \exp\left[-z_1 f \eta\right] \qquad (30)$$

Ordinarily, electrochemical adsorption isotherms would have to be written, e.g. a Frumkin-like isotherm, as given in e.g. Eqn. 2.31, which includes a lateral interaction parameter, g:

$$\frac{\theta_{I_2}}{1-\sum \theta_i} = a_{4_1} K_1 \exp\left[g \cdot \sum \theta_i\right] \cdot \exp\left[f \eta\right] \qquad (31)$$

"g" expresses the way in which increased coverage changes a given species' adsorption energy [89:p.518] and it might be expected that there would be as many g parameters as

---

[f] An important example of this is in the hydrogen evolution reaction [89:p.116].

there were individual types of interactions between adsorbed species. Only in the limiting case where the total electrode coverage, $\Sigma\theta_i$, is low, i.e. $(1-\Sigma\theta_i \rightarrow 1)$ and perhaps also $g = 0$ (but not necessarily), could the potential-dependence be elaborated as developed above in e.g. Eqn. 2.28 in which surface activities were used. If saturation coverage were to prevail, i.e. $\Sigma\theta_i \rightarrow 1$, (for instance at elevated potentials) the coverage and hence the measured rate would become potential-independent. It is therefore important to identify such limiting situations (with a.c. impedance or potential relaxation experiments) since it is the potential-dependence of the rate that is used to elucidate mechanism in electrochemical kinetics. As a final point, the $\theta = 1$ condition usually does not arise because in multi-step reactions, there is usually a following *desorption* step that prevents this, except, of course, in underpotential deposition where no *continuous* Faradaic reaction in time takes place.

### 2.5.2. Rate Equation for Consecutive Electrochemical Reactions

In order to derive the rate equation for the reaction described by Scheme 2.1, the potential-dependent activity expressions for $I_{rds}$ (Eqn. 2.28) and $I_{rds+1}$ have to be substituted back into the rate equation for the rds (Eqn. 2.21). This then gives Eqn. 2.32, the *net overall rate equation for the multi-step electrochemical reaction having a single rds:*

$$i_{net} = zF\left(-a_{A_1} k_{rds}\left[\prod_{k=1}^{rds-1} K_k\right]\exp\left[-\left(\gamma_p + z_{rds}\beta\right)f\eta\right] + a_{A_{n+1}} k_{-rds}\left[\prod_{k=(rds+1)}^{n} \frac{1}{K_k}\right]\exp\left[\left(\gamma_f + z_{rds}(1-\beta)\right)f\eta\right]\right) \quad (32)$$

The first term in Eqn. 2.32 is the cathodic term, *negative* by convention (see footnote b) and where, for simplification, $\gamma_p$ has replaced the sum term in the exponential of Eqn. 2.28. $\gamma_p$ is the total number of electrons transferred prior to the rds. The second term in Eqn. 2.32 is the anodic term which, due to the way its quasi-equilibrium expression is constructed, contains the activity of the overall *product* of the reaction, $A_{n+1}$, the reciprocal of the individual quasi-equilibrium constants, $K_i$'s, and $\gamma_f$ the number of electrons

transferred following the rds.

Grouping potential-independent terms into an exchange current-density term and identifying the arguments of the exponentials as transfer coefficients simplifies the rate equation to:

$$i_{net} = i_o\left(\exp\left[\alpha_a f\eta\right] - \exp\left[-\alpha_c f\eta\right]\right) \tag{33}$$

and this is obviously a BV type of equation (cf. Eqn. 2.20), but where $\beta$ and $(1-\beta)$ in that equation have become replaced respectively by *transfer coefficients*:

$$\alpha_c = \gamma_p + z_{rds}\beta \tag{34i}$$

for the cathodic reaction and

$$\alpha_a = \gamma_f + z_{rds}(1-\beta) \tag{34ii}$$

for the anodic reaction. The first terms in Eqns. 2.34*i* and *ii* are contributions from quasi-equilibrium or non-rate-limiting steps while the second terms are contributions from the rds. Thus preceding and following electron transfers in a reaction mechanism add *integer* contributions[ε] in the transfer coefficients for the rds.

## 2.6. Modifications to the Consecutive Electrochemical Reaction Rate Equation

The rate expression derived in the previous section, Eqn. 2.32, is able to relate complex consecutive electron-transfer reaction mechanisms to experimental potential vs logarithmic current-density relations. When $\beta$ is assumed to be 1/2, the Tafel slopes $(1/\alpha f)$ predicted by this relation can only have values less than or equal to 120 mV dec$^{-1}$ for electron-transfer limited reactions, since electrons transferred in non-rds steps will add integers in the expected $\alpha$ values (i.e. add to $\beta$) and therefore would *decrease* the Tafel slope below 120 mV dec$^{-1}$. For instance, the usual cathodic Tafel slope of 120 mV dec$^{-1}$ for a one electron-transfer over a symmetric barrier is decreased to 40 mV dec$^{-1}$ for one preceding quasi-equilibrium electron-transfer and to 24 mV dec$^{-1}$ for two, etc.

---

[ε] Note that this is only true when the total surface coverage by intermediates is sufficiently small to allow the approximation: $(1-\theta_B-\theta_D\ldots) \rightarrow 1$ (see §2.5.1).

The effect of the occurrence of chemical steps, multi-electron-transfers, or a *rds* that is a dissociation or combination step (i.e. one that involves a change of stoichiometric *coefficients*) will now be examined. Another possible mechanism, a rds having a stoichiometric *number* greater than one, is much more complicated than these others and will be discussed separately in a section that follows.

### 2.6.1. Chemical Steps

If a step within the general mechanism does not involve an electron-transfer its involvement in determining the potential-dependence of the rate will depend on whether it occurs in the rds or not. If some step, *f*, limited by the rds, is a chemical step, its quasi-equilibrium expression will be:

$$a_{I_f} k_f = a_{I_{f+1}} k_{-f} \tag{35}$$

which when rearranged gives:

$$a_{I_{f+1}} = a_{I_f} K_f \tag{36}$$

This term is obviously independent of potential and so its only affect is a trivial one, $K_f$ is multiplied in amongst all the other quasi-equilibrium constants ($\prod K_i$'s).

However, if the rds itself is a chemical step, the transition-state does not involve electron-transfer and hence $\beta$ does not play a part in the net rate (Eqn. 2.37):

$$i_{net} = zF\left(-a_{I_{rds}} k_{rds} + a_{I_{rds+1}} k_{-rds}\right) \tag{37}$$

which is, in this case, potential-independent, although the surface activities of the intermediates, $I_{rds}$ and $I_{rds+1}$ will be indirectly potential-dependent if their prior formation involves electron-transfer reactions. This situation can be described by the transfer coefficients developed previously, Eqn. 2.34i & ii, but where $z_{rds}$ in these would be zero.

### 2.6.2. Multi-Electron-Transfers

A multi-electron-transfer, if rate-limiting (unlikely as these are considered to be [see footnote a]), would modify the transfer coefficients (Eqns. 2.34i and ii) by multiplying the potential-dependence of the rds (the $\beta$ part of Eqn. 2.32) by the number

of electrons involved in this transfer, $z_{rds}$. If not during the rds, such a multi-electron-transfer step would simply contribute to (and disappear into) $\gamma_p$ or $\gamma_f$.

### 2.6.3. Combination or Dissociation as a Rate-Limiting Step

When an electrochemical combination or dissociation step is rate-limiting for a given reaction a unique potential-dependence of the non-rds steps arises due to the change in stoichiometric coefficients[h] between reactant and product of the rds. The simplest examples to envisage are 1) where $\omega$ equivalents of some reactant combine to form a single product in an electrochemical reduction reaction, e.g. $2H^+ + 2e^- \rightarrow H_2$ *or* 2) where a single reactant splits into $\omega$ equivalents of some product, e.g. $Cl_2 + 2e^- \rightarrow 2Cl^-$.

Considering this latter case where a dissociation (reduction) step is rate-limiting, its net rate equation would be written as:

$$i_{net} = zF\left(-a^{s}_{I_{rds}} k_{rds} \exp\left[-z_{rds}\beta f\eta\right] + \left(a^{s}_{I_{rds+1}}\right)^{\omega} k_{-rds} \exp\left[z_{rds}(1-\beta) f\eta\right]\right) \qquad (38)$$

Note that the change in stoichiometric coefficients in this rate-limiting step (1 to $\omega$) affects only the potential-dependence of the surface activity of the product, $I_{rds+1}$, which, in fact, is raised to the $\omega$-th power in Eqn. 2.38. If the potential-dependence of the activities of the intermediates is expanded by the usual quasi-equilibrium approach (Eqns. 2.24 to 2.28) the net rate equation for a reaction, the rds of which is a dissociation is:

$$i_{net} = zF\left(-a_{A_1} k_{rds}\left[\prod_{k=1}^{rds-1} K_k\right]\exp\left[-\left(\gamma_{E-P} + z_{rds}\beta\right) f\eta\right] + a^{\omega}_{A_{n+1}} k_{-rds}\left[\prod_{k=rds+1}^{n} \frac{1}{K_k}\right]^{\omega} \exp\left[\left(\omega\gamma_{E-F} + z_{rds}(1-\beta)\right) f\eta\right]\right) \qquad (39)$$

[h] A stoichiometric *coefficient*, $\omega$, refers to the number of reactant or product equivalents involved in a given step while a stoichiometric *number*, $\nu$, is the number of repetitions of a given reaction step necessary for achievement of an overall multi-step reaction. Although a relative change of $\omega$ in a step usually necessitates that all following steps (in the case of a dissociation) occur $\nu = \omega$ times, the distinction between $\omega$ and $\nu$ should be underlined since a mechanism having a rds with a stoichiometric number greater than one has a unique affect on the theoretical transfer coefficients and will be discussed in §2.7.

where $\gamma_{E\text{-}P}$ and $\gamma_{E\text{-}F}$ are the numbers of electrons transferred in *elementary*[i] electron-transfer steps prior to and following the rds, respectively.

It is at this point that we depart from the terminology used by Bockris and Reddy [86:p.1007] in their often cited, generalized, transfer coefficients, Eqns. 2.1i and ii, i.e. $\gamma_p$ and $\gamma_f$ and introduce $\gamma_{E\text{-}P}$ and $\gamma_{E\text{-}F}$. The difference between these sets of electron-number parameters is that in the latter an electron transferred in a step that occurs say, $\nu$ times (i.e. has a stoichiometric number $\nu$, greater than one) is counted only once and not the $\nu$ times it actually has to occur for one turnover of the overall reaction. This added "complication" to the electron-*accounting* will show more clearly how stoichiometric coefficients and numbers enter into experimentally obtainable transfer coefficients and hence will demonstrate the link between mechanism and experiment.

The transfer coefficients for a *rds that is a dissocation step* are therefore:

$$\alpha_c = \gamma_{E\text{-}P} + z_{rds}\beta \qquad \text{(40i)}$$

$$\alpha_a = \omega\gamma_{E\text{-}F} + z_{rds}(1-\beta) \qquad \text{(40ii)}$$

while those for a *rds that is a combination (reduction) step* are:

$$\alpha_c = \omega\gamma_{E\text{-}P} + z_{rds}\beta \qquad \text{(41i)}$$

$$\alpha_a = \gamma_{E\text{-}F} + z_{rds}(1-\beta) \qquad \text{(41ii)}$$

## 2.7. Tafel Slopes Greater Than 118 mV dec$^{-1}$

### 2.7.1. Foreword

The theoretical transfer coefficients derived from the hypothetical reaction mechanisms considered so far, Eqns. 34i & ii, Eqns. 40i & ii and Eqns. 41i & ii, can predict, if $\beta = 1/2$ is assumed, Tafel slopes that are either *less* than 118 mV dec$^{-1}$ or

---

[i] "elementary" meaning a reaction step that refers to a single transition-state. Electrons, in this case, are thus "counted" for the individual transition-states, and *not* for the $\nu$ times the step actually has to occur for a turnover of the overall reaction. This seemingly minor point has importance to later conclusions. The subscript terminology means: $\gamma$ *E*lementary-*F*ollowing, -*P*revious and (as will be necessary later) -*S*toichiometric.

infinite (for a chemical rds with no quasi-equilibrium electron-transfer steps). They cannot, however, explain Tafel slopes significantly *greater* than 120 $mV\,dec^{-1}$ that are, in fact, sometimes observed for the Al electrodeposition reaction from the thf hydride-baths.

Tafel slopes that are not infinite but substantially greater than 120 $mV\,dec^{-1}$ can be explained by: 1) an arbitrary assumption that $\beta < 1/2$; 2) the affect of barrier-layer films [97-99] (but this is usually only in the case of anodic reactions, viz. not for electrodeposition and dissolution reactions); and 3) an electrochemical reaction mechanism where the rds is a chemical step *and* has a stoichiometric number, $\nu$, greater than two (refer to Eqn. 2.1). This latter possibility will be developed below in terms of a general multi-step reaction mechanism, the reason for which is to make clear that a rds having a $\nu$ greater than one can only give a fractional contribution to *one* transfer coefficient (either $\alpha_c$ or $\alpha_a$), but not *both*. This point is particularly significant to the discussion in the next chapter which examines published mechanisms for the electrodeposition and dissolution of aluminum from the hydride-bath. One particular published mechanism (see §3.3.1) was based, as we have found during the course of the present research, upon an incorrect application of the theoretical transfer coefficients (Eqns. 2.1i & ii) arising directly from a stoichiometric number greater than one.

### 2.7.2. Stoichiometric Number: The Problem

The number of times a given reaction step must occur for one turnover of the whole reaction is known as the *stoichiometric number*, $\nu$. The stoichiometric number of a reaction is specifically the number of times the *rds* has to occur. This quantity was originally defined by Horiuti for the hydrogen reaction [100,101]. A more recent benchmark for the treatment of the stoichiometric number in the theoretical evaluation of transfer coefficients is the derivation of Bockris and Reddy (B&R) in their monograph [86:p.1005], where $\nu$ forms a parameter of the experimentally accessible transfer coefficients (shown earlier Eqns. 2.1i & ii). The concept of a stoichiometric number has, however, suffered from inconsistent and ambiguous presentations in the electrochemical

literature and is still, in fact, poorly understood [102].

At first glance, the first terms of these transfer coefficients, i.e. the first on the lhs of Eqns. 2.1i and 2.1ii, seem to be able to give fractional contributions (i.e. 0 - 1) for *both* anodic and cathodic transfer coefficients simultaneously due to $\nu$ in these terms; e.g. if $z_{rds} = 0$ and $\nu > \gamma_p$ and $\gamma_f$. This, in fact, is not possible and in order to prove this and to establish the appropriate use of these transfer coefficients they will be derived here for the two general types of reaction mechanism that require use of a stoichoimetric number (Schemes 2.2 and 2.3, shown below).

### 2.7.3. Reaction Mechanisms Involving a Stoichiometric Number Greater Than One

In the closed reaction sequences considered in the present work, stoichiometric numbers greater than one can arise *only* in order to satisfy a material balance for a reaction step preceding or following the rds that creates or consumes $\nu$ intermediates in a single transition-state.

The first of these cases, represented by Scheme 2.2, is the situation where some

Scheme 2.2. Consecutive Electrochemical Reaction Scheme Involving a Dissociation Step Occurring Before the Rds

| | | | | | |
|---|---|---|---|---|---|
| Step 1. | $A_1 + z_1 e^-$ | $\rightleftarrows$ | $I_2$ | } | Group I |
| . | . . . . . | | | | |
| i-1. | $I_{i-1} + z_{i-1} e^-$ | $\rightleftarrows$ | $I_i$ | | |
| i. | $I_i + z_i e^-$ | $\rightleftarrows$ | $\nu I_{i+1}$ | | |
| i+1. | $\nu[I_{i+1} + z_{i+1} e^-$ | $\rightleftarrows$ | $I_{i+2}]$ | } | Group II |
| . | . . . . . | | | | |
| rds. | $\nu[I_{rds} + z_{rds} e^-$ | $\rightleftarrows$ | $I_{rds+1}]$ | | |
| . | . . . . . | | | | |
| j. | $\nu[I_j + z_j e^-$ | $\rightleftarrows$ | $I_{j+1}]$ | } | Group III |
| . | . . . . . | | | | |
| n. | $\nu[I_n + z_n e^-$ | $\rightleftarrows$ | $A_{n+1}]$ | | |

facile and therefore non rate-limiting *dissociation* step occurs before the rds and produces, from a unit reactant, $\nu$ identical intermediate equivalents; this is step $i$ in Scheme 2.2. These $\nu$ intermediates must react in respective subsequent steps, including the rds, $\nu$ times, corresponding to a stoichiometric number > 1 for the reaction.

In the second case (Scheme 2.3), some non rate-limiting step, occurring after the rds in the reaction sequence, *combines* $\nu$ intermediate equivalents into a unit product $I_{j+1}$ in a reduction step and this is *step j* in Scheme 2.3. The $\nu$ equivalents that must react and combine in *step j* require that all prior steps, including the rds, be repeated $\nu$ times to supply this step.

Scheme 2.3. Consecutive Electrochemical Reaction Scheme Involving a Combination Step Occurring After the Rds

| | | |
|---|---|---|
| Step 1. | $\nu[A_1 + z_1e^-$ | $\rightleftarrows I_2]$ |
| . | . . . . . | |
| i. | $\nu[I_i + z_ie^-$ | $\rightleftarrows I_{i+1}]$ |
| . | . . . . . | |
| rds. | $\nu[I_{rds} + z_{rds}e^-$ | $\rightleftarrows I_{rds+1}]$ |
| . | . . . . . | |
| j. | $\nu I_j + z_je^-$ | $\rightleftarrows I_{j+1}$ |
| . | . . . . . | |
| n. | $I_n + z_ne^-$ | $\rightleftarrows A_{n+1}$ |

The rate of the overall reaction is controlled by the transition-state of the rds thus the *net* rate expression will be:

$$i_{net} = zF\left(-a_{I_{rds}}^{s} k_{rds} \exp\left[-z_{rds}\beta f\eta\right] + a_{I_{rds+1}}^{s} k_{-rds} \exp\left[z_{rds}(1-\beta) f\eta\right]\right) \qquad (42)$$

Note, in Eqn. 2.42, that the overall current corresponds to z electrons, although that for the rds is only $\nu$ times that for one turnover of this reaction step (i.e. $z_{rds}\nu \leq z$). The potential-dependent exponential term is also independent of $\nu$ and this may be explained if we recall that the effect of an applied overpotential in electrochemical kinetics is to

modify the relative energies of reactant and product curves and, by extension, that of the transition-state for the elementary (recall footnote i) reaction step. The potential-dependence of the energy of the transition-state is sensitive to the number of electrons transferred *in* it, but *not* the $\nu$ times that it must occur per turnover of the overall reaction; thus the exponential in Eqn. 2.42 is independent of $\nu$.

### 2.7.4. Prior Dissociation, Forward Reaction Direction

We consider first Scheme 2.2, i.e. a prior dissociation giving a rds having a stoichiometric number $\nu$. The surface activities of the intermediate species participating in the rds, will again be potential-dependent and can be evaluated, taking into consideration the usual quasi-equilibrium assumptions. In order to understand the significance of the potential-dependence it is useful to split the reaction steps into three groups and to focus on the dissociation step and rds separately. For the prior dissociation scheme, the groups (shown in Scheme 2.2) are: Group I, up to step $i$, the dissociation step; Group II, from the dissociation step to the rds and; Group III all steps following the rds which are important only when the reverse reaction is considered. The dissociation reaction step (or equally, a combination step; Scheme 2.3) can be thought of as that step that gives rise to the necessity that subsequent steps (or preceding steps, in the case of a combination) occur more than once. We shall call this step the *stoichiometry-determining* step. This separation of the reaction steps is done because it helps to identify clearly and specifically where and how $\nu$ becomes a part of the potential-dependence of the reaction rate and hence ultimately the transfer coefficients.

Thus to expand the potential-dependence of the surface activity of the reactant (intermediate) of the rds, and hence of the forward, reductive reaction direction, we build up progressively from the initial reactants. The potential-dependence of Group I reaction steps would be exactly that which was evaluated previously (§2.5) for the simple consecutive reaction sequence, since there is no change in *molecularity* between (or *stoichiomet-*

*ric coefficients*[j] of) reactant and product for any of these reaction steps. Thus the potential-dependence of the activity of the reactant of the dissociation step, $I_i$, is given by Eqn. 2.28 (but where "*i - 1*" is used as the limit for the sum and product in that equation).

The surface activity of the product of the dissociation step (step *i*) is defined by equating the rates of the forward and reverse directions of this reaction step, i.e. assuming quasi-equilibrium:

$$z_i F a_{I_i}^s k_i \exp[-z_i \beta f\eta] = z_i F \left(a_{I_{i+1}}^s\right)^\nu k_{-i} \exp[z_i(1-\beta) f\eta] \qquad (43)$$

which, upon rearrangement, gives:

$$\left(a_{I_{i+1}}^s\right)^\nu = a_{I_i}^s K_i \exp[-z_i f\eta] \qquad (44)$$

Note for Eqn. 2.43 that, unlike the case where "*net*" rate expressions (e.g. Eqn. 2.42) and hence all the electrons transferred in the overall reaction, are considered, only those electrons transferred in the single step (*step i+1*) are written in these quasi-equilibrium expressions (i.e. $z_i$ in Eqn. 2.43). This point is moot, though, because the number of electrons becomes cancelled in rearrangement (i.e. Eqn. 2.44). Substituting for the activity of $I_i$, i.e. Eqns. 2.28 with the limit of "*i - 1*" viz. for steps up to the dissociation in *step i*, and taking the $\nu$-th root gives Eqn. 2.45:

$$a_{I_{i+1}}^s = a_{A_1}^{1/\nu} \left[\prod_{k=1}^{i-1} K_k\right]^{1/\nu} K_i^{1/\nu} \exp\left[-\left[\sum_{k=1}^{i-1} z_k + z_i\right] \frac{f\eta}{\nu}\right] \qquad (45)$$

To continue the evaluation of the potential-dependence of activities of intermediates, we now consider Group II reaction steps, i.e. those between the dissociation step and the rds. The quasi-equilibrium expression for the first of these, *step i+1*, is:

$$\nu z_{i+1} F a_{I_{i+1}}^s k_{i+1} \exp[-z_{i+1} \beta f\eta] = \nu z_{i+1} F a_{I_{i+2}}^s k_{-i+1} \exp[z_{i+1}(1-\beta) f\eta] \qquad (46)$$

When this relation is rearranged to solve for the surface activity of the product of this step, the stoichiometric number will *cancel*. Although this step (and in fact all others in

---

[j] See footnote h.

Group II) individually occurs $\nu$ times, they are, in fact, independent of $\nu$, and hence the potential-dependence of the Group II reaction steps, *steps i+1* through *rds-1*, will be (analogously to Eqn. 2.28) given by:

$$a^s_{I_{rds}} = a^s_{I_{i+1}} \left[\prod_{k=i+1}^{rds-1} K_k\right] \exp\left[-\left[\sum_{k=i+1}^{rds-1} z_k\right] f\eta\right] \tag{47}$$

Then, if we substitute for the surface activity of $I_{i+1}$ from Eqn. 2.45:

$$a^s_{I_{rds}} = a^{1/\nu}_{A_1} \left[\prod_{k=1}^{i} K_k\right]^{1/\nu} \left[\prod_{k=i+1}^{rds-1} K_k\right] \exp\left[-\left[\frac{1}{\nu}\sum_{k=1}^{i} z_k + \sum_{k=i+1}^{rds-1} z_k\right] f\eta\right] \tag{48}$$

which is the potential-dependence of all intermediates affecting the rate of the forward, reductive, direction of the reaction.

If we identify where $\nu$ arises in Eqn. 2.48, it is clear that Group I steps (see Scheme 2.2) and the dissociation step contribute in a power of $1/\nu$ that of Group II steps, i.e. those between the dissociation and the rds (*steps i+1* to *rds-1*) and thus portions of both the pre-exponential and the exponential (potential-dependent) terms in Eqn. 2.48 are dependent on $\nu$ while other portions are independent of $\nu$.

### 2.7.5. Prior Dissociation, Reverse Reaction Direction

Considering now the reverse, anodic, reaction direction of the same reaction, Scheme 2.2, the surface activity of the cathodic product of the rds, $I_{rds+1}$, (which is now the reactant for the reverse anodic reaction) will be potential-dependent if it is an intermediate. The Group III steps, now all those following the rds, are all repeated $\nu$ times[k], but when their quasi-equilibrium expressions are derived (for instance for the surface activity of $I_{rds+1}$) they will all be independent of $\nu$, just as was the case for Group II reaction steps in the forward direction (Eqn. 2.46 and the related text); thus $\nu$ has no bearing on the potential-dependence, given by Eqn. 2.49, of these steps (*steps rds+1* to *n*):

---

[k] It is assumed that the $\nu$ intermediates formed in the preceding dissociation do not recombine in the same reaction.

$$a^{s}_{I_{rds+1}} = a_{A_{n+1}}\left[\prod_{k=rds+1}^{n}\frac{1}{K_k}\right]\exp\left[\left[\sum_{k=rds+1}^{n} z_k\right]f\eta\right] \tag{49}$$

When Eqns. 2.48 and 2.49 are substituted into Eqn. 2.42, the result is:

$$i_{net} = zF\left(-a_{A_1}k_{rds}\left[\prod_{k=1}^{i}K_k\right]^{1/\nu}\left[\prod_{k=i+1}^{rds-1}K_k\right]\exp\left[-\left(\frac{\gamma_{E-S}}{\nu}+(\gamma_{E-P}-\gamma_{E-S})+z_{rds}\beta\right)f\eta\right]\right.$$
$$\left. + a_{A_{n+1}}k_{-rds}\left[\prod_{k=rds+1}^{n}\frac{1}{K_k}\right]\exp\left[(\gamma_{E-F}+z_{rds}(1-\beta))f\eta\right]\right) \tag{50}$$

which is the net rate equation for a *reaction whose rds has a stoichiometric number of* $\nu$ arising from a *previous dissociation step*. The resulting transfer coefficients are:

$$\alpha_c = \frac{\gamma_{E-S}}{\nu} + (\gamma_{E-P} - \gamma_{E-S}) + z_{rds}\beta \tag{51i}$$

*and*

$$\alpha_a = \gamma_{E-F} + z_{rds}(1-\beta) \tag{51ii}$$

where $\gamma_{E-F}$, $\gamma_{E-P}$ and $\gamma_{E-S}$ have replaced the summation terms in the exponentials of Eqn. 2.50 and are the total numbers of electrons transferred in elementary (footnote *i*) electron-transfer steps following the rds, prior to the rds and those up to and including the *stoichiometry-determining step* in the case of a previous dissociation (or including and following the stoichiometry-determining step for a following combination). Note that the number of elementary electrons transferred between the dissociation step and the rds is given by $\gamma_{E-P} - \gamma_{E-S}$, but that the *actual* number of electrons transferred in these steps is $\nu$ times that, viz. $\nu(\gamma_{E-P} - \gamma_{E-S})$. The added coefficient, $\gamma_{E-S}$, is used in order to maintain links to both the familiar terminology of B&R (Eqns. 2.1i and 2.1ii) and the stoichiometry-determining step. These points, it is hoped, will re-enforce the connection between mechanistic situations and these kinetic derivations.

### 2.7.6. Following Combination Step

The second case, represented by Scheme 2.3, involves a *combination* (reduction)

*step* following the rds, e.g. in step $j$, will also gives rise to a stoichiometric number, $\nu$, for the rds. The transfer coefficients for this case, following a similar derivation as above, are:

$$\alpha_c = \gamma_{E\text{-}P} + z_{rds}\beta \qquad (52i)$$

*and*

$$\alpha_a = \frac{\gamma_{E\text{-}S}}{\nu} + (\gamma_{E\text{-}F} - \gamma_{E\text{-}S}) + z_{rds}(1-\beta) \qquad (52ii)$$

### 2.7.7. Electron-Number Coefficients

The preceding/following electron-number coefficients ($\gamma$) used here are slightly different and, in fact, less general than those employed by B&R (viz. $\gamma_p$ and $\gamma_f$) in their transfer coefficient analysis (Eqn. 2.1). They are, however, related and for a *preceding dissociation* the expressions that link them are:

$$\gamma_p = \gamma_{E\text{-}S} + \nu\cdot(\gamma_{E\text{-}P} - \gamma_{E\text{-}S}) \qquad (53i)$$

*and*

$$\gamma_f = \nu\cdot\gamma_{E\text{-}F} \qquad (53ii)$$

Substitution of these $\gamma_p$ and $\gamma_f$ expressions into the B&R transfer coefficients (Eqn. 2.1) demonstrates immediately the equivalence of the derivations, but we believe that the expanded transfer coefficients derived here are expressed in a fashion that is more directly relevant to their use in mechanism determination. Our notation, while requiring the distinction between combination and dissociation cases, shows more clearly and specifically how the *type of mechanism* involved determines the transfer coefficients. Additionally, substituting $\nu = 1$ into either of the above coefficients (Eqn. 2.51 or 2.52) reduces them to those for a simple consecutive electrochemical reaction, Eqns. 2.35i & ii.

One important point of clarification of the B&R relations arises from the treatment here as follows. If we consider a stoichiometric number arising due to a preceding dissociation, the *non-rds* contribution to the anodic transfer coefficient is $\gamma_f/\nu$ (Eqn. 2.1i) in B&R's terminology and $\gamma_{E\text{-}F}$ (Eqn. 2.49i) according to the terminology used here. It would seem from first glance at the B&R transfer coefficients that the non-rds steps

following the rds could contribute a fraction (i.e. less than one) to the transfer coefficients if $\nu > \gamma_f$. The non-rds part of the anodic transfer coefficient from the present derivation clearly demonstrates that the contribution of $\gamma_{E\text{-}F}$ to $\alpha_a$ can only be of *whole numbers* since only integral numbers of electrons can be transferred in electrochemical steps. Thus, the conclusion is that for either a preceding dissociation or a following combination, either of the non-rds terms, $\gamma_p / \nu$ or $\gamma_f / \nu$, can be less than one, but that if either one is less than unity, then the other *must* be a whole number.

The B&R transfer coefficient analyses have often been cited in literature dealing with mechanisms and kinetics of multi-step electrochemical reactions. However, it has been found in literature related to the subject of this thesis that the seemingly simple and straight-forward transfer coefficients of B&R have been applied improperly to the determination of the mechanism of the aluminum electroplating reaction in the hydride-bath [39]. This error was found to be due entirely to the mistaken assumption that *both* anodic and cathodic non-rds terms, i.e. $\gamma_p / \nu$ *and* $\gamma_f / \nu$, of B&R's theoretical transfer coefficients could *simultaneously* give fractional contributions and so account for the transfer coefficients derived from experimental Tafel plots. This particular work and their deduced mechanism will be discussed more thoroughly in the next chapter.

As a final note, it is conceivable that $\nu$ could be nonintegral, although it would be a fraction based on small integers. As an illustrative example consider a simplified reaction mechanism for aluminum reduction:

$$\begin{aligned} 3\,(Al^{3+} + 2e^- &\rightarrow Al^+) \\ 3Al^+ &\rightarrow 2Al + Al^{3+} \end{aligned} \qquad (54)$$

If this reaction were limited by the first step, the stoichiometric number for that step would be divided by two since obviously the reaction produces two aluminum atoms by disproportionation and thus the actual stoichiometric number would be 3/2.

## 2.8. Summary

All of the various rate equations that have been derived in this chapter have the form of the general BV equation for a multi-step consecutive reaction, i.e. Eqn. 2.33.

The derived transfer coefficients, $\alpha_c$ and $\alpha_a$, which can be obtained from experimental current versus potential relations, are summarized in Table 2.1 for each of the modifications to the consecutive electrochemical step type of mechanism considered here.

A stoichiometric number greater than one for the rds will arise specifically when a reaction step other than the rds involves a change in *molecularity*, due to either preceding dissociation or following combination steps (speaking for the reductive direction of reaction). Such reaction mechanisms are the only ones amongst those considered here that can give rise to an $0 < \alpha < 1/2$ condition when $\beta$ is assumed to be 1/2, but a necessary condition is that the $\alpha$ for the opposite direction of the reaction must be a whole number.

Table 2.1. Summary of derived transfer coefficients

| Mechanism details | $\alpha_a$ | $\alpha_c$ | Comments |
|---|---|---|---|
| A single electrochemical reaction step | $z(1-\beta)$ | $z\beta$ | Eqn. 2.20 |
| Multiple electrochemical reaction steps | $\gamma_f+z_{rds}(1-\beta)$ | $\gamma_p+z_{rds}\beta$ | Eqns. 2.33i & ii |
| Multiple electron transfer in rds | $\gamma_f+z_{rds}(1-\beta)$ | $\gamma_p+z_{rds}\beta$ | $z_{rds}$ can be greater than one<br>Eqn. 2.33i & ii |
| Chemical and electrochemical reaction steps | $\gamma_f+z_{rds}(1-\beta)$ | $\gamma_p+z_{rds}\beta$ | $z_{rds}$ is zero if the rds is a chemical step<br>Eqn. 2.33i & ii |
| rds has a stoichiometric coefficient | | | |
| rds is a dissociation | $\omega\gamma_{E\text{-}F}+z_{rds}(1-\beta)$ | $\gamma_{E\text{-}P}+z_{rds}\beta$ | Eqn. 2.40i & ii |
| rds is a combination | $\gamma_{E\text{-}F}+z_{rds}(1-\beta)$ | $\omega\gamma_{E\text{-}P}+z_{rds}\beta$ | Eqn. 2.41i & ii |
| rds has a stoichiometric number of $\nu$ | | | $\nu$ involves only those electrons transferred before a diss$^n$ or after a comb$^n$ |
| A dissociation before the rds | $\gamma_{E\text{-}F}+z_{rds}(1-\beta)$ | $\gamma_{E\text{-}S}/\nu+(\gamma_{E\text{-}P}-\gamma_{E\text{-}S})+z_{rds}\beta$ | Eqn. 2.51i & ii |
| A combination after the rds | $\gamma_{E\text{-}S}/\nu+(\gamma_{E\text{-}F}-\gamma_{E\text{-}S})+z_{rds}(1-\beta)$ | $\gamma_{E\text{-}P}+z_{rds}\beta$ | Eqn. 2.52i & ii |

# Chapter 3 Literature Review on the Hydride-Baths and Their Mechanisms of Plating

## 3.1. Foreword

Aluminum can be electrodeposited at appreciable rates from a *hydride-bath* composed of $AlCl_3$ and $LiAlH_4$ dissolved in thf at concentrations between 0.3 and 2.0 M. The rate of the electrodeposition of Al is limited by the rate of the electron-transfer reactions, while that due to the nucleation and lattice-building of the Al phase is only a limitation at very high overpotentials or in the early stages of deposition onto foreign substrates. Nucleation and growth will be discussed in detail later (Chapter 8), but the mechanism of the required electron-transfer reactions will be reviewed here first.

It will be shown later (Chapter 5) that the distribution of component aluminates [41] varies with the baths' $Cl^-$ to $H^-$ ratio. This ratio, denoted by "*r*", is actually $[AlCl_3] / [AlH_4^-]$. It has been noted during the course of the present thesis work that the mechanistic parameters of the process of electrodeposition from the hydride-bath also vary with bath composition, specifically when $AlCl_3$ is in greater proportion than $AlH_4^-$, i.e. $Cl^-$-rich and in the opposite case, $H^-$-rich. Since Al possesses three valence electrons and only one stable oxidation state, the reduction of $Al^{3+}$ solution species necessarily involves a multi-step, multi-electron mechanism of the type considered in Chapter 2. This chapter examines the reaction mechanisms that have been published attempting to account for the electrochemical behaviour observed for hydride-baths of various compositions.

## 3.2. Experimental Results From Al Deposition and Dissolution Experiments

*Transfer coefficients*, $\alpha$'s, evaluated from steady-state *Tafel* relation measurements are central to mechanism elucidation (e.g. see Chapter 2). The $\alpha$'s for the aluminum reduction reaction onto, and dissolution from, aluminum itself were evaluated in the present work and also elsewhere [38-41 [a]] to be *ca.* $\alpha_c = \alpha_a = 1/2$ in $Cl^-$-rich baths and

[a] The last of these references is actually concerned with work on the same components, but in a mixture of thf and toluene. The mechanism and kinetics were not found to be different from those in pure thf.

*ca.* $\alpha_c = 1/3$ and $\alpha_a = 2/3$ in $H^-$-rich baths. Although, all experimental results were similar (only one group [39,40] has studied the $H^-$-rich bath), there has not been any degree of concensus with regard to the reaction mechanisms deduced.

Mechanism analyses in all the above cited works have made use of the principles developed by B&R (discussed in Chapter 2) for interpretation of Tafel slopes for generalized mechanisms of multi-step reactions the overall rates of which are limited by that of a single step (the rds). Their derived transfer coefficients which were discussed in Chapter 2, have been widely applied to the examination of multi-step electrochemical reactions and are reproduced here:

$$\alpha_c = \frac{\gamma_p}{\nu} + z_{rds}\beta \qquad \text{(1i)}$$

*and*

$$\alpha_a = \frac{\gamma_f}{\nu} + z_{rds}(1-\beta) \qquad \text{(1ii)}$$

where $\gamma_p$, $z_{rds}$ and $\gamma_f$ are respectively the number of electrons transferred in reaction steps *preceding*, *during* and *following* a rds, $\nu$ is the so-called stoichiometric number [100] of the rds and $\beta$ the *symmetry factor* of the kinetic barrier of the rds when this step involves an electron-transfer.

## 3.3. Published Mechanisms

The published mechanisms that are the subject of the present discussion will first be summarized below in the order they have appeared in the literature and then discussed in more detail later. The four cited works [38-41] are from three separate groups and the postulated mechanisms are reproduced below. All these three works have examined the electrochemical behaviour in $Cl^-$-rich baths, but only in the first of these were attempts made to report and explain the behaviour also in $H^-$-rich baths.

The mechanism of Galova and coworkers [39,40] is given in Scheme 3.1 in which they attempt, in a single reaction scheme, to account for two parallel mechanisms for Al deposition from either the $Cl^-$-rich or the $H^-$-rich baths. For the $Cl^-$-rich bath, step *1* is the rds. The underlines and double underlines are used in Scheme 3.1 to relate products

of antecedent steps to respective reactants in subsequent steps.

Scheme 3.1. Al Electrodeposition Mechanism According to Galova et al.

| | | | | | | | |
|---|---|---|---|---|---|---|---|
| Step 1 | $3AlX_4^-$ | + | $3e^-$ | → | $\underline{3AlX_2\cdot}$ | + $6X^-$ | |
| 2 | $\underline{2AlX_2\cdot}$ | | | ⇄ | $Al_2X_4$ | | } chemical |
| 3 | $Al_2X_4$ | | | ⇄ | $\underline{Al^+}$ | + $AlX_4^-$ | } steps |
| 4 | $\underline{AlX_2\cdot}$ | + | $e^-$ | ⇄ | $\underline{Al^+}$ | + $2X^-$ | |
| 5 | $\underline{2Al^+}$ | + | $2e^-$ | ⇄ | 2Al | | |
| Overall: | $2AlX_4^-$ | + | $6e^-$ | → | 2Al | + $8X^-$ | |

The alternate reaction pathways both have the same first and last steps, *1* and *5* respectively, but the difference lies in whether, for the second step, the reaction goes through the chemical steps, *2* and *3*, or the electrochemical step *4*. Steps *2* then *3* or step *4* are alternate parallel pathways and hence are part of separate mechanisms. The two have been combined in Scheme 3.1 and then, curiously, the other reaction steps (*1* and *5*) have been balanced as if they occurred *simultaneously*. To clarify this point, consider step *1*. If either of the chemical steps (*2* or *3*) in Scheme 3.1 is the rds (proposed as the case for $H^-$-rich baths) then it would be necessary for step *1* to occur *twice* to satisfy the material balance for the chemical step. If the reaction proceeds through the electrochemical step *4* then step *1* would have to occur only *once*. Thus, when these two alternatives are combined, step *1* occurs *three* times as is written in Scheme 3.1. This point can lead to some confusion and will be considered later.

The mechanism of Graef [41], who examined only the $Cl^-$-rich bath, is much clearer and is given in Scheme 3.2:

Scheme 3.2. Al Electrodeposition Mechanism According to Graef

| | | |
|---|---|---|
| Step 1 | $3[Al^{3+} + e^- \rightarrow Al^{2+}]$ | |
| 2 | $3Al^{2+}$ | $\rightleftarrows Al + 2Al^{3+}$ |

where step *1*, a single electron-transfer, repeated three times (i.e. $\nu = 3$), was taken as the rds followed by a facile disproportionation [41]. $Cl^-$ or $H^-$ ligand rearrangement or dissociation was not considered within the mechanism which makes it rather unrealistic.

The mechanism of Badawy et al. [38] for the $Cl^-$-rich bath is:

Scheme 3.3. Al Electrodeposition Mechanism According Badawy et al.

| | | | | | | | |
|---|---|---|---|---|---|---|---|
| Step 1 | $AlX_4^-$ | + | $e^-$ | $\rightleftarrows$ | $AlX_2^{\bullet}$ | + | $2X^-$ |
| 2 | $AlX_2^{\bullet}$ | + | $e^-$ | $\rightleftarrows$ | $Al^+$ | + | $2X^-$ |
| 3 | $Al^+$ | + | $e^-$ | $\rightleftarrows$ | Al | | |

a reaction sequence involving three successive electron-transfers with ligand dissociation in which, it was proposed, the rds was not the same for both reductive and oxidative reaction directions. In the forward, cathodic reaction direction, step *1* is the rds and in the reverse anodic reaction direction, step *3* is the rds, that is, it is the *first* electron transferred in either direction that limits the reaction.

For $H^-$-rich baths, however, these authors stated that "activation polarization was not observed". Whether this was meant to imply that all steps were at equilibrium and that some other mechanism applied was not clear from their discussion.

It will be noted that several of the reaction steps would involve electron-transfer with displacement of the ligand $X^-$ as a free anion, which is reminiscent of electro-organic "$S_N2$"-type processes, e.g. as for known reductions of alkyl-halides of the type:

$$RX + e^- \rightarrow R^{\bullet} + X^- \qquad (2)$$

### 3.3.1. Discussion of the Mechanism According to Galova et al.

A practical aspect of the electrodeposition reaction from hydride plating baths is

that they show complicated mixed control in their Tafel plots. The measured rate of an electrochemical reaction can be limited by any of a number of processes, for instance when solution diffusion of reactants and products or surface-diffusion of reaction intermediates along the electrode surface is slow, or when complete electrode coverage by reactive intermediates is limiting. In order to extract mechanistic parameters from steady-state Tafel plots, however, the rate must be limited exclusively by the activation energy of one of the electrochemical (or chemical) steps of the overall reaction (or by the *kinetics* of the reaction). By rotating the substrate electrode, which creates forced solution convection towards and from the reaction sites at the electrode/solution interface, solution diffusion limitation can often be eliminated. A surface-diffusion limitation, e.g. in crystal-building processes, cannot be eliminated by electrode rotation, but such a limitation is expected only at low overpotentials, anyway [89:p.209].

Galova et al. [39,40] recorded Tafel relations for $H^-$-rich and $Cl^-$-rich baths and made back-reaction correction to their experimental Tafel plots near the reversible potential. This procedure (which will be examined more closely in §6.6.4) involves replacing the measured current-density, $i$, by a "corrected" current term, $\log(i/(1-\exp[z/\nu f|\eta|)$, that accounts for the fact that at low overpotentials the reverse reaction rate becomes appreciable and diminishes the measured current. The correction expands down toward $E_r$ the overpotential region from which slopes can be evaluated from Tafel plots and additionally allows determination of $\nu$ by the substituted value of $z/\nu$ (z is unequivocally equal to three for aluminum) that gives the best fit correction curve. The stoichiometric number they determined was three for both $Cl^-$-rich and $H^-$-rich baths.

The determined transfer coefficients for $Cl^-$-rich baths were *ca.* $\alpha_a = 1/2$ and $\alpha_c = 1/2$. The authors fitted these to the following mechanistic parameters of the B&R relation (Eqn. 3.1i and 3.1ii): $\gamma_p = 0$; $\gamma_f = 0$; $r_{rds} = 1$ and $\nu = 3$ which correspond to a thrice occurring rds in which a single electron is transferred; the authors seem to identify this as *step-1* of Scheme 3.1. Values for the $H^-$-rich baths were *ca.* $\alpha_a = 2/3$ and $\alpha_c = 1/3$ and these were fitted to the following parameters: $\gamma_p = 1$; $\gamma_f = 2$; $r_{rds} = 0$ and

$\nu$ =3, which correspond to an rds being a *chemical* step (i.e. $r_{rds} = 0$) that occurs three times for each turnover of the reaction in which one electron is transferred before and two after the rds (for the reductive direction of reaction) in non-rate-limiting steps. The problem with their treatment is that these experimentally derived parameters do not actually correspond to values expected for mechanisms that they have proposed. This is all rather confusing, and so we have compared in Table 3.1 the parameters for the transfer coefficients that were experimentally observed and those that correspond to the proposed mechanisms (compare the $\alpha$'s in the first two rows with those in the last three).

Table 3.1. Transfer Coefficients and Mechanistic Parameters From Galova's Work

| | $\gamma_p$ | $r_{rds}$ | $\gamma_f$ | $\nu$ | $\alpha_a$ | $\alpha_c$ |
|---|---|---|---|---|---|---|
| From Experimental Observation | | | | | | |
| $Cl^-$ | 0 | 1 | 0 | 3 | $^1/_2$ | $^1/_2$ |
| $H^-$ | 1 | 0 | 2 | 3 | $^2/_3$ | $^1/_3$ |
| From Proposed Scheme 3.1 | | | | | | |
| $Cl^-$ electrochemical | 0 | 1 | 2 | 1 | $^1/_2$ | $^5/_2$ |
| $Cl^-$ chemical | 0 | 1 | 1 | 2 | $^1/_2$ | 1 |
| $H^-$ | 2 | 0 | 1 | 1 | 2 | 1 |

Galova's mechanism in Scheme 3.1 suffers from some serious inconsistencies in logic, seeming not to correspond at all to the conclusions of the transfer coefficient analysis given above. In order to try to clarify this problem we consider the $Cl^-$-rich bath, for which Galova proposed the thrice occurring reaction step, step *1*, as rate-limiting. *Step-1* does indeed occur three times as written in Scheme 3.1, but only because the two alternate reaction mechanisms were considered simultaneous (which, n.b., they do not; they occur in baths of *different* composition).

There are two possible mechanisms in which step *1* could be the rds. Step *1* (as

rds) would occur only *once* for a purely "electrochemical" mechanism (i.e. steps *1-4-5*) and would give B&R parameters of $\gamma_p = 0$; $\gamma_f = 2$; $r_{rds} = 1$ and $\nu = 1$ corresponding to transfer coefficients of $\alpha_a = 5/2$ (!) and $\alpha_c = 1/2$. If, for the same rds, the mechanism involved the chemical steps (i.e. steps *1-2-3-5*), step *1* would occur *twice* and would give B&R parameters of $\gamma_p = 0$; $\gamma_f = 1$; $r_{rds} = 1$ and $\nu = 2$ corresponding to transfer coefficients of $\alpha_a = 1$ and $\alpha_c = 1/2$ (cf. in Table 3.1).

Thus the proposed mechanism for $Cl^-$-rich baths cannot account for the $\alpha$'s experimentally observed by Galova. A possibility that would, however, be consistent with the experimental $\alpha$'s is if the rds was not the same for *both* reaction directions, but was the first oxidation electron for the anodic direction of reaction (step *5*) and the first reduction electron for the cathodic direction (step *1*). It is, of course, not at all impossible for a reaction mechanism to change with potential when displaced from equilibrium; shifting potential-energy surfaces of intermediates, reactants and products of the reaction could easily make some other transition-state kinetically limit the rate of the overall reaction at appreciable overpotentials. This point is considered later in the present thesis work (§6.6.5), but Galova did not consider this possibility.

For the $H^-$-rich baths the $\alpha$'s were $\alpha_a = 2/3$, $\alpha_c = 1/3$ for which a mechanism limited by one of the chemical steps is assumed to occur three times, preceded by transfer of one electron and succeeded by two. According to Galova's mechanism in Scheme 3.1, however, the chemical steps proposed as being the rds *do not* occur three times (i.e. have $\nu = 3$), but take place only *once* and this is inconsistent with their evaluated stoichiometric number. They have also confused the number of electrons transferred before and after the rds. If $\alpha_c = 1/3$ when the rds is a chemical step, it is required that $\gamma_p / \nu = 1/3$ corresponding to one electron transferred prior to the rds, but according to their reaction mechanism for the $H^-$-rich bath, *step-1* has to occur *twice* to supply the material for the chemical steps in the overall reaction.

Beyond these difficulties is the fact that arose out of the examination of transfer coefficients given in Chapter 2. Amongst the parameters of the transfer coefficients of

B&R, one of the non-rds terms (either $\gamma_p / \nu$ or $\gamma_f / \nu$) can be fractional while the other has necessarily to be a whole number. Given that all $\alpha$'s were found to be near to 1/2 it is clear that the rds for both $Cl^-$-rich and $H^-$-rich baths must be an electrochemical step.

The mechanism proposed by Galova et al., as reproduced in Scheme 3.1, it is seen, has almost nothing to do with the conclusions the authors themselves deduced from their experimental $\alpha$'s. By lumping the parallel reaction pathways into a single mechanism and balancing them both as if they occurred simultaneously, the essence of the separate mechanisms was lost.

### 3.3.2. Discussion of the Mechanism According to Graef

Graef [41] examined the mechanism for Al deposition only from the $Cl^-$-rich baths. Instead of measuring actual steady-state currents he developed pseudo-Tafel relations from current-transients in response to potential steps for a series of overpotentials. Extrapolation of the short-time region of these (for $t^{1/2}$) back to time zero supposedly eliminated the effects associated with mass-transfer and nucleation. This procedure seemed, however, to offer no such advantage, since the resulting transfer coefficients were $\alpha_c = \alpha_a = 0.3$, which, being symmetrical, the author "extrapolated" to mean that the $\alpha$'s were actually equal to 0.5!

The mechanism proposed on the basis of these "extrapolated" transfer coefficients was a *thrice* occurring rds involving a single electron-transfer (*step-1* in Scheme 3.2) followed by a chemical step in which the three equivalents so formed disproportionated to give a deposited metallic aluminum atom (*step-2* in Scheme 3.2) while regenerating two $Al^{3+}$ ions. No mention was made of an independently calculated stoichiometric number in this work and thus the "extrapolated" transfer coefficients are an inadequate basis for the proposed mechanism.

The mechanism, unlike our previous example, however, is consistent with the B&R transfer coefficients. It is clear that the condition $\alpha_a = \alpha_c = 1/2$ (if that were actually the case) will arise when:

$$\frac{\gamma_f}{\nu} = \frac{\gamma_p}{\nu} = 0$$

*and*

$$z_{rds}\beta = z_{rds}(1-\beta) = 1/2$$

when $\beta$ is taken as 0.5[b]. The subsequent disproportionation reaction would be essentially invisible in the transfer coefficients since no electrons are exchanged with the electrode, but there is precedent for such disproportionation reactions amongst Al species of intermediate valence (§1.3).

### 3.3.3. Discussion of the Mechanism According to Badawy et al.

Badawy et al. [38] proposed a mechanism comprised of three single electron-transfers (given in Scheme 3.3 for $Cl^-$-rich baths) based upon transfer coefficient values of $\alpha_a = \alpha_c = 1/2$, determined at a rotated electrode (1200 rpm) in the usual Tafel region ($\eta$ greater than 118 mV). They proposed that step *1* was rate-determining on deposition but step *3* on dissolution. Their experimental results seem to contradict those of Galova and our own here, in which, even when electrodes were rotated (as in our work), kinetically-controlled Tafel regions (i.e. of significance to mechanism determination) were always of restricted range and generally required back-reaction correction. No mention was made in their work of a derived stoichiometric number for the reaction even though they did measure the charge-transfer resistance, a closely related quantity (§6.6.3).

It is usually assumed in electrochemical kinetic analyses that the rate-determining transition-state is the same for both anodic and cathodic directions of reaction. For example, this assumption is obviously inherent in the BV equation (Eqn. 2.20) in that $\beta$ and $(1-\beta)$, comprising parts of the cathodic and anodic transfer coefficients, necessarily relate to the *same* energy barrier. This assumption is carried through all of the expanded transfer coefficients that we have derived in Chapter 2 (*viz.* Table 2.1) including the often cited ones of B&R (Eqn. 3.1) to which Badawy et al. also made reference in their work.

---

[b] The symmetry factor, $\beta$, taken as equal to 0.5 here, is discussed in greater detail in Chapter 7.

At equilibrium, of course, the same step *must* be operative in both reaction directions as a condition of thermodynamical reversibility. Although the possibility of different rds's for the forward and reverse directions of the Al electrodeposition reaction can indeed explain the observed transfer coefficients, some justification in support of their proposition is required considering that it contradicts commonly accepted assumptions of electrochemical kinetics, but none was offered. Also, a number of their experimental observations seemed to contradict their supposition; the first was that their derived exchange current-density values, $i_o$'s, extrapolated from the anodic and cathodic branches were, in all cases, nearly the same. $i_o$ is a measure of the equilibrium rate which depends on the effective concentration of species reacting and the height of the energy barrier of the rds. That the $i_o$ values extrapolated from the two branches (which showed only a single slope) gave the same value suggests that the anodic and cathodic reactions correspond to the same transition-state (by Eqn. 2.19 that defines $i_o$ with respect to a single transition-state) within the relatively wide potential range they examined. Secondly was the observation that the sum of the anodic and cathodic transfer coefficients was one. Transfer coefficients of 1/2 generally indicate direct equivalence to the symmetry factor of the transition-state, $\beta$, and if the anodic and cathodic $\alpha$'s sum to one, this suggests that they are complementary "fractions" of the potential affecting the *same* transition-state. Thirdly, no changes in Tafel slope were reported which would have marked a transition to other, different, reaction barriers from the necessarily singular one that must apply near the reversible potential.

For the $H^-$-rich bath, the authors stated that the same mechanism was operative as in the $Cl^-$-rich bath but that there was "apparently no activation polarization" in that case. What then did limit the kinetic performance of this bath they did not mention, however.

### 3.4. Summary

The work of these three aforementioned groups represents the sum total of all mechanistic work published on the hydride-bath. Amongst these, only in the work of Galova et al. [39,40] has an attempt been made to account for the behaviour in the *two*

types of bath, $Cl^-$-rich and $H^-$-rich, but their derived mechanism was so replete with inconsistencies as to disqualify itself from consideration. Graef's experimental work and results on the mechanism of reaction is considered to be incomplete. His mechanism was based solely upon the transfer coefficients from a "pseudo"-Tafel plot for which the derived values were, in fact, wrong (at $\alpha_a = \alpha_c = 0.3$), but even so, his proposed mechanism turned out to be consistent with the more complete experimental observations in the present thesis work. The work of Badawy supposed a different rds in anodic and cathodic reaction directions which was not clearly supported by any experimental or rational evidence.

It should be emphasized that, apart from the somewhat different behaviour in the $H^-$-rich bath, all the previous work has shown basically similar electrochemical behaviour. The above works present a particularly good sampling of the inadequate, and sometimes incorrect application of the electrochemical tools to the elucidation of complex reaction mechanisms and underlines the necessity for clarifying the mechanism of electrodeposition of Al from the hydride-bath and the theoretical treatments on which it has been based (as has been done in Chapter 2).

## 3.5. Mechanistic Considerations of the Electroreduction of Aluminum

In order to put the problem that forms the subject of the present thesis into context, a plausible mechanism for the electrodeposition of Al is required that can explain both sets of experimentally observed transfer coefficients, in the $H^-$-rich baths *ca.* $\alpha_c = 1/3$ and $\alpha_a = 2/3$, and in the $Cl^-$-rich baths *ca.* $\alpha_c = \alpha_a = 1/2$ as determined from behaviour at relatively at low overpotentials (*ca.* $< 100$ mV) where kinetic control prevails.

Non-rds steps have been shown to add integers to the transfer coefficients or, when the rds has a stoichiometric number greater than one, a fraction less than one is possible for one $\alpha$ but, where for the other $\alpha$, it must be a whole number (*viz.* Table 2.1). Thus in the data obtained in the present work (to be examined in §6.7), the fact that the experimental $\alpha$'s are all found to be near to 1/2 is consistent with the rds being a simple single electron-transfer and that there are no other electrons transferred in *other*

electrochemical steps; this situation is consistent with a stoichiometric number of three ($\nu = 3$). The task at hand therefore appears to be to explain the fact that $\beta$ varies between 1/2 and 1/3 amongst the $Cl^-$-rich and $H^-$-rich baths. The electrochemistry of the hydride-bath system will be examined in Chapter 6 and the significance of $\beta$ and nature of its variation with bath composition will be considered in Chapter 7.

# Chapter 4 Experiments and Methods

## 4.1. Introduction

Experimentation on the electroplating of aluminum required the use of strictly anhydrous solutions, employing in the present work tetrahydrofuran (thf) as solvent. This necessitated adoption of experimental conditions quite different from those commonly involved in aqueous-solution electrochemistry, and substantially more demanding from the point of view of handling of solutions and recognition of time-effects in the results due to instabilities of the reagent solutions containing various aluminum-complex solutes. Some of the special requirements for this work and particular difficulties that arose are described in the sections of this chapter which follows.

## 4.2. Equipment

### 4.2.1. Glove Boxes

All manipulations were carried out in inert-atmosphere glove boxes under a slight positive pressure of argon (equivalent to about 1 or 2 cm of water). Either a Vacuum Atmospheres Dri Lab HE 113-145 provided with an HE 63-P pressure controller and Dri Train HE463 gas scrubber or a fiberglass glove box was used. The latter box was modified to permit subambient temperature control experiments. For that purpose ethylene glycol would be cooled in a large dewar flask outside the glove box with a cold finger immersion cooler (Cryocool CC-100 II) and circulated with a peristaltic pump through nalgene tubing into the glove box via valve-controlled feed-through inlets and through a glass cooling jacket and condenser. The coolant was not in contact with the atmosphere of the glove box. About 3 litres of glycol were used in this loop and the flow rate was typically about 300 ml $min^{-1}$. A small pool of mercury was provided to improve thermal contact between the glass cooling jacket and the electrochemical cells or reaction vessels. After permitting sufficient time for temperature equilibration to be attained it was found that the established temperature as measured with a mercury thermometer ($\pm 0.2°$), would not fluctuate by more than 0.5° C during the course of an experiment. Electrical contact with the electrochemical cell inside the glove box was established with sealed electrical

feed-throughs.

Standard research grade argon was passed through columns of molecular sieves and hot copper turnings to remove traces of water and oxygen and an open dish of phosphorus pentoxide was kept inside the boxes to getter moisture from the atmosphere. The gas columns were cleaned regularly by heat drying the molecular sieves and re-reducing the hot copper turnings in a flow of hydrogen gas. The quality of the inert-atmosphere in the former box was very good (down to 2 ppm combined water and oxygen, determined by the lifetime of a broken incandescent light bulb [53]), while that of the other glove box which was modified to permit temperature control was not as good.

### 4.2.2. Electrochemical Equipment

Electrochemical experiments were conducted with an EG&G PAR 173 potentiostat coupled with a PAR 376 logarithmic current converter. The potential was controlled by means of a Hokuto Denko HB-104 signal generator which permitted ramp, step and pulse programs of potential (or current) to be addressed to the electrode. The current output was fed to a Nicolet 310 oscilloscope. If background noise was too large, the current response would be smoothed by a 10 ms filter included on the PAR 376 current converter, but only if this procedure was found not to affect the response significantly. The cited uncertainty for the PAR 173 is $\pm 0.1$ mV for potential and $\pm 0.2\%$ of the full-scale current ranges. Alternatively, an EG&G PAR M273 potentio-/galvanostat coupled to an AT computer and controlled by commercial software (M270) was used for some experiments. IR compensation was not applied *in situ* since the hardware circuit was unpredictable on the PAR 376 current module.

The solutions studied all had significant resistances (200 - 2000 $\Omega\,cm^{-1}$), but the error in applied potential due to IR-drop introduced by this was small since the actual currents passing in most cases were small due to the small areas of the electrodes used.

A.C. impedance spectra were recorded using an EG&G PAR 273 potentiostat coupled to a Schlumberger 1255 Solartron HF frequency response analyzer (FRA) or a Schlumberger 1286 potentiostat and Schlumberger 1255 Solartron HF FRA, both controlled by PC computer and commercial software (ZPLOT, Scribner). The applied

a.c. signal amplitude was usually 5 mV and the frequency range from 500 kHz to 0.1 or 0.05 Hz. The response of the instruments was checked regularly by recording the impedance spectrum for a "dummy-cell" composed of high-tolerance, hardware, resistors and capacitors. Some of the instruments gave a variable, background, phase shift at high frequencies which defined the practical upper frequency limit of the instrument. Electrical leads between a.c. impedance equipment and electrochemical cells should preferably be as short as possible to reduce interference from stray capacitances arising from these. Since experiments were necessarily conducted inside sealed, inert-atmosphere, glove boxes, this required the use of extra electrical leads and feed-through boxes. Only very high quality, shielded, electrical leads were employed to connect to the electrochemical cell, and impedance response was checked with a dummy-cell *inside* the glove boxes.

### 4.2.3. Cells and Electrodes

Experiments were conducted in cells having three-electrode arrangements. All cells were made of pyrex glass fabricated by the Ottawa University glass-shop. Cells were of two general and simple designs depending on whether or not a rotated working electrode was used. If not, they were cylindrical and flat bottomed having a 30 ml working volume with ground glass tops that could mount a variety of fabricated electrode feed-throughs. Electrodes were held in place by threaded glass compression fittings using Viton or Butyl O-rings and drilled teflon screw caps. A 1 cm teflon-coated magnetic stirring bar was used for solution agitation in this cell. For the rotating disc configuration, glass cells were of a cone/teardrop shape, where the narrow end was rounded and served as the bottom of the cell. This design permitted small analyte volumes (from 15 - 30 ml) and effective solution mixing. An opening in the centre of the broad end gave access to the working electrode rotator-assembly while smaller openings off to the sides gave access to the reference and auxiliary electrodes. These cells were not sealed.

Detachable polished disc electrodes were fabricated from gold and platinum wire sealed in soft, "soda lime" glass and glassy carbon (GC) rod set into fitted glass tubes with epoxy resin (Araldite), of apparent surface areas 0.0012 - 0.005 $cm^2$ in the cases of gold and platinum, and 0.08 $cm^2$ in the case of GC. The wires were cut flush with the

glass and then polished on a rotating plate sanding machine (Struers DAP-V) with successively finer grits of SiC sandpaper, typically 500, 1200, 2400, 4000, followed by diamond pastes, 1 and 0.1 $\mu$m (Buehler). Electrodes were cut short, to between 4 - 5 cm long, in order that they could fit into a SEM sample chamber for examination if necessary. These electrodes could be attached to longer lengths of glass tubing with heat-shrinkable plastic and teflon tape for use in a simple three-electrode electrochemical cell or could be fitted into a homemade teflon adaptor (securely with an O-ring) attached to a rotator shaft for rotating-disc electrode experiments.

The purpose of electrode rotation is to create forced solution convection at the electrode surface and thence eliminate the effects of diffusion of species in solution. The leads of the short indicator electrodes were coiled tightly and electrical contact to the stainless steel rotator shaft was accomplished by pushing the electrode into the teflon adaptor, contacting and compressing a coiled piece of copper wire fitted into the adaptor assembly. The rotator (AFASR Analytical Rotator, Pine Instrument Co.) was continuously adjustable to $10^4$ rpm.

The reference electrode, against which all potentials[a] are measure, was an aluminum wire (99.999% Aldrich) contained in a glass tube bathed in the analyte solution. The tube, which had a small opening ($\approx$2 mm diam.), could be positioned in the cell close to the working electrode; this provided reproducible positioning and avoided shorts between electrodes in the cell. The area of the reference electrode was generally at least an order of magnitude larger than that of the working electrode. A Ag/AgCl electrode, used as a standard reference for non-aqueous solvents [103] containing $Cl^-$ ions was tried, but was attacked by the bath. The commonly used procedure of employing the $E_r$ of an added electroactive couple at Pt, for instance a reversible nonpolar species like ferrocene and related compounds, as a reference was not employed. No effort was made to isolate compartments of the cell and thus the composition of the solution bathing the reference

[a] Potential and overpotential are used somewhat interchangeable in this thesis since the potential of the reference electrode was $E_r$ for Al itself. They would sometimes be different, however, due to local compositional differences between reference and working electrodes in which case, overpotential was measured relative to the point at which the Al reaction switched from plating (cathodic) to stripping (anodic).

aluminum wire varied as did the different solutions examined. This means that the $E_r$ of the reference was not constant between baths of different composition, but since kinetic rather than thermodynamic measurements were the focus of the thesis work, this variability of the reference electrode was not a great concern. The auxiliary electrode was aluminum wire (again 99.999%) formed into a coil to provide a large electrode area relative to the working electrode (usually $>2$ cm$^2$) and therefore several orders of magnitude large than the working electrodes.

### 4.2.4. Scanning Electron Microscopy

Submicron resolution images of substrate morphology were recorded with a SEMCO Nanolab 7 scanning electron microscope and substrate elemental analyses could be accomplished with an on-board energy dispersive X-ray detector attachment.

Special small sized electrodes used in the electrochemical investigations (see above) were secured in place in the sample chamber with wire on a modified stud and were oriented at a 45° angle with respect to the electron beam. The 45° angle gave a limited area of focus, but was necessary due to the instrument's restricted sample chamber arrangement. Grounding to the instrument was accomplished via the leads for the sample substrate electrodes and thus imaging resolution depended upon the electrical conductivity and contact between the examined deposits and the underlying substrate. Resistivity due to the surface oxide on Al and poor deposit adhesion of some of the mounted samples resulted in less than excellent micrographic images, but on-screen observations none-the-less gave a good indication of surface micro-structure. The above limitations were deemed tolerable since the above protocol was simple, permitting immediate re-use of sample electrodes in electrochemical experiments and obviated the usual sputtering of conductive gold layers onto non-conducting samples (required for imaging) which would necessarily have to be polished off afterwards.

### 4.2.5. Nuclear Magnetic Resonance Studies

All NMR experiments were conducted on a Varian XL-300, 300 MHz Fourier transform nuclear magnetic resonance spectrometer at room temperature. This instrument

is operated at a magnetic field of 7.05 T (or 70.5 kGauss) giving resonant frequencies of 79.195, 116.65 and 75.473 MHz for $^{27}Al$, $^{7}Li$ and $^{13}C$, respectively, and the spectral widths characteristics of these nuclei were 320, 35 and 250 ppm. A 90° excitation pulse of 5 $\mu$s duration was applied to all samples and the resulting free induction decays summed, transformed and stored by a dedicated computer. The pulse train was repeated until the signal-to-noise ratio was deemed acceptable; this varied from about 250 times (or about 5 minutes acquisition time) for $^{27}Al$ and $^{7}Li$ to up to 3000 times or more (> 1 hour) for $^{13}C$ since, in this case, the changes of the solvent $^{13}C$ resonance being examined, associated with time-dependent solvent decomposition, would be expected to be small relative to the resonances of the bulk solvent.

It was not possible to employ an *in situ* reference species in the case of the hydride-bath samples; hence these samples were run "unlocked" using 0.7 M $Al(NO_3)_3$ in $D_2O/H_2O$ (75%) and 1 M LiCl in $D_2O/H_2O$ (75%) as external references for Al and Li. The scale for $^{13}C$ spectra was set relative to the known resonant frequency of the low frequency ("upfield") $\beta$-carbon peak at 25.1 ppm for the bulk thf solvent.

The relative abundances of species corresponding to the various Al resonances could be integrated with the on-board software when these resonances were well separated. When they overlapped the relative species' contributions were estimated from the experimental peak shape and the known positions of the various aluminates' resonances, performing integrations with a planimeter.

Approximately 1 ml samples were withdrawn from the hydride-baths at various times during the electrochemical experiments, transferred to standard NMR tubes and run on the spectrometer as soon as possible. The samples were transferred inside an Ar-filled glove box and sealed with a plastic cap, then wrapped with parafilm tape, no other special precautions being taken.

### 4.3. Hydride-Bath Preparation

$AlCl_3$ (Mallinckrodt, analytical reagent grade) was sublimed at 195°C before use and $LiAlH_4$ powder (Aldrich, 99.5%) was used as received. Tetrahydrofuran (thf)

(BDH) was distilled from potassium and benzophenone (with the kind assistance of Mike Tjepkema of Dr. Fallis's lab). Solutions of $LiAlH_4$ in thf were prepared by refluxing an excess of $LiAlH_4$ in thf for 3-5 hours. The remaining solid $LiAlH_4$ would be allowed to settle and samples of the $LiAlH_4$-thf solution were then carefully pipetted off for use or quantitative analysis by complexometric titration for Al (see below). It was found that the maximum $LiAlH_4$ concentration in thf was between 0.35-0.4 M.

$AlCl_3$ is soluble in thf to about 0.8 M at room temperature, but its solubility increases in the presence of $LiAlH_4$ [34]. Solid $AlCl_3$ was added in small portions at a time to stirred, cooled $LiAlH_4$-thf solutions (0-5°C). This precaution is required since the additions are accompanied by evolution of a considerable amount of heat which if not controlled can lead to solution decomposition. After each addition of $AlCl_3$ the temperature of the solution would increase and clouds of what was probably HCl, would appear above the solution (from the reaction of $AlCl_3$ with any traces of $H_2O$). The resulting solutions were slightly yellow-brown in colour. Separate thf solutions of neat $LiAlH_4$ and $AlCl_3$ could be prepared and subsequently mixed together, but it was found that the $AlCl_3$ solutions were not stable for very long, usually having to be used within a day or two since their yellow-brown colouration would invariably darken and, when left for a longer time the solution would in some cases solidify to a solid mass.

The preferred procedure was thus the controlled addition of $AlCl_3$ directly to cooled $LiAlH_4$ solutions in roughly the desired proportions. Attempts to prepare exact compositions usually met with failure due to the unstable nature of these baths particularly in the early stages of their lifes where the variation of composition was found to be most severe. Solution composition was, therefore, only roughly controllable. These solutions, once prepared, would again be allowed to stand and often a grey precipitate would settle. The supernatant would be decanted and used in electrochemical experiments, samples being withdrawn at various points through the lifetime of the bath for analysis (see below). The baths would, however, give good reproducible electrochemical behaviour for between two days and up to a week. The whole preparation procedure would take about a day and these $AlCl_3$ + $LiAlH_4$ solutions, unlike the neat $AlCl_3$-thf solutions had shelf-lives (unused) of more than a month depending upon ambient condi-

tions and what concentrations and compositional ratios were used. The speciation and time-dependence of these baths was studied as described in Chapter 5.

## 4.4. Solution Analysis by Atomic Emission Spectroscopy

Quantitation of the above prepared solutions was in some cases performed by means of inductively-coupled plasma atomic emission spectroscopy (ICP AES) (Thermo-Jarrell Ash AtomScan25, courtesy of John Loop, Geology Department, University of Ottawa) for aluminum and lithium. Samples of about 500 $\mu$l would be measured accurately with a micrometer burette (Gilmont Instruments), digested for at least 10 minutes in a small amount of boiling $HNO_3$ to homogenize the sample as well as to evaporate the organic solvent and diluted to 1 litre with distilled water such that the total acid concentration was about 2% in accordance with protocols of analysis by this instrument. A series of standards were made from accurately ($\pm$ 0.1 mg) weighed Al metal (99.999%) and rigourously dried LiCl (BDH, AnalaR) diluted in 2% nitric acid. A few grains of $HgSO_4$ (JT Baker) were added to the aluminum sample to promote dissolution. The concentrations of these standards compared closely with those for commercial standards used by the Geochemistry lab.

Analysis was carried out at wavelengths chosen with due consideration of possible interferents with "9-point" background correction. The instrument's software would automatically set output to the "ppm" scale by internal calibration against the standards. Sample flasks and bottles were made of glass, but interference from adsorption of analyte ions on the sides of glass was not significant due to the acidity of the sample. The samples would be shaken then aspirated into the plasma. Analyses were run in triplicate and only accepted if standard deviation between the results was below 2%.

## 4.5. Complexometric Back-Titration for Determination of Aluminum

Aluminum was determined quantitatively by complexometric back-titration [104]. Accurately measured 0.05 ($\pm$ 0.0005) M solutions of zinc sulphate ($ZnSO_4 \cdot 7H_2O$, JT Baker) and disodium ethylenediaminetetra-acetate ($Na_2$-EDTA, BDH or EDTA-acid, JT Baker, + 2·NaOH, BDH) were prepared. The concentration of the Zn standard solution

was confirmed by ICP-AES analysis for Zn and the EDTA by titration against this Zn solution. Alternatively, multiple samples of the aluminum standard solution were titrated. The resulting simultaneous equations could be solved for the concentrations of EDTA and $Zn^{2+}$. The % difference between these determinations and the original measured concentrations was no more than 2%.

1 ml samples of the thf solutions would be removed from the glove box and replicate aliquots of between 0.40 - 0.70 ($\pm$ 0.02) ml withdrawn either in a micrometer burette or a disposable pasteur pipette to a fine mark, the volume at which would subsequently be determined in a burette to 0.01 ml with water. These aliquots were then transferred drop by drop to an Erlenmeyer flask containing about 50 ml of mildly acidified water to avoid the precipitation of $Al(OH)_3$ which is known to occur in Al solutions at pH 7 and above up to pH 11 [105]. Care had to be exercised in this transfer since the hydride solution reacts extremely violently with water and could hence result in splatter and loss of the sample or clogging of the tip of the transfer pipette. 10 or 20 ml of a standard EDTA solution were added to these aliquots and their pH adjusted to between 7 and 8 with addition of NaOH or an ammonia buffer solution, pH being measured with pHydrion Vivid 1-11 indicator strips or Alkacid Test Ribbon (Fischer). The samples were then boiled in a fumehood for at least five minutes to ensure complete complexation of the aluminum and to evaporate the thf, then cooled to room temperature and their pH's adjusted basic again. Eriochrome Black T indicator (Fischer) solution (0.5 wt%) in triethanolamine (Aldrich) was added to the samples (< *ca.* 0.3 ml) and the colour at the outset was sky-blue.

The samples were back-titrated with the zinc sulphate solution. The colour change of the Eriochrome indicator at the end-point occurs as the EDTA with which the $Zn^{2+}$ binds becomes exhausted giving excess $Zn^{2+}$ that is now free to bind with the indicator. Unbound by Zn the indicator is sky-blue in colour while when bound it is pink. Near the end-point each drop of $Zn^{2+}$ solution turns the analyte solution pink, but this colour changes back to blue within 10 seconds. The final end-point colour is actually a mild grape-juice purple and thus a control of the indicator in water was used as a reference since the end-point was often quite subtle.

Other ions in solution will also be bound to the EDTA but analysis depends on the large formation constants of analyte and titrant (i.e. $Al^{3+}$ and $Zn^{2+}$). EDTA is a hexaprotic chelator which at pH 7-8 will have five positive charges. It forms 1:1 complexes with most metal ions, even when these metal ions are monovalent. The formation constants for $Al^{3+}$ and $Zn^{2+}$ are $2.0 \times 10^{16}$ and $3.16 \times 10^{16}$, respectively [106]. The slightly higher formation constant for $Zn^{2+}$ could result in its preferred binding to, and displacing $Al^{3+}$ from EDTA instead of to the indicator. This could obscure the end-point and so titrations should be conducted rapidly. Formation constants for other species present in these solutions ($Li^{+}$: $6.17 \times 10^{2}$ and $Na^{+}$: 46) are significantly lower than the two of interest and thus will not interfere. Eriochrome black T is a dye molecule composed of two substituted napthalene moieties linked by an azo group. At pH 7-8 it is di-negative in charge and blue in colour, which becomes "wine-red" when complexed with a metal ion such as $Zn^{2+}$. It has been observed that if solutions are not sufficiently basic the titration end-point is not sharp.

## 4.6. Titration of Chloride Ion by the Mohr Method

Chloride was titrated by the Mohr method [107]. Samples of between 0.40-0.60 ($\pm$ 0.02) ml were transferred to mildly acidified water in Erlenmeyer flasks to promote dissolution. The pH would be adjusted with an NaOH solution (calcium carbonate, as directed in the published procedure, was found to be ineffective) on pHydrion Vivid 1-11 indicator strips or Alkacid Test Ribbon (Fischer). 1 to 2 ml of 5% potassium chromate solution would be added and the samples titrated with a standard silver nitrate solution (*ca.* 0.2 M) to the first permanent appearance of a reddish brown (buff) colour. The solutions were initially clear yellow, with a slight greenish tinge at the appropriate pH, but upon addition of the silver standard titrant the analyte solution becomes milky yellow in colour as the white coloured AgCl precipitates. When all the $Cl^{-}$ has been precipitated as AgCl, the first excess of silver will form a second precipitate of $Ag_2CrO_4$ which is brick-red in colour. The stability constant of the chromate is substantially lower than that for the chloride and so no silver chromate will precipitate until essentially all of the chloride has been already precipitated. The pH of the medium must be controlled. In

acid, the chromate can be converted to dichromate in the following equilibrium:

$$2CrO_4^{2-} + 2H^+ \rightleftarrows Cr_2O_7^{2-} + H_2O \quad (1)$$

which is displaced to the right in acid forming silver *dichromate* which is considerably more soluble than the chromate.

In base, silver oxide which is colourless could become precipitated as in the following equilibrium:

$$2Ag^+ + 2OH^- \rightleftarrows 2AgOH_{(s)} \rightleftarrows Ag_2O_{(s)} + H_2O \quad (2)$$

Thus, the determination of chloride by the Mohr method must be carried out in a medium of pH 7 to 10, since in either acid or base the end-point is diffused by the above reaction equilibria.

# Chapter 5 NMR Studies of Speciation of $^{27}$Al-Complexes in the Hydride Plating Baths

## 5.1. Introduction

### 5.1.1. Foreword

The use of Nuclear Magnetic Resonance (NMR) spectroscopy is particularly informative for the study of complex systems examined in the present work as it provides a procedure for examination of the speciation of Al-complexes in the hydride-bath as a function of composition of the reaction solution. The $^{27}$Al nucleus gives well resolved NMR spectra and thus, direct information on the state and coordination of the Al centre is obtainable from this technique.

The following sections will cover the NMR experiments conducted on the hydride-bath. As an introduction, basic aspects of the theory of nuclear magnetic resonance relevant to the present work will first be presented to put the chemical shift and linewidth determinations, and the pulsed Fourier transform technique in focus[a].

The spectra of hydride-baths of varying compositions are analyzed. The chemical shifts and linewidths of the aluminate species present in the hydride-bath will be discussed with respect to their symmetry and bonding.

$^{7}$Li-NMR spectra were also recorded for a number of samples in an attempt to identify any distinct ion-pairing in the bath and $^{13}$C-NMR was studied to investigate any thf solvent decomposition that may take place during lengthy bath operation or electrochemical experiments.

### 5.1.2. NMR: Theoretical Background

Nuclear particles or nucleons possess spin angular momentum. Elements (e.g. $^{12}$C, $^{16}$O, $^{32}$Si, etc) that possess an even number of each kind of nucleon do not have an overall nuclear spin angular momentum since the nucleons couple. In this case the nuclear spins are cancelled which means that these nuclei cannot be examined by NMR.

---

[a] More complete descriptions may be found in any of the many monographs in this field, for instance [108-111].

On the other hand, elements that have an odd number of nucleons, or an even number but with odd numbers of both protons and neutrons (e.g. $^{2}H$, $^{6}Li$, $^{10}B$, $^{14}N$), will possess an overall nuclear spin angular momentum, associated with which is a magnetic moment and dipole. The proton, with spin 1/2, is the element most studied by NMR spectroscopy, but this technique may be applied to any element possessing a nuclear magnetic moment.

As with electron spin, which may be more familiar to chemists, the nuclear spin of nucleons is described by half integral values and the total spin of a nucleus is described by the spin quantum number, I. Elements with $I = 1/2$ have magnetic dipoles, those with $I = 3/2$ have, in addition, magnetic quadrupoles and those with $I = 5/2$ will have magnetic octupoles. A nucleus of spin quantum number I may take $2I+1$ different orientations with respect to an arbitrary axis, $m_I = I, I-1, \ldots, -I$, and these levels will all be degenerate in the absence of an applied magnetic field. In an applied magnetic field of flux density B ($T = kg\,s^{-2}A^{-1}$) the energy corresponding to the magnetic moment, $\mu_z$ ($A\,m^2$), along the axis of the applied field, z, is given by Eqn. 5.1:

$$E_{m_I} = -\mu_z B \tag{1}$$

$\mu_z$, along this z axis, depends on the $m_I$ spin orientations and the energy of the nuclear spin angular momentum which is the bracketted term in Eqn. 5.2:

$$E_{m_I} = -\gamma\left(\frac{h}{2\pi}\right)m_I B \tag{2}$$

where $\gamma$, the magnetogyric ratio, relates the nuclear magnetic moment to the nuclear spin angular momentum. Nuclear structure is not sufficiently well understood to calculate $\gamma$; thus empirical constants, nuclear $g_I$ factors, are used to express the nuclear spin magnetic moment in terms of the nuclear magneton, $\mu_N$, this having a value of $5.051 \times 10^{-27}\ J\,T^{-1}$. These are related in Eqn. 5.3:

$$E_{m_I} = -g_I \mu_N m_I B \tag{3}$$

The selection rule for nuclear spin transitions is $\Delta m_I = \pm 1$ and thus for magnetic fields of about 10 T the transitions between the spin states correspond to energies in the

microwave region ($10^7$ - $10^{10}$ Hz).

The technique is a sensitive probe of the electrical environment of a particular resonating nucleus. The magnetic fields arising from the electrons arranged around a resonant nucleus, from those of neighbouring nuclei and, to a lesser extent, from the nuclear spins of these latter, all contribute to a local magnetic field, $\delta$B, experienced by a particular resonant nucleus. This adds to the magnetic field of the instrument, $B_{inst}$, to give a total magnetic field which is characteristic of the nucleus in a particular environment:

$$B_{env} = B_{inst} + \delta B \qquad (4)$$

The varying magnetic fields of different environments split the nuclear spin energy levels to varying extents and thus come into resonance at different frequencies. If the overall magnetic field experienced by a nucleus is *larger* than another it is said to be *shielded*, giving resonance "upfield" or at *lower* frequency in a given field. Resonant frequencies are practically measured relative to accepted reference species and thus a unitless relative chemical shift, $\delta$, is used (in ppm):

$$\delta = \frac{\nu - \nu_{ref}}{\nu_{ref}} \times 10^6 \qquad (5)$$

where $\nu$ is the frequency of the transition, $\nu_{ref}$ that of the accepted reference for the same element. An added feature of the technique is that the integrated area of the resonance plots give relative proportions of nuclei in different environments.

### 5.1.3. NMR: Fine Structure

The influence of adjacent nuclear spins tends to influence the resonant nucleus by an order of magnitude less than that due to neighbouring electron density and this nuclear spin interaction leads to what is termed a *fine structure* effect. If we consider a macroscopic sample, there will exist an equal probability that the nuclear spin magnetic moment vector of each of the adjacent nuclei will be either parallel or antiparallel to that of the probe nucleus and these different orientations of the adjacent nuclear spins will add to or

subtract from the magnetic field at the resonant nucleus. This brings these species, of a given chemical environment but with different adjacent nuclear spin magnetic moment vector orientations, into resonance at slightly different frequencies which causes the resonance, otherwise expected to be a *singlet*, to be split into a series of related peaks or a *multiplet*. The peaks are defined by a *coupling constant* and thus fine structure can give valuable clues as to number and kind of adjacent nuclei.

### 5.1.4. NMR: Quadrupolar Relaxation and Symmetry

The subsequent relaxation of excited nuclear spin levels is of practical importance in NMR experiments. Very slow relaxation times will lead to resonance saturation and hence a rapid depletion of the signal which, in extreme cases, may not give an observable signal at all. Very fast relaxation times will broaden resonances to a point where they may become completely obscured. This is due to the fact that very short excited-state lifetimes create quantum uncertainty in the reciprocal frequency scale which results in resonance broadening. Excited nuclear spins are not susceptible to spontaneous emission in the microwave region, but may relax by any of a number of processes that involve coupling of matched magnetic moments associated with the excited state and neighbouring dipoles or the like. Amongst these are spin-lattice (or medium), unpaired electron-nuclear, and quadrupolar relaxation. The latter of these is usually dominant over all other mechanisms; thus quadrupolar nuclei often give only very broad overlapping resonances.

The quadrupolar relaxation mechanism is very sensitive to the distributed *electric field gradients* around a resonant nucleus. These gradients depend on the spacial distribution of electron-density due to bonds and lone pairs. If there is any symmetry amongst the substituents distributed around the nucleus, the field gradients due to the individual substituents will be cancelled, thus decreasing the rate of relaxation resulting in sharp resonances, as for instance is the case for the octahedral $[Al(H_2O)_6]^{3+}$, which is the accepted reference for the Al nucleus. Linewidths can therefore be a sensitive probe of local symmetry, coordination structure and hence speciation. In addition to this, chemical-exchange amongst related species can give rise to line-broadening. Therefore, processes such as interconversions or ligand transfers (due to substitutionally labile

ligands) on the same time-scale as the experimental pulsing cycle, result in a nucleus jumping between two environments and thus its contribution to the recorded free induction decay of an NMR experiment is a collage of the decay characteristics of the different environments, giving rise to line-broadening.

### 5.1.5. NMR: Practical Aspects

#### 5.1.5.1. Experimental Configuration

Before present-day *pulsed* techniques were developed, a typical NMR spectrometer would hold either the magnetic field or the microwave irradiating frequency constant (usually the latter) while scanning the other. In pulsed NMR, instead of the constant *milliwatt* microwave frequency field used in a magnetic field scanning experiment, the system is subjected to a *kilowatt* pulse of microsecond duration containing all necessary frequencies. This pulse causes saturation excitement of all spins and once the pulse ends the transient response of the system is a free induction decay (FID) of all these excited nuclear spins. The pulse train is usually repeated many times in rapid succession, the repetition rate being dependent, of course, upon the relaxation time of the particular nucleus and the resulting FID's added; this greatly increases the signal-to-noise ratio. Taking the Fourier transform (FT) of the total FID converts that transient response to a function of frequency which gives the response spectra in their usual units. Quadrupolar nuclei are well suited to FT-NMR since their typically fast relaxation times permit rapid pulsing, allowing many repeated response experiments to be summed and averaged in a relatively short time.

#### 5.1.5.2. Decoupling

*Decoupling* is a double resonance technique used to simplify NMR spectra by removing fine structure due to coupling with adjacent nuclei. The technique involves the simultaneous application of a microwave signal corresponding to the resonance of an adjacent element that could couple to the analyte nucleus; for instance proton ($^1$H-) decoupling is widely used. The decoupling signal equalizes the populations of the spin

levels of the adjacent nuclei which effectively averages out the contribution of the nuclei and collapses any multiplets into singlets. In pulsed-FT experiments continual decoupling pulses are superimposed on the repeating pulse-FID train of the probe nucleus; pulses are used in order to avoid the severe sample heating that otherwise would be caused by a continuous signal.

## 5.2. NMR Response of the $^{27}Al$ Nucleus

The element aluminum lends itself readily to studies by means of NMR. It has a large chemical shift range, a single isotope and high sensitivity to detection. $^{27}Al$'s 5/2 nuclear spin makes it an octupolar nucleus and thus subject to quadrupolar relaxation, but fortunately its quadrupole moment is relatively small so that line-broadening is not usually a significant problem for many aluminum containing species and Al therefore has a large relative receptivity. The linewidths for $^{27}Al$ can vary from 3 to 6000 Hz [111].

The chloroaluminate species examined in the present work exhibit fine structure due to coupling between the Al and H nuclei. Cl has two abundant isotopes ($^{35}Cl$: 75.53%; $^{37}Cl$: 24.47%) and both have nuclear spins of 3/2 and large quadrupolar moments. The resulting rapid quadrupolar relaxation of this nucleus is responsible for averaging-out any fine structure, and in fact no discernible Al-Cl coupling was observed in the species examined here.

The aluminate species that are present in the hydride-baths result from ligand mixing of the components $AlCl_3$ and $LiAlH_4$ in thf via the Schlesinger reaction [112] as:

$$AlCl_3 + AlH_4^- + 2thf \rightleftarrows AlH_xCl_{3-x}\cdot 2thf + [AlH_{4-x}Cl_x]^- \qquad (6)$$

The distribution of hydrido-chloro-aluminate species formed in this reaction depends on the molar ratio "r" of $AlCl_3$ to $AlH_4^-$ ion introduced into the donor etheric solvent. The complexes are of three general types: anions that are tetrahedral and of general formula $[AlH_xCl_{4-x}]^-$ (x = 0-4), uncharged species known to be solvent coordinated [41] and hence are trigonal bipyramidal of general formula $AlH_xCl_{3-x}\cdot 2thf$ and additionally cations (the result of auto-ionization of the uncharged species), also solvent coordinated, having octahedral structure and general formula $[AlH_xCl_{2-x}]^+\cdot 4thf$. Fig. 5.1 shows the possible aluminate complexes and their coordination geometries.

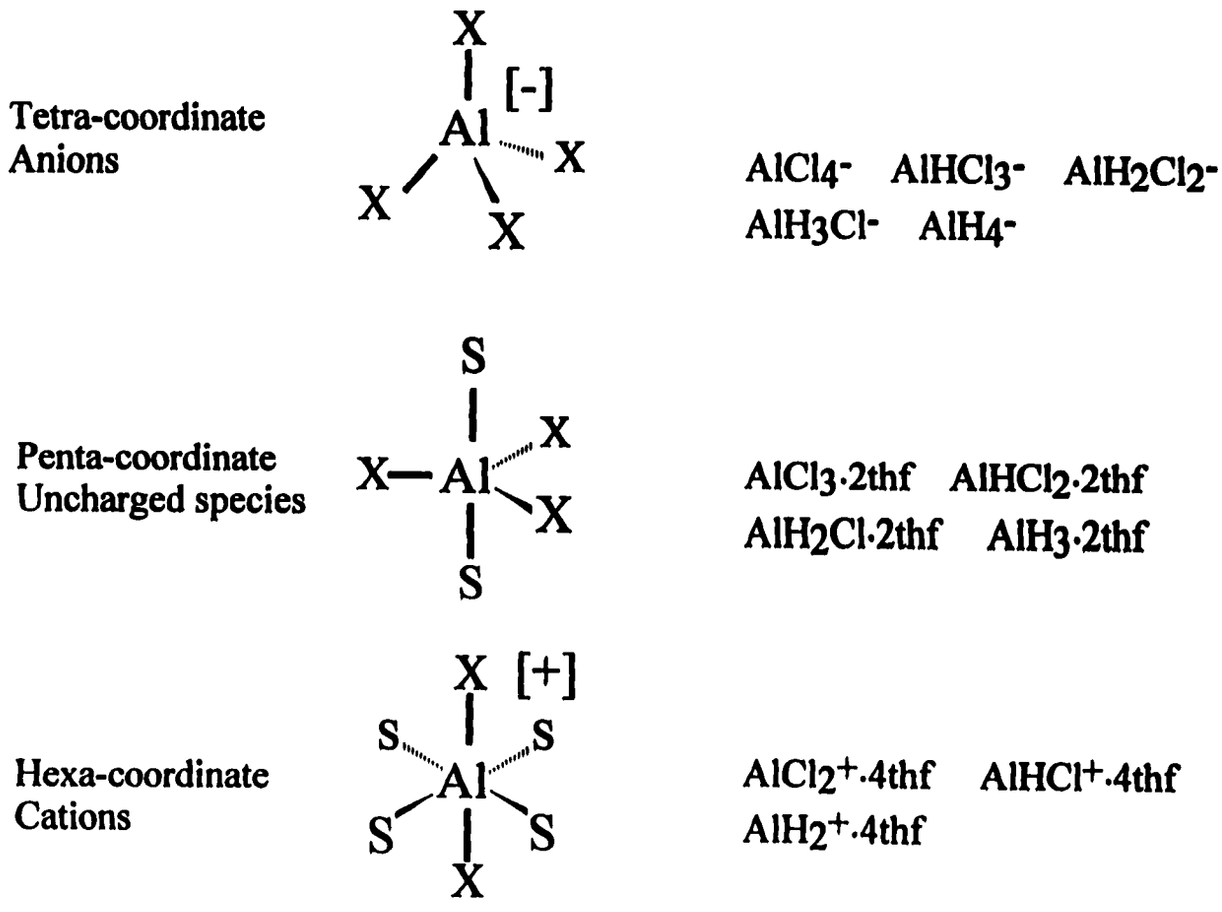


**Fig. 5.1.** Structures of aluminate species possibly present in the hydride-bath.

The $^{27}$Al-NMR chemical shifts of these are grouped, predictably, according to the degree of substitution at the aluminum atom (refer to Table 5.2). The resonances of the hexacoordinate species are found at about 0 ppm [111:p.167] similar to that of the reference $[Al(H_2O)_6]^{3+}$ species, those of the pentacoordinate, uncharged species are at higher frequencies, between 64 and 108 ppm, and at even higher frequency are the tetra-coordinate anionic species, within the region 95 to 130 ppm, which are most likely not solvent coordinated from the known behaviour of $AlH_4^-$ [113].

## 5.3. Experimental

$^{27}$Al- and $^{13}$C-NMR spectra were recorded with $^1$H-decoupling to examine speciation (ligand coordination) and characteristics of the solvent in the baths. Study of $^1$H-NMR of the hydrido-aluminates was not attempted since any information would probably have been swamped out by the thf $^1$H-solvent signals in the undeuterated solvent, while the use of the deuterated analogue on the scale required was precluded due to its prohibitive cost.

An indication of the relative error in the chemical shift for aluminum may be gained from the fact that the position of the $AlCl_4^-$ resonance (at 102.8 ppm) was found to vary by not more than 0.2 ppm amongst results for all the separate experiments in which it was observed (numbering at least twenty) with the scale being set by an external aqueous reference. Peak assignments for solutions of low Al content were made taking into account that the sample holder was constructed in part from Al which led to a broad ill-defined background resonance between 0 and 100 ppm.

## 5.4. Results and Discussion

### 5.4.1. Results: $AlCl_3$ and $LiAlH_4$ Controls

Separate thf solutions of neat $AlCl_3$ and $LiAlH_4$ were examined as controls. The $^{27}$Al-NMR spectrum (Fig. 5.2a) of a 0.5 M $AlCl_3$ solution in thf consists of three distinct peaks: a sharp one at 103 ppm, one broad one corresponding to large abundance at 68 ppm and another of low abundance at $\approx$15 ppm. These peaks correspond to previously characterized [114,115] resonances of $AlCl_4^-$, $AlCl_3 \cdot 2thf$, and $[AlCl_2]^+ \cdot 4thf$ species,

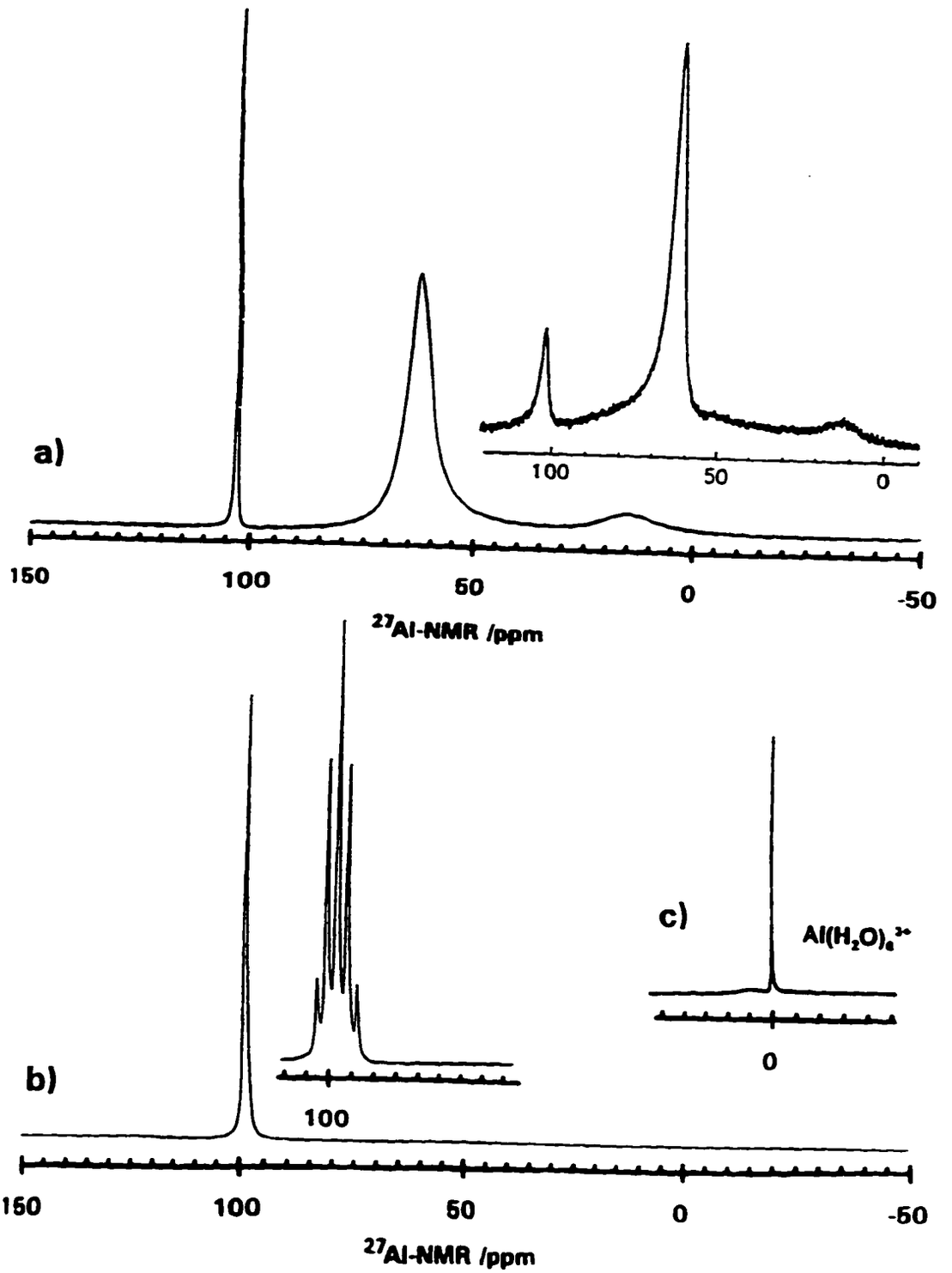


**Fig. 5.2.** $^{27}$Al-NMR proton decoupled spectra. a) 0.5 M $AlCl_3$ in thf and in its inset is the spectrum of a 1/10th dilution of the $AlCl_3$ solution; and b) 0.4 M $LiAlH_4$ in thf where in its inset the spectrum is recorded without proton decoupling. c) Spectrum of the aluminum reference solution, $Al(NO_3)_{3\,aq}$ which was run separately.

respectively. The first and last of these arise when $AlCl_3$ auto-ionizes in thf as:

$$2AlCl_3 \cdot 2thf \rightleftarrows AlCl_4^- + [AlCl_2]^+ \cdot 4thf \quad (7)$$

The relative abundances of these ions were similar at *ca.* 15%, consistent with the equilibrium of Eqn. 5.7 for which a $K_{eq}$ can be calculated as $4(\pm 2) \times 10^{-2}$. The small extent of auto-ionization of the $AlCl_3$ (Eqn. 5.7) results in generally low solution conductivities (< 0.5 mS cm$^{-1}$ for the 0.5 M solution). Peak positions were no different in a 1/10 diluted sample (shown in the inset of Fig. 5.2a) and the relative abundances remained the same, but the linewidth of the $AlCl_4^-$ resonance was broadened considerably (by a factor of 3) and the signal-to-noise ratio was poorer in the diluted sample, as expected. The $AlCl_4^-$ line-broadening has been observed elsewhere [115] and associated with ligand-exchange processes that seem to involve $AlCl_4^-$, more so at lower concentrations.

The $^{27}$Al-NMR spectrum of 0.4 M $LiAlH_4$ in thf is shown in Fig. 5.2b and exhibits only a *singlet* peak at 98 ppm corresponding to the tetrahedrally symmetric $AlH_4^-$ anion. Even at large signal expansion no other hydrido-aluminates (for instance $AlH_3 \cdot 2thf$) were detectable. When the sample was run without $^1$H-decoupling a quintet was observed (inset Fig. 5.1b) which arises from the expected coupling between the Al atom and its four $H^-$ ligands. Two concentrations were examined (*ca.* 0.4 and 0.04 M) and no appreciable difference between the spectra was observed apart from a decreased signal-to-noise ratio.

### 5.4.2. Aluminate Speciation in the Plating Baths

The hydride-bath solutions studied were of three general types: balanced (e.g. r = 1:1), excess $AlCl_3$ or $Cl^-$-rich (e.g. r = 3:1), and excess $LiAlH_4$ or $H^-$-rich (e.g. r = 1:3). Representative $^1$H-decoupled spectra of those general types of solutions are shown in Fig. 5.3. $AlCl_3$-rich, i.e. $Cl^-$-rich baths favour *uncharged* aluminates of higher $Cl^-$-content and therefore lower $H^-$-content while $H^-$-rich ones favour *anionic* aluminates of higher $H^-$-content. All experimentally observed peaks could be related to species for which literature assignments are available [114-117], except one proposed here as due to $[AlH_2Cl]^-$.

Fig. 5.3a shows the $^{27}$Al-NMR spectrum of a $Cl^-$-rich plating bath, r = 4:1,

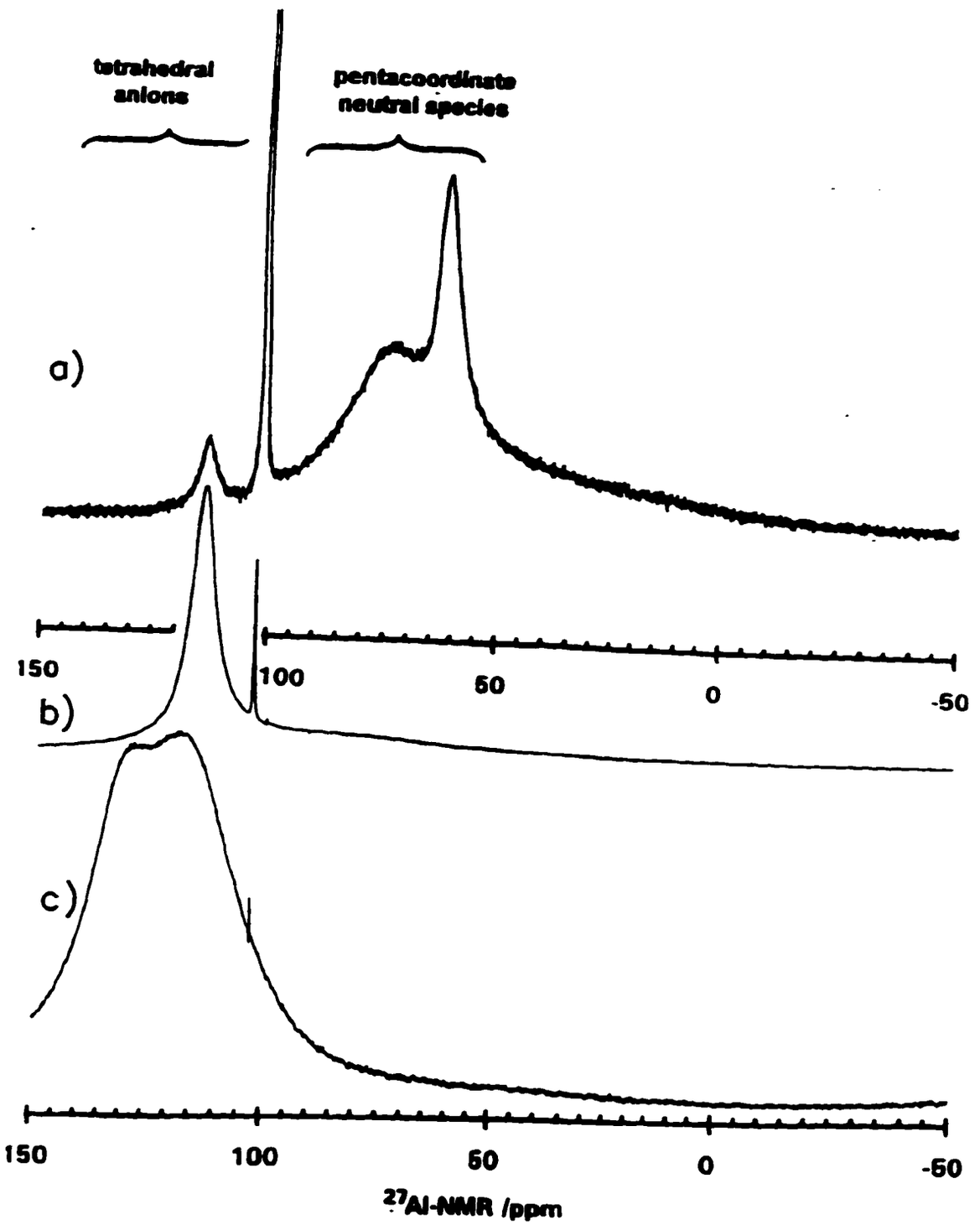


**Fig. 5.3.** $^{27}$Al-NMR spectra as a function of bath composition. **a)** r = 4:1; $[_{Al}]_{total}$ = 1.2 M, **b)** r = 1:1, $[Al]_{total}$ = 1 M; and **c)** r = 1:3, $[Al]_{total}$ = 0.6 M.

$[Al]_{total}$ = 1.0 M, at a sufficient vertical scale expansion that all peaks were distinct. Amongst the uncharged pentacoordinate aluminates, resonances for $AlCl_3 \cdot 2thf$ (64 ppm) and a broad one for $AlHCl_2 \cdot 2thf$ (77 ppm) were identified. Amongst the tetracoordinate anions a sharp and strong resonance for $AlCl_4^-$ (103 ppm, not shown full-scale) and, at higher frequency, a broader one for $[AlHCl_3]^-$ (114 ppm) were observed.

As the ratio of $LiAlH_4$ to $AlCl_3$ was increased the population of anionic and higher $H^-$-content aluminates rose as indicated by a shift to higher frequencies in the species' resonances characteristic of the decreased degree of coordination of the anions relative to that of uncharged aluminates and of a decreasing electron-density contribution from $H^-$ relative to $Cl^-$. In Fig. 5.3b the resonance responses at less than 100 ppm for the uncharged mixed aluminates have almost vanished except for a very weak resonance, (*ca.* 75 ppm) due to $AlHCl_2 \cdot 2thf$. Among the anions, only trace amounts of $AlH_4^-$ are observable at 97 ppm. The sharp $AlCl_4^-$ resonance at 103 ppm indicated higher abundance, but the dominant species (peak at 114 ppm) corresponded to $[AlHCl_3]^-$.

Closer examination of this 114 ppm peak showed that it is, in fact, complex, being composed of the superimposed resonances of several aluminates which, for symmetry reasons, display rather broad resonances. This aspect is revealed in more detail in the spectra of Fig. 5.4 for hydride-baths having r values between 1.5:1 and 1:2 in *a* through *c*. For the highest $Cl^-$-content (Fig. 5.4a) a large abundance resonance for $AlCl_4^-$ is seen (its magnitude is demonstrated in the inset of Fig. 5.4a where the spectrum is reproduced full-scale) as well as one for $[AlHCl_3]^-$. Increasing the $H^-$-content, i.e. for the r = 1:1.2, $[Al]_{total}$ = 0.8 M bath, decreased the $AlCl_4^-$ abundance but produced a shoulder on the high-frequency side of the 114 ppm, $[AlHCl_3]^-$ resonance (Fig. 5.4b).

The spectrum for an r = 1:2, $[Al]_{total}$ = 0.6 M solution (Fig. 5.4c) is dominated by a peak centred at 114 ppm, but modified by shoulders on both the high and low-frequency sides. A residual resonance for $AlCl_4^-$ is also detectable. The shoulders arise, of course, from other species having resonances in this region, *viz.* between 108 and 130 ppm, for example, $[AlH_2Cl_2]^-$, $[AlH_3Cl]^-$ and $AlH_3 \cdot 2thf$, all of which have broad linewidths, particularly for the third species, being from three to ten times broader than the identified resonance at 114 ppm (see Table 5.2). Thus it would *not* be surprising that a

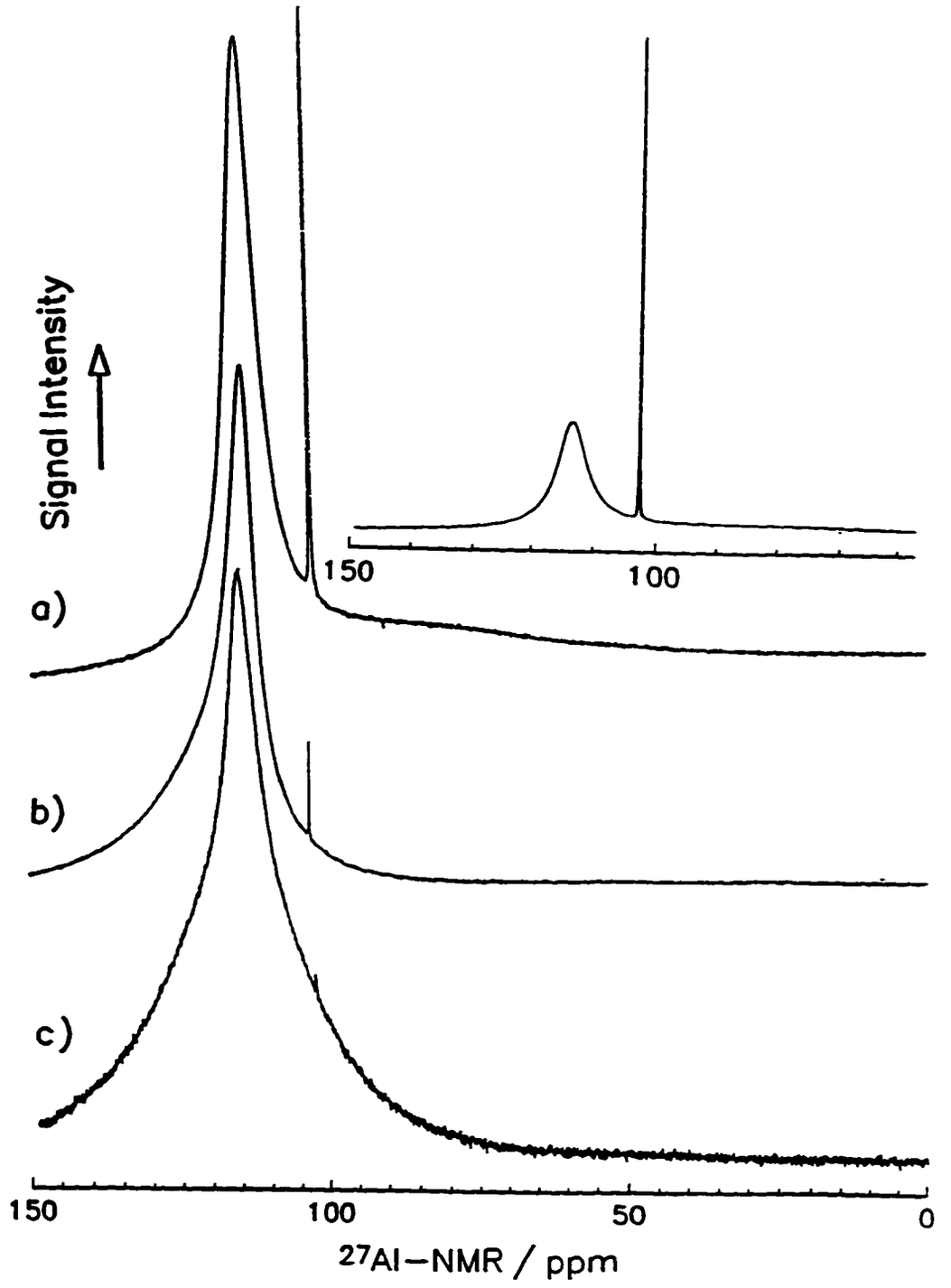


**Fig. 5.4.** **$^{27}$Al-NMR proton decoupled spectra demonstrating the complexity of the anionic aluminate resonances. a) r = 1.5:1, $[Al]_{total}$ = 1 M, b) r = 1:1.2, $[Al]_{total}$ = 0.8 M, c) r = 1:2, $[Al]_{total}$ = 0.6 M. a) is an expansion and the inset here demonstrates actual peak heights.**

mixture of these would give overlapping resonances leading to an ill-defined peak.

In $H^-$-rich baths the higher $H^-$-substituted aluminates are expected to become more prominent. The spectrum for an r = 1:3, $[Al]_{total}$ = 0.6 M bath, back in Fig. 5.3c, showed a trace amount of $AlCl_4^-$ and a large, broad overlapping resonance with peaks at about 116 and 130 ppm; the former corresponds to $[AlH_2Cl_2]^-$ and the latter, it is proposed, is due to $[AlH_3Cl]^-$ given its chemical shift value and the particular composition of that bath. Other species, particularly $AlH_3$·2thf at 108 ppm, could be masked beneath the identified peaks which could account for the apparent deficit of uncharged species in the baths (see discussion below).

### 5.4.3. Fine Structure

The fine structure of many of the samples were analyzed by comparing their $^{27}Al$-NMR spectra as measured with and without $^1H$-decoupling (as mentioned earlier, coupling with Cl atoms is not anticipated). The only mixed ligand aluminates to show well defined peak splitting (here and in the referenced literature) are $AlH_4^-$, which gave a quintet (shown earlier in Fig. 5.2b) and $[AlHCl_3]^-$, shown in Fig. 5.5, which gave a doublet due to Al-H coupling with the single hydrogen atom. Careful inspection of the spectra in Fig. 5.5 run with and without $^1H$-decoupling seems to *just* demonstrate the fine structure for $AlHCl_2$·2thf centred at about 77 ppm. The 77 ppm resonance appeared sharper with $^1H$-decoupling than when run without. No clear doublet was observed, but the "sharpening" is consistent with an apparent doublet, split by only a couple of hundred Hz, collapsing to a singlet with $^1H$-decoupling. All the mixed aluminates are expected to exhibit splitting, but only those having relatively narrow linewidths to begin with (i.e. $AlH_4^-$ and $[AlHCl_3]^-$) would be expected to demonstrate such an effect unequivocally. Examining fine structure could quantify specific electronic and bonding characteristics of the different aluminates, but due to the broadness of most of the resonances with respect to the anticipated coupling constants, no analysis of the latter was attempted and the significance of these results is restricted to confirmation of speciation.

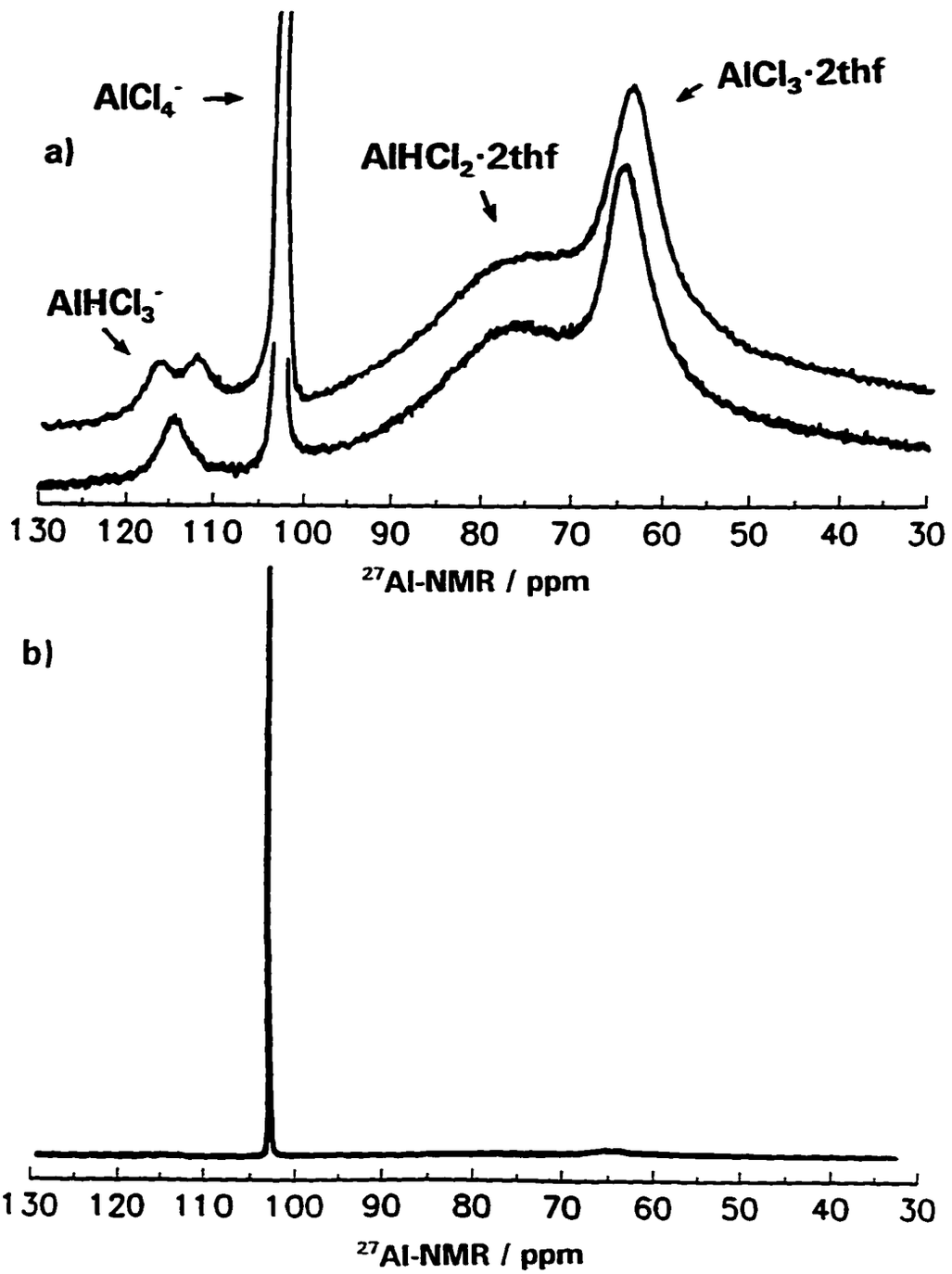


**Fig. 5.5.** $^{27}$Al-NMR spectra for an r = 4:1, $[Al]_{total}$ = 1.2 M hydride-bath **a)** recorded *without* (upper curve) and *with* (lower curve) proton decoupling. **b)** The same spectrum is shown with no vertical expansion to show the relative magnitude of the 103 ppm resonance.

### 5.4.4. Analysis of Relative Compositional Ratios

Table 5.1 lists data for relative species abundances corresponding to the spectra of Fig. 5.3 where, in some cases, the contributions from underlying peaks were estimated by deconvolution of shoulders when they were sufficiently distinct, e.g. as in Fig. 5.3b. The ratios of $Cl^-$ to $H^-$ ligands, and anionic to uncharged aluminates, for the baths of Fig. 5.3 are given in the last four columns of Table 5.1. These ratios were calculated from the compositional ratio, r ($AlCl_3$ to $LiAlH_4$ concentrations), of the baths determined by complexometric and Mohr titrations, alternately, from the integrated areas under the assigned NMR peaks, and are compared here. The values determined from titration and the NMR signals for a given bath should agree and thus, comparing them, should serve as a cross-check of the composition.

Table 5.1. Analysis of Relative Abundances of Aluminate Species from $^{27}$Al-NMR Data

| Bath r; $[Al]_{total}$ | Relative Abundance, % | | | | | $Cl^-/H^-$ ligand ratio[a] | | Anion/uncharged aluminate[b] | |
|---|---|---|---|---|---|---|---|---|---|
| | $AlCl_3$ | $AlHCl_2$ | $AlCl_4^-$ | $AlHCl_3^-$ | $AlH_3Cl^-$ | r | NMR | r | NMR |
| 4:1; 1.2 M | 12 | 33 | 52 | 3 | | 3.00 | 8.72 | 0.25 | 1.20 |
| 1:1; 1.0 M | | | 5 | 72 | 23 | 0.75 | 1.84 | 1.00 | ∞ |
| 1:3; 0.6 M | | | | 55 | 45 | 0.33 | 0.91 | 3.00 | ∞ |

[a]the proportion of $Cl^-$ to $H^-$ is calculated from r and from NMR peak integration; [b]the ratio of anions to uncharged species is calculated as in *a* where it is noted that all $LiAlH_4$ is anionic and all $AlCl_3$ is uncharged.

The ligand ratio calculated from the NMR data, however, showed a *surplus* of $Cl^-$ (up to about three times) compared with that expected from r. At the same time a *deficit* of uncharged aluminates (more significant than the $Cl^-$ surplus) was indicated. The initial source of both $Cl^-$ and uncharged species in the bath is $AlCl_3$ which, if underestimated by titration, should have given a surplus of *both* $Cl^-$ *and* uncharged aluminates. This could not have been the case so that the anomalies are not explained by an erroneous titration.

A possible explanation for the $H^-$ deficit may be the inadvertent omission of higher

$H^-$-content aluminates from the anion region, 100 - 130 ppm, of the chloro-hydrido-aluminate spectrum, the resonances in which are known to be very broad and are thus obscured beneath the sharper resonances, e.g. of $[AlHCl_3]^-$ at 114 ppm. This would result in an underestimation of the $H^-$-content and ergo an overestimation of $Cl^-$-content in this region of the NMR spectra. Another possibility could be that some decomposition reactions take place involving the uncharged aluminates, possibly with the participation of trace amounts of water, for example:

$$2AlHCl_2{\cdot}2thf + 6H_2O \rightarrow 2Al(OH)_3\downarrow + 4HCl\uparrow + H_2\uparrow + 4thf \quad (8)$$

$$2AlH_2Cl{\cdot}2thf \rightarrow 2Al\downarrow + 2H_2\uparrow + Cl_2\uparrow + 2thf \quad (9)$$

$$2[AlH_3Cl]^- \rightarrow 2Al\downarrow + 3H_2\uparrow + 2Cl^- \quad (10)$$

Pressure from evolving gas was observed to build up over solutions contained in sealed containers upon standing.

## 5.5. Ligand-Exchange Equilibria

The distribution of aluminate species of varying ligation and charge (Fig. 5.1) in the hydride-bath depends on the relative abundance of $Cl^-$ to $H^-$. Since the component species are $AlCl_3$ and $LiAlH_4$, baths with r = 3:1, 1:1 and 1:3 are expected to give mixed-ligand products having simple stoichiometries. Thus, the resulting aluminates of these *primary ligand-exchange* processes would be described by the following equilibria:

$$3AlCl_3{\cdot}2thf + Li^+AlH_4^- \rightleftarrows 3AlHCl_2{\cdot}2thf + Li^+AlHCl_3^- \quad (11)$$

$$AlCl_3{\cdot}2thf + Li^+AlH_4^- \rightleftarrows AlH_2Cl{\cdot}2thf + Li^+AlH_2Cl_2^- \quad (12)$$

$$AlCl_3{\cdot}2thf + 3Li^+AlH_4^- \rightleftarrows AlH_3{\cdot}2thf + 3Li^+AlH_3Cl^- \quad (13)$$

Beyond giving an indication of the expected aluminate species for given *r* values, these equilibria should also predict the relative abundances of uncharged to anionic species.

Fig. 5.3a (earlier) shows the spectrum for an r = 4:1 bath in which all the resonances of species on the rhs of the equilibrium of Eqn. 5.11 were clearly observed including that for the "surplus" $AlCl_3{\cdot}2thf$ (i.e. that which was beyond the ideal 3:1 ratio for equilibrium 5.11); additionally, however, there was a resonance for $AlCl_4^-$ exhibiting an unexpectedly high abundance (52%). Such a result is surprising given that auto-ionization of $AlCl_3{\cdot}2thf$ in the $AlCl_3$ control (equilibrium 5.7) was only *ca.* 15%. Ligand-

exchange of some other aluminate to give $AlCl_4^-$ in an equilibrium of the kind:

$$2[AlHCl_3]^- \rightleftarrows [AlH_2Cl_2]^- + AlCl_4^- \quad (14)$$

could not explain its abundance either, since a commensurate $[AlH_2Cl_2]^-$ resonance should then also have been observed, but was not. It is probable that significant aluminate decomposition takes place, producing $Cl^-$ that binds to $AlCl_3$.

The NMR spectrum for such an r = 1:1 bath, corresponding to the equilibrium of Eqn. 5.12, was given in Fig. 5.3b. The uncharged $AlH_2Cl{\cdot}2thf$, on the rhs of equilibrium 5.11, was not observed at all in the spectrum (nor indeed in that of any of the solutions of varied *r* studied); instead of $[AlH_2Cl_2]^-$ expected on the basis of equilibrium 5.11, $[AlHCl_3]^-$ and $[AlH_3Cl]^-$ were identified, the latter only as a weak shoulder. The seeming instability of the uncharged and anionic *di*hydrido-aluminates suggests the further possible equilibria, Eqns. 5.15 and 5.16:

$$AlH_2Cl{\cdot}2thf + Li^+AlH_2Cl_2^- \rightleftarrows AlH_3{\cdot}2thf + Li^+AlHCl_3^- \quad (15)$$

$$3AlHCl_3^- \rightleftarrows [AlH_3Cl]^- + 2AlCl_4^- \quad (16)$$

Indeed, a substantial presence of $AlH_3{\cdot}2thf$, which could be practically unobservable since its linewidth is known to be large and its resonance would be in the region of the complex peak at 114 ppm, could offer a possible explanation for the apparent absence of uncharged aluminates (as calculated from the NMR abundances).

Such relations offer possible reasons for both the noted absence of "dihydride" species in the baths and the presence of $[AlH_3Cl]^-$ and $AlCl_4^-$. The species distribution in this bath, however, remains speculative since the breadth of the resonances of the various species from equilibria Eqns. 5.15 and 5.16 did not permit their reliable deconvolution.

Fig. 5.3c shows the NMR spectrum of an r = 1:3 bath corresponding to equilibrium 5.13. $[AlH_3Cl]^-$ was indeed identified in the experimental spectrum of this bath, but $[AlH_2Cl_2]^-$ was also present in roughly the same abundance. This spectrum could (as was the case in the 1:1 bath type) be complicated by the presence of $AlH_3{\cdot}2thf$ but, again, such a species could not be unequivocally proven.

The primary equilibria (Eqns. 5.11, 5.12 and 5.13), which are based on the initial *r* values of the baths, should determine both the proportion of uncharged to anionic aluminates and the predominant species or, at least, the species around which the aluminates

present should be distributed (considering subsequent ligand-exchange equilibria). It is obvious from the experimental spectra in Figs. 5.2 and 5.3 and the above discussion that the actual speciation is more complex than would be expected only on a statistical basis. The abundance of $AlCl_4^-$ was much greater than could be accounted for simply by ligand-exchange reactions. Free $Cl^-$, as might arise as the byproduct from chemical reduction of chloro-aluminum species in solution, is not expected to be stable in thf, given this solvent's poor acceptor number ($A_n = 8.0$ where a good acceptor such as water has $A_n = 54.8$) would thus likely be bound to $AlCl_3$ [118]. The $Cl^-$ abundance in the hydride-baths demonstrates the significant amount of decomposition that seems to accompany solution preparation and aging and this has been observed (if not discussed) elsewhere [117].

Interestingly, $AlH_4^-$ was not observed in any of the mixed baths except sometimes in trace amounts which arose only (as expected) when there were no $Cl^-$-containing species present. The *di*hydrido-aluminates, $AlH_2Cl{\cdot}2thf$ and $[AlH_2Cl_2]^-$, were unusually low in abundance. The former was not identified in any of the NMR spectra and the latter, while indeed being present in the $H^-$-rich baths, gave abundances far below that which would have been expected on the basis of the statistics of the proposed ligand-exchange equilibria. The evident instability of the dihydrido-aluminates could be due to their high reactivity (see below).

## 5.6. Chemical Reactivity of Mixed Ligand Aluminates

Aluminum can be electroplated at appreciable rates from mixed aluminate hydride-baths, but interestingly not from either of the homo-ligated aluminate species (Chapter 6). Additionally, the mechanism of the electrochemical reaction was observed to vary, i.e. there was a difference of experimental transfer coefficients between the baths' compositional extremes (see §6.8.2). It is therefore important to identify the aspects of the reactivity and speciation that are possibly responsible for the Al electroplating and dissolution reactions. The relative chemical shifts and linewidths from NMR results of the aluminate analogues are examined and discussed with respect to this point.

Beyond their use for speciation of the various hydride-baths employed in the present work, NMR results may also be analyzed to characterize the reactivity of the

mixed ligand species present in the hydride-baths. Comparison of the relative chemical shifts and linewidths of aluminates observed in the baths can lend some insight into their reactivity since relative NMR chemical shifts arise due to variation of electron-density at a resonant nucleus; a resonant nucleus' own electrons (i.e. as determined by its oxidation state), the characteristics and number of bonds formed with adjacent atoms and, to a lesser extent, the electronic characteristics of these adjacent atoms, all contribute to the electrical environment. Inferring bonding information from such comparisons in the case of $H^-$ and $Cl^-$ must be done with care, since the $H^-$ ligand possesses only two valence-shell electrons and $Cl^-$ eight (not to mention this latter's inner-shell electrons).

### 5.6.1. Chemical Shifts of the Mixed Aluminates

Predicting chemical shifts from measures of the electron-donative power of substituents, based, for instance, on their electronegativity or donor number [17], has seen some success in the case of Al. Chemical shift variation with successive ligand substitution has been shown to give both *linear* trends for mixed solvent coordination in octahedral aluminum cations [111:p.170] and *second-order* behaviour including ligand-ligand interactions for a number of aluminum species with mixed ligands including $Cl^-$:$Br^-$, $Cl^-$:$I^-$ [119]. Generally, however, these relations are not particularly reliable.

Table 5.2 lists characteristic NMR data for the species that are possibly present in the hydride-bath (note that those in parentheses are literature values for species that were either not observed in the present work or, in the case of $AlH_3$·2thf, differed markedly from literature values). The chemical shifts for the uncharged *pentacoordinate*, doubly-solvated aluminates varied almost uniformly with ligand substitution by $H^-$, shifting to higher frequencies by 13, 13 and 18 ppm. $AlH_2Cl$·2thf was not directly identified in the present work, but has been reported elsewhere [117]. What could have been a resonance due to $AlH_3$·2thf was observed distinctly in several spectra near to the reported chemical shift for this species [117] at 108 ppm (see Fig. 5.6c later), but its linewidth was much less than that cited in the reference and hence is associated here with the concentration-dependence of another species' resonance (see §5.8). The presence of $AlH_3$·2thf was, however, inferred here from the apparent deficit of *uncharged* aluminates in the

speciation of the higher $H^-$-content baths.

Table 5.2. $^{27}$Al-NMR data

| Chemical Shift ppm( )[a] | Species | Linewidth/ Hz | Coupling Constant/ Hz ( )[a] |
|---|---|---|---|
| *tetracoordinate species* | | | |
| 130s[b] | $[AlH_3Cl]^-$ | 1400[c] | |
| 116s | $[AlH_2Cl_2]^-$ | 1200[c] | |
| 114d | $[AlHCl_3]^-$ | 400 | 330 |
| 103s[c] | $[AlCl_4]^-$ | 50 | |
| 97q | $AlH_4^-$ | 50 | 170 |
| *pentacoordinate species* | | | |
| 108s | $AlH_3 \cdot 2thf$ | 1100(3000) | |
| (90s) | $AlH_2Cl \cdot 2thf$ | (2500) | |
| 77s | $AlHCl_2 \cdot 2thf$ | 2200 | |
| 64s[c] | $AlCl_3 \cdot 2thf$ | 300-500 | |
| *tricoordinate species* | | | |
| (65)[f] | $AlH_3$ | (3000) | |
| *hexacoordinate species* | | | |
| 20s | $[AlCl_2]^+ \cdot 4thf$ | broad | |
| 0s[g] | $[Al(H_2O)_6]^{3+}_{aq}$ | 20 | |

All resonances corresponded to those cited in [117] except where noted. s: singlet; d: doublet; q: quintet; [a]brackets indicate resonances for species cited in the literature, that were not observed directly in this work or that were, but the values of which were significantly different; [b]observed here, but not reported in literature; [c]estimate; [e]from [114]; [f]from [116]; [g]$^{27}$Al reference.

In the case of the *tetracoordinate* aluminates, $[AlH_xCl_{4-x}]^-$, the first three $Cl^-$ substitutions by $H^-$ ligands shift the resonance frequency non-uniformly in the order 11, 2, then 14 ppm higher. This general trend may suggest, beyond simply the reduced electron-density of $H^-$ relative to $Cl^-$, a stronger Al-Cl than Al-H bond which is, in fact, indicated by thermodynamic data in Table 5.3. Although the gas-phase diatomic bond strengths given in Table 5.3 do not relate directly to the bonding situations in the tetra- and pentacoordinated aluminates, due to different hybridizations, they do indicate that $Cl^-$ forms stronger bonds (almost by a factor of two) than does $H^-$ in similar bonding situations: compare H and Cl bonds with Al and Li in Table 5.3.

Table 5.3. **Bond Strengths of Diatomic Molecular Species Having Possible Relevance to the Mixed Aluminate Plating Baths**

| Bond | Bond Strength kJ $mol^{-1}$ |
|---|---|
| **Al-Cl** | **511** |
| **Al-H** | **282** |
| Li-Cl | 469 |
| Li-H | 238 |
| **Al-Al** | **186** |
| Al-O | 512 |
| Al-Li | 174 |
| Cl-H | 432 |

**Values from [1:p.F197] reportedly measured in the gas phase either spectroscopically or by mass spectrometric analysis.**

The final $H^-$ substitution in the tetrahedral series gives $AlH_4^-$ having anomalously, relative to the above series, a resonance at 97 ppm, *lower* than for the other anion resonances, even for $AlCl_4^-$. This result for $AlH_4^-$ versus $AlCl_4^-$ suggests more electron-density resides over the Al nucleus in the $AlH_4^-$ leading to a shorter, and thence a stronger Al-H over Al-Cl bond in the unmixed anions, but this is difficult to reconcile with the known bonding differences referred to above.

More probably a geometric steric effect is operative in these aluminates with regard to their relative chemical shifts. Four $H^-$ ligands arranged in a tetrahedron around the Al atom would be able to approach much closer than could four $Cl^-$ ligands. This interpretation is consistent (as explained below) with bond distances derived from semi-empirical molecular geometry calculations [120] for tetrahedral aluminates as well as geometrically unhindered analogues (Table 5.4).

In this comparison the bond distances calculated for the trigonal planar geometry, the existence of such species being perhaps questionable, are assumed to represent the bond distances in the absence of any geometric contraints. This is done in order to maintain internal consistency in the comparative analysis since the calculated values are only semi-quantitative, depending largely on the choice of basis parameter set used (for

instance AM1 in this case).

Table 5.4. Values of Bond Distances in Tetrahedral Anions of Calculated[a] Geometries

| Species | Al-Cl nm | Al-H nm | Calc'd Charge at Al | $\Delta G_{form}$/ kJ mol$^{-1}$ |
|---|---|---|---|---|
| $AlCl_3$ | 0.187 | - | +0.72 | -585 |
| $AlCl_4^-$ | 0.224 | - | +0.57 | -1045 |
| $[AlHCl_3]^-$ | 0.227 | 0.143 | +0.44 | -845 |
| $[AlH_2Cl_2]^-$ | 0.230 | 0.144 | +0.19 | -635 |
| $[AlH_3Cl]^-$ | 0.231 | 0.145 | - 0.27 | -415 |
| $AlH_4^-$ | - | 0.145 | - 1.08 | -205 |
| $AlH_3$ | - | 0.143 | - 0.82 | +55 |

a: semi-empirically calculated (AM1) [120].

Comparing the top two and bottom two values in Table 5.4 demonstrates that the calculated Al-Cl bond distance changes considerably (by nearly 0.04 nm longer) between the hindered and unhindered geometries, whereas the Al-H bond distance does not. The Al-Cl bonds are found to be sterically constrained in $AlCl_4^-$ while the Al-H bonds in $AlH_4^-$ are not. Given the inverse-square dependence of electrostatic force on distance, the lower frequency chemical shift position of $AlH_4^-$ relative to $AlCl_4^-$ is not surprising.

Substitution of the bulky $Cl^-$ ligand would probably disrupt the special bonding situation in $AlH_4^-$ and this is consistent with the 33 ppm shift to *higher* frequency for $[AlH_3Cl]^-$ (cf. Table 5.2). Although the relative bond distances from the molecular orbital calculations [120] can explain the somewhat unexpected relative chemical shift positions of the homo-ligated anions, the relative calculated bond distances of the *mixed* ligand aluminates are not able to account for the large chemical shift that accompanies the first $Cl^-$ ligand substitution of $AlH_4^-$. In fact, calculated Al-Cl bond distances for the tetrahedral aluminates varied by only 0.007 nm. Additionally, the resonances of all mixed ligand aluminate anions were found to lie at frequencies higher than those for both unmixed aluminates and this indicates that the presence of *both* $Cl^-$ and $H^-$ decreases the

electronic interaction between these ligands and Al. This suggests that some special energetic situation arises in the mixed ligand analogues that might be at the basis of their more facile Faradaic discharge in the Al electroplating processes (Chapter 6).

It should be mentioned that comparitive discussion of varying bonding situations present in the aluminate complex on the basis of elemental electronegativities or the *hard-soft acid-base* theory of chemical bonding of Pearson [121,122] is difficult due to the individual nature of $H^-$ as a ligand.

### 5.6.2. Linewidths of the Mixed Aluminates

The variation of linewidths for most aluminate analogues was found to be consistent with the progressive differences of symmetry of the mixed ligand species, but with several interesting exceptions. This is succinctly apparent if the uncharged and anionic aluminates are grouped into pairs according to their symmetry as follows: the $D_{3h}$ $AlH_3 \cdot 2thf$ and $AlCl_3 \cdot 2thf$; the $C_{2v}$ $AlH_2Cl \cdot 2thf$ and $AlHCl_2 \cdot 2thf$ ; the $C_{3v}$ $[AlH_3Cl]^-$ and $[AlHCl_3]^-$; and the $T_d$ $AlH_4^-$ and $AlCl_4^-$. These pairs, since of the same symmetry, should have comparable linewidths. It was observed, however, in Table 5.2 that the aluminates of higher $H^-$-content had linewidths markedly larger than the higher $Cl^-$-content analogues in all cases, except for $AlH_4^-$. The anomalously large linewidths of many of the higher $H^-$-content aluminates suggests that some factor other than only symmetry is operative in determining these species' linewidths.

As a matter of completeness, it was found that the uncharged pentacoordinate aluminates all had broader linewidths than the anions. $AlCl_3 \cdot 2thf$, a trigonal bipyramid as a *trans*-isomer, has pseudo-$D_{3h}$ symmetry. Although $D_{3h}$ is a highly symmetric space group and a sharp signal linewidth is expected, this aluminate is not strictly speaking $D_{3h}$ due to the nonsymmetric coordination configuration of the interaction with the coordinating thf. Additionally, two isomers are possible (*trans* and *cis*, shown in Eqn. 5.17). The latter of these is of lower symmetry and would demonstrate a broader resonance linewidth than the other. If the resonances of these two were superimposed upon one another or they were chemically-exchanging between each other within the time-scale of the experimental pulse, broad linewidths are anticipated.

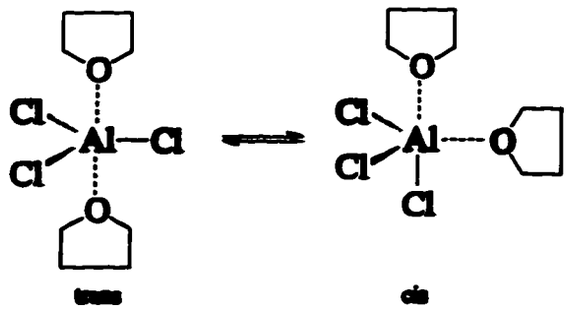

(17)

The anomalies in the NMR behaviour of these analogous compounds are consistent with possible *ligand-exchange line-broadening* due to *mutual ligand labilization*, perhaps catalyzed by the $H^-$ ligand, but necessarily involving the $Cl^-$ ligand as well (recall that the resonance linewidth for $AlH_4^-$ is very narrow). It is known that chemical-exchange of ligands between nearby aluminates at a rate comparable to the timescale of the experimental measurement can broaden lines [108]. Although the homo-ligated compounds of aluminum are all covalently bonded and not susceptible to ligand-exchange [123], less is known of mixed ligand species and it is possible that the presence of more than one ligand type, necessarily including $H^-$ in this case, could labilize all ligands such that exchange reactions would become rapid. This sort of situation is consistent with the broadened resonance lines *and* higher frequency chemical shifts with $H^-$ substitution trends noted here. Higher frequency chemical shifts result from the labilized ligands since these would be further away from, and hence contribute less to, the electrical and magnetic environment of a resonant nucleus. This effect could contribute to the broadening of *all* the mixed aluminate resonances, where only the strikingly anomalous examples would be experimentally apparent.

These trends lend qualitative support to the idea that there is some kind of mutual ligand-labilization process operative within the mixed aluminates. The $H^-$ ligand has an important role in catalyzing ligand lability in a seemingly progressive manner, where aluminate complexes of higher $H^-$ ligand substitution are found to be more reactive, except in the special case, discussed above, of $AlH_4^-$. Comparison could be made between experimental and theoretically calculated linewidths where these latter would be based on electric field-gradients, bond distances and angles, nuclear quadrupole coupling

constants, etc. The uncertainty in such calculations, however, even when all parameters are estimable, is usually rather large for elements other than those of the first row [108]; thus only qualitative comparisons are possible.

## 5.7. $^{7}$Li-NMR Behaviour of Hydride-Baths

$Li^{+}$ ions are the major cationic species in the hydride-baths. For a number of solutions $^{7}$Li-NMR was investigated to examine whether any ion-pairing was evident. Only *singlet* $^{7}$Li resonances were observed in all baths studied, even though $^{27}$Al-NMR spectra of the same samples, confirmed significant concentrations of a multitude of anionic aluminate species in many of the samples studied. A general trend was the shifting of the lithium peak downfield with higher $H^{-}$-content of the bath (0.64 - 0 ppm). Sample dilution was found to shift the peaks downfield, an effect that is consistent with facile chemical-exchange or in other words there was no [$Li^{+}$-$AlX_4^{-}$] ion-pairing in these solutions that might limit or determine the electrochemical behaviour of the aluminates.

## 5.8. Concentration-Dependence of Chemical Shifts

Nuclei that experience ligand-exchange at a rate faster than the experimental acquisition time should exhibit a chemical shift that is time-averaged between the different species involved. The chemical equilibrium for such a process would be:

$$M^{*}\text{-}H^{-} + M \quad \rightleftarrows \quad M^{*} + M\text{-}H^{-} \qquad (18)$$

where $M^{*}$ is the excited nucleus and $H^{-}$ the ligand being exchanged. Since reaction 5.18 is a bimolecular process, a concentration-dependence for the experimentally observed chemical shift for such exchanging species would be expected [123,124]. Although the concentration-dependence comparisons in this work were necessarily somewhat qualitative, several of the aluminates, especially the $H^{-}$-rich anionic species, exhibited a significant variation of peak position with concentration.

The time-dependence of speciation was another interesting aspect of the hydride-baths' reactivity and will be discussed in the next section. This time-dependence is relevant to the discussion here, of concentration-dependence, since the total aluminum concentration decreases over time in these baths due to decomposition with some

precipitation. Although the species distribution may also vary over time, a time-dependence experiment can also give a concentration-dependence of identifiable species.

Fig. 5.6 compares the $^{27}$Al-NMR spectra of, in "*a*", an r = 1:2, $[Al]_{total} = 0.5$ M bath and in "*b* - *e*" the time-dependence of behaviour of an r = 1:2.5, $[Al]_{total} = 0.45$ M bath. The broad peak at about 50 ppm observed in a number of the spectra is due to background from the instrument's sample compartment and gives a relative indication of the concentration of the other species present. The peak assigned to $[AlH_3Cl]^-$ rose from 129 to 132.5 ppm as concentration decreased and the $[AlH_2Cl_2]^-$ resonance varied from 116 to 111.5 to 106 to 104.5 ppm (Figs. 5.6*a* to *d*). These are very significant shifts considering that the $AlCl_4^-$ resonance (at 102.8 ppm) varied by no more than 0.2 ppm amongst the at least twenty different baths of varying composition in which it was observed.

Experimental control of both concentration and species distribution was not feasible for these baths, but the variations of peak positions of the identified resonances with concentration suggest that ligand-exchange occurs rather more readily in the mixed aluminates of high $H^-$-content than in those of high $Cl^-$-content where resonance shifts were absent. Species that showed no peak shifts were $AlCl_3 \cdot 2thf$, $AlHCl_2 \cdot 2thf$, $AlCl_4^-$, $[AlHCl_3]^-$ and $AlH_4^-$ although the concentration range was limited in the case of $AlHCl_2 \cdot 2thf$. The chemical-exchange seems, therefore to be linked to $H^-$ catalyzed reactivity of the mixed aluminates.

## 5.9. Time-Dependence of the Behaviour and Speciation of the Hydride-Baths

The hydride plating baths are known to be very moisture sensitive and it was found that reproducibility in electrochemical experiments was often not very good. In order to obtain some indication of any time-dependence of the aluminate speciation, $^{27}$Al- and $^{13}$C-NMR spectra of samples from an operating bath, taken at various times, were recorded and compared with those from sealed samples examined over the same time period. The "operating" bath was one that was employed in repeated electrochemical experimentation on plating of Al.

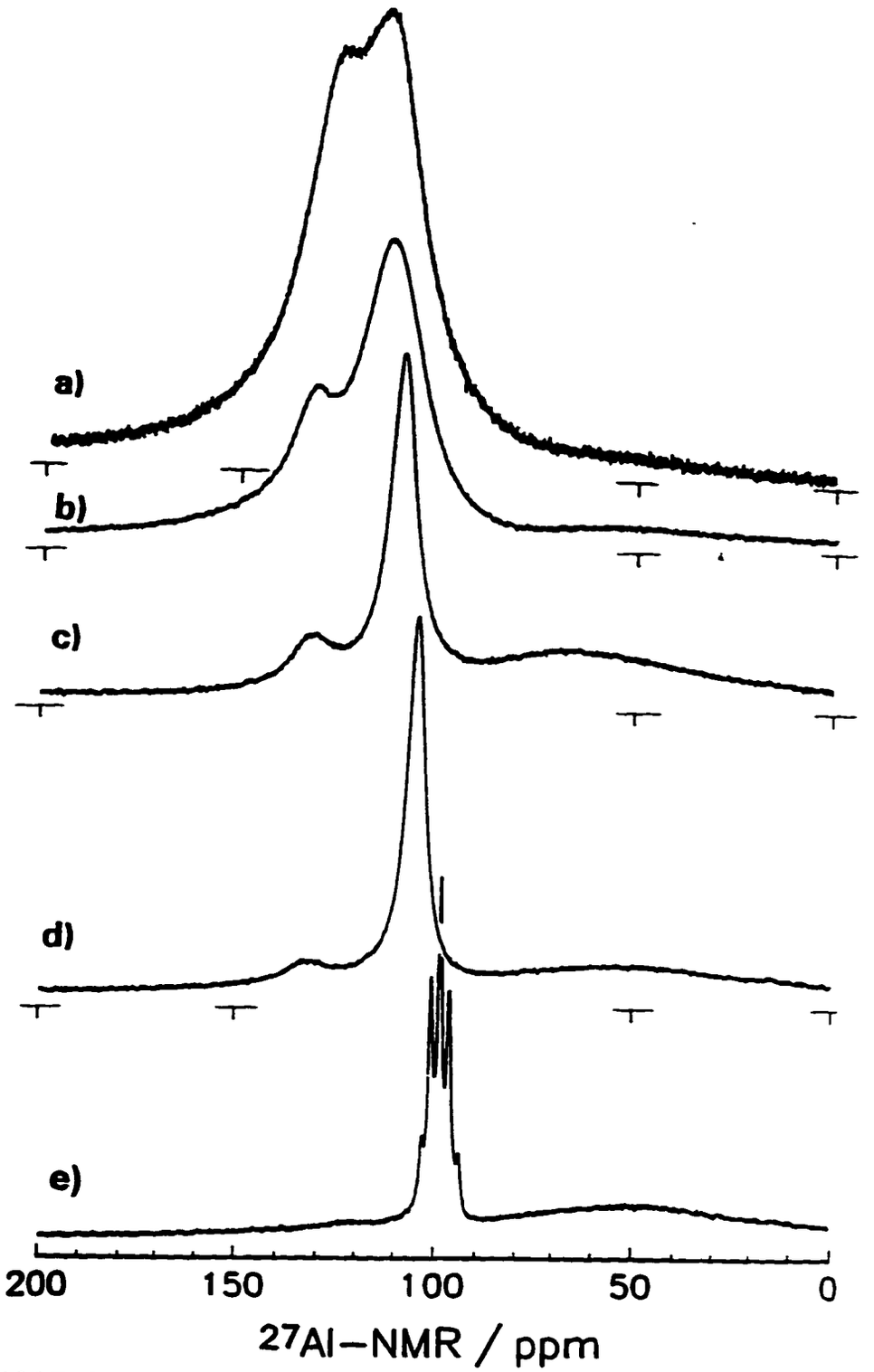


**Fig. 5.6.** $^{27}$Al-NMR proton decoupled spectra of hydride-baths of compositions: **a)** r = 1:2.5, $[Al]_{total}$ = 0.5 M; and in **b-e)** an r = 1:2.5, $[Al]_{total}$ = 0.5 M hydride-bath recorded at various times after its preparation **b)** 0 days; **c)** a sealed sample at 17 days; **d)** an operating sample at 17 days; and **e)** 27 days.

### 5.9.1. Time-Dependence of $^{27}$Al-NMR Behaviour

The time-dependence of the speciation in an r = 3.5:1, $[Al]_{total}$ = 0.7 M, $Cl^-$-rich operating bath over the course of 24 days is shown in Fig. 5.7. It was found that a sealed sample showed similar behaviour. Resonances for $[AlHCl_3]^-$ at 114 ppm, $AlCl_4^-$ at 103 ppm, $AlHCl_2 \cdot 2thf$ at 76 ppm and $AlCl_3 \cdot 2thf$ at 64 ppm were observed. With time, the relative abundances of $H^-$-containing aluminates decreased appreciably. Concurrently, a broad peak at 17 ppm (due to $[AlCl_2]^+ \cdot 2thf$) became more prominent. Whether this was due to the formation of this species or the commensurate decrease of all others is difficult to say since it was not possible to employ an internal standard in this system, so absolute concentrations could not be monitored. At long times (Fig. 5.7d), the spectrum became like that for the $AlCl_3$ control solution (Fig. 5.2a) although the proportions of species were not the same. In a $H^-$-rich bath (both sealed and operating samples) monitored over the same time as part of Fig. 5.6 ("*b* - *e*"), the $[AlH_3Cl]^-$ and $[AlH_2Cl_2]^-$ resonances indicated decreasing species abundance until ultimately only a single resonance [a quintet (un-$^1$H-decoupled) at 98 ppm], not previously present, appeared. This was due to $AlH_4^-$, and thus all $Cl^-$-containing complexes had become undetectable.

### 5.9.2. Time Dependence of $^{13}$C-NMR Behaviour

$^{13}$C-NMR spectra were also recorded concurrently in order to monitor the state of the thf solvent in the above two solutions over the same time period. Figs. 5.8 and 5.9 show $^{13}$C-NMR spectra of a *sealed* $H^-$-rich bath and an *operating* $Cl^-$-rich bath, respectively, over the course of 27 days. Strong peaks due to the $\alpha$ and $\beta$ carbons of thf appeared at 66.9 and 25.1 ppm, respectively, (identified as $C_\alpha$ and $C_\beta$ in Fig. 5.8) consistent with cited values [125]. Close to these, on the low frequency side, were very small abundance peaks. Since the relative abundances of decomposition-product were very small, the vertical expansion in the $^{13}$C figures was set so that the peak heights of the above mentioned weak peaks close to the major resonances of thf were all about the same. These did not seem to be associated with the coordination of the solvent with the uncharged aluminate species since the peak height ratio was found to be about constant

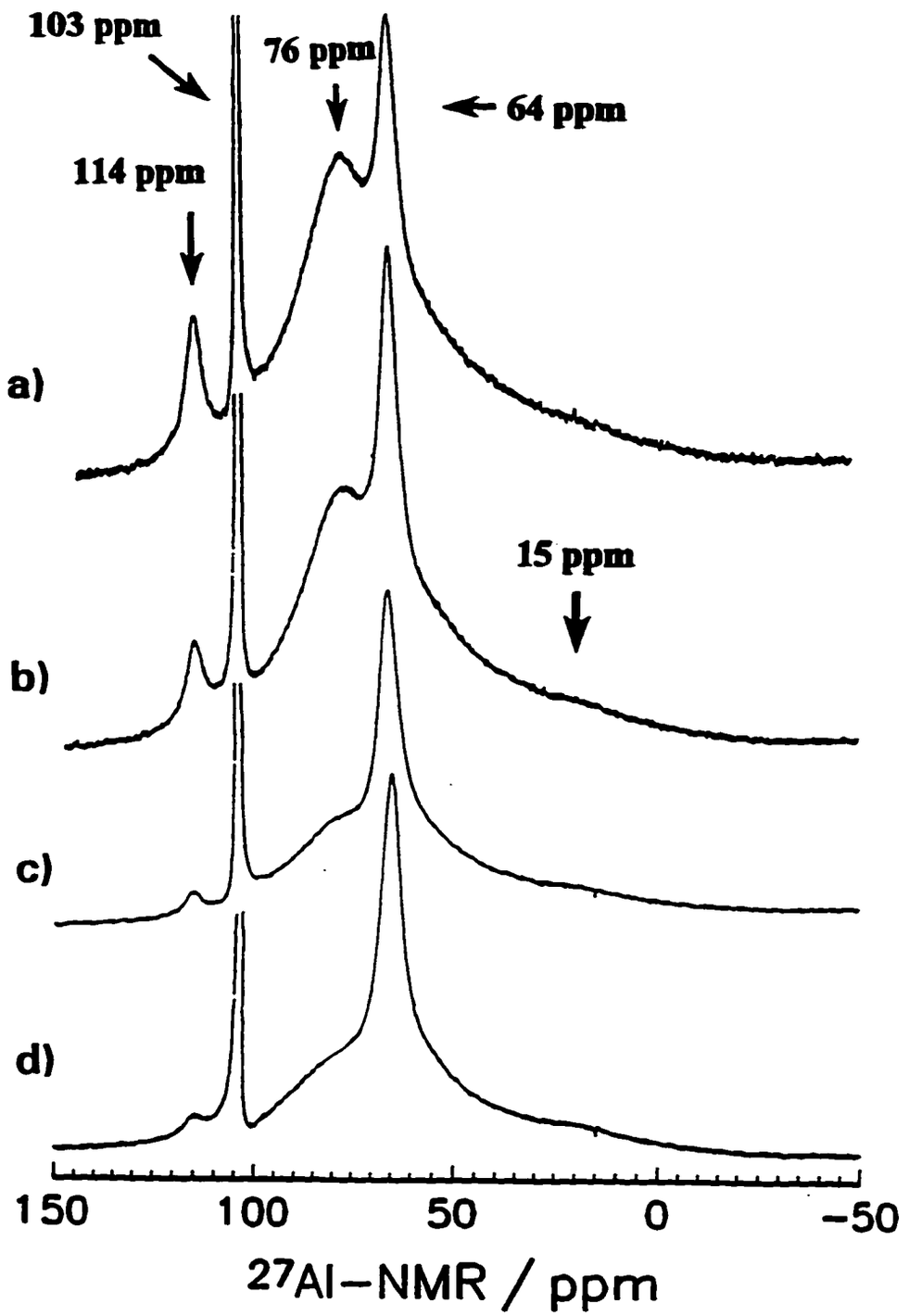


**Fig. 5.7.** $^{27}$Al-NMR proton decoupled spectra of an r = 3.5:1, $[Al]_{total}$ = 0.7 M, i.e. $Cl^-$-rich, *operating* hydride-bath recorded at various times after its preparation **a)** 0 days; **b)** 3 days; **c)** 7 days; and **d)** 23 days.

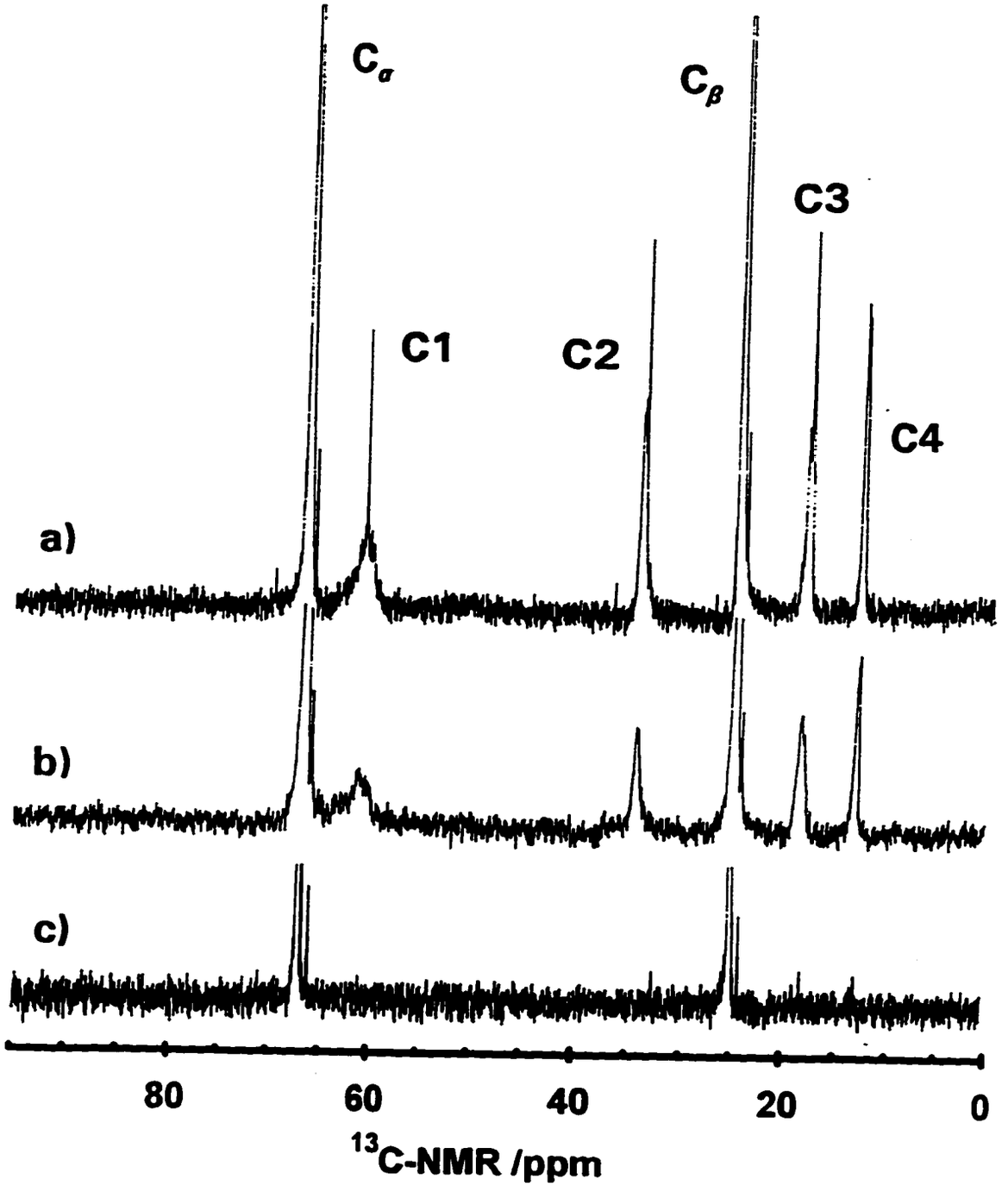


**Fig. 5.8.** $^{13}$C-NMR proton decoupled spectra of a sealed hydride-bath sample of composition r = 1:2.5, $[Al]_{total}$ = 0.5 M recorded at a) 27 days; b) 17 days; and c) 0 days after preparation for 6400, 1997 and 512 scans, respectively. The $\alpha$ and $\beta$ carbons of thf as well as the product peaks, C1 - C4 are indicated.

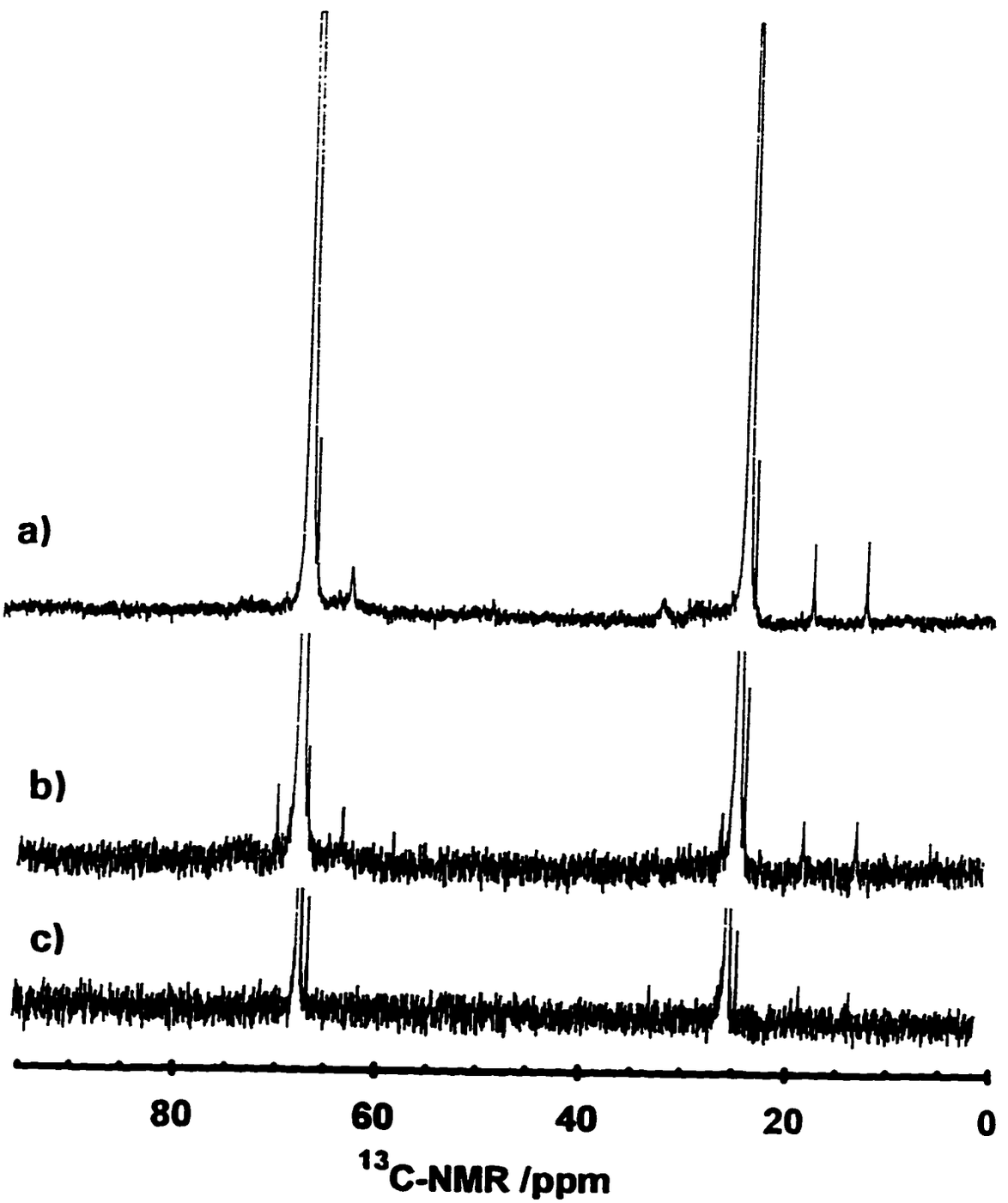


**Fig. 5.9.** $^{13}$C-NMR proton decoupled spectra of an *active* hydride-bath sample of composition r = 3.5:1, $[Al]_{total}$ = 0.7 M recorded at **a)** 27; **b)** 17; and **c)** 0 days after it was prepared for 6580, 3600 and 512 scans, respectively.

(*ca.* 0.3%) for all spectra, where differences should have arose due to the varying degree of solvent coordination with composition and ergo time, where, in fact, no characteristics of coordinated solvent molecules could be deciphered from the $^{13}$C-NMR results.

The $^{13}$C-NMR spectra of a *sealed* $H^-$-rich bath sample, given in Fig. 5.8 showed evidence of low abundance decomposition-products almost immediately and these became more prominent with time. In an *operating* bath of the same composition these peaks grew more rapidly. They are identified as C1: 62.4; C2: 36.0; C3: 20.1; C4: 14.6 ppm in Fig. 5.7 and compare well with those for n-butanol, a close analogue of a possible solvent decomposition-product. A DEPT (distortionless enhancement by polarization transfer) experiment which is a multipulse, spin-echo technique that can separate a spectrum into individual spectra for carbons having one, two or three H atoms [126], demonstrated that the peak at 13 ppm was due to $-CH_3$, all others being due to $-CH_2$-'s. This decomposition-product is consistent with $AlX_2$-O-$C_4H_9$ and would arise from ring opening of the thf [127]. The reaction would involve the acidic attack of the aluminum on the oxygen atom of a coordinating thf molecule coupled to *proton* transfer (illustrated in Eqn. 5.19). Obviously, this mechanism requires at least one, preferably more, H ligands on an uncharged aluminate, solvated by thf. Note that protons in a $H^-$ environment should readily evolve $H_2$.

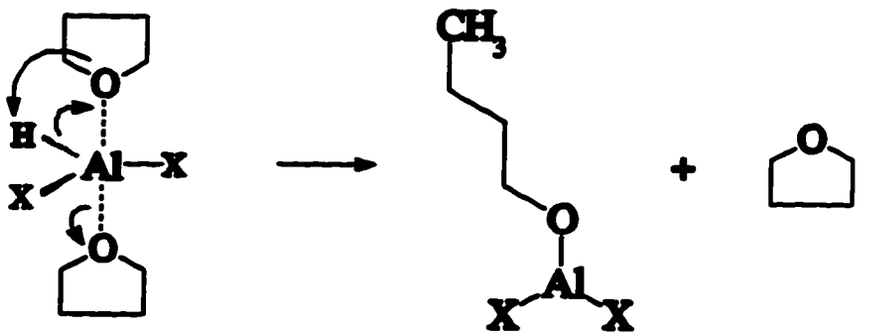


(19)

The C1 peak, which corresponds to the carbon adjacent to the oxygen atom, was considerably broader than the other $^{13}$C peaks in Fig. 5.8; this is because the C1 carbon would be the one most likely to be affected by any differences in ligand coordination at the aluminum atom which is just on the other side of the oxygen from this carbon; thus

this observed line-broadening could be due to the distribution of $Cl^-$ and $H^-$ ligands on the aluminum (i.e. the X's in Eqn. 5.19).

Solvent decomposition was slower in the $Cl^-$-rich baths, even though a greater proportion of uncharged and hence solvated aluminates are present; the time-course of the spectrum of an *operating* $Cl^-$-rich bath is shown in Fig. 5.9. Significantly, a $LiAlH_4$ control in thf showed no evidence of the decomposition-product, even over 45 days. This is consistent with the fact that the tetrahedral $AlH_4^-$ is a Lewis base rather than an acid and hence is not coordinated with the solvent oxygen atom. $AlCl_3$, shown to be solvent coordinated, would not decompose according to the above mechanism due to the absence of transferable H atoms.

## 5.10. Conclusions

In an effort to characterize the speciation, reactivity and stability of the hydride-bath for plating Al, the baths were examined by NMR. The hydride-baths were shown to contain up to nine different aluminate species (see Fig. 5.1 and Table 5.2) and the distribution of these varied with bath composition.

The time-dependence of the bath's speciation has been characterized and is attributed to the reactivity of the component species and hence their susceptibility to decomposition. Solute decomposition was observed to give an excess of $Cl^-$ ligand-containing aluminates and a deficit of identifiable uncharged aluminates expected on the basis of the relative amounts of $AlCl_3$ and $LiAlH_4$ added. The *dihydrido*-aluminates, particularly the uncharged one, were of unusually low abundance in the mixed ligand baths probably due to their reactivity and susceptibility to auto-decomposition. A solvent decomposition reaction involving the $H^-$-rich uncharged species was observed and the decomposition product was identified. $H^-$-rich aluminate species appear to be much more reactive than $Cl^-$-rich analogues which probably also has a bearing on the different electrochemical behaviours observed between the compositional extremes of the hydride-bath.

A "catalytic" role of $H^-$ was indicated from analysis of the trends found in chemical shifts, linewidths and concentration-dependence of chemically analogous aluminates. It is suggested that the $H^-$ ligand, when in the presence of at least one $Cl^-$ ligand, activ-

ates the lability of other substituent ligands and it is this factor that facilitates the electrochemical reduction of these aluminates, where significantly, neither of the homo-ligated aluminates may be electrochemically reduced to deposit elemental Al. The electrochemistry of these baths is examined in the next chapter.

# Chapter 6 Electrochemistry of Electrodeposition and Dissolution of Aluminum

## 6.1. Foreword

The ligand interchange which arises upon mixing $AlCl_3$ with $LiAlH_4$ in thf, known as the Schlesinger reaction [112] (Eqn. 5.1 in Chapter 5) and used by synthetic organic chemists for fine tuning the reducing properties of $AlH_4^-$, is an important aspect of the reactivity of the aluminates that comprise the hydride electroplating baths and indeed is essential to the electrochemical reversibility of the Al reduction/re-oxidation reaction. The material in this chapter reports the electrochemical behaviour of the hydride-bath which was found to vary seemingly continuously, if not entirely reproducibly, with component ratio between its compositional extremes. Included here will be the examination of:

1) the cyclic-voltammetry of electroplating and stripping of Al onto inert metal substrates;

2) the results of chronopotentiometric experiments;

3) the results of electroplating Al onto itself and the theory associated with practical steady-state polarization (Tafel) measurements, including:

- the definition of the lower limit of overpotential for which conclusions of mechanistic significance can be reached;

- a procedure for back-reaction correction;

and

- a means to determine the stoichiometric number from Tafel results;

4) an introduction to the theory of *a.c.* impedance and results obtained from its application to Al electrodeposition and dissolution processes;

for hydride-baths of varying composition in order to characterize and explain the Al reduction reaction in these media.

## 6.2. Experimental Notes

The recorded currents were normalized to the apparent geometric area of the working electrodes used, which were in most cases Au polished with diamond paste down to 0.25 $\mu$m. The aluminum deposits were of much larger surface area than the apparent

area of the underlying substrates, as was noted from their observed morphologies (see Chapter 8). It is not possible, however, to quantify the surface roughness in any given experiment since the electroactive surface changes in a continuous fashion during the electrochemical experiments that involved electrodeposition and dissolution, and thus all current-densities are *apparent values*.

Potentials, applied versus an Al pseudo-reference (a 99.999% Al wire in the same bath) were corrected, after measurement, for IR drop. Solution resistance was often significant, varying from 200 - 2000 $\Omega\,cm^{-1}$, but since the electrode area was in most cases very small, so were the resulting measured currents; hence the effect of the appreciable solution resistances on the electrochemical results was small or, at least, correctible.

Tafel polarization measurements were recorded by sweeping the potential sufficiently slowly, or stepping it with sufficiently long delay, to ensure the process was always in a steady-state. Checks of this condition were performed regularly by simply holding a given potential constant during an experiment and noting whether the current changed. Current-potential data were digitalized in all cases and treated with "spreadsheet" software. The Tafel plots were corrected for the back-reaction current component according to §6.6.3 taking $z = 3$ (three electrons for the aluminum deposition reaction) and *integer* values of $\nu$. Potential, as the independent variable in all Tafel experiments reported in this thesis, was plotted on the x-axis (note: this is not a universal convention).

## 6.3. Cyclic Voltammetry of $LiAlH_4$ and $AlCl_3$ Control Solutions

### 6.3.1. $LiAlH_4$ Control

In an effort to isolate and explain factors that could influence the reactivity of the hydride-bath, controls of the individual inorganic components in thf were first examined. In Fig. 6.1a are shown cyclic voltammograms for a 0.002 $cm^2$ Au working electrode in a 0.3 M $LiAlH_4$-thf solution recorded at a sweep-rate of 50 $mV\,s^{-1}$ with potential limits of -1.0 V and +0.8 V (solid curve) and -0.5 V and +0.8 V (dashed curve). The conductance of this particular solution was found to be *ca.* 1 $mS\,cm^{-1}$. Scanning in the negative direction from +0.2 V gave little reduction current until the onset of a major cathodic

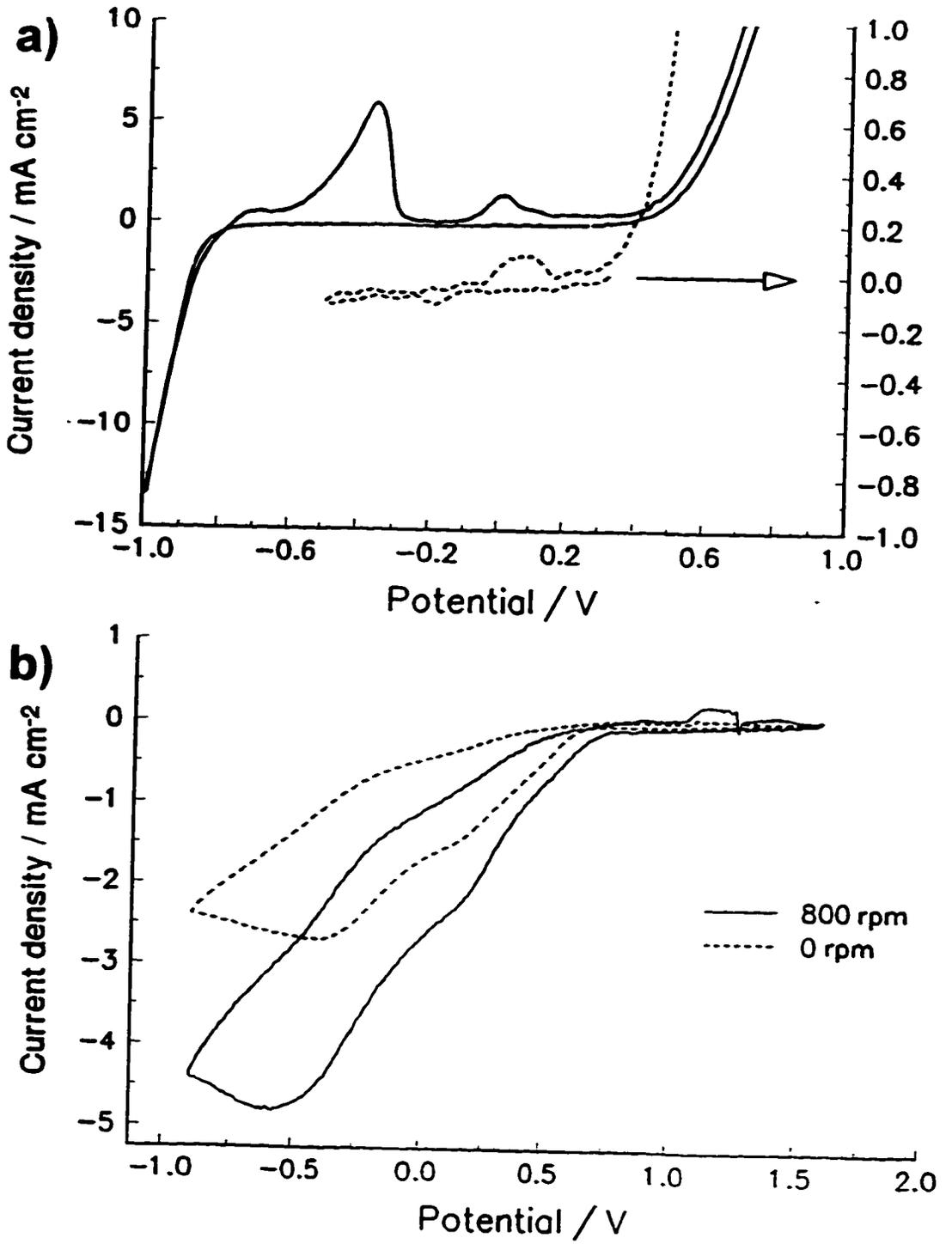


**Fig. 6.1.** Cyclic voltammograms at Au (area: 0.002 $cm^2$) of a) 0.3 M $LiAlH_4$ in thf (dashed curve is a scan with limits restricted to -0.5 V and whose scale is on the right axis); and b) 0.7 M $AlCl_3$ in thf at a sweep rate of 50 mV/s. Potentials are versus Al wire in the same solution, and Al is the auxiliary electrode.

process at -0.75 V. When the sweep direction was reversed the current became slightly larger on the return-scan, giving a reverse loop and a current cross-over at about -0.795 V. The onset overpotential referred to above, the larger return-scan current and the current cross-overs are characteristic of a limitation by nucleation and growth in the formation of a new phase [128] and the cross-over potential at or near the transition from cathodic to anodic currents is usually taken as the reversible potential for the process which is hence -0.795 ($\pm$0.005) V in this case.

Continuing the sweep in the positive direction, three oxidation peaks were observed; a small one having a current maximum at -0.75 V, a large one at -0.35 V and an intermediate, somewhat complicated one at 0.0 V. These peaks are associated with the cathodic process below -0.8 V since when not scanned beyond this negative limit (dashed curve) none of the peaks referred to above were observed and the measured current was much smaller.

The dashed curve in Fig. 6.1a is an example for which the cathodic limit was -0.5 V where only a very small feature attributable, perhaps, to the stripping of Al was recognizable. This anodic Al stripping peak, identified by the dashed curve, perhaps also makes a distinct contribution, albeit as a small shoulder on the positive side of the 0.0 V peak, in the voltammogram scanned down to the major cathodic process (solid curve). At potentials further positive to these aforementioned peaks, a rapidly rising irreversible oxidation current was observed, attributable to solvent decomposition.

The electrochemical processes observed in the $H^-$ control bath were the plating and stripping of metallic phases which showed no dependence on electrode rotation, and thence on solution diffusion within the potential limits examined. The major cathodic process, given the large potential (scaled versus the Al reference) and the significant magnitude of the observed currents, with due consideration of the species present, was likely the deposition of metallic Li and/or, more probably, alloys thereof with Al. There are no standard potential, $E^\circ_s$, data available for the reduction of $Li^+$ and $Al^{3+}$ in thf, but from aqueous solution data [1:p.D151]:

$$Li^+ + e^- \rightarrow Li \qquad -3.04\ V \qquad (1)$$

$$Al^{3+} + 3e^- \rightarrow Al \qquad -1.66\ V \qquad (2)$$

the difference between these is -1.38 V. Considering the weaker solvating strength of thf relative to water, as read from a lower donor number, $D_n$, [17], and the known positive trend of reversible potential ($E_r$) with decreasing strength of solvation[a] (decreasing solvent $D_n$) for electroactive cations [82], it is probable that the peak at about -0.795 V corresponds to the reversible potential for Li deposition in thf. The various anodic peaks observed in Fig. 6.1a are probably due to the stripping of different Li or Li alloy phases. The anodic to cathodic charge balance seemed poor for the process; thus, the anodic charge for the series of oxidation peaks (excluding solvent decomposition) was only about 55% that of the reduction charge passed, and significantly, little Al seemed to be deposited.

### 6.3.2. $AlCl_3$ Control

Fig. 6.1b shows cyclic voltammograms for a Au electrode in a 0.7 M $AlCl_3$-thf solution recorded at a scan-rate of 50 mV $s^{-1}$ for the electrode at rest (dashed curve) and rotated at 800 rpm (solid curve). $AlCl_3$ has been shown to auto-ionize in thf to an extent of about 30% (see §5.4.1) giving $[AlCl_2]^+ \cdot 4thf$ and $AlCl_4^-$; thus such solutions are somewhat conductive and the bath examined (results in Fig. 6.1b) had a conductivity of *ca.* 0.2 mS $cm^{-1}$. Scanned in the negative direction from +1.6 V, a cathodic current started at about +0.75 V (dashed curve; 0 rpm). Two features were observed, a shoulder at about +0.2 V and a peak giving a diffusion decay tail at -0.3 V. On the return-scan the cathodic current (negative) remained appreciable and a shoulder was clearly visible at about +0.25 V but anodic currents were always small. With rotation (solid curve; Fig. 6.1b) the cathodic current increased, the aforementioned peak maxima were shifted negatively and exhibited a small reoxidation current (at about +1.2 V). This is clearly an irreversible diffusion-controlled process, unlike the kinetically-controlled phase deposition noted in the $LiAlH_4$ control experiment.

No Al could be deposited from this bath even though significant cathodic charge

---

[a] This can be made a little clearer by saying: an increasing ease (positive potential shift) for reduction of a cation is observed when it is less well solvated.

was passed. Electrodes cycled within the cathodic current regime for an extended time did not show any evidence of deposited Al, although a grey precipitate was observed in solutions after extended cycling. The positive potential limit in this bath was about +1.7 V defined by a solvent oxidation reaction which was found to be slightly reversible (i.e. a small amount of associated reduction current was observed, but has not been shown in Fig. 6.1b).

### 6.3.3. Comments on the Results of Cyclic Voltammetry Experiments on the Controls

Very little Al was depositable from either of the control baths. A process that appeared to be the deposition of Li was dominant in the $LiAlH_4$ control bath, as well as a very small amount of Al co-deposition, on the order of 1/100th that of Li. Stripping of the deposited material occurred at low potential (relative to the Al reference) in the $LiAlH_4$-rich bath, and the Al stripping reaction, although providing only a small current contribution, was identified at *ca.* 0.0 V. In the $AlCl_3$ bath no deposited material was observed, even though a significant cathodic process was evident.

The nature of the background oxidation reaction which defined the positive potential limit differed between the controls. In the $H^-$ control the background process was completely irreversible and started at lower potentials, while in the $Cl^-$ control the background oxidation reaction would commence at higher potentials and gave a little re-reduction current. A more significant background reaction in the $H^-$-rich bath indicated the role of $H^-$ (perhaps by means of its coordination to $\alpha$-carbons) in promoting electrochemical oxidation of the solvent which probably parallels the *chemical* reaction involving the thf solvent examined by $^{13}C$-NMR in §5.9.2. Conductivity of the controls was low, from 0.2 to 1 $mS\,cm^{-1}$ due to the small extent of dissociation of $AlCl_3$ and the low concentrations of $LiAlH_4$ obtainable in thf, respectively.

## 6.4. Cyclic Voltammetry in the Hydride-Bath

### 6.4.1. $H^-$-Rich Solutions

When the two control components, $AlCl_3$ and $LiAlH_4$, are mixed in thf the electro-

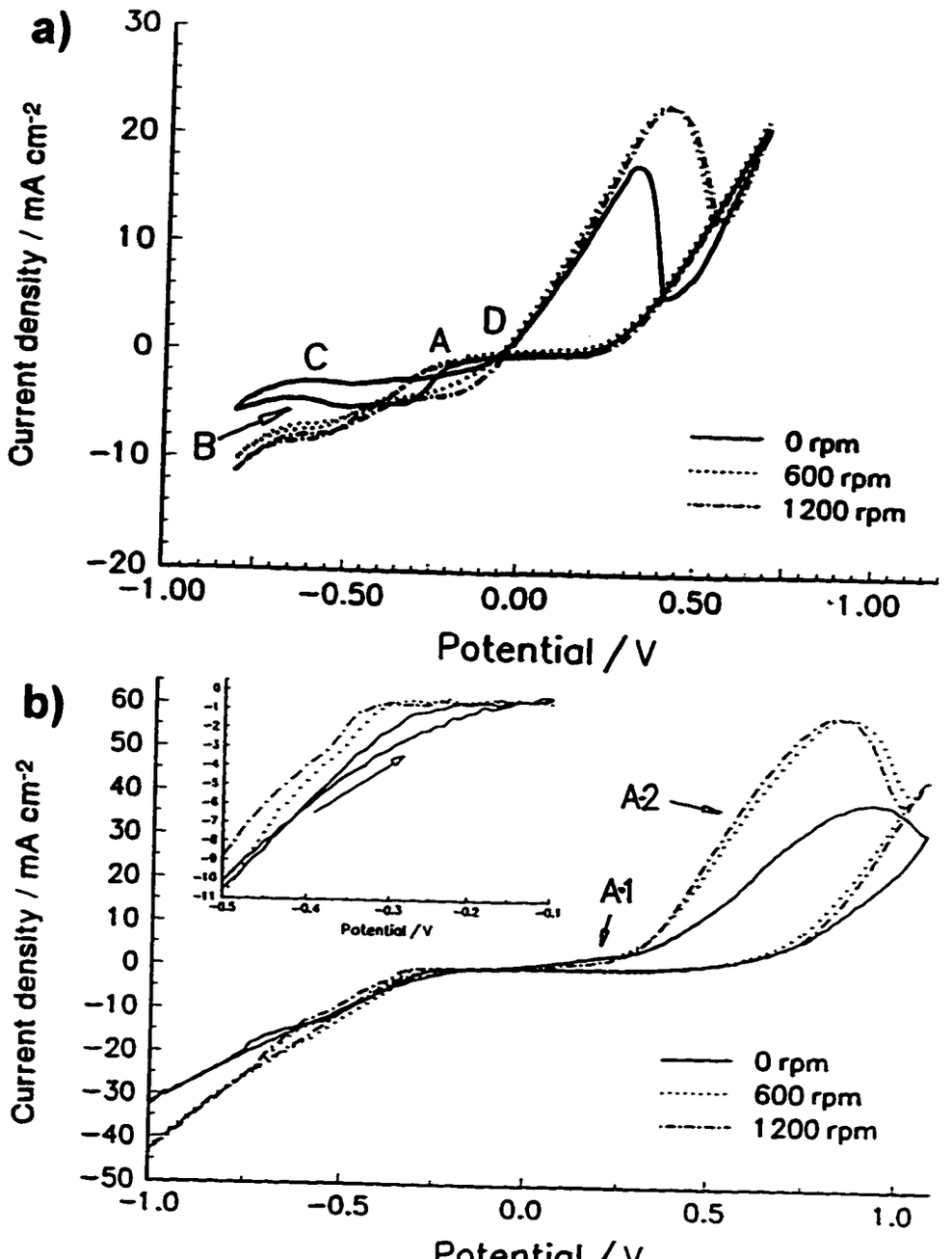


**Fig. 6.2.** Cyclic voltammograms at Au (area: 0.002 $cm^2$) **a)** of an r = 1:4, $[Al]_{total}$ = 0.4 M hydride-bath at rotation rates of 0, 1200 and 2400 rpm (solid, dotted and dot-dashed curves, respectively); and **b)** in an r = 4:1, $[Al]_{total}$ = 0.9 M hydride-bath at rotation rates of 0, 600 and 1200 rpm (solid, dotted and dot-dashed curves, respectively) scanned at 50 mV/s. Inset of **b)** is an expansion of the same data demonstrating the variation of onset overpotential with rotation; where for simplicity the anodic directions of the voltammograms with rotation have been omitted and the arrow indicates the anodic-going branch of the 0 rpm voltammogram.

chemical behaviour is strikingly different from that of either of the controls. Fig. 6.2a shows the cyclic-voltammetric response of a Au electrode in an r = 1:4 value (i.e. $AlCl_3$:$LiAlH_4$), $[Al]_{total}$ = 0.4 M hydride-bath scanned at 50 mV $s^{-1}$ with rotation rates of 0, 1200 and 2400 rpm (solid, dotted and dot-dashed curves, respectively). If we follow a negative-going scan for a quiescent solution on a clean (deposit free) electrode starting at 0.0 V, a potential of about -0.15 V is required before the cathodic process starts (see "*D-A*" in Fig. 6.2a). After this "onset" the current grows, but soon reaches a plateau. Beyond about -0.7 V the cathodic current increases again (see "*B*"), a behaviour most likely associated with the deposition of Li or an Al-Li alloy, by analogy with the $LiAlH_4$ control results.

When the potential was reversed within the region where the Li reaction can take place (as in Fig. 6.2a), the cathodic current during this positive-going scan decreased giving what is clearly a small anodic current peak ("*C*") superimposed upon, and subtracting from the continuing (initial) current for the cathodic process. Following this, the return-scan current crossed over the current-profile recorded during the initial negative-going scan twice and at "*D*" in Fig. 6.2a eventually gave a positive (anodic) current due to the onset of stripping of the deposited Al phase. The overpotential for current onset and the cross-overs indicated control by nucleation and growth of a new phase onto an inert substrate, here Au.

As the electrode was swept to higher positive potentials the current continued to rise as the previously deposited Al phase continued to be oxidatively stripped at an increasingly rapid rate until the current finally fell as the phase became completely stripped giving way to the anodic background reaction. The charge associated with anodic stripping was always better than 90% of that of the deposition process (corrected for background reaction).

Rotation of the working electrode had the effect of delaying the onset of the cathodic current (compare the solid and dashed curves at "*A*" in Fig. 6.2a) by up to a maximum of about 0.1 V. Notwithstanding the "*late*" start, however, the plateau current with rotation would ultimately be larger, reaching a limit at about 2400 rpm in this bath.

Beyond -0.7 V the second cathodic process, proposed as the deposition of Li, was noted as in the quiescent case. Rotation had little effect on the aspect of the stripping reaction positive of 0.0 V, where the continued stripping to higher positive potentials with rotation is simply a consequence of the enhancing effect of rotation on the extent of prior cathodic deposition.

The higher onset overpotentials observed when the working electrodes were rotated is explained by considering the mechanism of nucleation which usually controls the initial formation of a new phase onto a foreign substrate. Nucleation requires the establishment of a supersaturation of depositing atoms before a nucleus can be spontaneously born. The role of the applied potential is to control the concentration of adatoms contributing to the local supersaturations. Forced convection, as arises from electrode rotation, has the effect of disrupting the local regions of supersaturation upon which nucleation depends, thus requiring larger potentials to compensate for this. Once established, the growing grains no longer require supersaturation conditions since further incorporation onto their own lattices is much easier (for most materials) and hence diffusion becomes limiting, which is why the phase ultimately grows at a higher rate when the system is rotated.

Even at the rotation limit (*ca.* 2000 rpm), a plateau in the cathodic reaction rate in the $H^-$-rich bath was always observed (beyond which Li plating would start). This limit to the effect of rotation indicates either imperfect rotation (off-centre, wobbly rotation) or more probably a transition to some other controlling process (an alternate reaction).

### 6.4.2. Cyclic Voltammetry in the $Cl^-$-Rich Bath

#### 6.4.2.1. Cathodic Behaviour

Fig. 6.2b shows a series of voltammograms for Au in an r = 4:1, $[Al]_{total} = 0.9$ M hydride-bath at rotation rates of 0, 600 and 1200 rpm (solid, dotted and dot-dashed curves, respectively) scanned at 50 mV $s^{-1}$. The potential for current onset was typically somewhat larger in the $Cl^-$-rich than in the $H^-$-rich baths, being about -0.25 V or so in this example in the absence of rotation (recall *ca.* -0.15 V for the $H^-$-rich bath). The presence of the second cathodic process (Li deposition), noted in the $H^-$-rich baths, was

not clearly observed in the $Cl^-$-rich baths. For all voltammograms the current was larger on the return-scan (if only slightly so in Fig. 6.2) giving familiar current cross-overs. The effect of rotation was the same as in the $H^-$-rich baths, delaying current onset (demonstrated more clearly in the inset of Fig. 6.2b) and leading to ultimately larger currents which reached a limit, in the potential window studied, at about 1200 rpm. Again, as in the $H^-$ baths, nucleation and growth limited the initial stage of phase development.

The scan-rate dependence of the voltammetric response of an $r = 3.2{:}1$, $[Al]_{total} = 1.1$ M bath for scan-rates between 5 - 2000 mV $s^{-1}$ is shown in Fig. 6.3a and the inset is an expansion of the cathodic onset region. At the slowest scan-rates, the onset of deposition was at about -0.18 V or so and was essentially the same for all sweep-rates (we notice in the inset of Fig. 6.3a that this is the potential where all curves depart from zero current). In the cathodic regime this experiment illustrates the time-dependence of the nucleation process that initially limits deposition. A current maximum on the return-scan is a clear indication of incomplete nucleation. The cathodic charge passed up to the maximum (for the voltammograms in which one was observed, as in Fig. 6.3a) varied with scan-rate and corresponded to the equivalent of a few hypothetical monolayers of deposited Al (1000 $\mu C\,cm^{-2}$; that for a complete (111) monolayer is *ca.* 870 $\mu C\,cm^{-2}$). The nature of this limitation is not entirely clear, but will be examined further in Chapter 8.

#### 6.4.2.2. Anodic Features of Voltammograms in $Cl^-$-Rich Baths

The anodic branch of the voltammogram of a typical $Cl^-$-rich baths gave two distinct stripping processes above 0.0 V, one of which occurred below about +0.4 V, referred to here as A-1, which gave an arrest, or under more extreme experimental conditions (such as for scan-rates greater than 500 mV $s^{-1}$ in Fig. 6.3a), a small decline to give a distinct peak. At more positive potentials a second stripping process, A-2, was observed which gave a current peak and decline down to the background as the deposit became fully stripped. The prominence of the A-1 process depended qualitatively upon the composition of the bath, while higher $Cl^-$-contents gave smaller magnitudes for this process.

Comparing the aluminum stripping reaction in the cyclic voltammograms of the

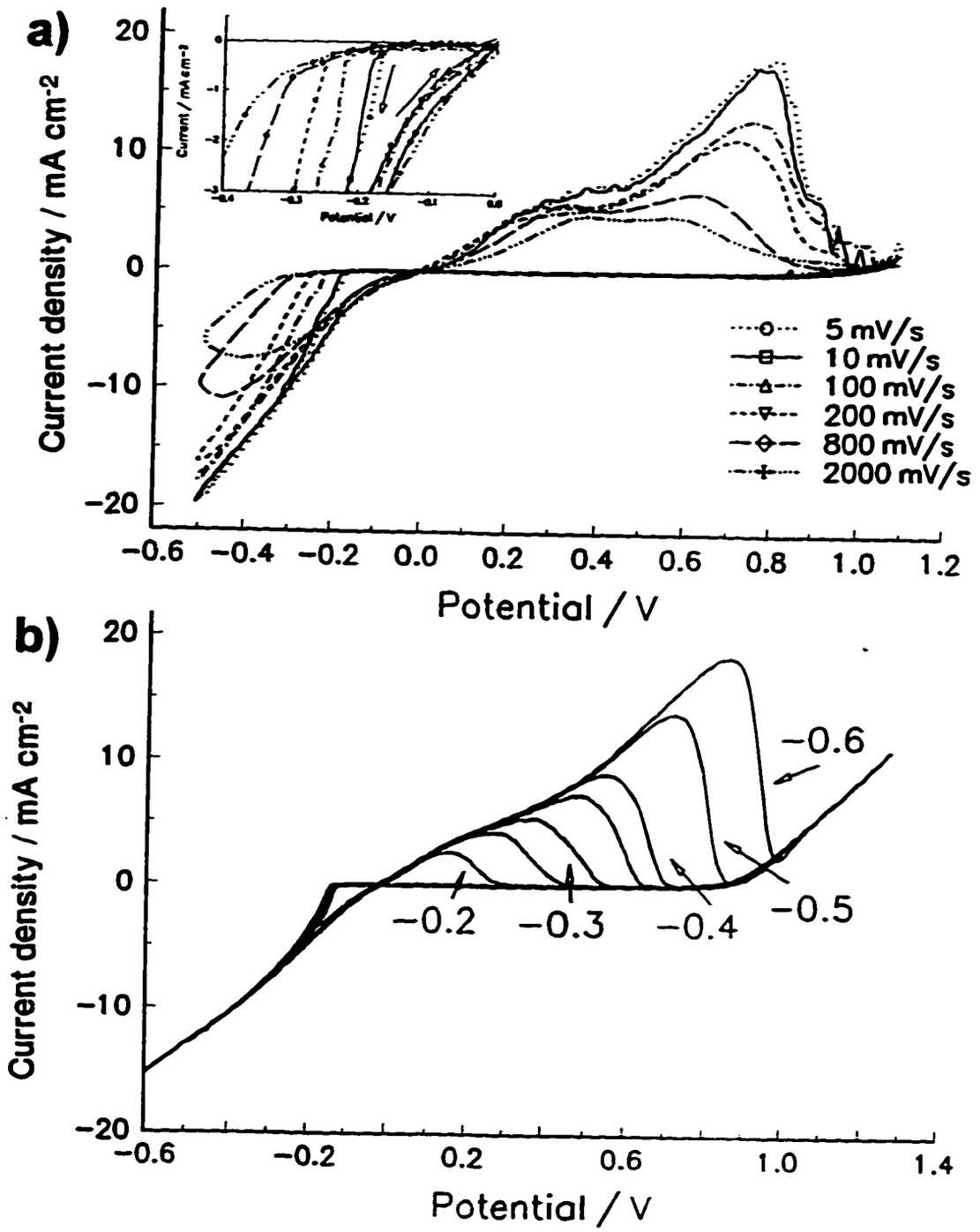


**Fig. 6.3.** a) Scan-rate dependence of cyclic voltammograms at Au (area: 0.005 $cm^2$) of an r = 3.7:1, $[Al]_{total}$ = 1.1 M hydride-bath at scan-rates as indicated in the figure. b) Cyclic voltammograms at Au in an r = 2.7:1, $[Al]_{total}$ = 0.9 M hydride-bath scanned between +1.4 V and varying cathodic limits of -0.2, -0.25, -0.3, -0.35, -0.4, -0.5 and -0.6 V at a scan-rate of 10 mV/s.

various $Cl^-$-rich baths under discussion here, having compositions r = 4:1 (Fig. 6.2b), r = 3.2:1 (Fig. 6.3a) and r = 2.7:1 (Fig. 6.3b), the size of the A-1 feature decreases with increasing r. Electrode rotation had little effect on the participation of the A-1 process (although not clearly demonstrated in Fig. 6.2b due to superposition of the A-2 process), but gave a dramatic increase in the rate of the A-2 process in the direction of oxidation (Fig. 6.2b).

The scan-rate dependence of the anodic stripping peaks in the r = 3.2:1 bath shown in Fig. 6.3a is interesting. The current for the A-1 process at various scan-rates remained largely the same, overlapping up to about +0.4 V, decreasing only at scan-rates above about 500 mV $s^{-1}$. Conversely, that for the A-2 peak diminished considerably with scan-rate. The anodic stripping charge was in all cases greater than 95% of that for deposition.

The significance of the two anodic features is not entirely clear. It is unlikely that the two separate anodic processes (A-1, A-2) correspond to stripping of energetically different phases which, if this were the case, should have given nearly the same charge proportion of these two supposed phases at all scan-rates. This, in fact, was not the case and, additionally, the scan in the negative direction showed no peaks or inflection points that could support this possibility either. When diffusion controls an electrochemical reaction the expected cyclic-voltammetric behaviour is that, with increasing sweep-rate, a trend for increase in peak current arises along with a shift of peak positions on the potential scale away from $E_{1/2}$. This kind of behaviour was not observed for the A-1 process and thus diffusion was not limiting its rate. Considering that the *charge* corresponding to A-1 decreased with increasing scan-rate (since the *current* was nearly constant for all scan-rates in Fig. 6.3a, and charge = current x time), the process is evidently not related to a surface adsorbed species (which would show constant charge).

Fig. 6.3b shows the result of depositing Al up to varying negative potential limits (indicated in the figure) on the subsequent anodic stripping curve for an experiment at a Au disc electrode in an r = 2.7:1, $[Al]_{total}$ = 0.9 M hydride-bath, scanned at 10 mV $s^{-1}$. The purpose of this experiment was to examine whether the negative potential limit for a given scan had any effect on the following stripping processes. The anodic curves,

corresponding to successively larger amounts of previously deposited Al, in fact all coalesced to a *single* stripping curve but each individual curve would depart from the main one (see Fig. 6.3b) as its respective deposit became completely stripped. Stripping charge (corrected for the background) was found again to be at least 95% that of the charge for deposition in all cases.

The oxidation reactions in $Cl^-$-rich hydride-baths are clearly composed of a mixture of anodic processes involving a single-phase deposited metal, one limited by diffusion, the other not. The one at lower potential, given its decreasing prominence with increasing $Cl^-$-content (cf. Figs. 6.3b, 6.3a and 6.2b), must be associated with either higher $H^-$-content or anionic species (characteristic of species in higher $H^-$-content baths).

### 6.4.3. Cyclic Voltammetry in Aged $H^-$-Rich Baths

Due to the moisture sensitivity of the reactants and the virtual impossibility of excluding traces of water in practical experimentation, the composition of all the hydride-baths was found to be time-dependent (as examined in §5.8). Showing particularly interesting behaviour in this regard were some aged $H^-$-rich baths. These would exhibit, in some cases, cyclic-voltammetric behaviour such as that in Fig. 6.4 for an r = 1:2.2, $[Al]_{total}$ = 0.5 M bath scanned at 50 mV $s^{-1}$, upon which experiments were conducted periodically over the course of five days. The behaviour here is reminiscent of that of the $LiAlH_4$-thf control solution, specifically in that Li re-oxidation at between -0.5 and -0.4 V was much more prominent in the aged bath than typical for fresh $H^-$-rich baths of the same composition, such as in Fig. 6.2b. Unlike the results for the control, however, much more Al could be deposited and hence stripped from the *mixed* aluminate baths. A smaller onset overpotential (about -0.10 V) was noted in these plots compared to that for the two previously examined types of baths.

The effect of electrode rotation on the cyclic voltammetry, observed in Fig. 6.4a, was to delay, in the usual way, the onset of deposition and, at more negative (cathodic) potentials, to increase the overall Al deposition and stripping current. The prominence of the Li stripping peak (at about -0.45 V) decreased with electrode rotation. It is anticipated that when the supply of aluminate species (reactants for the thermodynamically

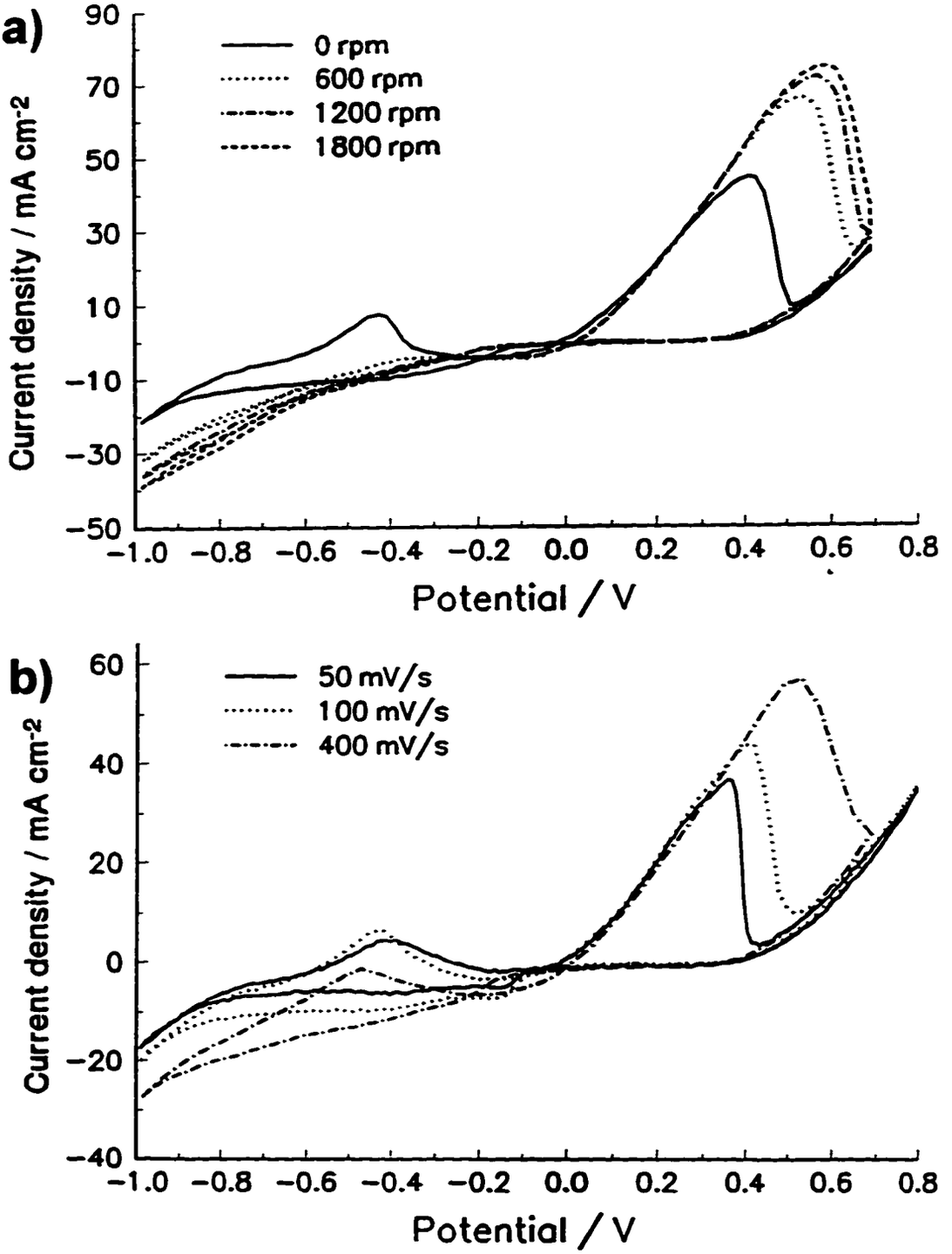


**Fig. 6.4.** Cyclic voltammograms at Au showing **a)** the rotation-dependence (rotation rates listed in the legend) at a scan-rate of 50 mV/s; and **b)** the scan-rate dependence (scan-rates listed in the legend) for an unrotated electrode in an "aged" (see text) r = 1:2.2, $[Al]_{total}$ = 0.5 M hydride-bath.

preferred reaction) is slow (i.e. in the absence of rotation), the Li reaction will be more significant; this is consistent with the fact that, with rotation, Li reduction and re-oxidation was suppressed.

Interestingly, the scan-rate dependence of the initial electrodeposition of Al on Au, shown in Fig. 6.4b, was markedly different from that observed for other hydride-baths. While the scan-rate dependence of currents for the $Cl^-$-rich bath, shown previously in Fig. 6.3a, gave behaviour typical of nucleation-control, viz. delayed onset of deposition, reduced currents (and ultimately reverse current loops) with increasing scan-rate, that for the aged $H^-$-rich bath gave, in contrast, diffusion-controlled behaviour, i.e. the currents increased with increasing scan-rate. Nucleation and growth must be facile in this $H^-$-rich bath, with the result that diffusion of species through solution is rate-limiting. Considering that the maximum currents in these baths were of a similar magnitude to those in other mixed aluminate baths, even though the concentrations of electroactive species in $H^-$-rich baths are low to begin with (due to limited $LiAlH_4$ solubility in thf), this suggests that the *kinetics* of the Al electrodeposition reaction are improved and not that, say, bulkier species in the $H^-$-rich baths has slowed the rate of diffusion, which is counter-intuitive anyway, since aluminates with a greater proportion of $H^-$ ligands would be smaller and probably have better mobility.

### 6.4.4. Anodic Background Reaction in the Hydride-Bath

Any background reaction can seriously limit practical application of any electrochemical system. The extent and nature of the anodic background reaction in the hydride-baths varied generally with $r$ (the $Cl^-$ to $H^-$ ratio). It was significant in the $LiAlH_4$ control (Fig. 6.1a) and more so in $H^-$-rich than in $Cl^-$-rich baths. The background reaction was diffusion-controlled and slightly reversible in the $Cl^-$-rich baths and in the $AlCl_3$ control (Fig. 6.1b). Comparing the hydride-bath cyclic voltammograms of Fig. 6.2a and 6.2b directly at say +0.7 V shows that the current for the background reaction in the $H^-$-rich bath was *ca.* five times larger than in the $Cl^-$-rich bath, even though the total $H^-$-content of the two baths was roughly the *same*.

The background reaction(s) in the hydride-baths showed a substrate dependence.

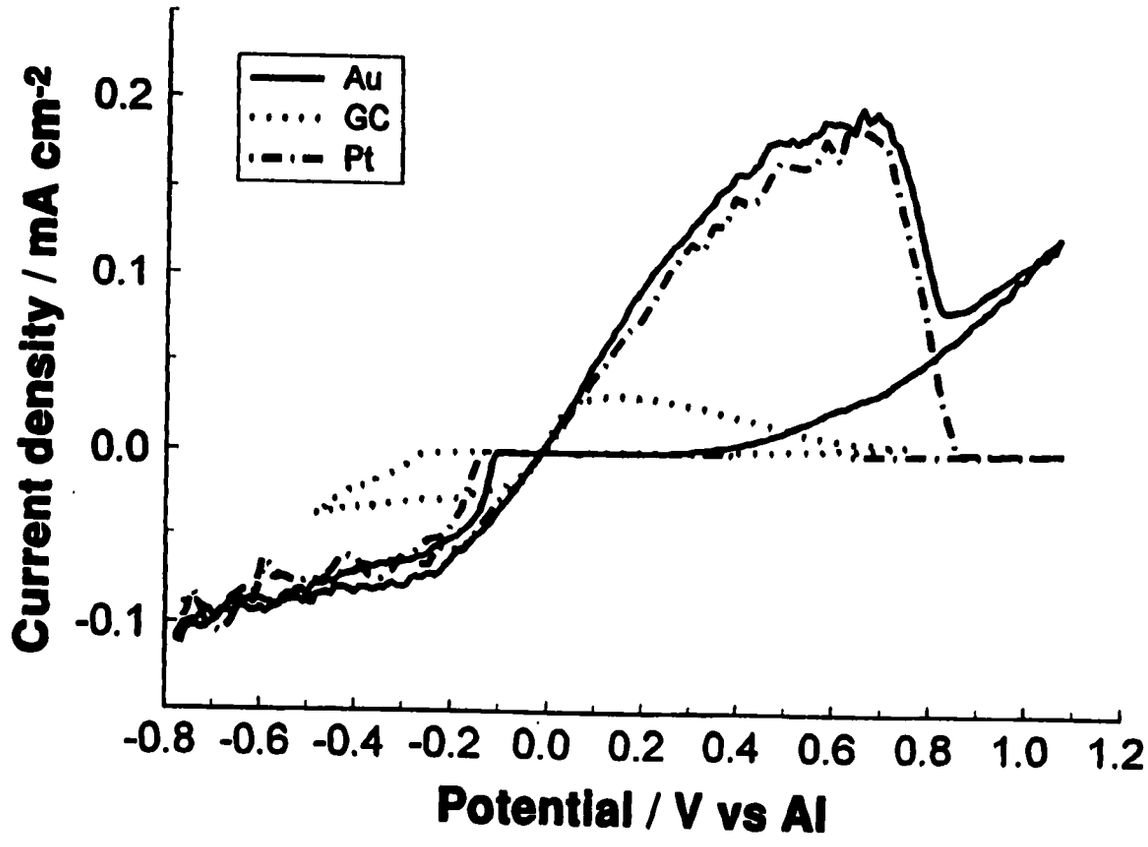


**Fig. 6.5.** Cyclic voltammograms recorded in a r = 1:1.3, $[Al]_{total}$ = 0.8 M hydride-bath showing the plating and stripping on Au, GC and Pt inert working electrodes rotated at 600 rpm.

Fig. 6.5 includes separate cyclic voltammograms recorded in an r = 1:1.3, $[Al]_{total}$ = 0.8 M hydride-bath showing the plating and stripping on Au, glassy carbon and Pt inert working electrodes all rotated at 600 rpm. The background reaction was found to be significant only at Au. The exact nature of the products of this reaction are unknown, but some pitting of Au substrates subjected to extended experimentation was observed in SEM micrographs. Gold is known not to be stable to $Cl^-$ environments in aqueous media, being readily oxidized by complexing anions [103:p.68]. The prominence of the background reaction in $H^-$-rich baths points to the possible role of higher $H^-$-content species giving some irreversibly formed reaction product.

## 6.5. Discussion of Results of the Cyclic Voltammetry Experiments

### 6.5.1. Solution Aluminates

$Cl^-$-rich baths have been cited as media for depositing high-purity aluminum plate [52], while in $H^-$-rich baths significant co-deposition of Li is evident. In the present work aluminum was found to be electrodeposited and electrodissolved from virtually all bath compositions that contained both $H^-$ and $Cl^-$. There were, however, a few interesting differences between the anodic and cathodic processes in these baths.

The electrochemical reactions in the hydride-bath involve various Al complexes (see §5.4) as reactants and thus for the reduction reaction three ligands are released when aluminum is deposited (from an uncharged aluminate) as:

$$AlX_3 + 3e^- \rightleftarrows Al + 3X^- \quad (3)$$

while for the oxidation of metallic aluminum three ligands must be captured. This is not a trivial point since the solvent, thf, although a good donor ($D_n = 20.0$), is a relatively poor acceptor ($A_n = 8.0$) [118]; thus the released ligands, $X^-$'s, are less stable when solvated by thf and this necessitates the presence of other, ancillary aluminates in the region of the interface to accommodate the ligands released in the overall Al electrodeposition reaction. Uncharged acidic aluminates, e.g. $AlX_3$, can fulfill this requirement, e.g.:

$$3X^- + 3AlX_3 \rightleftarrows 3AlX_4^- \quad (4)$$

or aluminate anions can supply ligands for the Al dissolution reaction (e.g. in the reverse of Eqn. 6.4).

It was demonstrated in Chapter 5 that the ligands of $AlCl_3$ and $LiAlH_4$ mix when these species are combined in thf to form the hydride-bath giving essentially a smooth variation of the distribution of mixed ligand aluminates and *uncharged* or *anionic* species with varying composition. The ligand mixing of r moles of $AlCl_3$ and one mole of $AlH_4^-$ in thf is as follows:

$$r{\cdot}AlCl_3 + AlH_4^- + 2r{\cdot}thf \rightleftarrows r[AlH_{3-x}Cl_x{\cdot}2thf]^0 + [AlH_{(4-(3r-x))}Cl_{(3r-x)}]^- \qquad (5)$$

which describes the basis on which the distribution of aluminates in a given bath is determined. It defines more precisely, however, the proportion of uncharged to ionic species and hence ligand acceptors to donors, which will be given exactly by *r*, ignoring any auto-ionization of uncharged species. $Cl^-$-rich baths have a majority of uncharged, *ligand acceptor* species and lower equivalent conductivities while $H^-$-rich baths have a majority of anionic, *ligand donor* species and higher equivalent conductivities, although these baths are usually of lower total concentration due to the limited solubility of $LiAlH_4$.

The electrochemical behaviour expected on the basis of the relative concentrations of ligand donor and acceptor aluminates was born out, in a qualitative way, in the cyclic voltammetry behaviour of the baths. In the cathodic regime the $H^-$-rich baths demonstrated a significant electrode-rotation dependence of the measured current, while there was almost none at all in the anodic regime (see Fig. 6.2a). This is consistent with the proportions of aluminate types and their respective ancillary roles in the $H^-$-rich baths. Anion ligand donors are abundant in $H^-$-rich baths and these are necessary for the electro-*dissolution* reaction; hence no diffusion control is expected; uncharged acidic ligand acceptors are, in contrast, in short supply and are necessary for the electro*deposition* reaction which results in a significant diffusion-dependence of the kinetics of this reaction. In $Cl^-$-rich baths the reverse behaviour was observed, i.e. a much more significant rotation-rate dependence for the anodic than for the cathodic direction of reaction, this again being consistent with the distribution of ligand donor and acceptor species in solution.

### 6.5.2. Cyclic Voltammetry: Summary of Experimental Behaviour

The variety of cyclic-voltammetric behaviour exhibited in these baths for Al deposition and dissolution is a result of the distribution of the aluminates whether due directly to their reactivity or their roles as ligand acceptors or donors (as discussed above). Given that neither of the controls (in Fig. 6.1) gave deposited Al, their identified component species, $AlH_4^-$, $AlCl_3 \cdot 2thf$, $AlCl_4^-$ and $AlCl_2^+ \cdot 4thf$ obviously do not participate directly in the electrochemical reduction reaction. The reactivity of the mixed ligand aluminates has been characterized in the present work by $^{27}$Al-NMR as described in Chapter 5, and there appears to be a relation between the varying reactivities of these and their electrochemical behaviour, although improved electrochemical kinetic facility also seems to be accompanied by greater bath instability.

In $H^-$-rich baths the Al stripping reaction was found to be facile and independent of solution diffusion. With increasing $Cl^-$-content the prominence of this "$H^-$" stripping feature decreased continuously to the advantage of another, higher potential, more diffusion-dependent, stripping process. Conversely, the electrodeposition of Al was more facile in the $Cl^-$-rich baths, although not independent of solution diffusion as was the stripping reaction in the $H^-$-rich baths. However, it was less diffusion-dependent than its own (reverse) anodic branch.

On clean inert substrates, baths of all compositions required significant potentials for onset of deposition currents, but this behaviour (implying nucleation) tended to diminish with increasing $H^-$-content. The role of the higher $H^-$-content complexes, involved in the initially limiting nucleation process, is unclear.

## 6.6. Chronopotentiometry

The results of chronopotentiometry experiments on two representative hydride-baths are shown in Fig. 6.6. These experiments can give information on the stability of the deposited aluminum phase. The experimental protocol was to deposit Al onto an Au substrate electrode at a constant applied cathodic *current* (10 or 20 mA cm$^{-2}$ in Fig. 6.6) for a controlled amount of time while monitoring the potential. After the prescribed time, the deposit would be stripped at a constant *anodic* current of the same magnitude

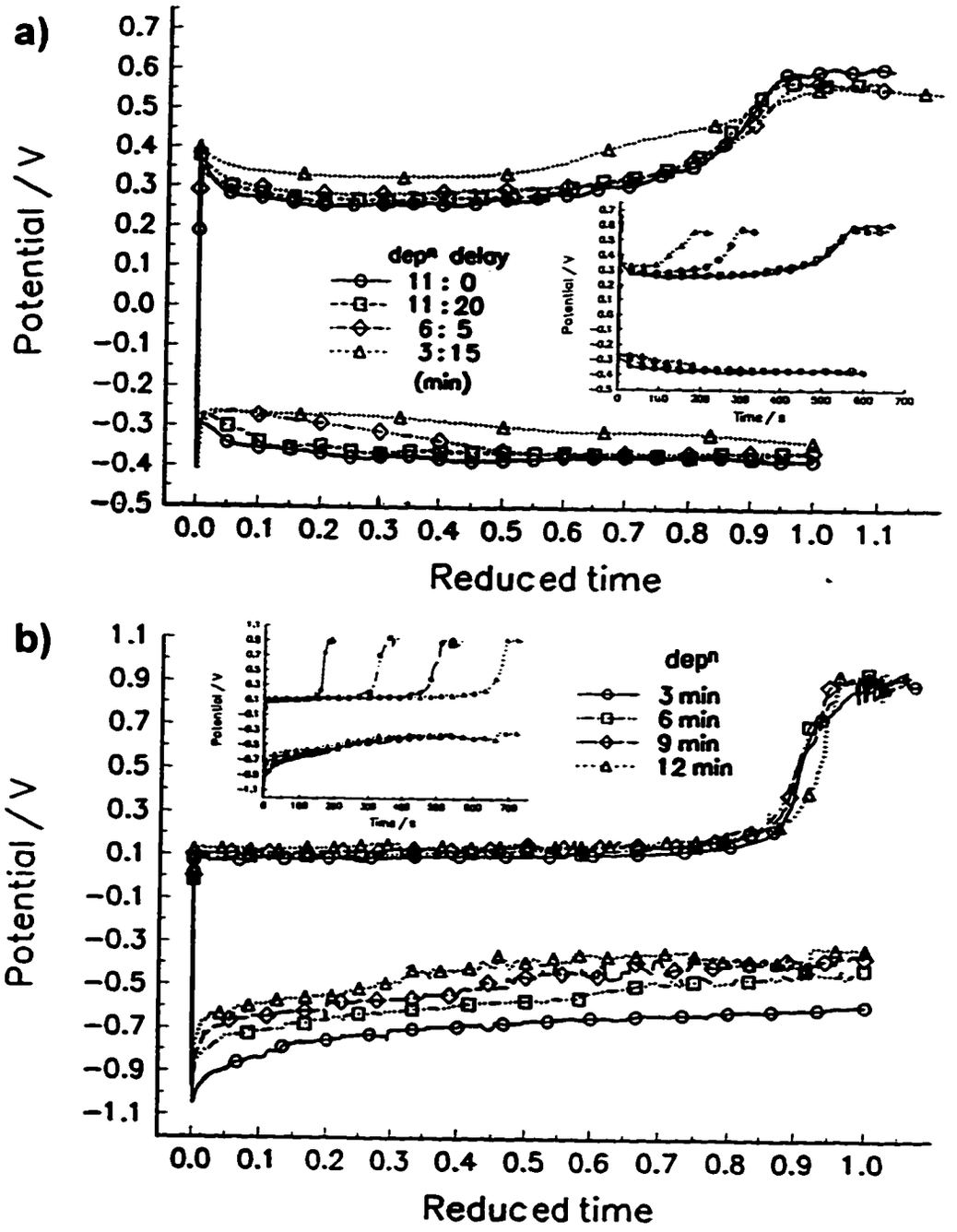


**Fig. 6.6.** Chronopotentiograms in reduced time (see text) from the hydride-bath for **a)** a 0.002 $cm^2$ Au electrode held at 10 mA $cm^{-2}$ for the deposition and delay times indicated in the legend in an r = 2.8:1, $[Al]_{total}$ = 0.9 M bath; and **b)** held at 20 mA $cm^{-2}$ for the deposition times indicated in the legend in an r = 1:2.5, $[Al]_{total}$ = 0.5 M bath at an electrode rotation rate of 500 rpm. The insets in both **a** and **b** are the same data, but in actual time. The negative potential transients are those for the deposition of Al, while the positive ones are for stripping.

until the complete removal of the deposit was signalled by an expected significant potential change. This potential change occurs as the thermodynamically more facile Al electrodissolution reaction ends and another, less facile reaction (background solvent decomposition or Au oxidation) starts to carry the applied current, which then requires a larger potential to maintain it. In some cases, as for the $Cl^-$-rich bath of Fig. 6.6a, delays at open-circuit were effected between the plating and stripping transients. The cathodic (plating) branches in Fig. 6.6 are at negative potentials and the stripping curves for different deposition times were more easily compared by a normalized or reduced-time representation. The original data are reproduced in the insets of these figures.

The cathodic potentiograms initially showed a potential spike corresponding to the potential required to charge up the double-layer and create the concentration of adatoms necessary to initiate nucleation. It would then fall as the deposition reaction shifted away from a limitation by nucleation and the initial stages of growth of nuclei. For the $Cl^-$-rich bath (Fig. 6.6a), the potential slowly became more negative, reaching a plateau after about 200 s (see inset). This increasing cathodic potential behaviour was not always observed in all $Cl^-$-rich baths. The charge passed up to the start of the plateau corresponded to the equivalent of about 500 ppm of the total aluminum solution content or about 10,000 equivalent monolayers of deposited aluminum. It is unclear what gave this behaviour, but it could be associated with limitations specific to the particular bath and its species distribution, or peculiarities of the particular reference or counter electrode reaction in the experiment. For the $H^-$-rich bath, Fig. 6.6b, after an initial potential maximum, the potential would decay to a plateau. These experiments did not include open-circuit delays but depositions were carried out for varying times.

The significant conclusion from these experiments, however, is with regard to the current efficiency of the deposition and dissolution reaction in these baths which gives an indication of the stability of the deposited phase. Thus if there was some chemical reaction going on which involved the deposited metal, the anodic-to-cathodic charge-ratios from the potentiograms for different deposition times (or for varying delay times at open-circuit) would decrease with longer delay and deposition times. The anodic to cathodic current efficiency was found, however, not to vary for any of the galvano-

static/open-circuit programmes applied for either the $Cl^-$- or $H^-$-rich baths. Thus the deposited phase was stable in the hydride-bath solutions, there being no decomposition of the deposited phase in the time-scale examined here (up to 30 minutes) which is that over which most of the electrochemical experiments had been performed.

Additionally, this experiment gives an indication of the time-dependence of steady-state polarizations. This is pertinent to the validity of the results of such polarization experiments for calculation of Tafel parameters.

## 6.7. Tafel Polarization Experiments: Theoretical Considerations

### 6.7.1. Foreword

The cyclic-voltammetric response of the hydride-bath indicated that a number of processes controlled the observed current depending on conditions: on clean inert substrates nucleation and growth was initially limiting while, for plating onto aluminum as substrate, diffusion or reaction kinetics could be limiting depending on bath composition and overpotential. In order to characterize the kinetics and mechanism of a given electrochemical reaction it is usual to examine the (logarithmic) steady-state current as a function of potential (Tafel relation) with appropriate analysis of derived transfer coefficients (Chapter 2). "Steady-state" means that the observed current is not measuring the rate of some decaying process, due e.g. to capacitance, diffusion or nucleation, etc. and, for mechanistic and kinetic relevance, the current must also be limited by the rate of the electrochemical process itself and not some other process, e.g. surface processes or steps in solution diffusion or electrocrystallization.

Generally speaking, kinetic-control (rather than diffusion) will prevail, if at all, at lower overpotentials. Various complicating factors can arise when trying to derive reaction mechanisms from Tafel relations, e.g. interference from the reverse reaction at low overpotential and from diffusion or the onset of other parallel reaction mechanisms at high overpotential. When reaction kinetics only clearly control the measured current at low overpotential, as was indicated for the Al reaction in the hydride-bath, it becomes desirable to consider also the behaviour at lower overpotentials, which can be accessed by correcting for the reverse reaction. As will be described the mechanism of the electrode

reaction defines the lower limit of the kinetically-controlled (Tafel) region and also affects the back-reaction correction. This limit and the role of the back-reaction will be treated in this section with due consideration of the complicated electrochemical mechanism possibilities that were discussed in Chapter 2. The following derivations are important for the subsequent discussion (§6.7) of whether a *single* transition-state limits both anodic and cathodic directions of the Al reaction. A single one is a basic assumption of *all* kinetic relations, but a mechanism for the Al reaction in the hydride-bath involving two separate ones has been proposed, §3.4.3 [38]. The consequences of discrete transition-states can be quite significant for the way results are analyzed and discussed.

### 6.7.2. Tafel Region of Experimental Polarization Curves

Considering the general Butler-Volmer (BV) equation, Eqn. 2.20, that describes the relationship between overpotential and the resulting anodic and cathodic currents, it is only at sufficiently large overpotentials (either positive or negative) that the net potential-dependence of the overall current will be described by *only one* of the exponential terms in the BV equation. The lower limit of that kinetic, or so-called *Tafel* region is defined by the potential at which the rate of the back-reaction (as calculated from the reverse reaction exponential term in the BV relation) represents less than 1% of the rate of the forward process. In this region the reverse reaction(s) is (are) negligible in rate and hence the experimental slopes can be related directly, if kinetic control prevails, to the kinetic transfer coefficient of that particular branch of the reaction.

For a simple multistep reaction ($\nu = 1$) described by the extended BV equation, Eqn. 2.33, the lower overpotential limit of the cathodic Tafel region is calculated from the condition that the ratio of cathodic and anodic overpotential terms in the rate equation for this reaction (Eqn. 2.33) is greater than 100, viz.:

$$\frac{\exp\left[-\left(\gamma_p + z_{rds}\beta\right) f\eta\right]}{\exp\left[\left(\gamma_f + z_{rds}(1-\beta)\right) f\eta\right]} = \exp\left[-\left(\gamma_f + z_{rds} + \gamma_p\right) f\eta\right] \tag{6}$$

$$= \exp[-zf\eta] \geq 100$$

where $z$ is the total number of electrons transferred in one turnover of the whole reaction, $\gamma_p$, $\gamma_f$ and $z_{rds}$ are the numbers transferred before, after and during the rds, respectively, for a given reaction mechanism as defined earlier. The total number of electrons transferred for this reaction is equal to:

$$z = \gamma_p + z_{rds} + \gamma_f \tag{7}$$

which has thus been used to simplify Eqn. 6.6.

The result in Eqn. 6.6 is equivalent (but the inverse) for the anodic reaction; thus, at 25° C, overpotentials greater than $\left| 118 \cdot / z \text{ mV} \right|$ (e.g. 59 mV for 2 electrons) are necessary to distinguish the anodic and cathodic branches.

Things are a little different for a reaction involving a rds having a stoichiometric number > 1, say for the case of a *preceding* (reductive or chemical) *dissociation*, described previously in §2.7.4, for which the total number of electrons transferred is:

$$z = \gamma_{E\text{-}S} + \nu \cdot \left( \left( \gamma_{E\text{-}P} - \gamma_{E\text{-}S} \right) + z_{rds} + \gamma_{E\text{-}F} \right) \tag{8}$$

where recall that the electron-number coefficients are the numbers of electrons transferred in *elementary* steps 1) up to the *dissociation* (stoichiometry-determining step), $\gamma_{E\text{-}S}$; 2) up to the rds (which includes the $\gamma_{E\text{-}S}$ steps above), $\gamma_{E\text{-}P}$; 3) during, $z_{rds}$; and 4) after the rds, $\gamma_{E\text{-}F}$[b] (in reduction steps). Note in Eqn. 6.8 that since all elementary reaction steps after the dissociation must occur $\nu$ times, all the corresponding terms are multiplied by $\nu$.

From the BV-like rate equation describing this reaction type, Eqn. 2.50, the definition of the cathodic Tafel region limit for this case is Eqn. 6.9, which is simplified by comparing the second term in Eqn. 6.9 to Eqn. 6.8:

$$\frac{\exp\left[ -\left( \frac{\gamma_{E\text{-}S}}{\nu} + \left( \gamma_{E\text{-}P} - \gamma_{E\text{-}S} \right) + z_{rds}\beta \right) f\eta \right]}{\exp\left[ \left( \gamma_{E\text{-}F} + z_{rds}(1-\beta) \right) f\eta \right]} \tag{9}$$

$$= \exp\left[ -\left( \frac{\gamma_{E\text{-}S}}{\nu} + \left( \gamma_{E\text{-}P} - \gamma_{E\text{-}S} \right) + \gamma_{E\text{-}F} + z_{rds} \right) f\eta \right] = \exp\left[ -\frac{z}{\nu} f\eta \right] \geq 100$$

[b] This terminology for elementary reaction steps has been discussed earlier (see Eqn. 2.48 and §2.7).

The lower overpotential limit of the Tafel region for both cathodic and anodic reaction branches is defined for this case by $\left| 118 \cdot \nu/z \text{ mV} \right|$ which, for the aluminum reaction, is 39 or 118 mV depending on whether $\nu = 1$ or 3, respectively.

### 6.7.3. Linearized BV Equation

At sufficiently small overpotentials the exponential terms of the BV-like equations may be linearized since exp[x] is approximately 1 + x for small values of x. If x is 0.1 the error of this approximation is 5%, if 0.02, the error is 1%. These tolerances correspond to overpotentials less than $2.6 \cdot \nu/z$ and $0.5 \cdot \nu/z$ mV, respectively. The general multistep BV relation, Eqn. 2.33, may be linearized, and if terms are combined and Eqn. 6.8 considered, reduces to Eqn. 6.10:

$$\begin{aligned} i_{net} &= i_o\left[\left(1+\left(\left(\gamma_f+z_{rds}(1-\beta)\right)f\eta\right)\right) - \left(1+\left(-\left(\gamma_p+z_{rds}\beta\right)f\eta\right)\right)\right] \\ &= i_o\left[\gamma_f+z_{rds}+\gamma_p\right]f\eta \;=\; i_o z f\eta \end{aligned} \tag{10}$$

For a more complicated BV relation, for instance one involving a rds having a stoichiometric number greater than one arising from a preceding (reductive or chemical) dissociation, linearization gives Eqn. 6.11:

$$\begin{aligned} i_{net} &= i_o\Big( \left[1+\left(\gamma_{E\text{-}F}+z_{rds}(1-\beta)\right)f\eta\right] \\ &- \left[1+\left(-\left(\frac{\gamma_{E\text{-}S}}{\nu}+\left(\gamma_{E\text{-}P}-\gamma_{E\text{-}S}\right)+z_{rds}\beta\right)f\eta\right)\right]\Big) \end{aligned} \tag{11}$$

When terms are combined and simplified (considering Eqn. 6.8), this reduces to:

$$i_{net} = i_o\left[\frac{\gamma_{E\text{-}S}}{\nu} + \gamma_{E\text{-}F} + z_{rds} + \left(\gamma_{E\text{-}P}-\gamma_{E\text{-}S}\right)\right]f\eta = i_o\frac{z}{\nu}f\eta \tag{12}$$

At low $\eta$, the slope of the linearized BV relation is given by Eqn. 6.13:

$$\frac{d\eta}{di} = \frac{\nu}{z}\cdot\frac{1}{fi_o} = R_{CT} \tag{13}$$

which is termed the *charge-transfer resistance*, $R_{CT}$ and $i_o$ is the exchange current-density for the reaction. The latter quantity can, of course, be determined by extrapolating Tafel relations back to $\eta = 0$ (i.e. based on the slopes of linear regions within the high $\eta$, exponential region of semi-logarithmic Tafel plots).

Significantly, $R_{CT}$ from low, and $i_o$ derived from high $\eta$ regions may be combined through Eqn. 6.13 to determine the ratio $z/\nu$, the ratio of the number of electrons transferred and the stoichiometric number of the rds, parameters important to mechanism elucidation. This calculation is only valid, of course, if there is indeed an observable, kinetically-controlled Tafel region and if the electrochemical reaction has the same mechanism in both the low and high $\eta$-regions.

### 6.7.4. Back-Reaction Correction: The Allen-Hickling Transformation

#### 6.7.4.1. Stoichiometric Number Equal to One

At transitional overpotentials between the Tafel and linear polarization regions, the BV relation is thought to offer no kinetic information since both forward and reverse reactions are of comparable rate. It can happen, however, that a given reaction is not under kinetic control in the usual Tafel region (i.e. $|\eta| > 118 \cdot \nu/z$ mV); for example some other process such as diffusion could be limiting at high current-densities or different mechanisms could prevail at low and high current-densities. If this is so, the Tafel parameters, $i_o$, $\alpha_a$ and $\alpha_c$, cannot be determined. Back-reaction correction can, however, expand the (semi-logarithmic) Tafel region down to a few millivolts of overpotential and unlock this transitional region. Allen and Hickling in their work on the electrochemistry of sulphur in alkaline solution [129] developed a transformation of the usual BV equation which corrects for the back-reaction rate contribution, enabling separate evaluation of forward and reverse reaction rates for nearly all overpotentials, down to the reversible potential.

Starting this derivation again from the general BV multistep rate equation, Eqn. 2.33, and considering the cathodic reaction direction first, we substitute $\gamma_f$ in the anodic

term by $z-\gamma_p-z_{rds}$ (from Eqn. 6.7) which gives for the rate equation:

$$i_{net} = i_o\left(\exp\left[\left(z-\gamma_p-z_{rds}+z_{rds}(1-\beta)\right)f\eta\right] - \exp\left[-\left(\gamma_p+z_{rds}\beta\right)f\eta\right]\right) \quad (14)$$

out of which may be factored $\exp[-(\gamma_p+z_{rds}\beta)f\eta]$ which leaves Eqn. 6.15.

$$i_{net} = i_o\left(\exp\left[-\left(\gamma_p+z_{rds}\beta\right)f\eta\right]\cdot\left(\exp[zf\eta]-1\right)\right) \quad (15)$$

By multiplying both sides of this expression by -1 (a matter of bookkeeping; see below) and taking natural logarithms we obtain the intermediate expression Eqn. 6.16:

$$\ln(-i_{net}) = \ln(i_o) - \left(\gamma_p+z_{rds}\beta\right)f\eta + \ln(1-\exp[zf\eta]) \quad (16)$$

Then, collecting the net current, $i_{net}$, and back-current correction into a single term and converting *ln* to *log* terms, we obtain Eqn. 6.17:

$$\log\left(\frac{-i_{net}}{1-\exp[zf\eta]}\right) = \log i_o - \eta\cdot\frac{\left(\gamma_p+z_{rds}\beta\right)f}{2.3026} \quad (17)$$

The use of this equation is analogous to that of the usual Tafel plot, but where instead of the observed net current, $i_{net}$, a back-reaction corrected term is plotted versus potential. At large negative overpotentials, the exponential in the denominator of the correction term will tend to zero and hence give no correction, but at smaller negative overpotentials the denominator will be smaller than one and will hence give a relatively increased, corrected current. The correction is, of course, only significant at lower overpotentials, for instance it is only 2% at 100 mV for a one-electron reaction.

Now considering the anodic reaction direction, $z-\gamma_f-z_{rds}$ can replace $\gamma_p$ in the cathodic term of the BV equation, out of which may be factored $\exp[\gamma_f-z_{rds}(1-\beta)f\eta]$, to give Eqn. 6.18:

$$i_{net} = i_o\exp\left[\left(\gamma_f+z_{rds}(1-\beta)\right)f\eta\right]\cdot\left(1-\exp[-zf\eta]\right) \quad (18)$$

which upon taking the natural logarithm, collecting the net current, $i_{net}$, and back-reaction correction into a single term, converting to common, base 10 logarithms gives:

$$\log\left(\frac{i_{net}}{1-\exp[-zf\eta]}\right) = \log i_o + \eta\cdot\frac{\left(\gamma_f+z_{rds}(1-\beta)\right)f}{2.3026} \quad (19)$$

Doing some bookkeeping of signs, negative overpotentials correspond to negative cathodic currents. $-i_{net}$ of Eqn. 6.17 will take account of the fact that negative currents result from negative overpotentials ensuring that the argument of the logarithm is positive while the exponential term in the denominator assures that increasing *negative* overpotentials will *decrease* the contribution of the correction.

For the anodic correction expression, Eqn. 6.19, the negative sign in the argument of the exponential of the correction term accounts for positive overpotentials and since anodic current is positive we need not worry about the argument of the logarithm. The mechanistic parameters in the overpotential term we recognize as being nothing other than the initial transfer coefficients $\alpha_a$ and $\alpha_c$ for the particular mechanism. Thus the correction maintains the integrity of the transfer coefficients and reduces to the general Tafel relation at higher $\eta$'s.

### 6.7.4.2. Back-Reaction Correction: Stoichiometric Number Greater Than One

The above derivation is quite general and can be applied to more complicated reaction mechanisms. Here we consider a reaction with a rds having a stoichiometric number $\nu$ resulting from a preceding dissociation, for which the total number of electrons transferred is given by Eqn. 6.8. We replace $\gamma_{E\text{-}F}$ by $(z/\nu - \gamma_{E\text{-}S}/\nu - (\gamma_{E\text{-}P}-\gamma_{E\text{-}S}) - z_{rds})$ (from Eqn. 6.8) in the cathodic direction term of Eqn. 2.50 and factor out $\exp[(-\gamma_{E\text{-}S}/\nu - (\gamma_{E\text{-}P}-\gamma_{E\text{-}S}) - z_{rds}\beta)f\eta]$. The resulting rate equation is:

$$i_{net} = i_o \exp\left[-\left(\frac{\gamma_{E\text{-}P}}{\nu} + (\gamma_{E\text{-}P}-\gamma_{E\text{-}S}) + z_{rds}\beta\right)f\eta\right]\left(\exp\left[\frac{z}{\nu}f\eta\right]-1\right) \qquad (20)$$

Conducting the same manipulations as in Eqns. 6.14 to 6.17, multiplying both sides by -1, taking natural logarithms, collecting the correction term and converting to common logarithms gives:

$$\log\left(\frac{-i_{net}}{1-\exp\left[\frac{z}{\nu}f\eta\right]}\right) = \log i_o - \eta\frac{\left(\frac{\gamma_{E\text{-}S}}{\nu} + (\gamma_{E\text{-}P}-\gamma_{E\text{-}S}) + z_{rds}\beta\right)f}{2.3026} \qquad (21)$$

For the anodic correction term, $\gamma_{E\text{-}P}$ may be replaced by $(z/\nu - \gamma_{E\text{-}S}/\nu + (\gamma_{E\text{-}S} - \gamma_{E\text{-}F}) - z_{rds})$ in the anodic direction term of Eqn. 2.50. Factoring out $\exp[(\gamma_{E\text{-}F} + z_{rds}(1-\beta))f\eta]$ yields Eqn. 6.22:

$$i_{net} = i_o \exp[(\gamma_{E\text{-}F} + z_{rds}(1-\beta))f\eta]\left(1 - \exp\left[-\frac{z}{\nu} f\eta\right]\right) \tag{22}$$

which may be compared to the simpler Eqn. 6.18. Taking natural logarithms, collecting terms and converting to common logarithm gives Eqn. 6.23:

$$\log\left(\frac{i_{net}}{1 - \exp\left[-\frac{z}{\nu} f\eta\right]}\right) = \log i_o + \eta \frac{(\gamma_{E\text{-}F} + z_{rds}(1-\beta))f}{2.3026} \tag{23}$$

which may be compared for this case to the simpler Eqn. 6.20.

The Allen-Hickling transformations for the cathodic and anodic reaction directions, Eqns. 6.21 and 6.23 are analogous to the respective simpler Eqns. 6.17 and 6.19, but in the latter two expressions the total number of electrons transferred per turnover of the overall reaction, z, used in these former relations, are now divided by the stoichiometric number, $\nu$, of the rds, i.e. $z/\nu$. The resulting transfer coefficients are again equivalent to the usual, uncorrected coefficients in Table 2.1 which, as it turns out, they are for all reaction mechanism possibilities. The preceding derivation is of importance when, later, consideration will be given to the possibility of the anodic and cathodic reactions being controlled by separate transition-states.

### 6.7.4.3. Application of Back-Reaction Corrections to Experimental Data

The procedure for the use of this correction is to plot the logarithm of $|i_{net}|/(1 - \exp[-(z/\nu)f|\eta|])$ vs. $\eta$, and this gives a linear relation down to within a couple of millivolts from the reversible potential in the semi-logarithmic plot; the slopes of the branches will be $\alpha_a f/2.3026$ and $-\alpha_c f/2.3026$ for the anodic and cathodic directions, respectively, and thus are no different from the ordinary, uncorrected Tafel slopes and transfer coefficients listed in Table 2.1, but become accessible down to very

small $\eta$ values.

The effect of back-reaction correction is demonstrated in Fig. 6.7 for the cathodic direction of a steady-state polarization curve of the Al reaction for an r = 1.5:1, $[Al]_{total}$ = 0.8 M bath. The inset of this figure shows the original data up to -200 mV. The uncorrected data for the back-reaction do not possess a sufficiently wide linear region (noted particularly in the inset) to enable a definitive Tafel slope to be determined. Without prior information on the stoichiometric number ($\nu$ = 1 or 3 are reasonable choices for Al) the question of whether to utilize the Tafel slope measured at overpotentials greater than 40 or 120 mV is also uncertain at first sight since one limit would be respectively more appropriate than the other. The lines plotted in Fig. 6.5 are for the same data but back-reaction corrected using different values of $\nu$ /z consistent with possible aluminum reaction mechanisms ($\nu$ /z taken as 1, 1.5, 3). z is necessarily three for aluminum and $\nu$ > z is not mechanistically possible. The corrected curve that gave the best and longest range of linearity was that for $\nu$ /z = 1 (i.e. $\nu$ = 3) and the dotted line drawn just above has a slope of *ca.* 120 mV dec$^{-1}$ and is included here as a guide for comparison between the linearities of the corrected curves. It is seen that the correction extends the Tafel region down to less than about 5 mV of overpotential in this example.

### 6.7.5. Non-Singular Rate-Determining Steps

An interesting and important addendum to this development is to consider the fact that all general mechanistic analyses (and ergo transfer coefficients in Table 2.1) assume that the kinetic barrier and hence the rds in a given sequential multi-step reaction mechanism is the same for *both* reaction directions (viz. "*singular*"), for instance the use of $\beta$ and 1 - $\beta$ in the ordinary BV equation (Eqn. 2.20) is a tacit expression of this assumption. In the event that two *different* steps (viz. "*non-singular*") are rate-determining for the anodic and cathodic reaction directions of the reaction, all the expressions of Chapter 2, the definition of the Tafel region and the back-reaction correction developed in this chapter are inapplicable and the generality of equalities such as Eqn. 6.6 or 6.8 is lost and the

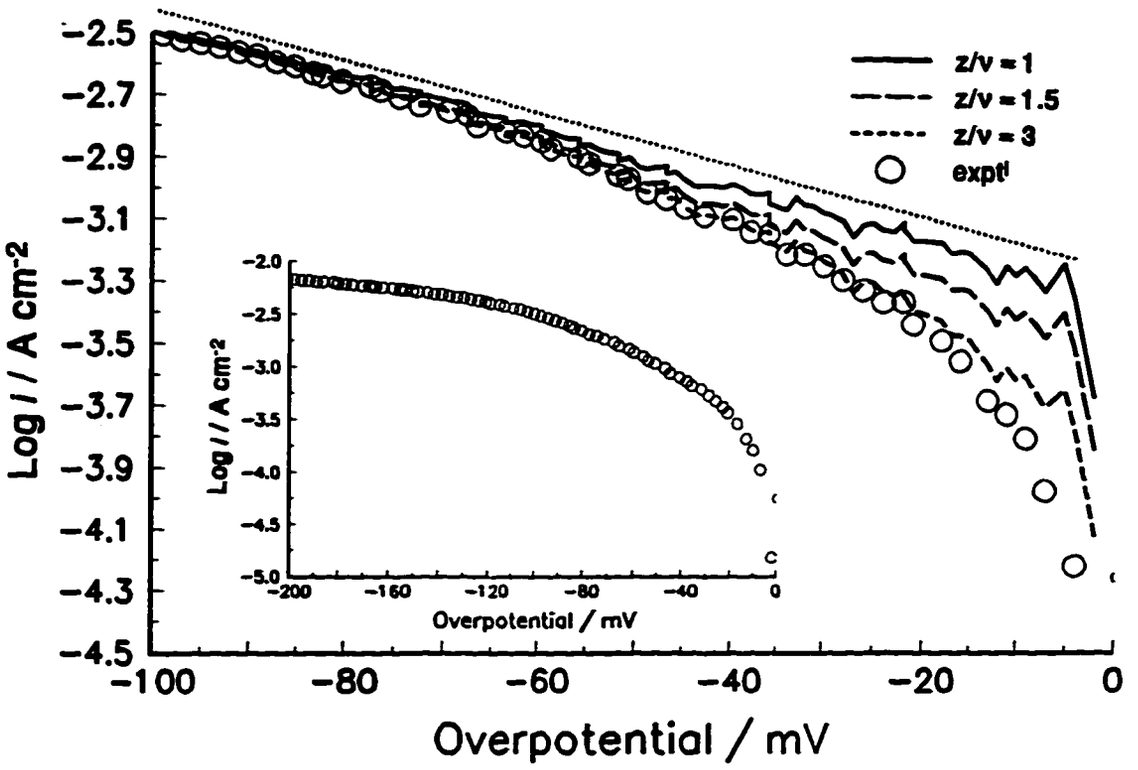


**Fig. 6.7.** Cathodic steady-state polarization curve for the deposition of Al from an r = 1:1.5, $[Al]_{total}$ = 0.4 M hydride-bath onto an electroplated Al disc (on a gold substrate), area: 0.002 $cm^2$, recorded at 5 mV/s at a rotation rate of 500 rpm corrected for solution IR drop. Circles represent original experimental data (shown for a larger range in the inset) and lines are from back-reaction correction by Eqn. 6.23 for listed values of $z/\nu$.

anodic and cathodic Tafel branches do not necessarily "see" all the reaction electrons.

Near to the reversible potential of any reaction, say $\eta < |10\ \text{mV}|$, the reaction *must* necessarily be the same in both reaction directions given that equilibrium must prevail at $E_r$. It can be envisaged, however, that an applied overpotential could shift the various potential-energy surfaces of possible species and intermediates involved in a multistep reaction independently of one another with the result that *different* transition-states could control the rate of the overall reaction at different overpotentials, for instance for the anodic and cathodic directions of a reaction. Ordinarily, a shift with overpotential from one rds to another will give an observable inflection point in experimental Tafel plots [89:p.109] as control of the reaction shifts from one transition-state, and hence mechanism, to another. If the assumptions of the quasi-equilibrium approximation (§2.5) were to hold in both regions and gave separate linear Tafel slopes, the separate mechanisms could be evaluated from the transfer coefficients determined from these slopes, but they would have possibly completely unrelated mechanistic parameters.

The result of a different transition-state limiting one reaction direction compared with the other is difficult to treat in general terms; thus, apart from the facts that Eqns. 6.6 and 6.8 are no longer valid nor any of the substitutions that rely on them, it becomes necessary to replace $\beta$ and $1 - \beta$ with $\beta_c$ and $\beta_a$, which are now unrelated to one another as the former pair were.

We consider a specific case central to the subject of this thesis, i.e. the aluminum electroreduction reaction which involves the transfer of three electrons. Al is known to have no stable intermediate oxidation states and thus a possible potential-energy surface for a hypothetical reaction mechanism involving three subsequent single-electron transfers would be described by *low* reactant and product energies (for $Al^{3+}$ and $Al^{0}$), *large* activation energy barriers to both the reduction of $Al^{3+}$ and oxidation of $Al^{0}$ and *shallow* potential wells for $Al^{2+}$ and $Al^{1+}$ (that for the latter, being, perhaps somewhat deeper due to its complete 3s orbital). Thus the transfer of the first electron would be rate-limiting in either reaction direction (note that this possibility has been recognized previously and was discussed in Chapter 3). This picture is, of course, equivalent to

saying that the rds is different for the two directions of reaction. Note that this is a different case from a *single* transition-state involving the *simultaneous* transfer of three electrons since its potential-dependence would necessarily involve $3\beta$ and $3(1-\beta)$ (i.e. would be *rather large*!) for the cathodic and anodic branches.

The result of this hypothetical aluminum reaction mechanism on, say, the back-reaction correction (as in §6.5.3.1) is that the BV relation would be of the form:

$$i_{net} = i_o(\exp[\beta_a f\eta] - \exp[-\beta_c f\eta]) \tag{24}$$

If we carry out the back-reaction correction development of Eqns. 6.14 to 6.17 for the cathodic reaction, i.e. factoring out one of the exponentials gives Eqn. 6.25:

$$i_{net} = i_o(\exp[-\beta_c f\eta]\cdot(\exp[(\beta_a+\beta_c)f\eta]-1)) \tag{25}$$

Multiplying by -1, taking logarithms, rearranging, then converting the logarithms gives:

$$\log\left(\frac{-i_{net}}{1-\exp[(\beta_a+\beta_c)f\eta]}\right) = \log i_o - \frac{\beta_c f\eta}{2.3026} \tag{26}$$

The correction contains the term $\beta_a+\beta_c$ which is now a *continuous* quantity if the two symmetry factors are taken likewise to be continuous (i.e. $0<\beta<1$) as they indeed should be, and not an integer or a ratio of integers as seen previously in Eqns. 6.17 and 6.19 or Eqns. 6.21 and 6.23 where a single transition-state was assumed.

As described in §6.6.3, comparing linear and exponential regions of Tafel plots provides a means to determine the mechanistically significant ratio $z/\nu$. An obvious problem arises from the possibility, considered presently, of discrete rate-determining steps since the low overpotential, linear region ($\eta<5$ mV) will very likely be controlled by a single rds (consistent with the condition for thermodynamic equilibrium) while, at higher overpotentials, some other reaction mechanism would predominate with the result that erroneous $z/\nu$ values would be calculated. Extreme caution is, therefore necessary when divining reaction mechanisms from experimental observables when a single transition-state may not be indicated.

Necessary, but not sufficient proof of a single rds would be that $\beta_a$ and $\beta_c$ sum to

1, i.e. that they represent fractions of the electrical energy $zF\eta$ influencing the same reaction barrier and that the $i_o$'s, extrapolated from the anodic and cathodic Tafel branches are identical, i.e. that they result from equilibrium reaction rates over the same barrier. It is to be noted in the case of the above hypothetical example for aluminum where the first electron in either direction is rate-limiting, that if the sum of the anodic and cathodic symmetry factors ($\beta_a + \beta_c$) used in the correction term, Eqn. 6.26, were, coincidently, equal to about one, then the measured steady-state electrochemical behaviour would be *indistinguishable* from that for the case of a single transition-state having a stoichiometric number equal to three, (i.e. $\beta_a + \beta_c \approx 1 = 3/3 = z/\nu$).

We see, in conclusion, that back-reaction correction opens up very low overpotential regions to experimental scrutiny (Fig. 6.7) and it is conceivable then that the transition from equilibrium conditions, where a single transition-state must prevail, to the situation where non-singular (different) transition-states arise *could* be identified.

### 6.8.1. Tafel Polarization Experiments: Results

The steady-state polarization measurements on the electrochemical behaviour of Al in the hydride-baths tended to suffer from irreproducibility. The baths themselves are composed of a complicated distribution of aluminate species of varying chemical and electrochemical reactivity (see Chapter 5). This situation results in a susceptibility to chemical decomposition, whether amongst themselves or with water, the latter being an impurity that is nearly impossible to exclude completely from the baths, and thus the $[Al]_{total}$ as well as the species' distribution is time-dependent and exacerbated by the high volatility of the solvent, thf (b.p. 67° C). Given the significant irreproducibility of the results and the lack of exact control possible in solution preparation, the only procedure for derivation of meaningful trends was to compare a relatively large body of results.

The Tafel plots recorded for the hydride-baths usually did not give wide linear regions and thus it was necessary to apply back-reaction corrections to all experimental data (hence the detailed discussion of the required procedure in the previous sections). It was found that in the majority of cases a correction involving $z/\nu = 1$ gave the widest

region of linearity for both anodic and cathodic reaction directions, usually extending down to about 10 mV and up to 100 mV or better in some cases. The slopes of the curves were determined by linear regression of digitized current/voltage data corrected for IR, back-reaction and apparent surface area factors; the potential limits of any given curve would be defined by the criterion of a minimum *correlation coefficient* [130] of 0.999 for the fitted line.

Typical Tafel plots for the electrodeposition onto and electrodissolution from aluminum itself (deposited initially onto polished Au substrates) from hydride-baths of various compositions are shown in Fig. 6.8. Plotted on the y-axis is the common logarithm of the measured current-density and associated back-reaction correction (dotted curve), and on the x-axis overpotential, the displacement from the $E_r$ for the reaction.

Fig. 6.8a shows a Tafel plot for an r = 2.3:1, $[Al]_{total}$ = 1 M hydride-bath at an electrode rotation rate of 500 rpm. Baths of this composition usually exhibited symmetric anodic and cathodic current branches and Tafel slopes of about 120 mV dec$^{-1}$ as calculated from the appropriate regions of the corrected (dotted) curve. The correction curves were generally smooth and linear down to near $E_r$ where error and overcorrection would have given scatter (such data points have been deleted from Figs. 6.8 for clarity). The extent of this scatter was defined by the instrumental range used to record the small currents near to $E_r$. The effect of a coarser range on the scatter is to be noted particularly in Fig. 6.8b by the "chunkiness" of the experimental curve near $E_r$ and the low overpotential limit of the corrected curve which was not as low as for other curves. Extrapolation of the linear regions back to the appropriate $E_r$ gave the $i_o$'s for the reaction.

Fig. 6.8b shows a Tafel plot for an r = 1:2.5, $[Al]_{total}$ = 0.35 M bath. Generally, baths in the $H^-$-rich regime showed asymmetric Tafel plots having different slopes, that for the anodic branch being less than 100 mV dec$^{-1}$ and that for the cathodic branch being quite high, usually > 150 mV dec$^{-1}$. For $H^-$-rich baths of increasing $H^-$-content (beyond *ca.* r = 1:2.5) Tafel plots would show an inflection point in the cathodic branch and beyond this would be observed another kinetically significant slope at overpotentials more negative than about -125 mV as in Fig. 6.8b. The slope of this region was 120 mV dec$^{-1}$

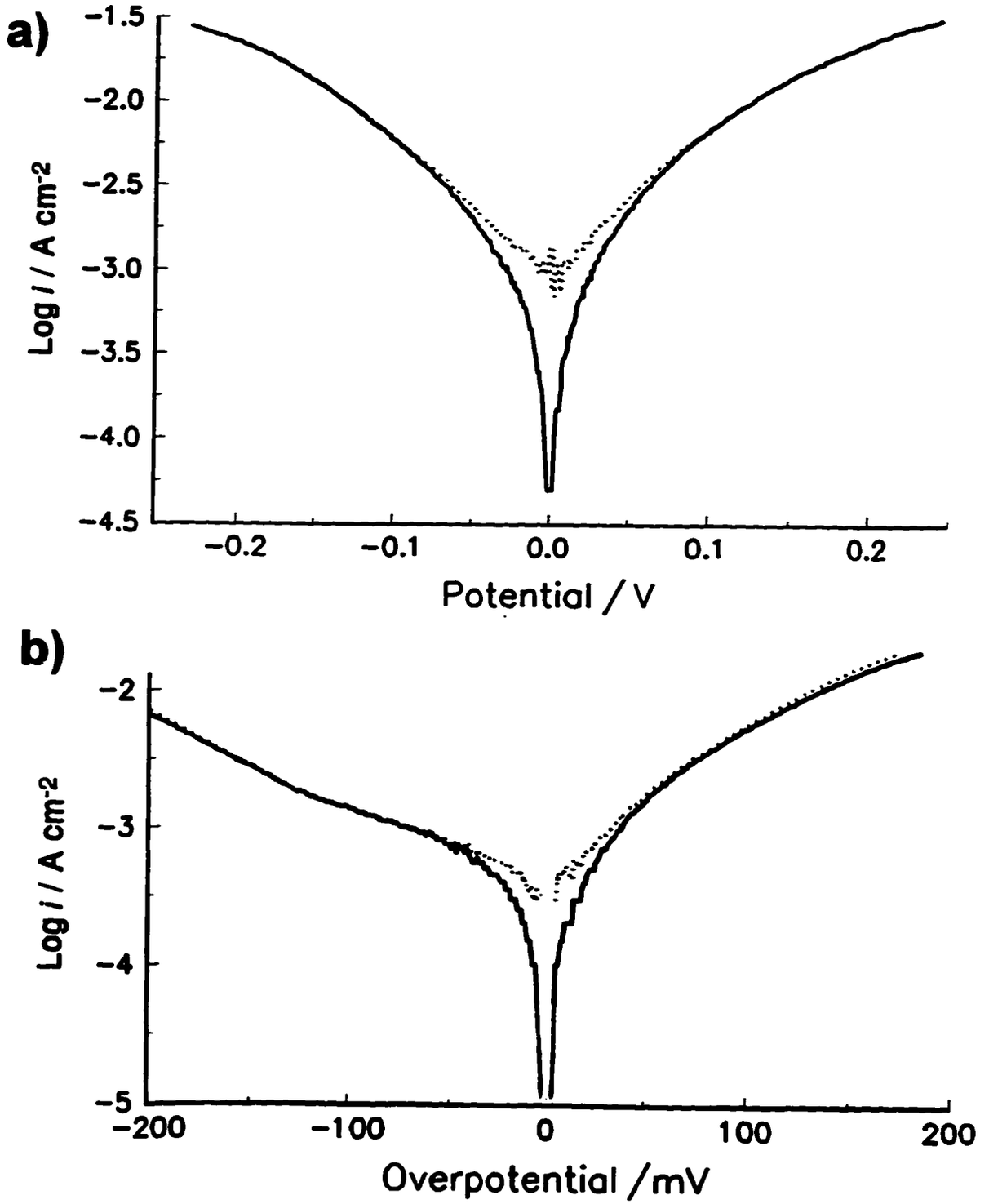


**Fig. 6.8.** Typical Tafel plots (log i vs $\eta$) in the hydride-bath: **a)** r = 2.3:1, $[Al]_{total}$ = 1 M; **b)** r = 1:2.5, $[Al]_{total}$ = 0.35 M; and **c)** r = 4.5:1, $[Al]_{total}$ = 1 M. Back-reaction corrected curves (dotted) calculated for $z/\nu = 1$ are also included.

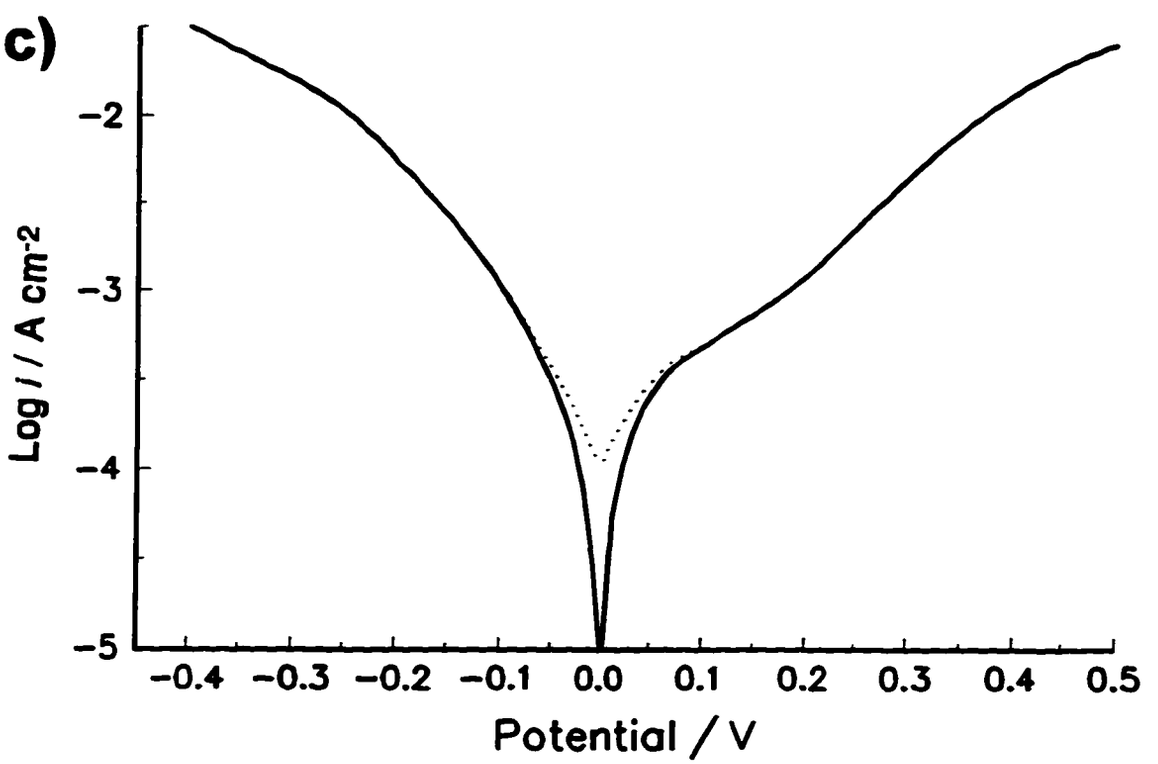


**Fig. 6.8.** Typical Tafel plots (log i vs $\eta$) in the hydride-bath: a) r = 2.3:1, $[Al]_{total}$ = 1 M; b) r = 1:2.5, $[Al]_{total}$ = 0.35 M; and c) r = 4.5:1, $[Al]_{total}$ = 1 M. Back-reaction corrected curves (dotted) calculated for $z/\nu = 1$ are also included.

and is consistent with a symmetric ($\beta = 0.5$), one electron process associated with the Li deposition reaction discussed in the cyclic voltammetry section.

In a few cases, steady-state behaviour showing two distinct anodic features was observed noted earlier in the cyclic voltammetry of $Cl^-$-rich baths (§6.4.2.2). An example is Fig. 6.8c which shows a Tafel plot for an r = 4.5:1, $[Al]_{total}$ = 1 M bath recorded at an equivalent scan-rate of 2 mV $s^{-1}$ for an electrode rotated at 500 rpm. Two separate stripping processes are observed, one at lower overpotential having lower slope and the other at higher overpotential with a greater slope.

### 6.8.2. Transfer Coefficients

Previous reports on this bath have described symmetrically valued Tafel slopes (i.e. $\approx$ 118 mV $dec^{-1}$; hence $\alpha_a = \alpha_c = 1/2$) [38-41] in $Cl^-$-rich baths and asymmetrically valued slopes in $H^-$-rich baths ($\alpha_a = 2/3$, $\alpha_c = 1/3$) [39,40]. These observations were reflected in the results of the present work, although several of the higher $Cl^-$-content baths gave what approached an inverse of the results for the $H^-$-rich baths, that is ($\alpha_a$ = 1/3, $\alpha_c = 2/3$). For instance, the slope of the higher overpotential anodic region in Fig. 6.8c corresponded, in fact, to $\alpha_a = 1/3$.

Table 6.1 lists all the recorded Tafel polarization results which were of sufficient quantity to be statistically significant, for hydride-baths of varying "r" and concentration. The 95% confidence intervals of the results, based on the statistical *t*-test [130], are included in parentheses. Direct analysis for trends in the exchange current-density data was not feasible for this data set due to the demonstrated bivariate dependence on the baths' $[Al]_{total}$ and compositional ratio, r, and peculiarities of the solubilities of the components. Given that $LiAlH_4$ has a maximum solubility in thf of about 0.4 M, while that of $AlCl_3$ varies from 0.8 to about 2.0 M, dependent on the $LiAlH_4$ content [34], the maximum total aluminum concentrations possible at the compositional extremes of the bath were significantly different and thus systematic concentration relations could not be deconvoluted.

Fig. 6.9 shows a plot of the $\alpha_c$ and $\alpha_a$ values of Table 6.1 and their respective

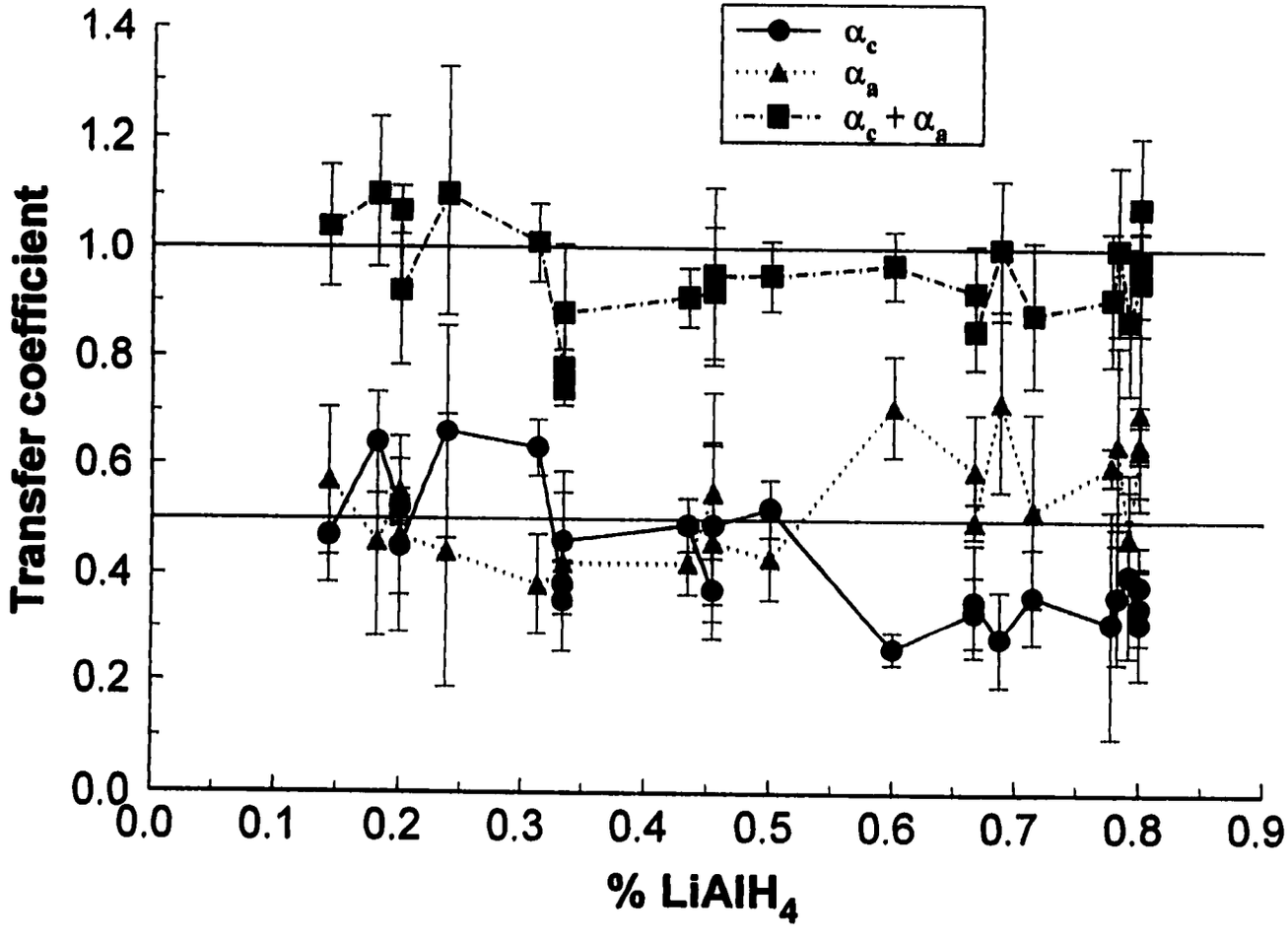


**Fig. 6.9.** A plot of measured transfer coefficients from Table 6.1 versus the %$LiAlH_4$ composing the bath from which measurements were taken.

Table 6.1. Tafel Polarization Results

| r | $[Al]_{total}$ mol dm$^{-3}$ | $\alpha_c$ | $\alpha_a$ | Log $i_o$ A cm$^{-2}$ | No. Obs. | Date |
|---|---|---|---|---|---|---|
| 6:1 | 1.6 | 0.47(0.07) | 0.57(0.10) | -3.59(0.22) | 7 | Fe95 |
| 4.5:1 | 1.2 | 0.64(0.07) | 0.46(0.14) | -3.60(0.20) | 6 | My95 |
| 4:1 | 1.0 | 0.52(0.02) | 0.55(0.04) | -2.62(0.20) | 10 | Jn96 |
| 4:1 | 1.0 | 0.45(0.07) | 0.47(0.14) | -3.43(0.36) | 4 | Fe95 |
| 3.2:1 | 1.4 | 0.66(0.15) | 0.44(0.19) | -3.24(0.17) | 5 | Mr95 |
| 2:1 | 0.5 | 0.63(0.04) | 0.38(0.07) | -3.21(0.25) | 15 | Jn94 |
| 2:1 | 1.2 | 0.38(0.03) | 0.40(0.02) | -2.14(0.25) | 10 | Jn95 |
| 2:1 | 0.6 | 0.35(0.02) | 0.39(0.03) | -2.01(0.15) | 9 | Jn95 |
| 2:1 | 0.7 | 0.46(0.07) | 0.42(0.13) | -3.13(0.30) | 7 | Ja95 |
| 1.3:1 | 0.4 | 0.49(0.04) | 0.42(0.04) | -2.80(0.10) | 7 | Fe94 |
| 1.2:1 | 0.5 | 0.37(0.04) | 0.55(0.14) | -2.34(0.33) | 7 | Jn95 |
| 1.2:1 | 0.6 | 0.49(0.11) | 0.46(0.14) | -3.48(0.18) | 8 | Au94 |
| 1:1 | 0.8 | 0.52(0.04) | 0.43(0.06) | -2.55(0.43) | 5 | De94 |
| 1:1.5 | 0.3 | 0.26(0.02) | 0.71(0.07) | -3.66(0.05) | 6 | My95 |
| 1:2 | 0.25 | 0.33(0.05) | 0.59(0.08) | -2.75(0.30) | 15 | Jn95 |
| 1:2 | 0.36 | 0.35(0.08) | 0.50(0.02) | -3.70(0.30) | 10 | Jn96 |
| 1:2.2 | 0.5 | 0.28(0.07) | 0.72(0.13) | -3.88(0.24) | 5 | Mr95 |
| 1:2.5 | 0.5 | 0.36(0.07) | 0.52(0.14) | -3.58(0.18) | 4 | Ja95 |
| 1:3.5 | 0.35 | 0.31(0.16) | 0.60(0.03) | -3.80(0.10) | 8 | Ap95 |
| 1:3.6 | 0.37 | 0.36(0.10) | 0.64(0.14) | -4.10(0.30) | 8 | Ap95 |
| 1:3.8 | 0.4 | 0.40(0.12) | 0.47(0.09) | -3.40(0.20) | 5 | Ap95 |
| 1:4 | 0.5 | 0.31(0.08) | 0.63(0.06) | -3.30(0.10) | 6 | Ap95 |
| 1:4 | 0.4 | 0.38(0.06) | 0.70(0.14) | -3.55(0.15) | 5 | De94 |
| 1:4 | 0.35 | 0.34(0.05) | 0.64(0.03) | -3.31(0.20) | 6 | Fe95 |

sums as a function of the H$^-$-fraction (from $LiAlH_4$) composing the respective plating baths. The two drawn vertical lines correspond to 0.5 and 1.0 and these values arise if, as will be proposed and explained later, the transfer coefficients (i.e. Eqn. 2.1) reduce to $\beta$ and $1-\beta$ for $\alpha_c$ and $\alpha_a$, respectively. $\beta = 0.5$ corresponds to a "symmetric" barrier where $\beta$ deacribes the relative geometry of the potential-energy surfaces of the reactant and product near their interaction arising around the rate-limiting transition-state. $\alpha_c$ seemed to vary more or less continuously from roughly 0.3 at high H$^-$-content and approaches 0.7 at high Cl$^-$-content. $\alpha_a$ was near 0.65 at high H$^-$-content and reached a minimum of 0.4 in the Cl$^-$-rich regime.

Table 6.2 lists the correlation coefficients for data in Table 6.1 as measures of the significance of linear relationships between measured $\alpha$'s and $i_o$'s with respect to the $\%H^+$ and $[Al]_{total}$ in the baths. The correlation coefficient, $\rho$, varies between $-1 \leq \rho \leq 1$ where values near to the extremes indicate strong positive or negative relationships in the data, while values near zero are an indication of independence of the variables. This coefficient is similar to the "Pearson product moment coefficient", $r$, which, when squared, is the well-known measure of correlation from linear regression analysis [130].

Table 6.2. Correlation Coefficients of Relations of $\alpha$'s and $i_o$'s with $\%H^+$ and $[Al]_{total}$

| Dependent variable | $\%H^+$ | $[Al]_{total}$ |
|---|---|---|
| $\alpha_{cathodic}$ | -0.704 | +0.609 |
| $\alpha_{anodic}$ | +0.607 | -0.377 |
| $\alpha_{total}$ | -0.157 | +0.305 |
| $i_o$ | +0.304 | -0.124 |

There was, of course, a significant scatter in the data and linear correlation was not particularly strong, but a marked trend in the relation between cathodic and anodic transfer coefficients and $\%H^+$-content of the baths is clearly demonstrated in Table 6.2: a positive one for $\alpha_a$ and a negative one for $\alpha_c$. Weaker and inverse relationships between $[Al]_{total}$ and the cathodic and anodic $\alpha$ data (column 2 of Table 6.2) are purely incidental, since higher $\%H^+$ is generally accompanied by smaller $[Al]_{total}$ in the composition of the experimental baths and have been included only for completeness. Interestingly, no correlation of $i_o$ with $[Al]_{total}$ was indicated from the data set. This is probably due to higher rates in $H^+$-rich baths which are limited to lower $[Al]_{total}$.

If the same transition-state is involved for cathodic and anodic reaction directions, the sum of the cathodic and anodic $\alpha$'s should be equal to one, when they are comprised of $\beta$ and $1-\beta$. The average of $\alpha_{total}$ for the data in Table 6.1 was calculated to be 0.949

$\pm 0.049$ (for a 99% confidence interval), a very clear result. Although the individual $\alpha$'s were noted to vary semi-continuously with $\%H^-$, there was no such relationship for $\alpha_{total}$. This is particularly relevant in relation to the possibility of non-singular transition-states (i.e. not the same for both reaction directions, see §6.6.5), since $\beta_c$ and $\beta_a$ for different energy barriers are independent of one another and unlikely to sum to one as is the case for a singular transition-state involving $\beta$ and $1-\beta$. The sum of the former pair would be expected to be different from *one* and might even demonstrate some sort of dependence on $\%H^-$ since the individual values were observed to vary with composition.

### 6.8.3. z/ν Ratio

It is to be noted with respect to the back-reaction correction curves used to calculate the $\alpha$'s and $i_o$'s in this work, that the z/ν ratio, that gave the best fit correction curve, should be the same as that calculated independently. The statistics for this ratio calculated from comparison of $i_o$ values extrapolated from high overpotentials, and $R_{CT}$ from quite low overpotentials (as per Eqn. 6.13) for 200 individual observations from 25 separate baths of varying $[Al]_{total}$ and compositional ratio, are given in Table 6.3. $Cl^-$-rich ($r \geq 2.0$) and $H^-$-rich ($r \leq 0.5$) compositions (columns 2 and 3) are separated in search for any trend that might distinguish the electrochemical behaviour between the compositional extremes. However, no trends with $[Al]_{total}$ were noted amongst any of the groupings and the mean of the data was equal to 1 (99% confidence interval), see Table 6.3.

Table 6.3. Calculated z/ν Values and Related Statistics for the Hydride-Bath: (99% confidence)$^{\#\,observns}$

| | All data | $Cl^-/H^-$ | |
|---|---|---|---|
| | | ≥ 2 | ≤ 0.5 |
| Cathodic | 0.976 (0.087)$^{74}$ | 1.003 (0.108)$^{22}$ | 1.062 (0.211)$^{35}$ |
| Anodic | 1.004 (0.118)$^{70}$ | 0.959 (0.101)$^{22}$ | 1.069 (0.145)$^{35}$ |
| Total | 1.036 (0.066)$^{197}$ | 1.114 (0.118)$^{74}$ | 1.024 (0.073)$^{91}$ |

The possibility of non-singular transition-states, as discussed earlier in §6.6.5, would give rise to independent values of $\beta_a$ and $\beta_c$ and the probability that their sum would *not* be equal to one is high. Given the uncertain relationship between the mechanisms at high overpotential and low (necessarily involving a *single* transition-state near $E_r$), it would be expected that a calculation involving $i_o$ and $R_{CT}$ would give some *arbitrary*, not necessarily constant value that would not be related to possible stoichiometric numbers, $\nu$'s, for a given reaction. Clearly, all data were very close to $z/\nu = 1$ for all bath compositions, and thus there was no significant departure from a mechanistically credible value (note that z and $\nu$ can only be integers) for this quantity which leads to the conclusion that the reaction under study involves a *single* transition-state for the potential region considered.

## 6.9. A.C. Impedance Behaviour of the Al Reactions

### 6.9.1. Foreword

As was central to the discussion in Chapter 2 on reaction mechanism, it is the potential-dependence of the surface concentration of reaction intermediates formed in electrochemical steps that is the key to mechanism determination from experimental Tafel results. If, however, the potential-dependence of these intermediates is defined by a bounded isotherm (see §2.5.1) and moderate to high coverage conditions obtain, Tafel relations will not have the same slopes as for limitingly low coverages with the result that erroneous transfer coefficients and hence reaction mechanisms would be derived. It is therefore necessary to identify whether the results of the Tafel analysis given in the previous section are indeed valid and not some result of a controlling isotherm.

A.C. impedance is a powerful technique that may be thought of as a kinetic spectroscopy for electrochemical systems. It is capable of resolving many characteristics of electrode reactions, giving, essentially, direct access to capacitances and resistances that describe aspects of the electrochemical interface and these results can have direct relevance to identification of reaction mechanisms. In order to understand the data and hence justify the conclusions drawn from these experiments, a certain limited amount of

theoretical introduction will be required for the uninitiated.

The technique involves the application, to an electrochemical cell, of a sinusoidally alternating potential[c] signal of small amplitude and of discreetly varying frequency superimposed upon some steady-state d.c. polarization. The magnitude of the resulting current *and* the phase angle between the applied potential and the resulting current are measured for the perturbed system. Phase angles can be readily measured with a.c. bridges, lock-in amplifiers or frequency response analyzers. The reason that this sort of experiment is interesting is that different *ideal* circuit components (resistors, capacitors or inductors) give markedly different responses to a.c. perturbations, and it has been shown possible to model elements of electrochemical interfaces with combinations of these simple ideal "equivalent-circuit" elements.

### 6.9.2. Theoretical Background

The instantaneous potential, $E_i$, for a sinusoidally oscillating signal of maximum potential $E_{max}$ may be represented as:

$$E_i = E_{max}\sin(\omega t) \tag{27}$$

where t is time and $\omega$ angular frequency (in rad $s^{-1}$), which differs from conventional frequency (in Hz) by $1/2\pi$. The current response, $I_i$, of a pure resistor of magnitude R (in $\Omega$) to an alternating potential is, by Ohm's law:

$$I_i = \frac{E_i}{R} = \frac{E_{max}}{R}\sin(\omega t) \tag{28}$$

which is of the same *phase* (sin($\omega$t)) as the applied potential perturbation, and thus the phase and magnitude of the oscillating potential and current are as illustrated in Fig. 6.10a.

In the case of a capacitor, its current-potential relationship is derived from the definition of absolute (i.e. not normalized to surface area) differential capacitance, $C' = dQ_i / dE_i$. Since $I = dQ/dt$, rearrangement gives:

---

[c] It is to be noted that, alternatively, the current can be modulated and the resulting potential monitored.

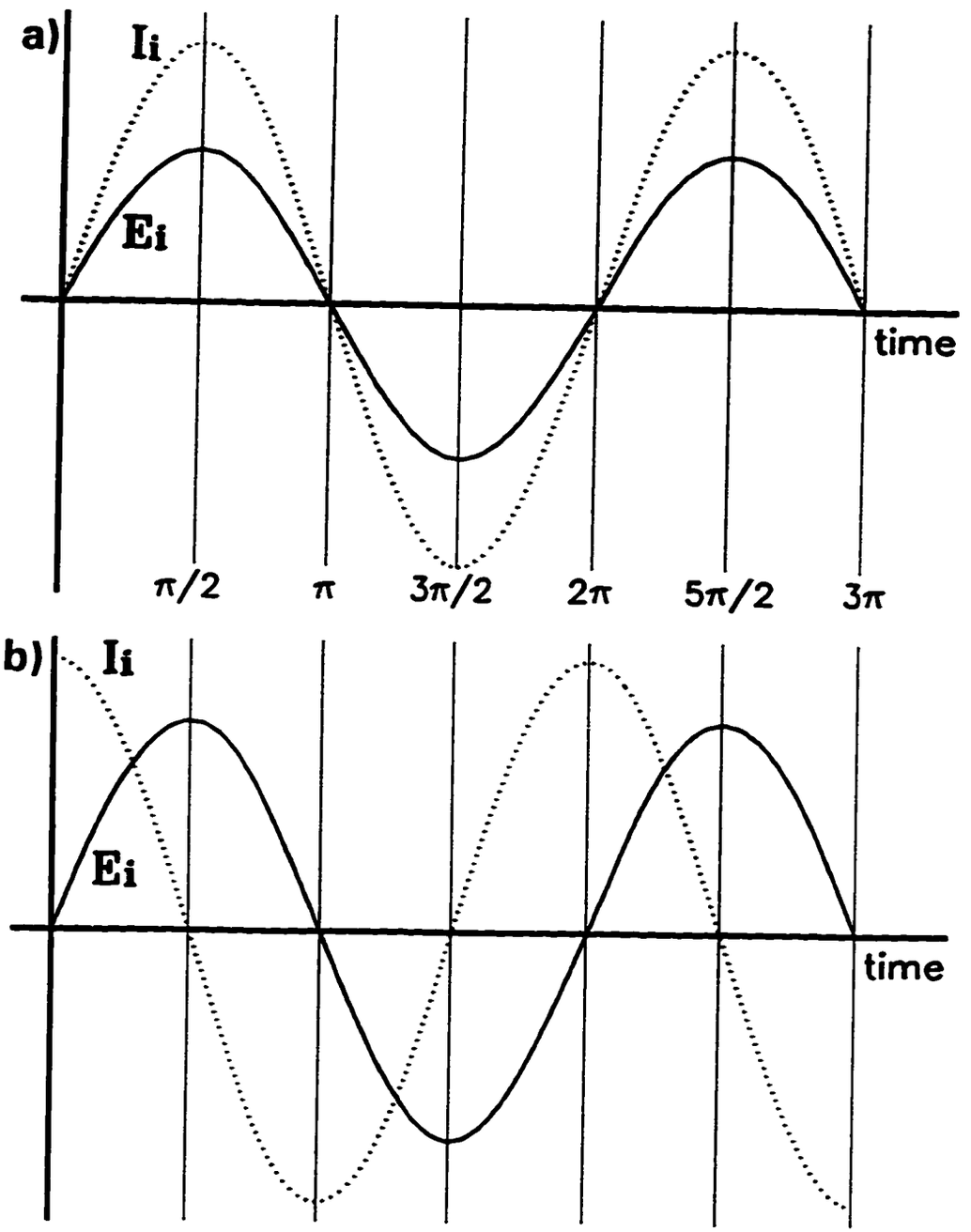


**Fig. 6.10.** Instantaneous potential (solid) and current (dotted) versus time showing the differences in magnitude and phase angle between a sinusoidally alternating potential and resulting current signal across **a)** an ideal resistor; **b)** an ideal capacitor.

$$I_i = \frac{dQ_i}{dt} = C'\frac{dE_i}{dt} \quad (29)$$

The potential in an a.c. experiment is time-dependent and given by Eqn. 6.27 which when included in Eqn. 6.29 and differentiated gives the current response of the capacitor:

$$I_i = \omega C' E_{max}\cos(\omega t) = \omega C' E_{max}\sin(\omega t + \pi/2) = \frac{E_{max}}{X_C}\sin(\omega t + \pi/2) \quad (30)$$

which is shifted by $\pi/2$ from that of the applied potential and thus the current signal is said to *lead* the potential by a 90° phase angle, as illustrated in Fig. 6.10b. The term $1/\omega C'$ has been replaced by $X_C$, the capacitive reactance, which is likened to resistance, R, but, of course, is frequency dependent.

Resistance and capacitive reactance (and similarly inductive reactance) are all *impedances*, $Z = E_i / I_i$. Since the phase angle behaviours of the two of interest here, $Z_R$ and $Z_C$, are orthogonal to one another, they are separable and it becomes useful to employ complex number notation where the resistance is *real* and the capacitive reactance is *imaginary*; thus $Z_C = -jX_C \equiv +X_C/j$, where $j = \sqrt{-1}$. Simplifying matters is that when impedances are combined in electrical circuits they add, as do resistances, linearly in series and inversely in parallel.

The great utility of considering these ideal circuit elements is that electrochemical interfaces can often be modelled (with a few caveats) after combinations of these in so-called *equivalent circuits*. Capacitances associated with the double-layer, $C_{DL}$, adsorption of *isotherm*- and *rds*-limited reaction intermediates, $C_P$ (termed the pseudocapacitance), or a geometric capacitance, $C_G$, can respond largely in the same manner as do pure capacitors. Electrochemical resistances can be those associated with solution or barrier film conductivity ($R_S$ or $R_F$) and the resistance to charge-transfer in an electrochemical reaction, $R_{CT}$. This latter is considered to be proportional to the inverse of the rate of a particular reaction step, i.e. $1/v$ (in any of the rate expressions we have considered in Chapter 2, e.g. Eqn. 2.16 or 2.17).

Unlike pure resistors and capacitors, however, many of the equivalent *electrochemical* circuit elements show significant potential-dependence, for instance $R_{CT}$ is

known to decrease exponentially as the overpotential is increased, consistent with the BV relation (Eqn. 2.20), $C_p$ varies non-linearly with its associated adsorption isotherm and $C_{DL}$ will vary with the potential-dependence of the double-layer structure. These phenomena are interesting characteristics of electrochemical systems and may be investigated by conducting a.c. experiments over a range of different steady-state d.c. polarizations, but it is important that in a given single experiment, very small potential perturbations (*ca.* 5 mV) are applied to ensure that the electrochemical system behaves linearly.

Experimentally, sinusoidally alternating, small-amplitude potential signals are applied to an electrochemical system over a range of frequencies (say $10^5$ - $10^{-2}$ Hz). The resulting data are the phase angle, $\phi$, between the input (potential) and output (current) signals and the magnitude of the impedance of the system, calculated as $Z = E_t/I_t$ at each analyzed frequency and d.c. polarization (determining $R_{CT}$). The dependent quantities may be plotted separately vs. frequency in a pair of so-called Bode plots or simultaneously in a so-called Nyquist plot, where the real and imaginary components of Z in complex notation, represented as $Z'$ and $Z''$ (both having units of Ω's) are plotted against each other. The Nyquist relation or so-called complex-plane plot, permits kinetic quantities to be read straight off these plots.

To get an idea of what the Nyquist plots should look like we first consider a few simple circuits. The impedance of a simple series combination of a resistor, R, and a capacitor, C, (as represented in the inset of Fig. 6.11a) would be:

$$Z = Z_R + Z_C = R - \frac{j}{\omega C} = Z' + Z'' \qquad (31)$$

Note that the real and imaginary components are directly separable. A Nyquist plot for such a circuit is shown in Fig. 6.11a. The result is a vertical line, the real part of the impedance, $Z'$, is frequency independent while the imaginary part, $Z''$ tends to zero at high frequency. The phase shift of a capacitor is *negative* with respect to resistors, thus the presentation convention is to plot the *negative* of the imaginary vs the positive real axis in the first quadrant, e.g. as in Fig. 6.11a. The total impedance, Z, is obtained simply by vector addition and the composite phase angle, $\phi$, by trigonometry is:

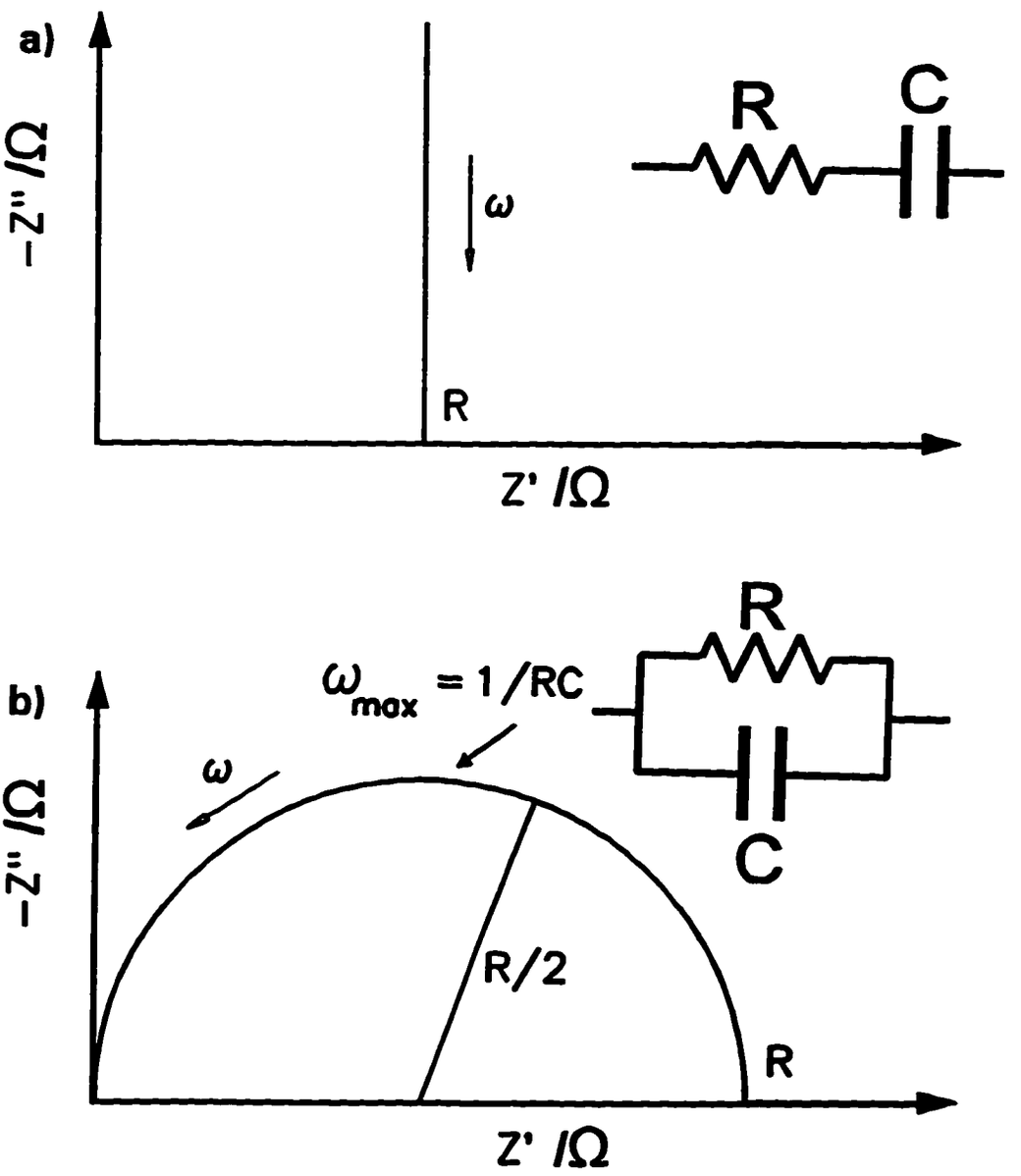


**Fig. 6.11.** Imaginary versus real impedance diagrams (Nyquist plots) for a resistor and capacitor **a)** in series; and **b)** in parallel. The insets illustrate the combinations.

$\tan\phi = X_C/R$. Note that the Nyquist spectrum for *one resistor* is just a single point on the real axis at a value equal to its resistance (for all frequencies) and for *one capacitor* it would be a vertical line on the Z″ axis (since it has zero real impedance).

The impedance of a parallel combination of a resistor, R, and a capacitor, C, (as represented in the inset of Fig. 6.11b) is calculated as:

$$\frac{1}{Z} = \frac{1}{Z_R} + \frac{1}{Z_C} = \frac{1}{R} + j\omega C = \frac{(1+j\omega RC)}{R} \tag{32}$$

The real and imaginary components are not directly separable in this result, but can be identified by rationalizing the numerator (multiplying top and bottom of Eqn 6.32 by the complex conjugate of the numerator) as in Eqn. 6.33:

$$\frac{1}{Z} = \frac{(1+j\omega RC)\cdot(-1+j\omega RC)}{R(-1+j\omega RC)} = \frac{-1-\omega^2R^2C^2}{R(1-j\omega RC)} \tag{33}$$

When the reciprocal is taken the result is:

$$Z = \frac{-R+j\omega R^2C}{-(\omega^2R^2C^2+1)} = \frac{R}{(\omega^2R^2C^2+1)} - \frac{j\omega R^2C}{(\omega^2R^2C^2+1)} = Z' + Z'' \tag{34}$$

and the real and imaginary parts are now separated. Both parts are frequency dependent and thus the form of the Z″ vs Z′ relation is not immediately apparent.

In order to get an idea of what this combination will look like on a Nyquist plot, we develop a relation between Z″ and Z′ by replacing $\omega$ amongst the terms of the last equality of Eqn. 6.34, first, in terms of Z′:

$$Z' = \frac{R}{(\omega^2R^2C^2+1)} \tag{35}$$

Cross-multiplication gives:

$$Z'\omega^2R^2C^2 + Z' = R \tag{36}$$

and therefore:

$$\omega^2 = \frac{R - Z'}{Z'R^2C^2} \tag{37}$$

Eqn. 6.37 can be substituted into the Z″ equality of Eqn. 6.34, this latter being squared before starting to avoid the inconvenient square-root that would result for $\omega$ from Eqn. 6.37. Thus:

$$Z''^2 = \frac{\omega^2 R^4 C^2}{(\omega^2 R^2 C^2 - 1)^2} = \frac{(R-Z')\cdot R^4 C^2}{Z' R^2 C^2}\cdot\left[\frac{(R-Z')}{Z' R^2 C^2}\cdot R^2 C^2 - 1\right]^{-2} \qquad (38)$$

$$= \frac{(R-Z')R^2}{Z'}\cdot\left[\frac{(R-Z')}{Z'} - 1\right]^{-2} = (R-Z')Z'$$

Cancelling common terms and then separating out $(R/2)^2$ reduces the expression to:

$$Z''^2 - RZ' + Z'^2 = 0 = Z''^2 - (Z' - R/2)^2 - (R/2)^2 \qquad (39)$$

which is simply the equation for a circle passing through the origin with diameter R, centered at R/2. The Nyquist spectrum for this is a semicircle shown in Fig. 6.11b.

Thus semicircles are observed for such parallel combinations from which R may be read directly from the diameter of the semicircle and C calculated from the semi-circle's maximum since $\omega_{max} = 1/RC$. RC is obviously the time constant for the given parallel combination. Since the a.c. technique is capable of scanning a very wide frequency domain, practically speaking about 8 or 9 orders of magnitude, it is often possible to resolve more complicated combinations of these RC circuits if their time constants are well separated. This is an elegant and important result since parallel and series/parallel resistor/capacitor combinations dominate the equivalent circuits of electrochemical interfaces.

Another phenomenon that gives rise to distinct behaviour in Nyquist plots is that due to diffusion of solution species involved in the electrode reaction. This so-called *Warburg impedance* is easily recognized in Nyquist spectra; it generally defines the low frequency limit of the impedance and gives a linear relation with a slope on Z″ vs Z′ of 45° (this is shown as part of Fig. 6.12b). Diffusion coefficients can be calculated from these impedance plots in the Warburg region. The Warburg line, of slope 45°, seems to tend to infinity as $\omega$ becomes smaller (see Fig. 6.12b), but actually will *ultimately* curve, either back down to the real axis for Faradaic reactions or for capacitive cells upwards giving a *vertical* line tending to infinity giving a so-called diffusional impedance, $Z_D$.

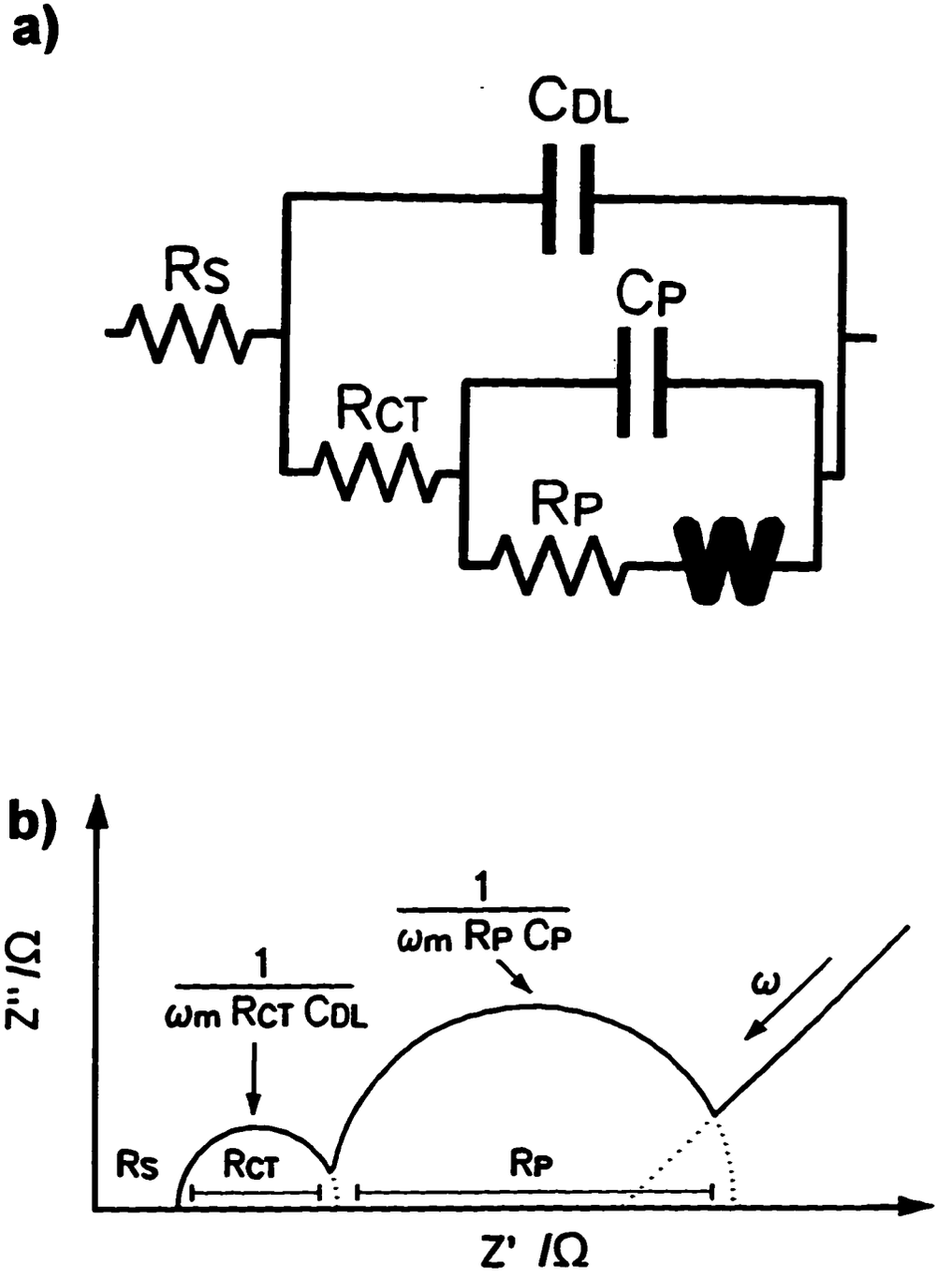


**Fig. 6.12.** **a)** Equivalent circuit used to describe a Faradaic reaction at an electrochemical interface, involving an adsorbed intermediate and a Warburg impedance. **b)** Hypothetical Nyquist plot for the equivalent circuit in "a" where the relative magnitudes of the branch's time constants were chosen to be well separated.

This diffusional impedance can be observed, under normal operating conditions when the diffusion length, L (i.e. the Nernst-layer thickness), is limited, as in special cases, e.g. along surfaces, into pores or through thin films, membranes or foils. It could be observed for diffusion in solution if the impedance was measured at low enough $\omega$ or if electrode rotation, which has the effect of reducing $L$ (as well as $R_D$) were to bring the impedance response into a normal frequency range (i.e. down to about 0.01 Hz). A relation for $Z_D$ [131,132] is:

$$Z_D = \frac{R_D \tanh\left(j\omega\frac{L^2}{D}\right)^{1/2}}{\left(j\omega\frac{L^2}{D}\right)^{1/2}} \qquad (40)$$

where $R_D$ is the diffusional resistance and D the diffusion coefficient of the electroactive species. This equation decribes a 45° line in a Nyquist plot that ultimately curves down to the real axis to give $R_D$. Electrode rotation has the effect of decreasing $L$ and $R_D$ within Eqn. 6.40 [132] which decreases the region of linear behaviour of this element and the value of $R_D$. Under *"semi-infinite" diffusion* conditions (in the absence of convection) only a 45° line is expected.

Practically speaking, the Warburg impedance will indicate whether diffusion controls the rate of an electrode reaction, where, depending on the relative rates of diffusion and reaction kinetics for the system, more or less of the frequency range will be occupied by the diffusive impedance, hence masking information on the kinetics of the underlying reaction. Usually, electrode rotation is employed to remove the Warburg impedance from the Nyquist plots and hence open up the kinetics of a reaction to study.

Solution resistance, $R_s$, significant in all practical electron and ion-conducting media, defines the high frequency limit of the impedance plot and when of modest magnitude ($< 50\ \Omega\,cm^{-1}$), behaves as a pure resistor. The solution resistance is generally added in series with all other circuit elements and simply shifts the kinetic spectra along the real, $Z'$, axis and hence can be read as the high-frequency intercept with this axis. When the solution resistance is large, however, as it can be in many non-aqueous media, poly-

mer, and solid electrolytes, etc., a so-called geometric capacitance, $C_G$ [133], arises in parallel with the solution resistance which gives an added semicircle at high frequencies.

In Fig. 6.12b all these elements are brought together in a hypothetical model for an electrochemical interface, the equivalent circuit of which is given in *a*. The circuit components represent aspects of the electrode reaction which include the solution resistance, $R_s$, a parallel combination of the double-layer capacitance and charge-transfer resistance across the interface, ($R_{CT}C_{DL}$), another parallel combination of a pseudocapacitance which is due to the potential-dependence of adsorption of an intermediate involved in the reaction and another charge-transfer associated with that adsorption, ($R_pC_p$), as well as an infinite Warburg impedance, (W), associated with diffusion of the reactants or products of the reaction from or to solution. The Nyquist plot for this system gives individual semicircles corresponding, for this hypothetical example, to well separated time constants for the double-layer and intermediate adsorption branches and a 45° line due to the Warburg component. As the d.c. polarization applied to the system is varied, as in a series of separate experiments, the Nyquist plot changes as the magnitudes of the charge-transfer resistances and capacitances vary, and possibly as the mechanism of the reaction changes with applied potential.

The use of these equivalents circuits for electrochemical systems does become complex, however, as systems become more complicated since it is known that *different* equivalent circuits can equally well represent the recorded impedance of a given electrochemical system, not to mention that some observed impedance features, for instance electochemical inductances or negative resistances, are difficult to conceptualize, but even so their use is an invaluable tool to help visualize the somewhat abstract results that the technique produces.

### 6.9.3. Pseudocapacitance Explained

The capacitance values of ideal electrostatic capacitors do not vary with potential, that is, the result of larger applied overpotentials would be the accumulation of proportionately larger charge ($C = dq/dE$) on the "plates" of the capacitor. The capacitance associated with the adsorption of some intermediate species involved in a multistep

reaction is, however, not ideal, but is a *special* type of capacitance, arising from an electron-transfer reaction. Due to the fact that the adsorption of species at interfaces is usually limited to a finite number of *available* sites on a substrate electrode, the potential-dependence of this capacitance is markedly different from that of the *double-layer* capacitance (for which there is no charge transfer) and hence the capacitance for an adsorbed intermediate is termed a *pseudocapacitance*, $C_p$.

The interesting potential-dependence of $C_p$ may be used to ascertain the involvement of adsorbed intermediates in electrochemical reaction mechanisms. It arises since the charge, q, that can be stored on this "pseudo-capacitor" is bounded by that ($q_m$) for, say, complete coverage by a monolayer of the adsorbed intermediate on the electrode substrate ($0 < \theta < 1$) and hence $q = q_m\theta$. The pseudocapacitance is thus described by:

$$C_p = q_m \frac{d\theta}{dE} \tag{41}$$

which is potential-dependent since $d\theta/dE$ is as well, described by the differential coefficient of an appropriate adsorption isotherm, e.g. Langmuir-ian or Frumkin-ian.

The essence of the potential-dependence of $C_p$ comes from the fact that most isotherms are "S"-shaped, asymptotically tending to zero and full coverages at low and high overpotentials, respectively. As an illustrative example consider the hydrogen evolution reaction (HER) at, for instance Pt where the reaction proceeds through the "discharge" of adsorbed hydrogen, $H_{ads}$. The recombination or electrochemical desorption step can be rate-limiting and thus under appropriate conditions a pseudocapacitance for $H_{ads}$ is observed because $\theta_H$ is dependent on potential; hence a $C_p$ arises as in Eqn. 6.41. An isotherm for the $H_{ads}$ coverage is shown in Fig. 6.13 in curve 2 (and the rhs axis). The $H_{ads}$ coverage varies with potential, hence also does the differential of its isotherm, $d\theta/dE$. Therefore a maximum arises at the point of the isotherm's highest slope and will tend to zero on either side of the maximum as the coverage fraction $\theta_H$ tends to either zero or unity as is shown by curve 1 (and the left axis) in Fig. 6.13.

This behaviour provides a means of identifying whether an adsorbed intermediate is involved at appreciable coverage in a given electrode reaction mechanism. Then,

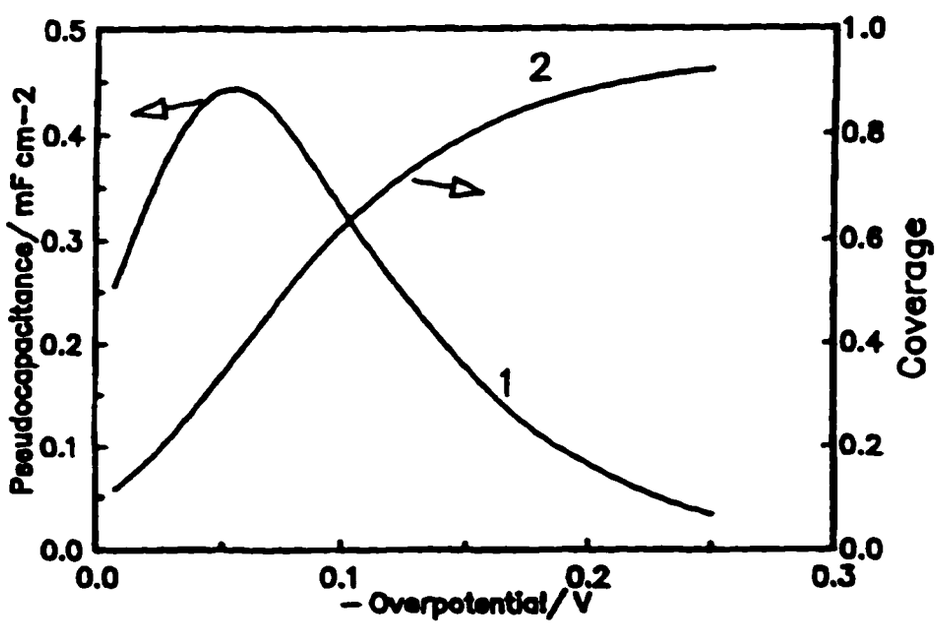


**Fig. 6.13.** Simulated plots of pseudocapacitance (curve 1) and $H_{ads}$ coverage (curve 2) versus overpotential for the hydrogen evolution reaction in base from [134].

depending upon the form of and the position along its isotherm (at a given d.c. polarization), complications can arise with respect to mechanism determination from Tafel slopes.

It is clear from the foregoing discussion that a series of a.c. experiments over an appropriate range of varying d.c. polarization potentials can give evidence as to the role of adsorbed intermediates. Thus behaviour showing a potential-dependent pseudocapacitance of shape similar to that for the HER at Pt (i.e. Fig. 6.13) is therefore necessary evidence for the role of adsorption of an intermediate in a given electrode reaction. An additional check of the nature of the pseudocapacitance is that the measured capacitance, easily calculated from Nyquist plots, should be of an order of magnitude consistent with the charge associated with the adsorption up to a monolayer (*ca.* 200 $\mu C\,cm^{-2}$ for each electron). In fact, the integrated value of a pseudocapacitance-potential spectrum should be equal to this monolayer charge. As a final remark, a complication may arise in practical circumstances and that is that at any potential, the RC time constants of processes involved for a given interfacial reaction can overlap, and so it is only from examination of values of the measured capacitances and charge-transfer resistances over a series of experiments at different d.c. polarizations that information on the kinetics and mechanism of a given reaction can be derived.

### 6.9.4. A.C. Impedance: Experimental Results

Nyquist plots from *a.c.* impedance measurements representative of the steady-state Al electrodeposition and dissolution reaction in the $Cl^-$- and $H^-$-rich hydride-baths are shown in Figs. 6.14 and 6.15, respectively, for applied negative overpotentials in *a*, and positive potentials in *b*, for electrodes rotated at 800 rpm. Note that the impedances have not been normalized to electrode area (0.002 $cm^{-2}$) and this is in order to demonstrate the relative values of the solution resistance that are involved; also the potentials shown in the legends are those before IR-correction. The frequency range for these spectra was from 500 kHz down to 0.05 - 0.1 Hz. All electrodes were rotated at 800 rpm.

### 6.9.5. Solution Element

A general characteristic of the impedance behaviour of all baths studied (e.g. Figs.

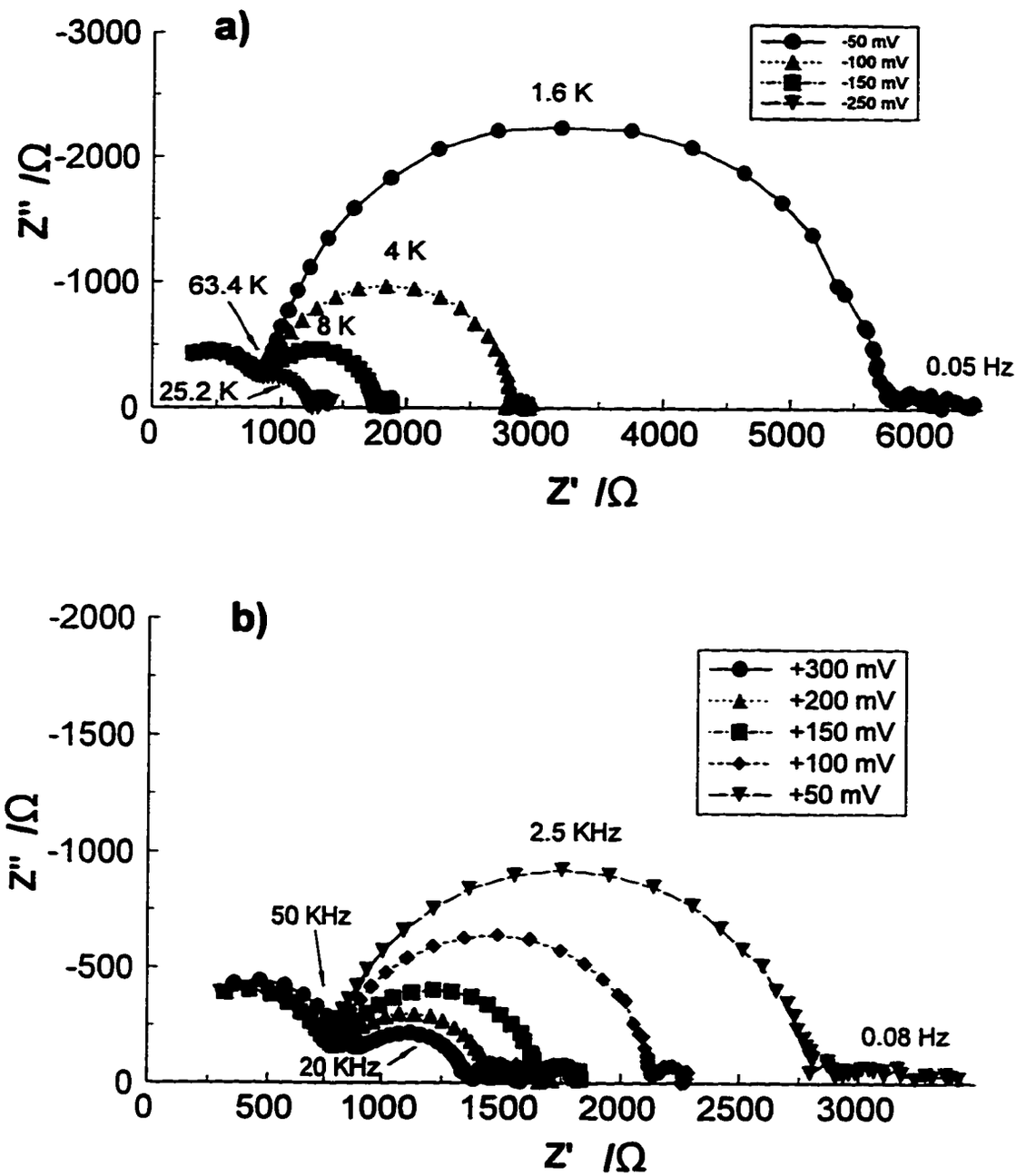


**Fig. 6.14.** Nyquist plot representation of the results of a.c. impedance in a Cl-rich bath, r = 3:1, $[Al]_{total}$ = 1.0 M for a) various cathodic d.c. polarizations; b) various anodic polarizations (see legends) from 500 kHz to 0.05 - 0.1 Hz at Al (deposited on 0.002 $cm^2$ Au) rotated at 800 rpm.

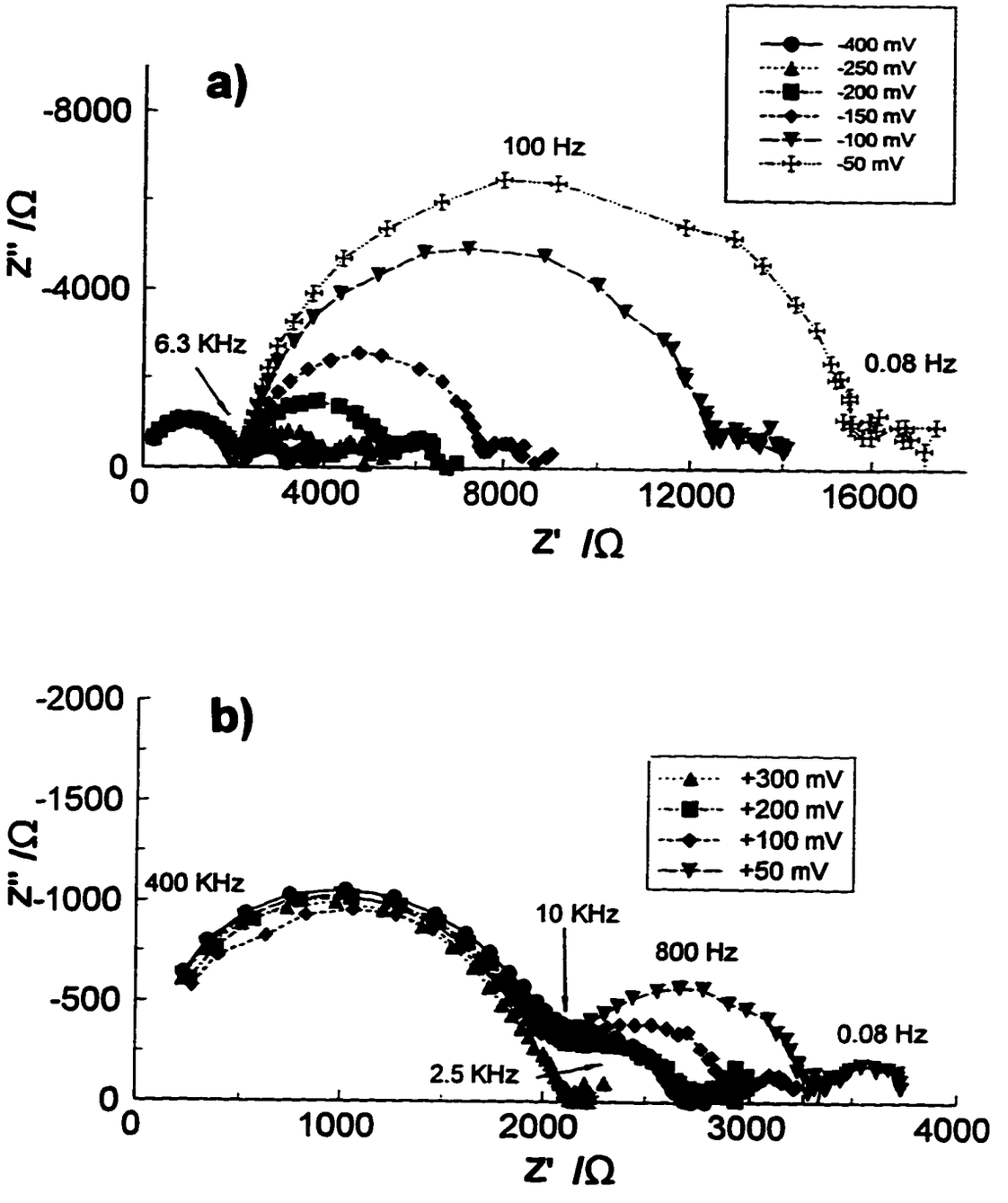


**Fig. 6.15.** Nyquist plot representation of the results of a.c. impedance in a H-rich bath, r = 1:2, $[Al]_{total}$ = 0.4 M for a) various cathodic d.c. polarizations; b) various anodic polarizations (see legends) from 500 kHz to 0.05 - 0.1 Hz at Al (deposited on 0.002 $cm^2$ Au) rotated at 800 rpm.

6.14 and 6.15) was a potential-independent semicircle starting from the high frequency limit of the spectra down to about 10 kHz. This "solution element" arises from the parallel combination of the solution resistance, $R_s$ and the solution geometric capacitance, $C_G$, where this latter is known to become significant for highly resistive media. The magnitude of $C_G$ was about $3 \times 10^{-7}$ F cm$^{-2}$ and was very nearly the same for all baths studied. $R_s$ (between working and reference electrodes in the cell) is determined from the low-frequency (high Z') intercept of this semicircle with the real axis and was about 800 Ω in this particular, $Cl^-$-rich bath ($[Al]_{total} = 1$ M), and *ca.* 2000 Ω in the $H^-$-rich bath ($[Al]_{total} = 0.4$ M). The slight increase of $R_s$ with potential in the $Cl^-$-rich bath (Fig. 6.14), but only at anodic potentials (in *b*, cf. *a* and *b* at the high Z' end of the solution element semicircle) is perhaps a consequence of local conductivity changes. The Al electrodissolution reaction involves coordination of free ionic ligands which results in a decrease in the number-density of ions (which are of low relative proportion to begin with in $Cl^-$-rich baths) in the immediate vicinity of the working electrode.

### 6.9.6. Charge-Transfer / Double-Layer Element

At lower frequencies a potential-dependent semicircle was observed in all spectra. This semicircle is attributed to the parallel combination of $R_{CT}$, the charge-transfer resistance for the reaction, and $C_{DL}$, the double-layer capacitance of the interface. The reciprocal of $R_{CT}$ should be proportional to the actual rate of the reaction and hence that measured in a Tafel polarization experiment. Figs. 6.16*a* and *b* show a comparison, between log $[1/R_{CT}]$, as derived from the potential-dependent semicircles in Figs. 6.14 and 6.15, and the *d.c.* log $[i_{ss}]$ (i.e. steady-state current-density) versus potential (Tafel) relations for the same baths, respectively. The potential-dependence of $1/R_{CT}$ and $i_{ss}$ (in *a* and *b*) correspond quite well, although there was some scatter and variance for the anodic branch data of the $H^-$-rich bath. Recall that $R_{CT}$ and $i_{ss}$ values are related through Eqn. 6.13, i.e. $R_{CT} = 1/fi_{ss}$.

From the potential-dependent semicircles in Figs. 6.14 and 6.15 $C_{DL}$ values can be calculated and are plotted, normalized to the *apparent* electrode area, as a function of

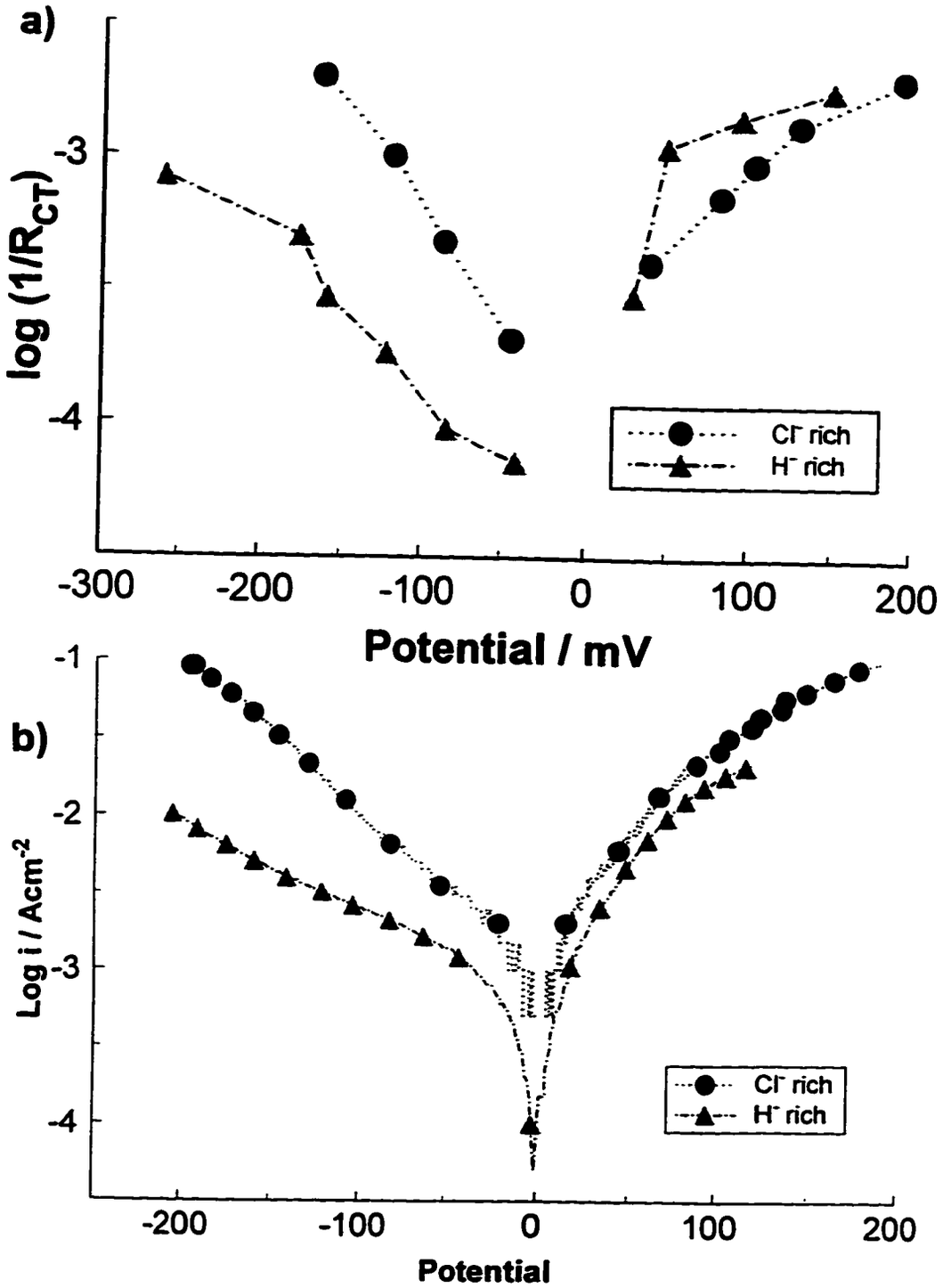


**Fig. 6.16.** A comparison between *a* and *b*, where a) are Tafel-like semi-logarithmic plots of the inverse of the resistance associated with the potential dependent semi-circles in Figs. 6.14 and 6.15 ($Cl^-$- and $H^-$-rich baths); and b) the actual recorded Tafel plots for the same baths.

potential in Fig. 6.17a. An interesting difference between $Cl^-$-rich and $H^-$-rich baths is clear: $C_{DL}$ increases substantially from *negative to positive* potentials in nearly all the $Cl^-$-rich baths studied but, contrary to this, from *positive to negative* potentials in the $H^-$-rich baths. The relative change of $C_{DL}$ was markedly larger in the $H^-$-rich baths (cf. *lhs* and *rhs* axes in Fig. 6.17*a* and *b*). These contrary trends between bath types for this potential-dependent loop were observed for all the experimental data for the hydride-bath and in Fig. 6.17b is shown the potential-dependence of $C_{DL}$ for five other hydride-baths of various compositions. The shapes of the $C_{DL}$ trends for the bath types are essentially the same, although their values did differ.

### 6.9.6.1. Double-Layer Capacitance

$C_{DL}$ can be readily evaluated from the Nyquist plots in Figs. 6.14 and 6.15 at the various potentials examined. The so-called double-layer "capacitor" refers to the assembly of a metal electrode, whose charge is variable by applied potential, being considered as one "plate" of the capacitor and the arrangement[d] of ions, other solutes and solvent dipoles in solution that compensate the charge of the metal electrode, as the other plate. The differential capacitance (by convention this is always an area-normalized value; in $F\,cm^{-2}$ and $F \equiv q/V$) of this double-layer depends, as does that of "hardware" capacitors, on the area of the plates (A), the dielectric constant ($\varepsilon$) of the region separating the "plates" of the capacitor and the distance (d) between them in metres by:

$$C = \frac{C'}{A} = \frac{\varepsilon \varepsilon_o}{d} \qquad (42)$$

where $\varepsilon_o$ is the permittivity of vacuum ($8.85 \times 10^{-12}\ F\,m^{-1}$) and C′ the measured capacitance. For the electrochemical double-layer capacitor the inter-plate region is described by a single layer (*primary layer*; see footnote *d*) of solvent molecules immediately

---

[d] The structure of the double-layer is assumed to conform to that of an established model [89:Chp.3], based on careful studies of double-layer capacitances. That of Devanathan, Bockris and Müller (DBM) [135] assumes a layer of solvent molecules immediately adjacent to the metal (*primary* layer), a secondary solvent layer, then the "Gouy" plane which is the closest that solvated cations can approach, i.e. not even their solvation spheres contact the metal surface directly. Anions are assumed unsolvated and therefore can contact the metal surface directly.

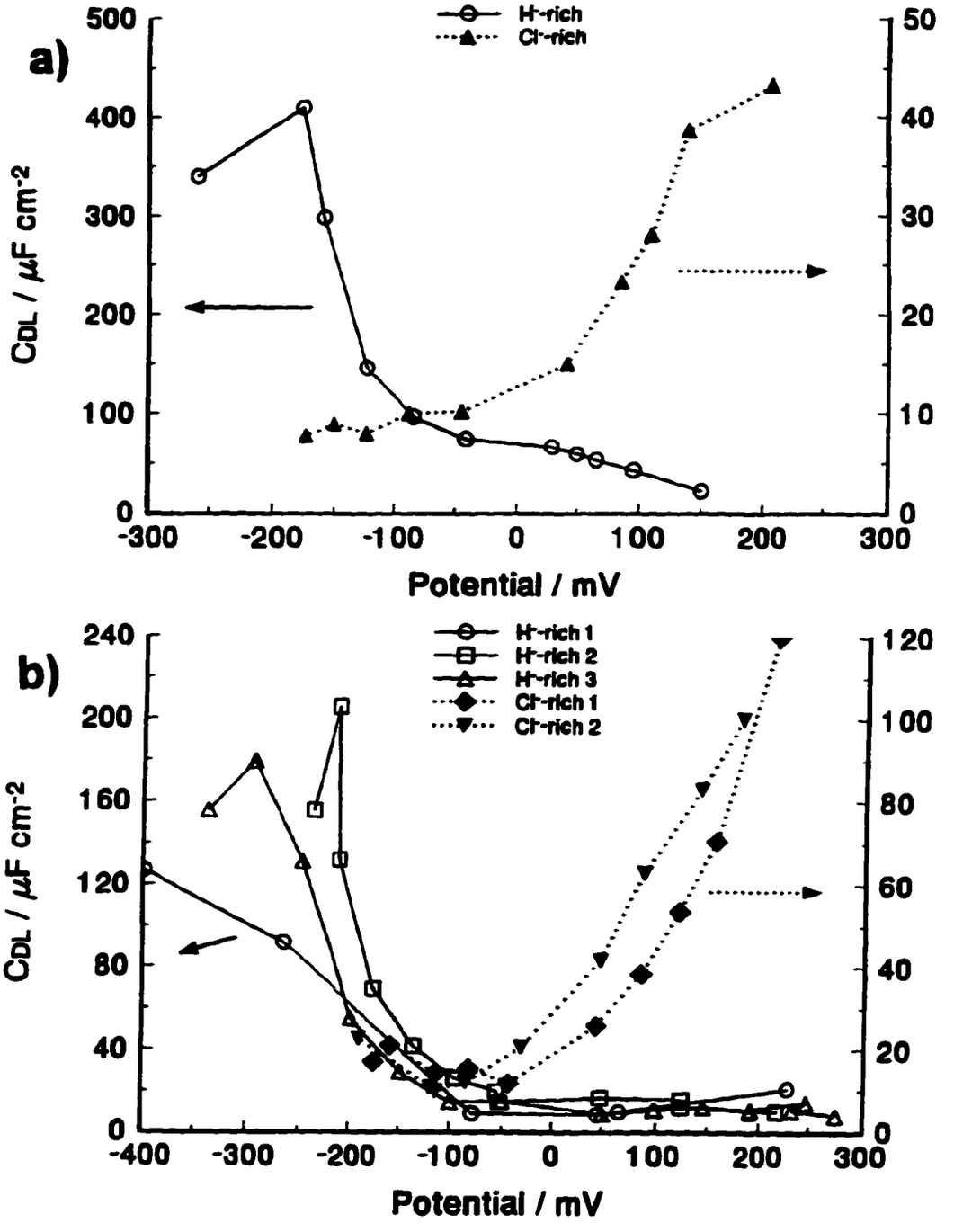


**Fig. 6.17.** Apparent double-layer capacitance ($\mu F\,cm^{-2}$) as a function of applied (IR corrected) potential for **a)** baths in Figs. 6.14 and 6.15 (▲ $Cl^-$-rich: r = 3:1, 1.0 M; ○$H^+$-rich: r = 1:2, 0.4 M); and **b)** for other baths of the following compositions, ○$H^+$-rich 1: r = 1:4.4, 0.33 M; □$H^+$-rich 2: r = 1:3, 0.3 M; ▲ $H^+$-rich 3: r = 1:1.5, 0.4 M; ◆ $Cl^-$-rich 1: r = 2.7:1, 0.8 M; ▼ $Cl^-$-rich: r = 2.3:1, 1.0 M.

adjacent to the metal interface.

The dielectric constant is a measure of a material's susceptibility to development of charge separation in a field and is a function of solvent polarity; e.g. a material with a larger dielectric constant would reduce the force between charges to a greater extent. A significant contribution to this effect comes from the randomness of orientation of the individual electric dipoles of the material. Water exhibits significant intermolecular structure (e.g. H-bonding) which has the effect of maintaining a random dipole orientation even in a field and thus has a high dielectric constant of 78.8 (at 298 K) relative to most other solvents at room temperature. In strong fields, as in the double-layer, this dipole orientation can approach "saturation" giving rise to the "saturation" value for the solvent dielectric constant which is much less than its randomly-oriented bulk value, for instance that for dielectrically saturated water is $\sim 6$ (cf. 78.8 in the bulk).

The magnitude of the $C_{DL}$ will vary between different solvents with their dielectric constants, both the bulk and saturation values of the medium. The minimum double-layer capacitance, e.g. at Hg, in water ranges from 18 - 50 $\mu F\,cm^{-2}$ at the potential of zero charge (pzc) and is known to depend on substrate and electrolyte [136,137]. The $C_{DL}$ in non-aqueous solvents has been less well characterized and, in fact, no literature values for thf were found. Its $C_{DL}$ would not be expected to be unlike that of other organic solvents whose values at the pzc (e.g. for Hg) are $\leq 10\ \mu F\,cm^{-2}$ [138], and is probably around 1 - 5 $\mu F\,cm^{-2}$ given its low dielectric constant.

$C_{DL}$ always shows a potential-dependence; ions from solution, attracted by the imposed charge on the metal side of the interface, whether specifically adsorbed at the interface or positioned in the Gouy layer (of the DBM model; see footnote *d*), disrupt the solvent dipole "saturation" at the interface as these primary layer molecules reorient to solvate the incoming ions instead of the interface. This increases the dielectric constant in this region and, in turn, the capacitance of the interface according to Eqn. 6.42. The magnitude of this variation in water, where the difference between the bulk and primary layer dielectric constants for water (78.5 to 6, respectively) is typically $\leq 50\ \mu F\,cm^{-2}$ in 1:1 electrolytes for potential excursions of about 0.5 V. Thf, with bulk $\varepsilon$ of 7.8, would

not be expected to give rise to as large a change as observed for water.

### 6.9.6.2. Variation of the Double-Layer Capacitance in the Hydride-Bath

A number of factors can contribute to a variation of the measured double-layer capacitance; the thickness (d) and dielectric constant ($\varepsilon$) of the double-layer, from Eqn. 6.42, and additionally, since $C$ is an extensive quantity, it also varies with the actual interfacial area. The thickness of the double-layer, defined in this case by the thickness of a thf molecule (for the primary layer), could be envisaged to change if the orientation of these molecules at the substrate interface were to change from an end-on interaction to one where thf laid flat, but that this could give a major contribution to the potential-dependence of the $C_{DL}$ is inconsistent with the asymmetry of the $C_{DL}$ trend observed (Fig. 6.17) and the fact that the trend was so very different in the two bath types. The very large difference between bulk and saturation dielectric constants for water explains the significant variation of $C_{DL}$ with potential in that solvent, but this effect will not be large for thf, the bulk dielectric constant of which is small (7.8). Even if this "saturation" effect was significant it should have been observed, if not necessarily to the same extent, on both sides of the pzc, but as seen in Fig. 6.17a this is clearly not the case.

The electrochemical deposition and dissolution reactions of Al being studied here undoubtably introduce a significant and continuously varying surface roughness and thus electrode area due to electrocrystallization of Al. This surface roughness is indicated from deposit morphology examination (§8.9.6). The electrode area used for normalization of the measured capacitances was in all cases the *apparent* area value for the underlying polished substrate and thus all capacitance values are *apparent* capacitances. A varying surface roughness of the deposits can explain the comparatively different magnitudes of $C_{DL}$ between separate experiments for given bath types (i.e. either $Cl^-$- or $H^-$-rich), as in Fig. 6.17b. Larger, but unknown, *real* areas would result in larger, overestimated, capacitances based on *apparent* areas.

Even though different baths gave varying apparent capacitances the trends in potential-dependence were similar for the bath types. The morphologies of phases depos-

ited at different rates or overpotentials can be quite different, for instance a greater degree of deposit roughness can sometimes be expected at higher rates. This potential-dependence, while perhaps accounting for some error in each point and between experiments, would not be able to explain the distinct trends in the behaviour of the two bath types, since increasing roughness with rate might be expected to be observed for both plating *and* stripping directions, not one preferentially. We note, however, that anodic dissolution can be used in some cases to smooth electro-deposits that are initially very rough, for instance in reverse pulse-plating [139] the basis of which is the application of short stripping pulses in a plating pulse-cycle and this is known to significantly smoothen deposits. However, this is not an important point in the present case, because the morphologies of Al deposits (Chapter 8) from the hydride-bath did not show the asperities of high area (such as dendrites) that are typical of deposits that can be anodically smoothed. Smoother deposits on the anodic potential side would give smaller electroactive surface areas which should have resulted in a decreasing trend in apparent $C_{DL}$ with increasing positive potential and this should have been observed for *both* bath types but, as was noted in Figs. 6.17*a* and *b*, the two baths showed behaviour inverse to one another.

An estimate of the $C_{DL}$ in thf, consistent with its low dielectric constant and known values of $C_{DL}$ for closely related solvents [137], would be *ca.* 5 $\mu F\,cm^{-2}$. Normalizing the $C_{DL}$-potential curves in Fig. 6.17b by equating the minimum $C_{DL}$ value for each curve to this estimated minimum gives maximum differential capacitances (within the potential region studied) close to 100 $\mu F\,cm^{-2}$ for the negative potential side for the $H^-$-rich bath and between 30 and 50 $\mu F\,cm^{-2}$ for the positive potential side for the $Cl^-$-rich bath. The magnitude and trend of the variation of capacitance observed in the $H^-$-rich bath cannot be explained by the structure double-layer in these solutions.

At about 100 $\mu F\,cm^{-2}$ for the maximum, this capacitance value is consistent with that for a pseudocapacitance associated with an electro-adsorption process. It is possible that a pseudocapacitive process could be superimposed upon the double-layer if the two individual "RC" time-constants for these were closely matched. The presence of a pseudocapacitance suggests an electron-transfer / electro-adsorption step, in quasi-

equilibrium, being rate-limited by a following *rds*. This reaction mechanism is, however, inconsistent with the results of the Tafel slope analysis for the Al deposition reaction given in §6.7 in that a mechanism involving a prior electro-adsorption step (for which the above mentioned pseudocapacitive element would be observed) should have given a cathodic transfer coefficient of 3/2 (i.e. quite large) instead of the 1/3 obtained for the $H^-$-rich baths (§6.7.2). In the $H^-$-rich baths (solid lines and data points in Fig. 6.17b), the pseudocapacitance at negative overpotentials could arise from an adsorption involved in the Li deposition reaction which has been shown to occur at these potentials in hydride-baths of this composition (§6.3.1 & §6.4.1).

For the $Cl^-$-rich bath, $C_{DL}$ increases with increasing positive potentials, but this variation was smaller than that observed in the $H^-$-rich bath (towards negative overpotentials), cf. lhs and rhs axes in Fig. 6.17. These baths have low concentrations of dischargeable anions, but, as was demonstrated in the analysis of the composition of the hydride-bath in §5.5, a significant excess of $Cl^-$ as $AlCl_4^-$ (a species from which Al is not depositable). We might draw an analogy to the known behaviour of $Cl^-$ at Hg [136] where a specific adsorption interaction between the anion and the electrode occurs. Because of the specific interaction, the number of anions at the metal surface would be in excess of that required to compensate the charge on the metal, which then requires a commensurate excess of cations in the neighbourhood of the electrode for electrical neutrality. The end result of this situation is that the double-layer stores more charge and hence gives larger capacitance values. This affect would only be observed at positive overpotentials where $Cl^-$ would be attracted to the Al substrate. The magnitude and trend of $C_{DL}$ is not consistent with a pseudocapacitive element.

### 6.9.7. Low Frequency Element

At low frequencies another element ($C_{LF}R_{LF}$) that was slightly potential-dependent was observed in the results for the two baths shown in Figs. 6.14 and 6.15. The apparent differential capacitance values associated with this process were very large, $> 0.10$ F cm$^{-2}$ and hence are *not* consistent with values possibly associated with a pseudocapacitance. Additionally, the $C_{LF}$ did not vary considerably with potential, although, since

small, the semicircles from which they were calculated were not well resolved.

It is to be noted that the low frequency element was observed only when the working electrode was rotated. In the absence of electrode rotation an infinite Warburg impedance ("infinite" in terms of the frequency range studied) was observed at elevated potentials, both positive and negative, which masked the low frequency region of the impedance of the Al deposition reaction in the hydride-bath. It is therefore possible that this low frequency element (observed for rotated electrodes) corresponds to a *finite* Warburg (i.e. Eqn. 6.40) and hence to the diffusion of species across a finite Nernst-layer. Although some kind of diffusion process is present, we must emphasize that it is the kinetics of the electrode reaction that determine the rate of the overall reaction in the first 200 mV on either side of $E_r$ in the hydride-bath.

### 6.9.8. Conclusions from the A.C. Experiments

A.C. impedance analysis has identified a number of equivalent RC components in the behaviour of the hydride-bath system: 1) at high frequencies a geometric capacitance and solution resistance (the geometric capacitance was found to seriously skew the results of potential-decay experiments, which is an alternate technique for characterizing electrode reactions involving adsorbed intermediates [140,141]; 2) at intermediate frequencies, the double-layer capacitance and charge-transfer resistance which demonstrated a marked potential-dependence; and 3) at low frequencies, another RC process for which the differential capacitance was not consistent with any electrochemical process at a working electrode, but could be due to solution diffusion.

The above discussion confirms that the experimental Tafel measurements and associated analysis of the mechanism of Al deposition in the hydride-baths are indeed valid, as derived from slopes of logarithmic polarization curves within potential regions generally less than 200 mV from $E_r$. The absence of pseudocapacitive elements attributable to an Al intermediate in either cathodic or anodic reaction directions proves that Al deposition and dissolution involves *neither* prior nor following electron-transfers. This is an important general conclusion.

## 6.10. Electrochemical Mechanism and Concluding Remarks

The results of experimentation on the hydride-bath suffered from problems of reproducibility throughout the work described here. It was only through the careful consideration of a large body of experimental results that it has been possible to reach significant conclusions on the kinetics and mechanism of the Al deposition reaction.

The arguments of §6.7.5 enabled it to be concluded that the same transition-state applies to both anodic and cathodic directions of the Al deposition reaction in the potential region from which Tafel slopes and hence meaningful kinetic data could be derived. A part of the basis for this conclusion was the lack of any observed inflection points in back-reaction corrected Tafel plots (particularly at low overpotential). The presence of an inflection point would have indicated a shift of rate-controlling steps from the equilibrium situation ($\eta = 0$) where a single transition-state *must* control both reaction directions and the non-equilibrium ($\eta \neq 0$) one where different forward and reverse rate-controlling steps could prevail.

The stoichiometric number was determined (on the basis of the assumption of a single transition-state) to be *three* for all bath compositions (§6.7.3 and Table 6.3). The values of the measured Tafel slopes were all near to that expected for a single electron-transfer step, neither preceded nor followed by any other non-rate-limiting electron-transfer steps, that is 118 mV dec$^{-1}$. The presence of any such quasi-equilibrium electron-transfer steps would lead to Tafel slopes of at most 39 mV dec$^{-1}$ (60 mV dec$^{-1}$ if the *rds* was a chemical step) and slopes as low as this were never observed in the present work.

The impedance results for the Al deposition and dissolution reaction indicated that within the potential region for which Tafel slopes were calculated, and hence a mechanism was derived (up to *ca.* 200 mV), there were no capacitive elements that were consistent with appreciable coverage by an adsorbed Al intermediate. Markedly different (in fact, opposite) potential-dependencies of the double-layer capacitance were noted between the $Cl^-$-rich and $H^-$-rich baths. In the $Cl^-$-rich bath the changing $C_{DL}$ was associated with the known effect a specific $Cl^-$ interaction has on $C_{DL}$ (§6.9.6.2). In the $H^-$-rich bath a very significant potential-dependence was attributed to a pseudocapacitance that overlap-

ped the $C_{DL}$. It was concluded that this pseudocapacitance was associated, not with the Al deposition reaction but with the parallel Li deposition reaction that had been shown to occur in the $H^-$-rich baths (§6.3.1, §6.4.1 and §6.4.3). The absence of pseudocapacitances associated with the Al reaction confirmed and validated the Tafel slope measurements and resulting mechanistic analyses reported here, that might otherwise have been seriously influenced by the necessity of taking into account an isotherm for an adsorbed intermediate. The specific nature of this influence is that the assumed F/RT (or $\gamma = 1$ to $\alpha$ [see Eqns. 2.34i and ii]) contribution to the potential-dependence of reaction rate for each quasi-equilibrium electron-transfer step would have become smaller the further we were along the isotherm of a given adsorbed intermediate (which would be defined by the particular steady-state $\eta$) to the limit of zero as $\theta \rightarrow 1$. In fact, only at low $\theta$ does $\gamma = 1$ so that Tafel slopes can be directly related to the actual reaction mechanism (see §2.5.1).

Given that prior and following electron-transfers have been proved to be absent in the mechanism of the Al deposition reaction, all three electrons must be transferred in a thrice repeated *single* step, which, since $\nu$ was determined to be three (§6.7.3), suggests the following as the only possible mechanism:

$$\begin{aligned} 3[AlX_3 \; + \; e^- \; &\rightarrow \; M\text{-}AlX_2 \; + \; X^-] \\ 3M\text{-}AlX_2 \; &\rightleftarrows \; M\text{-}Al \; + \; 2AlX_3 \end{aligned} \qquad (43)$$

a thrice occurring electron-transfer as rds followed by a facile chemical disproportionation of three $Al^{2+}$ intermediates. Although the disproportionation might seem entropically disfavoured, this step would actually be quite facile given the inherent instability of subvalent Al species (see §1.3).

The transfer coefficients for the Al deposition reaction from the hydride-bath between its compositional extremes varied from $\alpha_c = \alpha_a = 1/2$ in $Cl^-$-rich baths to $\alpha_c = 1/3$ and $\alpha_a = 2/3$ in $H^-$-rich baths. From the detailed analysis of the link between mechanism and Tafel slopes given in Chapter 2 we have proved that the change in mechanistic parameters between $Cl^-$-rich and $H^-$-rich baths could only be due to a variation of $\beta$, the symmetry factor of the transition-state of the rds and not due to a shift in mechanism as has been suggested [39,40]. Further discussion of the significance of this

fact on the mechanism of Al deposition from the hydride-bath must await a brief development of $\beta$ in the next chapter.

# Chapter 7 Symmetry Factor for Processes in the Hydride-Bath

## 7.1. Foreword

The mechanism of Al deposition from the hydride-bath, evaluated from steady-state polarization measurements and discussed in Chapter 6, involves a thrice occurring electron-transfer followed by a chemical disproportionation. Significantly, a variation of the measured kinetic parameters was noted in the electrochemical investigation between compositional extremes of the hydride-bath and this we have attributed to a changing symmetry factor, $\beta$. In this brief chapter will be described what is, in fact, the physical significance of $\beta$ and what its variation for the Al deposition reaction in the hydride-bath means. Note that it is not the intention here to give an exhaustive survey of the interpretations of the symmetry factor, but to develop an explanation for phenomena observed in the work on Al deposition.

## 7.2. Physical Definition of $\beta$

Recall that $\beta$ arises in the exponential terms of the Butler-Volmer rate equation in Chapter 2 (Eqn. 2.20):

$$i_{net} = i_o\left(\exp\left[z_{rds}(1-\beta)f\eta\right] - \exp\left[-z_{rds}\beta f\eta\right]\right) \quad (1)$$

and is the fraction of the applied overpotential, $\eta$, that affects the rate of the *forward* cathodic reaction. $\beta$ is a parameter central to electrochemistry, describing the influence of potential on the overall rate-limiting transition-state of a reaction. It should not be confused with $\alpha$, the transfer coefficient, which, as was explained in Chapter 2, is a composite term that includes $\beta$. For most electrochemical reactions $\beta$ is usually assumed to be equal to 1/2, and interestingly, it was accepted as such early on in the history of the development of electrochemical kinetics even before any conceptual basis for the assumption existed [142]. $\beta$ has the same kind of significance as the Brønsted factor in linear Gibbs energy relationships, e.g. for acid-base reactions [143].

The physical meaning of $\beta$ and how it relates to the physico-chemical properties of the reacting species involved in a given electrochemical reaction depends largely upon the model of the rate-limiting transition-state we choose to adopt. $\beta$ is not completely understood and is often accepted, rather uncritically, as equal to a value around 1/2.

The usual starting point from which a conceptualization of $\beta$ is drawn is the definition of the transition-state limiting the rate of a given reaction. We consider the electron-transfer reaction used as the basis of the kinetic development in Chapter 2 (§2.4), namely the electrodeposition (or electro-adsorption) of a metal atom A onto a substrate M from a solution species $A^+$ coordinated by ligands, $L^-$:

$$M(e^-) + A^+\text{-}L^- \rightleftarrows M\text{-}A + L^- \qquad (2)$$

The energetic course of such a reaction is usually described by potential-energy (PE) curves for the reactant, the metal *ion*, $A^+$, bound to a ligand[a] (the lhs of Eqn. 7.2) and the product, the metal *atom*, $A^0$, bound to the substrate surface (as on the rhs). The transition-state is accepted as the point (or region) of intersection of these two curves which is the optimal point of elongation of the metal ion-ligand or metal atom-substrate bond, where electron-transfer or tunnelling can occur and the respective energies required for these "optimum" stretches of either product or reactant define the heights of the activation energy barriers for either reaction direction.

Regardless of whether these PE surfaces are defined by Morse-like [88] curves for the vibrations of individual bonds as in the classical model [93] (and as was illustrated in Fig. 2.1) or as the summation of energy vs reaction coordinate contributions for the ion (solvation and ionization), atom (adsorption to substrate surface and repulsion from polar solvent) and electron [86:pp.959-973], $\beta$ will be defined in the same way, arising from the relation of applied overpotentials to the effect they have on the activation energy barrier of a given reaction and hence on its rate.

An applied overpotential across the reaction interface has the effect of shifting the

---

[a] Note that the ligand, written as $L^-$ here and in Eqn. 7.2, in this electron-transfer decomplexation reaction will often be an uncharged (solvating) solvent molecule.

PE curve of the reactant, $A^+$-$L^-$, with respect to the product, M-$A^0$. The effect that this shift has upon the height of the activation barrier is, of course, defined by $\beta$, the symmetry factor, so-called because it is a geometric factor, considered a measure of the relative slopes of reactant and product PE surfaces. A $\beta$ of 1/2 means that one half of the applied $\eta$ decreases the energy barrier of one direction of the reaction while the other half, $1-\beta$, increases the energy barrier to the other. The value of $\beta$ can be put on a more quantitative footing by analyzing the relationship between $zF\eta$ and $\Delta_\eta\Delta\bar{G}^{\circ\ddagger}_-$ or $(\Delta\bar{G}^{\circ\ddagger}_{\eta\neq 0}-\Delta\bar{G}^{\circ\ddagger}_{\eta=0})$, i.e. the cathodic activation energy. It is not easy to directly compare these quantities or the physical significance of $\beta$ from PE diagrams such as Fig. 2.1 and so analysis relies on linearized PE diagrams or, at least, linearization near the transition-state region, such as in Fig. 7.1. The reactant surfaces in the absence (solid curve) and presence of an applied overpotential (dashed curve) are shown in Fig. 7.1 along with the respective *cathodic* barrier heights. The substrate electrode (M) and ligand ($L^-$), this latter positioned just outside the OHP, (see Fig. 7.1) are considered frozen in place and the depositing metal ion/atom is assumed to move from one to the other.

On the basis of the simplifying assumptions that the slopes of these curves do not change with $\eta$ and that the relative positions of these curves do not move, i.e. based upon the position of the OHP (see Fig. 2.1 and §2.4.2), simple, if a little involved, trigonometry [86:p.922] can express $\beta$ in terms of characteristics of the reactant and product PE curves. Where $\theta$ is the angle of the PE surface of the reactant with respect to the reaction coordinate axis (see Fig. 7.1) and $\phi$ that for the product adsorbed on the substrate surface, the change in cathodic barrier with overpotential is given by:

$$\Delta_\eta\Delta G^{\ddagger}_- = \left(\frac{\tan\theta}{\tan\phi+\tan\theta}\right)zF\eta \qquad (3)$$

where the term in parentheses is $\beta$.

In Fig. 7.1, the PE surface of the product is more *acute* (or conversely less *obtuse*) in aspect than the reactant surface and hence represents a stronger bond than that

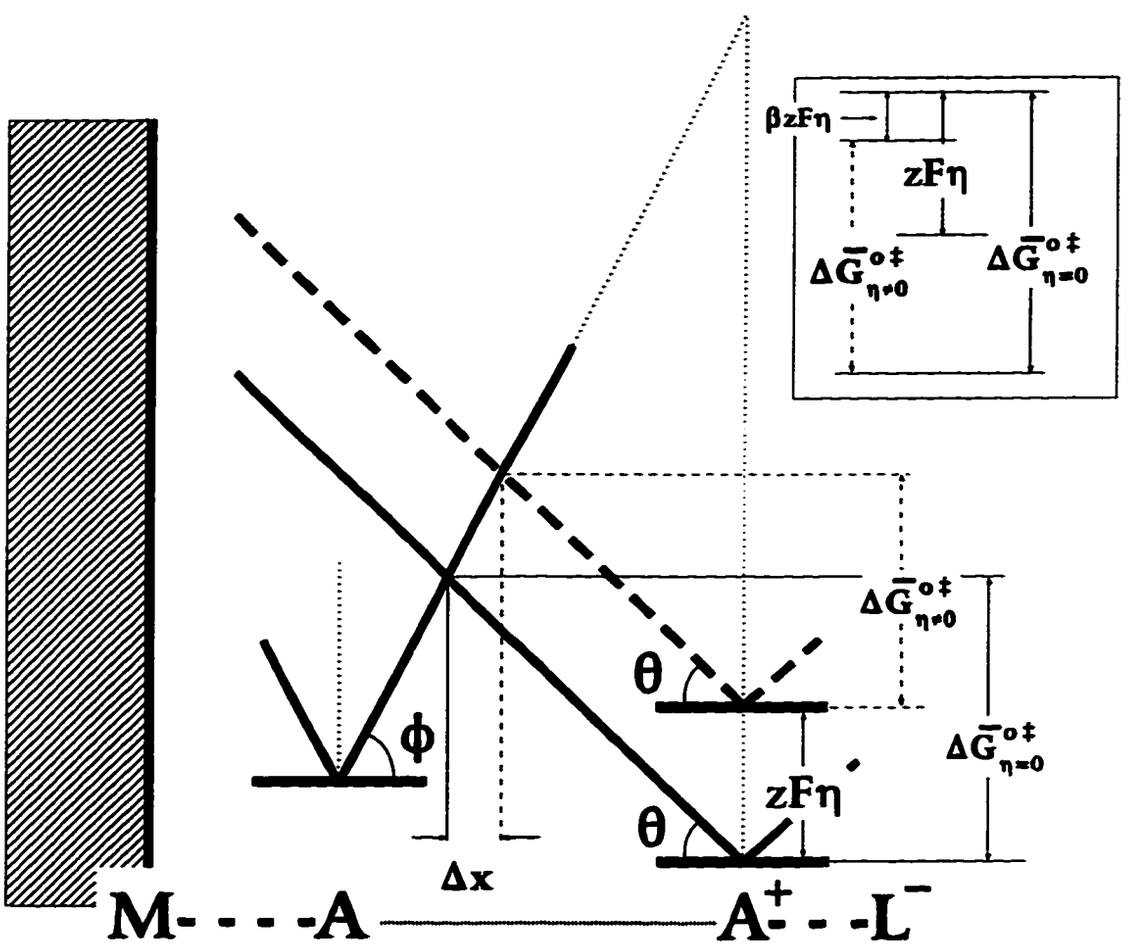


**Fig. 7.1.** A linearized potential-energy diagram showing the course of an electrochemical reaction. Reactant curves in the absence and presence of an applied overpotential (solid curve [$\eta = 0$], dashed curve [$\eta \neq 0$]) are shown. The magnitude of the *cathodic* activation barriers in the presence, $\Delta\bar{G}^{o}_{\eta\neq0}{}^{\ddagger}$, and absence, $\Delta\bar{G}^{o}_{\eta=0}{}^{\ddagger}$, of the applied $\eta$ are shown and redrawn in the inset box to scale in such a way as to compare their difference due to the applied $zF\eta$.

of the reactant. This situation corresponds to $\beta < 1/2$. Owing to the varying points of reference of the quantities illustrated in Fig. 7.1, comparison of the energy due to the applied overpotential, $zF\eta$, and the resulting change of the cathodic activation barrier, $\Delta_r\Delta\bar{G}^{\circ}_{-}{}^{\ddagger}$, is not particularly clear, therefore these quantities (as represented by the lengths of the drawn lines in Fig. 7.1) have been redrawn in the inset box and aligned to illustrate the fraction $\beta$ of the applied overpotential that ends up modifying the height of the cathodic energy barrier. The reverse oxidation is affected in the opposite way to that of the reduction reaction and the fraction that modifies the anodic barrier height is hence $1-\beta$ (or $\tan\phi/[\tan\phi + \tan\theta]$).

In order for the above trigonometry to hold and hence for $\beta$ to be constant, the slopes and relative positions of the reactant and product curves must not change with applied overpotential. Whether there is support for this or not seems to depend on the system involved; for instance, $\beta$ is known to vary little over a wide range for the hydrogen evolution ([144] and references therein) and the oxygen evolution reactions, while for the reduction of nitro-compounds in non-aqueous solutions a significant change with potential is observed [145:p.276]. Note that if the intersection that defines the transition-state were to occur near to the zero point energy of one of the curves (e.g. in the case of either so-called barrierless or activationless kinetics [145:p.278]), a change of $\beta$ with overpotential would be anticipated on the basis of this model since the slope near the base of a PE surface changes quite significantly with potential. This is demonstrated in Fig. 7.2 by the drawn tangent lines for intersection of the PE curves progressively closer to one of their zero point energies. It is often difficult to observe this effect experimentally since, for the high applied potentials necessary, solution diffusion is, in many cases, then rate-limiting. Additionally, it is conceivable that the changing electric field present at the electrified interface could affect the position of charged species with respect to the OHP.

Another closely related interpretation for $\beta$ is based upon the parabolic potential function of harmonic oscillators [145:p.275,145]; then:

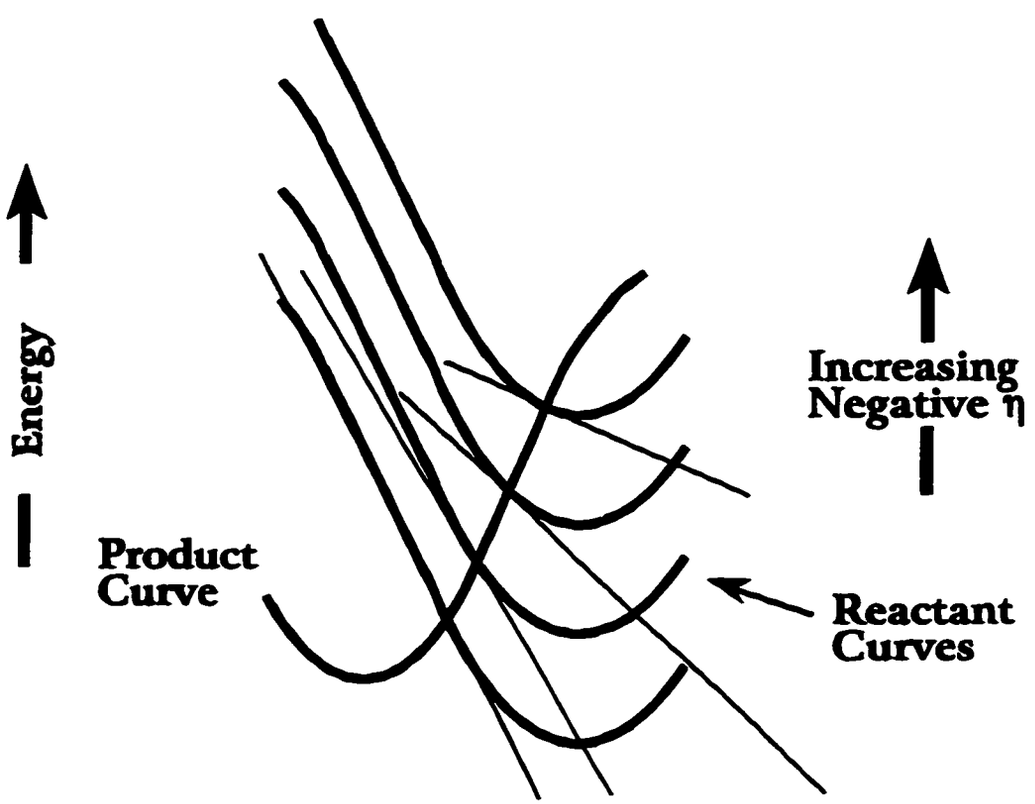


**Fig. 7.2.** Potential-energy diagram demonstrating the effect of PE surface curvature. The intersection of product and reactant curves progressively nearer to the zero point energy of the reactant curve gives considerably different slopes (drawn lines)

$$\beta = \frac{k_r^{1/2}}{k_r^{1/2} + k_p^{1/2}} \qquad (4)$$

where $\beta$ is defined in terms of vibrational force constants for bonds of the product, $k_p$, and reactant, $k_r$, of a given reduction reaction.

## 7.3. Aluminum Deposition Mechanism

The preceding introduction has demonstrated a link between experimentally accessible symmetry factors and the bonding characteristics of the individual species that are assumed to make up a reaction transition-state, where this transition-state has been defined by Fig. 2.1. In the work of the present thesis a clear change of transfer coefficients ($\alpha$) was noted for the Al deposition reaction from the hydride-bath, i.e. from *ca.* 1/2 to *ca.* 1/3 for bath compositions from low to high $H^-$-content, respectively. In the case where there are no prior or following electron-transfer steps in a reaction mechanism, $\alpha$ is directly equal to $\beta$, the symmetry factor for the transition-state.

$\beta$ of 1/2 corresponds to a "symmetric" reaction barrier, i.e. where both reactant and product bonds have similar energies, while a $\beta$ of 1/3 corresponds to an asymmetric barrier (as was illustrated in Fig. 7.1), where the product bond, for the depositing metal atom becoming attached to the substrate surface, is stronger than the reactant bond broken in the reaction step, the metal ion in the OHP bound to a ligand. We can use the bond energy model to explain the variation of $\beta$ in the hydride-bath.

It was concluded in the present thesis work that Al could be deposited from any of a number of chloro-hydrido-aluminates. The distribution of these in any bath varies in a somewhat continuous fashion with proportion of the component species, $AlCl_3$ and $LiAlH_4$. In $Cl^-$-rich baths, i.e. those that possess an excess of $AlCl_3$ over $AlH_4^-$, a greater proportion of $Cl^-$ ligands are expected, which was, in fact, confirmed in the speciation studies of the hydride-bath reported in Chapter 5. Cl will form stronger bonds with Al than will H (511 vs 282 kJ $mol^{-1}$ compared for diatomic, gas-phase bond energies from Table 5.3, see §5.6).

If it is accepted that the rds involves an electron-transfer/decomplexation step, the ligand released in this step is more likely to be $Cl^-$ in $Cl^-$-rich baths and $H^-$ in $H^-$-rich baths. Given the different energies of their bonds with Al (just mentioned), the observed variation of $\beta$ could be attributed to whether it was a $H^-$ or $Cl^-$ ligand that was being released in the coupled decomplexation step of the rds. This interpretation would assume an unchanging (or little changing) product bond (M-A in Figs. 2.1 and 7.1), say something like M-Al-$AlCl_2$, where the substrate would be composed of previously deposited Al. A difficulty with such a rds product is that an Al-Al bond (at 186 kJ $mol^{-1}$, cf. Table 5.3) is even weaker than an Al-H bond (and both of these are much weaker than an Al-Cl bond). If the decomplexation of the $Cl^-$ ligand is defined as the reactant curve and formation of Al-Al the product curve of the transition-state, their relative bond energies are inconsistent with a "symmetric" barrier or $\beta$ equal to 1/2 in $Cl^-$-rich baths.

An alternate product curve that could be consistent with $\beta$ being equal to 1/2 in the $Cl^-$-rich bath is an intermediate with one or possibly two bridging -Cl-'s. In this case, these bridging bonds formed in the rds could be of similar energy to the ligand bond (Al-Cl) broken. This possibility is consistent with the known role of Cl as an outer-sphere electron-transfer bridge in inorganic reactions [147]. The same bridging Cl situation is envisaged in the $H^-$-rich bath, but where, in this case, $H^-$ ligands would be those released in the decomplexation step.

Once partially reduced the surface species, $Al^{2+}$, could move readily along the substrate surface, hopping along the bridging Cl bonds, to a point where the disproportionation reaction that gives $Al^0$ can occur. This disproportionation step (in reaction 6.46) is itself complex, involving chemical electron-transfer between three intermediates and cannot be elucidated by electrochemical measurements.

# Chapter 8 Electrocrystallization in Electrodeposition of Al

## 8.1. Foreword

The following sections will describe the processes of electrocrystallization that are involved in the electrodeposition of Al, and develop the current-time models necessary to distinguish the various nucleation and growth mechanisms possible when an electroactive phase grows on an inert conducting substrate. The processes involved include the effects of solution diffusion and overlap of growing grains.

It will be necessary to explain the relationship of the elementary electrochemical reaction steps considered in Chapter 2 to the overall process of electrocrystallization of Al on itself or on other substrates. Electrochemical crystal building is a cooperative process involving a succession of metal ion (here complex ion) discharge events which, in the case of Al, require several electron-transfer steps coupled with desolvation or deligation in order to produce deposited neutral metal atoms.

When the depositing species is an ion of a multivalent element, as in the case with $Al^{3+}$ in solution, the overall electrocrystallization process becomes complicated by *consecutive* (or parallel) electron-transfer steps prior to the actual successive stages of crystal lattice building or grain growth from nuclei.

In order for metal crystals to be formed the deposition of metal atoms must take place either:

1) at step edges or kinks, reproducing the coordination geometry of the growing crystal lattice;

2) at emergent defects (e.g. spiral emergent dislocations) which present edge sites; or importantly

3) by generation of new nuclei on existing lattice planes (terraces) from, or around which, continued growth of the crystal can take place by the elementary steps referred to above.

The sequence of events in (1) or (3) is illustrated as part of Fig. 8.1.

The nucleation process and coupled subsequent growth is of major importance in determining the overall phenomenon of electrocrystallization and the type of morphology and electrodeposit eventually exhibits in the form of crystals. Under some conditions, the nucleation process itself, coupled with diffusion, can determine the kinetics of electro-

crystallization, especially at low overpotentials, rather than the rate-constant of one or other of the elementary electron-transfer steps. The latter are, however, intimately involved as steps in the *formation* of the initial critical nucleus and as successive reactions in the subsequent coupled growth around the formed nucleus. Once critical nuclei have been formed, then one or other of the elementary successive steps of the multi-electron-transfer (for the case of Al) can be rate-controlling according to the reaction scheme considered earlier (Eqn. 6.43).

The morphologies or crystal habits of electrodeposited metals depend on 1) the relative rates of growth of faces having different Miller indices and coordination geometries, and 2) the role of diffusion control and the consequent thickness of the diffusion-layer set up during electrodeposition, and thus on stirring or mass-transfer conditions in the bath.

It should be noted that §8.3 to 8.5 develop in a detailed manner the relations that describe the initiation of growth of electrochemical deposits according to theories of *nucleation and growth*. These relations incorporate ideas of deposit grain geometry, nucleation kinetics and the effect of the transition between individual grain and macroscopic deposit growth. The material is by no means new, in fact is applied routinely in the literature of electrodeposition, but the work to be described below formed the basis of the analysis of the Al electrocrystallization process that appeared to limit the initial phase formation. It turned out, however, that the behaviour of the deposition of Al from the hydride-bath in many ways disagreed with the theory to be presented here. The decision to include it here is more for the benefit of those whom might subsequently wish to apply it. Thus a caveat is given to the reader here.

## 8.2. Electrocrystallization

The electroplating of aluminum is a so-called "electrocrystallization" process involving Faradaic discharge of Al or complex-Al ions present in a solution or in a melt, as in the Hall-Heroult process for electrochemical smelting of metallic Al. In this section will be shown the development of a number of the mathematical relations that describe the rate of formation of a solid metallic phase from species initially in solution. When

the discharged metal phase is below its melting point the process is called electrocrystallization and can involve deposition onto a foreign inert conducting substrate or onto its own growing lattice. How the phase is formed and grows will obviously influence the ultimate macroscopic morphology of the deposit, e.g. crystal habits, but also lends information to understanding the kinetics of the underlying microscopic chemical and electrochemical processes.

Studying phase formation by electrochemical methods offers the advantages of precise control of the degree of supersaturation required for crystallization by simply applying a voltage, actually an overvoltage, across the system and the ability to easily monitor the progress of deposition via the resulting current-transient in time. The growth of the phase can only take place by a Faradaic process and thus the measured current (when the current-efficiency is 100%) is an exact measure of the rate with which the phase forms, whether by nucleation or incorporation into some sort of growing lattice.

Electrocrystallization is composed of a number of distinguishable steps: diffusion of ions to the electrode surface, electron transfer to give surface adatoms, surface diffusion of these adatoms, adatom accumulation to give local supersaturations leading to nucleation or incorporation of the electrodeposited adatoms into a lattice of the growing phase through cooperative lattice-building steps. These steps are not necessarily all in series; for instance, nucleation and incorporation into the substrate lattice are parallel processes. Practical electrode substrate surfaces usually possess many imperfections such as plateau edges, kinks and vacancies and examples of these are shown in Fig. 8.1. Incorporation into a growing lattice will be favoured at the energetically most stable sites, i.e. those offering the highest degree of coordination, for instance *F* in Fig. 8.1, although direct incorporation at such sites would involve a significant desolvation energy [148] for the ionic species in solution.

On a perfectly smooth single-crystal or on an inert substrate, incorporation of the depositing species into the lattice is not facile; thus nucleation and the subsequent growth of these nuclei is required and can be the current-limiting process. Nucleation necessitates a sufficiently high local concentration of adatoms being generated, termed a supersaturation, for lattice building to occur (usually at some kind of surface defect).

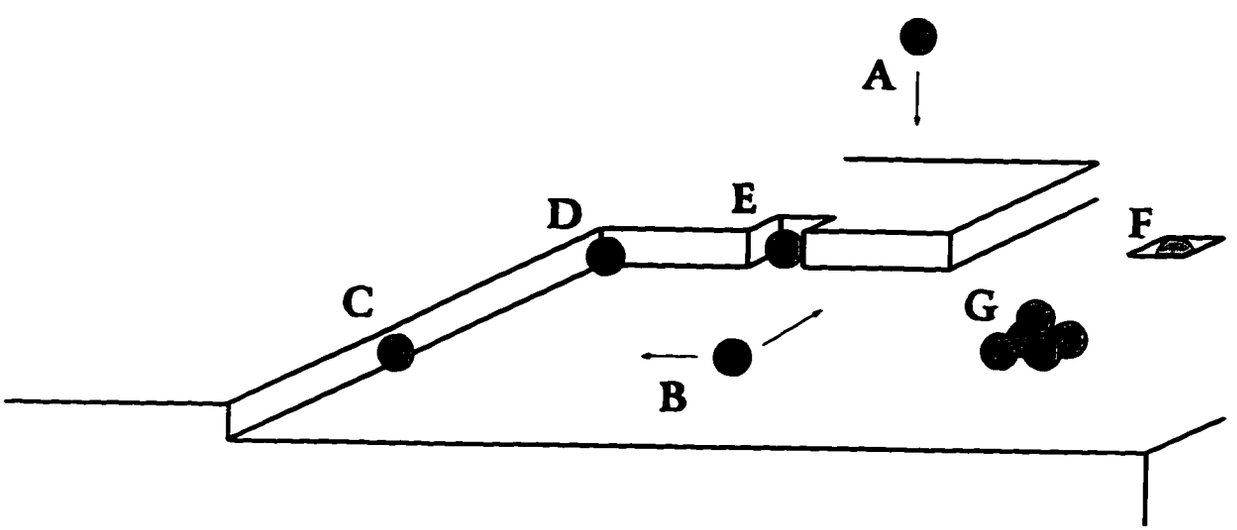


**Fig. 8.1.** Electrode substrate sites at which lattice building steps can occur; plateau edges (C), kinks (D), edge vacancies (E) and plane vacancies (F). Depositable material diffuses from solution (A), is reduced at the substrate surface at (B), and then diffuses to imperfections (C-F) or accumulates locally giving nucleation (G).

Those nuclei of sufficient size (supercritical) will continue to grow into *grains*[a] while those that are not will dissolve.

## 8.3. Kinetically-Controlled Growth

### 8.3.1. Geometry of Growth

It is useful for the mathematical development to assume that the established grains will grow according to some basic geometry. We consider first the growth geometry of a *single* grain on an infinite plane substrate so as to neglect the effect of interactions with substrate boundaries, and where the rate of diffusion of depositing solution species is not limiting. The rate of deposition, dm/dt (in mol $s^{-1}$), of a soluble electroactive species at a single grain in the absence of any parasitic side reactions is proportional to the measured current, $I_{(t)}$, and also the centre's change in volume, dV/dt, given by Eqn. 8.1:

$$\frac{dm}{dt} = \frac{I_{(t)}}{zF} = \frac{\rho}{M}\frac{dV}{dt} \qquad (1)$$

where m is the number of moles deposited, $I_{(t)}$ the measured current (A $cm^{-2}$) at time t, zF the depositing species' molar charge (C $mol^{-1}$), $\rho$ its density (g $cm^{-3}$), M its molar mass (g $mol^{-1}$) and V the volume ($cm^{-3}$) of the deposit.

If the grain is considered to be growing *three-dimensionally* as a *hemi*sphere, its changing volume can be expressed in terms of its changing radius, $d([2/3]\pi r_{(t)}^3)/dt$. Substituting this for the rate of volume change in Eqn. 8.1 and differentiating with respect to $r$ by the chain rule of calculus gives Eqn. 8.2:

$$\frac{I_{(t)\text{-}3D}}{zF} = \frac{2}{3}\frac{\rho}{M}\pi \cdot \frac{d}{dt}(r_{(t)}^3) = \frac{2}{3}\frac{\rho}{M}\pi \cdot \frac{d}{dr}(r_{(t)}^3)\frac{dr}{dt} = \frac{\rho}{M}2\pi r_{(t)}^2 \cdot \frac{dr}{dt} \qquad (2)$$

for the time-dependent current for a hemisphere growing from its periphery. The problem is to determine the time-dependence of the radius of the growing hemispheres, which is done as follows.

The volume of the grain can increase only at the two-dimensional boundary of the growing phase with a rate-constant k (mole $cm^{-2}$ $s^{-1}$). The rate of deposition across the

---

[a] "Grains" as per Avrami's terminology [149]

peripheral area, which for a hemisphere is $2\pi r_{(t)}^2$, can be equated to the rate of volume change of the deposit, (i.e. from the rhs of Eqn. 8.2):

$$k2\pi r_{(t)}^2 = \frac{I_{(t)\text{-}3D}}{zF} = \frac{\rho}{M}2\pi r_{(t)}^2\frac{dr}{dt} \qquad (3)$$

The equality between the first and last terms of Eqn. 8.3 may be solved by cancelling common terms, separating the variables and integrating both sides to isolate $r_{(t)}$ and thence obtain Eqn. 8.4:

$$r_{(t)} = \frac{Mkt}{\rho} \qquad (4)$$

This expression for $r_{(t)}$ can be substituted directly back into the lhs of Eqn. 8.2 and differentiated as in Eqn. 8.5:

$$\frac{I_{(t)\text{-}3D}}{zF} = \frac{\rho}{M}\frac{2}{3}\pi\left(\frac{kM}{\rho}\right)^3\cdot\frac{d}{dt}(t^3) = \frac{M^2}{\rho^2}2\pi k^3t^2 \qquad (5)$$

Note that $k$ here is assumed to remain constant over time and be independent of the direction of propagation of the phase, i.e. that k↔ for growth parallel to and k↑ for growth perpendicular to the plane of the substrate are equal (cases where they are different have been considered [150]).

In two-dimensions the growth is in the form of a disc [151], the volume of which is $h\cdot\pi r_{(t)}^2$, where h is the height of the disc (usually considered that of one atom or molecule). The radius as a function of time for a growing two-dimensional disc is derived as for the hemispherical case, but where the changing volume is $h\pi r_{(t)}^2$ and the rate of peripheral deposition is $kh2\pi r_{(t)}$. Deriving dV/dt for these discs in terms of $r_{(t)}$ (via Eqn. 8.2) and equating to the rate deposition, Eqn. 8.6:

$$\frac{\rho}{M}k2\pi r_{(t)}\cdot\frac{dr}{dt} = \frac{I_{(t)\text{-}2D}}{zF} = kh2\pi r_{(t)} \qquad (6)$$

The $r_{(t)}$ actually reduces to the same expression as was derived for the three-dimensional case in Eqn. 8.4. Thus the rate of two-dimensional growth is:

$$\frac{I_{(t)\text{-}2D}}{zF} = \frac{\rho}{M}\frac{dV}{dt} = \frac{\rho}{M}\pi h\left(\frac{kM}{\rho}\right)^2\frac{d}{dt}(t^2) = \frac{M}{\rho}2\pi hk^2t \qquad (7)$$

In one-dimension, the deposit would grow from a defined unchanging area away from the electrode (needle-like). The measured current is then independent of time.

### 8.3.2. Formation of Multiple Nuclei and Nucleation

The current-time relations of the previous section correspond to the growth of only a single nucleus. In a typical deposition experiment the measured current will be that due to the superposition of many growing grains [b], perhaps dispersed in size due to their differing times of inception. Thus it is necessary to know the rate of appearance of nuclei as a function of time. Nucleation is assumed to occur only on energetically preferred or "active" sites on the surface of the electrode substrate. In general, the number of active sites per unit area, $N_\infty$, is many orders of magnitude smaller than the surface atom density of the substrate which is about $10^{15}$ cm$^{-2}$. $N_\infty$, it should be noted, is known [154] to be dependent on potential, solution composition and substrate-surface Gibbs energy.

If the rate-constant for birth of nuclei that grow into grains, W (s$^{-1}$), is uniform over all available sites and time, the rate of nucleation, dN/dt, will be proportional to the number of empty sites ($N_\infty - N_{(t)}$) as in Eqn. 8.8:

$$\frac{dN}{dt} = (N_\infty - N_{(t)})W \tag{8}$$

where $N_{(t)}$ (cm$^{-2}$) is the number of sites occupied up to time t. If a negative sign is factored through the rhs, and variables separated, Eqn. 8.9 is obtained:

$$\frac{dN}{(N_{(t)} - N_\infty)} = -W dt \tag{9}$$

which if integrated gives:

$$N_{(t)} - N_\infty = \exp[-Wt + U] = \exp[U]\exp[-Wt] \tag{10}$$

where the constant of integration $U$ has been collected on the rhs. To solve for the constant the boundary condition $N_{(t)} = 0$ when $t = 0$ is used with the result that $U = N_\infty$. This may be substituted back into Eqn. 8.10 where rearrangement gives the temporal

[b] Nucleation, at ultramicroelectrodes, restricted to a single nucleus has been described [152,153].

distribution of nuclei, $N_{(t)}$:

$$N_{(t)} = N_{\infty}(1-\exp[-Wt]) \tag{11}$$

This relation assumes that all $N_{\infty}$ sites are accessible for all t and that on each of these there is an equal probability of nucleation taking place. If W is considered uniform over time, there are two limiting cases for this expression: when W is large relative to the growth rate-constant of the new phase (recall k, the growth constant in Eqns. 8.3 - 8.6), the exponential term will become zero even after quite short times. The number of sites is effectively equal to $N_{\infty}$ almost immediately after the onset of deposition and will obviously remains so for all subsequent times after, as per Eqn. 8.12:

$$N_{(t)} \approx N_{\infty} \tag{12}$$

This situation is termed *instantaneous* nucleation. When W is relatively small, the exponential may be linearized to 1 +(-Wt) giving Eqn. 8.13:

$$N_{(t)} \approx WN_{\infty}t \tag{13}$$

which corresponds to the case of *progressive* nucleation.

### 8.3.3. Combining Geometric Growth and Nucleation

The overall observed current will be the sum of rates of growth of all grains present on the substrate. If nucleation is instantaneous, $N_{\infty}$ grains (per unit area) of identical size will grow as per their defined geometry and hence the two- and three-dimensional geometric time-relations determined previously, Eqns. 8.5 and 8.7, are simply multiplied by $N_{\infty}$ to give Eqns. 8.15 and 8.14, respectively:

$$i_{(t)\text{-}2D\text{-}inst} = \frac{2\pi zFMhN_{\infty}k^2t}{\rho} \tag{14}$$

and

$$i_{(t)\text{-}3D\text{-}inst} = \frac{2\pi zFM^2N_{\infty}k^3t^2}{\rho^2} \tag{15}$$

where the current, $I_{(t)}$, is now normalized to the area of the electrode substrate, $i_{(t)}$, since $N_{\infty}$ is thus normalized.

If nucleation is progressive, the growing nuclei will be dispersed in size since their individual times of inception will vary and this distribution depends on the nucleation rate law. Coupling the temporal nuclear distribution function, i.e. Eqn. 8.10 with either of the geometric growth functions is *not* particularly straightforward. Simple multiplication of the distribution for $N_{(t)}$ by the growth function overestimates the contribution made by those grains nucleated after time zero (t = 0). The overall observed current at some time t will be the sum of the currents from all the individual $N_{(t)}$ growing grains:

$$i_{(t)} = \sum_{j=N(0)}^{N(t)} i_{(t-t_{oj})} \tag{16}$$

The currents from the individual grains all have different magnitudes since the grains are born at different times, i.e. the *jth* nucleus is born at $t_{oj}$ and thus contributes a current of $i(t-t_{oj})$ at time $t$. The treatment can be simplified by replacing $t-t_{oj}$ with $u_j$, the grains' ages or lifetimes. The summation may be replaced with an integral, since $N_{(t)}$ is extremely large here and may be considered continuous. Integration is carried out over all the lifetimes, du, of the grains present at the time of observation, t, from t to t-u where note that the lifetimes are measured *backward* in time from t. This may be written as Eqn. 8.17:

$$i_{(t)} = \int_{N(t)}^{N(t-u)} i(u)\,du \tag{17}$$

and $N_{(t-u)}$ describes the distribution of these lifetimes for $0 < u < t$.

The varying interval of integration in Eqn. 8.17 can be mapped to the time domain by the change-of-variable method for indefinite integrals [155]. The result is that Eqn. 8.17 reduces to a solvable form, Eqn. 8.18[c]:

$$i_{(t)} = \int_0^t i(u)\left(\frac{\partial N}{\partial t}\right)_{t-u} du \tag{18}$$

The $(\partial N/\partial t)_{t-u}$ term is effectively the change in the number of nuclei at time t-u which

---

[c] This procedure for combining the nucleation and growth laws has been given in seminal work in this field without explanation or reference [151,156]. This expression is termed a *convolution integral* which, here, we have obtained from integration by the change-of-variable method. The most common application of convolution integrals is when combining transforms of differential equations [157].

can be thought of as a *weighting* (or a *local magnification factor* [155]) for that particular lifetime, $u_t$. Integrating over all lifetimes will give the total current contribution of all grains.

Thus if the growth laws that we have considered (for the geometries of two-dimensional discs, Eqn. 8.7, and three-dimensional hemispheres, Eqn. 8.5) are combined with the nuclear distribution for progressive nucleation by way of the above convolution integral, Eqn. 8.18, we obtain Eqns. 8.19 and 8.20 for the initial stages of phase formation of a two- and three-dimensional, progressively nucleated, deposit on a foreign substrate, *viz*:

$$i_{(t)\text{-}2D\text{-}prog} = \frac{\pi z F M h W N_{\infty} k^2 t^2}{\rho} \tag{19}$$

and

$$i_{(t)\text{-}3D\text{-}prog} = \frac{2\pi z F M^2 W N_{\infty} k^3 t^3}{3\rho^2} \tag{20}$$

### 8.3.4. The Avrami Treatment

#### 8.3.4.1. Overlap of Nuclei Growing Under Kinetic Control

The above equations are based on the assumption that the grains grow independently of one another. This, however, introduces two errors as time progresses, due to either mutual overlap of individual growing nuclei or overlap and blocking of as-yet-unnucleated sites. For the first case, as the deposit propagates (whether two- or three-dimensionally) the boundaries of the grains, in the two-dimensional plane of the electrode, will grow independently of one another *only* up to the point where the boundaries of separate grains intersect. At this point, growth along the particular grain-grain axis (along which the grains intersected) will cease, but the grains will continue to grow from their perimeters or surfaces along their other free radial directions until they as well intersect with other grain edges (intersection with the substrate edges is neglected) until the surface is completely covered.

The geometric growth models of Eqn. 8.19 and 8.20 describe $N_{(t)}$ grains growing

independently of one another, but the fact is that $N_{(t)}$ grains growing in a practical experiment will eventually overlap and attentuate the expected transient current with time. In this section an expression will be derived for the growth of two-dimensional discs with analogies drawn to other geometries.

The problem of correcting for this overestimated current was considered in important papers by Avrami [158-160][d] in which the gross area, $A_{gross}$, is related to the actual or net area, $A_{net}$. $A_{gross}$ is the area that growing grains would occupy if they never overlapped, which, we note, is what the geometric growth models describe (e.g. Eqns. 8.19 and 8.20). It is usual to consider these areas with repect to that of the entire substrate area, A, in reduced form; for $A_{gross}$ we use the so-called *extended fractional area*, $F_{ex}$, which is essentially unbounded, i.e. $F_{ex} > 0$, and for $A_{net}$ the *actual fractional area*, $F_\theta$ which is bounded $0 \leq F_\theta \leq 1$. The essence of the Avrami theorem and the related quantities are given in Fig. 8.2. Note that what are called "areas" in much of the related literature are actually these fractional areas. The relationship between $F_{ex}$ and $F_\theta$ is given by the "Avrami theorem" in Eqn. 8.21:

$$\frac{A_{net}}{A} = F_\theta = 1 - \exp\left[-\frac{A_{gross}}{A}\right] = 1 - \exp\left[-F_{ex}\right] \qquad (21)$$

The basis of the Avrami theorem is that the initiation of nuclei is a *stochastic* process, likened to raindrops falling randomly on a pool of water. This analogy also extends to the resulting radial expansion of ripples which eventually overlap in a way also analogous to the circular or hemispherical extensions of the subsequently growing nuclei. At real polycrystalline surfaces, however, the development of nuclei is usually not, or not perfectly, stochastic, since nucleation is usually preferred at so-called active sites, surface defects, emergent spiral dislocations or step-edges.

The second error occurs only in the case of progressive nucleation. Recall that for the relation for $N_{(t)}$, Eqn. 8.6, it has been assumed that each site has equal probability of being nucleated. However, if grains born early in time grow to a point that blocks, as yet unnucleated sites, these blocked sites will have zero probability of contributing to the

[d] For a concise description of the derivation of Avrami's theorem refer to [151:p.173].

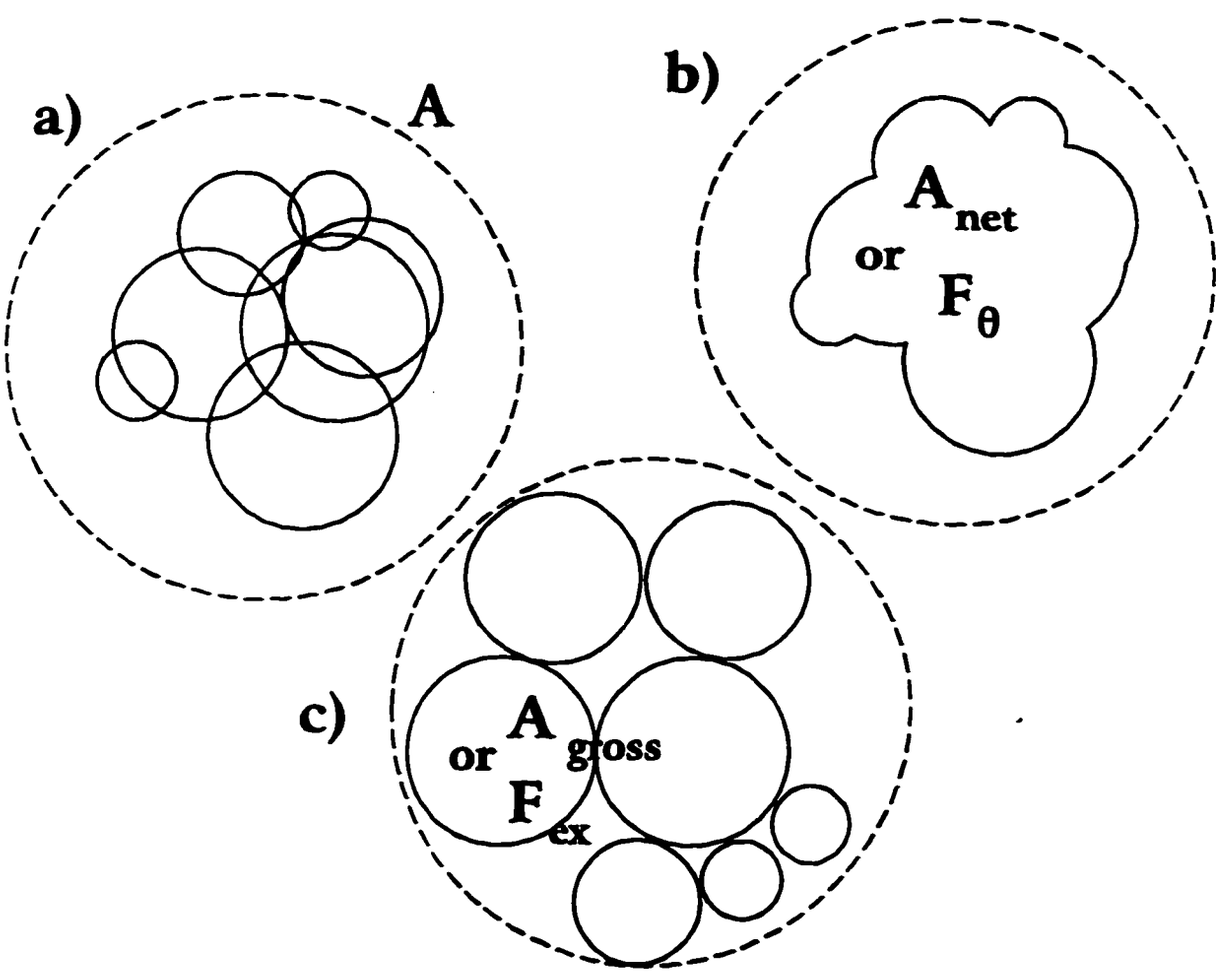


**Fig. 8.2.** An illustration of the growth of a) seven overlapping circular grains (solid circles) of various sizes on a substrate of area *A* (large dashed circle); (b)-(c) demonstrate the relationship between the net area, $A_{net}$, or fractional area (i.e. normalized to *A*), $F_\theta$, covered by the deposit in (a); and the gross or *extended* area, $A_{gross}$ or $F_{ex}$, in (c) (assuming no overlap between the individual grains).

depositing array. The result is that $N_o$ used in the nucleation law is not strictly constant, but decreases over time giving ultimately what is called a saturation number density, $N_{oo}$, which is examined again in §8.4.3. It has been shown that Avrami's treatment accounts for these "phantom nuclei" ingested by growth of previously formed grains [161].

### 8.3.4.2. Two-Dimensional Overlap

Fig. 8.3a shows theoretical current-transients for two-dimensional growth on a bare inert substrate for instantaneous and for progressive nucleation. In the initial stages of growth, before grain overlap, the current will be determined by the increasing edge length of the growing *discs* and hence Eqns. 8.14 and 8.19. Later, when the grains grow to the point where their boundaries start to intersect, competition between the increasing edge area of the radially propagating grains, and the deactivation of radial growth directions due to overlap, results in a slowing of the rate at which the current can increase. As a significant fraction of the electrode surface becomes covered, overlap will predominate giving a maximum in the current-time transient and proceeding, if subsequent layers are not nucleated, to decay to zero as in the curves of Fig. 8.3a. If, however, subsequent *new layers* are able to be nucleated on top of the grown grains, the current-transients for these layers would be like that for the first layer and the overall current would then be a complex superposition of the currents arising from all the individual layers as, for example is illustrated in Fig. 8.3b. The characteristics of the growth of these individual layers would be complicated by the facts that: 1) the rate-constant for nucleation upon the inert substrate would probably be different from that for nucleation upon the deposit itself and 2) the area of previously formed, or forming layers, upon which subsequent layers must be nucleated would obviously be dynamic in time and thus the nucleation law would have a time-dependent $N_o$.

To calculate the effect of overlap on the overall current-transient for the case of two-dimensional growth of a single monolayer we first consider the normalized *extended* charge, $q_{gross}$ ($C\,cm^{-2}$) corresponding to growth of completely independent grains (ignoring overlap), relative to that for a complete monolayer, $q_{max}$. These are related in Eqn.

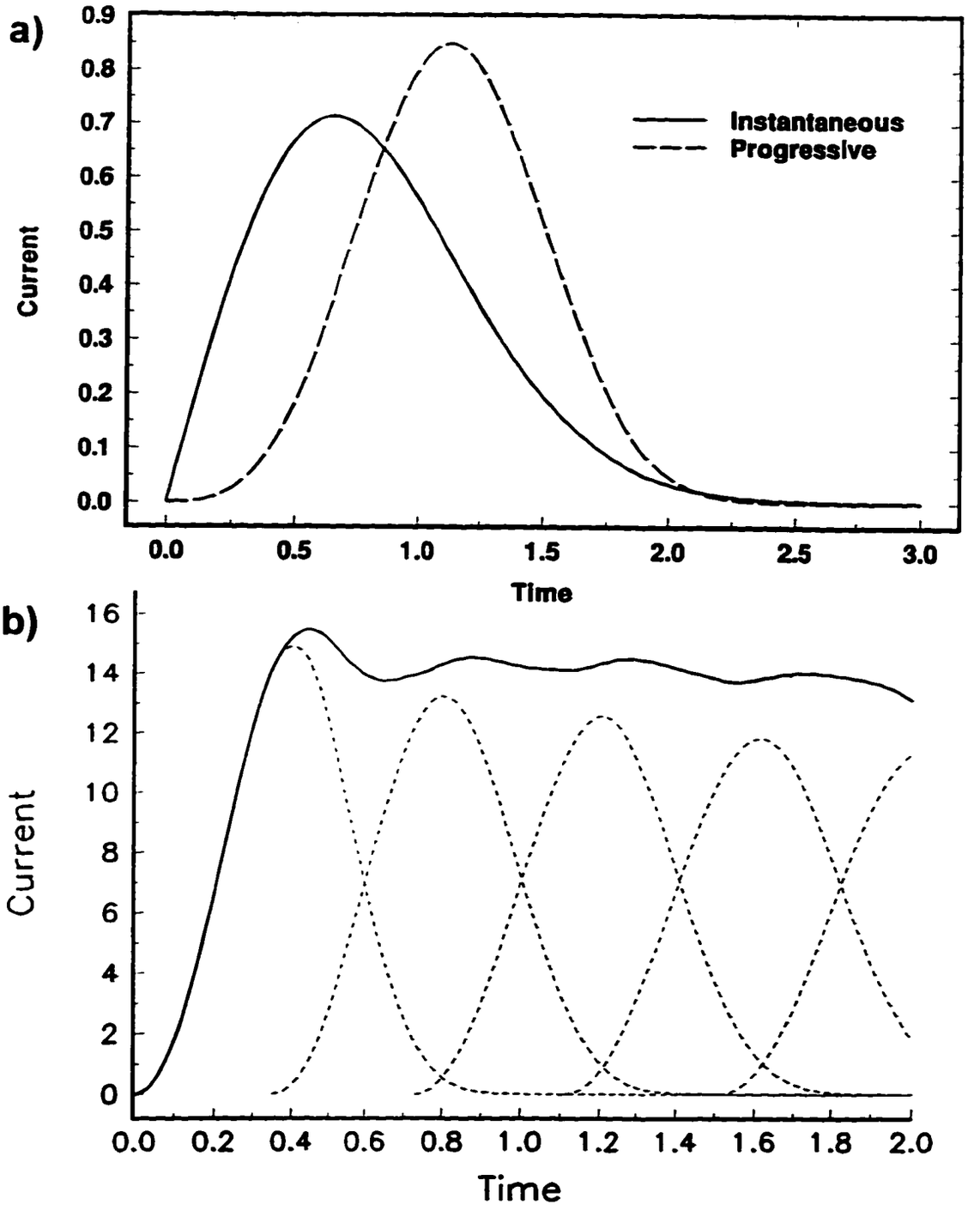


**Fig. 8.3.** **a)** Theoretical current transients as per Eqns. 8.29 and 8.30 for two-dimensional growth with *instantaneous* and *progressive* nucleation. Constants have been chosen appropriate to the case of the electrodeposition of Al from organic solvents in such a way that the charge under the curves is equal. **b)** The resulting current transient due to superposition of contributions from multiple monolayers.

8.22 by the extended area parameter, $F_{ex}$, of the Avrami theorem (Eqn. 8.21):

$$q_{grow} = F_{ex} q_{mon} \tag{22}$$

The normalized current or current-density, $i_{(t)grow}$, from the extended area will be:

$$i_{(t)grow} = \frac{d}{dt}(q_{grow}) = q_{mon}\frac{d}{dt}(F_{ex}) \tag{23}$$

while similarly for the current-density, $i_{(t)act}$, passing at the deposit's actual area, $F_\theta$:

$$i_{(t)act} = q_{mon}\frac{d}{dt}(F_\theta) \tag{24}$$

Rearranging the former quantity to isolate $q_{mon}$ and substituting this into the latter expression gives the relation between the extended and actual current-densities:

$$i_{(t)act} = i_{(t)grow}\frac{dF_\theta}{dt}\cdot\frac{dt}{dF_{ex}} = i_{(t)grow}\frac{dF_\theta}{dF_{ex}} \tag{25}$$

$F_\theta$ may be replaced by the result given by the Avrami theorem (Eqn. 8.20). Differentiation with respect to $F_{ex}$ gives Eqn. 8.26:

$$i_{(t)act} = i_{(t)grow}\frac{d\left(1-\exp\left[-F_{ex}\right]\right)}{dF_{ex}} = i_{(t)grow}\exp\left[-F_{ex}\right] \tag{26}$$

To obtain a solution for this, $F_{ex} = q_{grow}/q_{mon}$ is substituted into Eqn. 8.26 and $i_{(t)grow}$ is taken as either of the two-dimensional current-time relations (Eqn. 8.14 or 19 for instantaneous or progressive nucleation, respectively). The charge for the deposition of a monolayer, $q_{mon}$, ($C\,cm^{-2}$) is equal to $zFh\rho/M$. $q_{grow}$ may be obtained from these expressions by recognizing that it is related to $i_{(t)grow}$ by:

$$q_{grow} = \int_0^t i_{(t)grow}\,dt \tag{27}$$

The expression for $i$ for instantaneous nucleation, Eqn. 8.14, is integrated with respect to time as per Eqn. 8.27. This and $q_{mon}$ are divided to obtain $F_{ex}$ as in Eqn. 8.28:

$$F_{ex} = \frac{q_{grow}}{q_{mon}} = \frac{\pi zFMhN_\infty k^2 t^3}{\rho}\cdot\left(zFh\frac{\rho}{M}\right)^{-1} = \frac{\pi M^2 N_\infty k^2}{\rho^2}t^2 \tag{28}$$

This result for $F_{ex}$ and that for $i_{(t)\,gross}$, which is simply either of the two-dimensional growth relations that describe non-intersecting disc growth (Eqns. 8.14 or 8.19), can now be introduced into Eqn. 8.26 to give Eqn. 8.29, the expression for the current due to deposition of a monolayer by growth of discs:

$$i_{(t)\text{-}2D\text{-}inst} = i_{(t)gross}\exp\left[-F_{ex}\right] = \frac{2\pi zFMhN_{\_}k^2t}{\rho}\cdot\exp\left[-\frac{\pi N_{\_}M^2k^2}{\rho^2}t^2\right] \quad (29)$$

Conducting the same derivation for progressive nucleation gives:

$$i_{(t)\text{-}2D\text{-}prog} = i_{(t)gross}\exp\left[-F_{ex}\right] = \frac{\pi zFMhWN_{\_}k^2t^2}{\rho}\cdot\exp\left[-\frac{\pi WN_{\_}M^2k^2}{3\rho^2}t^3\right] \quad (30)$$

The shape of these current-time relations is shown graphically in Fig. 8.3a, plotted for some arbitrary constants to give equal charge for the two cases. The ultimate result of this treatment is that, at early times, the current grows with the geometry of the grains but is subsequently attenuated and eventually extinguished as these overlap and the surface becomes completely covered with the deposit. Experimentally, it is important to recognize this transition region since it can be mistaken for a linear growth relation.

#### 8.3.4.3. Three-Dimensional Overlap

In the absence of subsequent nucleation, overlap in two dimensions ultimately leads to complete extinction of growth as the surface tends to complete coverage. In three dimensions overlap does not give a decay to zero, but results in a transition to one-dimensional growth out into solution. The initial transient corresponds to the increasing area of hemispherical grains (nucleated accordingly). As the grains coalesce, growth in radial directions parallel to the plane of the substrate will be extinguished first, followed by those sequentially closer to the normal of the plane of the electrode giving way ultimately, to one-dimensional growth normal to the substrate. This is illustrated by the progressing "front" of instantaneously and progressively nucleated deposits in Figs. 8.4a and 8.4b. The result is a current maximum in the transient some time between the first grain intersection and their complete coalescence to a single phase (as shown in Fig. 8.3); the

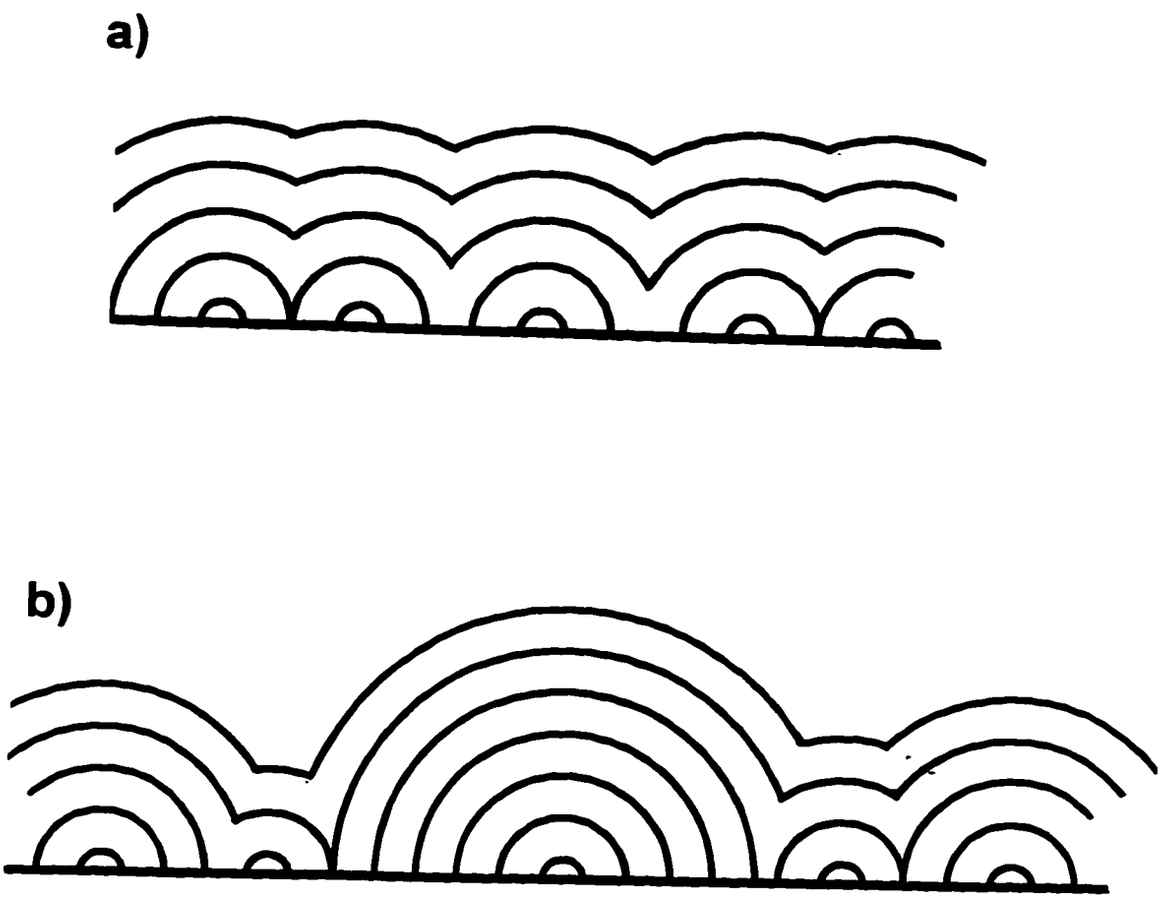


**Fig. 8.4.** Profiles of deposit thickness for an array of growing hemispherical grains nucleated **a)** instantaneously; and **b)** progressively.

current subsequently decays to a constant value due to one-dimensional growth from the resulting whole area of the substrate. This current maximum has been observed experimentally [162] and has been modelled by either the "death and rebirth" of growing grains [162,163] or by the extinction of radial growth directions as described above [161].

Modelling the whole transient is much more complicated in the case of three-dimensional growth and solutions are more varied in the literature. Avrami's treatment of nucleation cannot be applied directly to cases where nucleation is two-dimensional (i.e. in the plane of the electrode) but growth is pseudo-three-dimensional [164], i.e. in the plane of the electrode *and* out into solution where the deposit's area is not strictly bounded by the substrate area, *A*.

An approach to this problem treats an infinitesimal slice of the whole deposit at a given height above the substrate surface and applies Avrami's extended-to-actual area treatment for overlap of neighbouring discs. An integration with respect to height gives the actual volume of the deposit [161,165]. The resulting expressions tend to involve complicated integrals which must be solved numerically. In the case of reference [161] current maxima of 1.285zFk and 1.332zFk for instantaneous and progressive nucleation, respectively, are predicted that decay to a constant value of zFk after extended times.

Simplified relations that do not involve this maximum appear in the literature of this field [166]. In this case the current as a function of time is described by:

$$i_{(t)} = zFkF_\theta = zFk(1-\exp[-F_{ex}]) \qquad (31)$$

where $F_\theta$ is the changing fractional area from which the deposit grows and is substituted directly from the Avrami theorem (Eqn. 8.21) neglecting the concerns about its applicability mentioned above. $F_{ex}$ is equated to $i_{@\,grow}/i_{@\,ext}$, viz. the ratio of the current without overlap to the maximum current possible from the actual area of the substrate electrode, $i_{@\,ext} = zFk$. The result of the derivation gives Eqn. 8.32 and 8.33 for the instantaneous and progressive cases:

$$i_{(t)\text{-}3D\text{-}inst} = zFk\left(1 - \exp\left[-\frac{2\pi M^2 N_A k^2}{3\rho^2}t^2\right]\right) \qquad (32)$$

and

$$i_{(t)\text{-}3D\text{-}prog} = zFk\left(1 - \exp\left[-\frac{2\pi M^2 W N_A k^2}{3\rho^2} t^3\right]\right) \qquad (33)$$

which do not predict a current maximum, as discussed above, but rather a smooth transition from the initial geometric growth relations, Eqns. 8.15 and 20, at short times, to an asymptotic approach at long times to zFk, the current-density from the whole area of the substrate electrode.

### 8.3.5. Kinetic-Control: Concluding Remarks

The above approaches to incorporating grain overlap to give "*whole transient*" relations for three-dimensional, kinetically-controlled growth are not particularly satisfactory since they involve either complicated numerical methods or approximation for their their solution. These idealized models assume that the geometries of the growing grains are those of idealized shapes, e.g. hemispheres ignoring the fact that metal deposits usually grow as crystals, i.e. that involve regular lattices. This could result in a distribution of rate constants for incorporation at different crystallographic planes which in extreme cases could lead to significant differences from ideal geometries, giving e.g. facetted deposits.

From a practical standpoint, only the initial growth transient, before overlap, should be analyzed for the purpose of distinguishing different deposit growth mechanisms. Cognizance of the transient behaviour arising from overlap is important, however, in order to recognize the limits of the growth regime that can be obscured by interferences from the double-layer and adsorption phenomena at short times and grain overlap at longer times.

### 8.4.1. Diffusion-Controlled Growth

In the previous section current-time relations were developed for the growth of metallic deposits in the case where the kinetics of incorporation into a growing phase was rate-limiting. If, on the other hand, the rate of this step is relatively rapid compared to that of the transport of material to the growing phase from solution, diffusion will control

the rate of growth. Instead of the rate of growth of the deposit (described by the rate-constant *k*) dictating the current-transient, it is, in this case, the propagation of diffusion fields outward from the deposit (described by a diffusion coefficient D).

In the very early stages of deposition onto an inert substrate the surface density of distributed nuclei is small enough that each of the growing grains will have diffusion zones radiating from them hemispherically. Thus initially, hemispherical diffusion to individual three-dimensional hemispherical grains[6] is considered as limiting the growth rate [167,168]. The expression for the current-density limited by such spherical diffusion [169] is given in Eqn. 8.34:

$$i_{(t)} = zFc_{\infty}\left(\frac{D}{\pi t}\right)^{1/2} + \frac{zFD(c_{\infty}-c_{el})}{r_{(t)el}} \qquad (34)$$

where $c_{\infty}$ is the bulk solution concentration of the depositing species (mol cm$^{-3}$) from which deposition takes place, $c_{el}$ that at the surface of the electrode, D the depositing species' diffusion coefficient (cm$^2$ s), t time and $r_{(t)el}$ the radius (cm) of the growing hemisphere giving rise to the diffusional field. If $c_{el}$ may be assumed zero (a fair assumption for overpotentials greater than about 100 mV), and $r_{(t)el}$ is sufficiently small relative to $\pi t$, the first term may be neglected and so Eqn. 8.34 becomes Eqn. 8.35:

$$i_{(t)} = \frac{zFDc_{\infty}}{r_{(t)el}} \qquad (35)$$

The following points are significant when considering Eqn. 8.35. Firstly, this relation was initially developed to describe diffusion to a mercury hanging drop electrode and thus $r_{(t)el}$ *should* be a constant, but in the present case it refers to the growing grains, the radii of which are obviously *not* constant but increase continuously over time. The actual increase in $r_{(t)el}$ relative to the size of the diffusion zones created, however, is considered negligible and thus this point is not considered important [154]. The second point is that the concentration of depositing species is usually assumed zero at the

[6] Other deposit growth geometries can be considered, i.e. pyramids, cones, etc, but diffusion will always be hemispherical since the diffusion front propagates much faster than does the deposit's periphery, thus the deposit effectively acts as a point sink, the focus of a hemispherical diffusion field [154].

electrode surface (i.e. $c_{el} = 0$) which simplifies the mathematics. This assumption is equivalent to assuming immediate consumption (deposition) of the ions arriving at the electrode surface from the diffusion field. However, for small potential excursions, this will not be true, so $c_{el}$ will be given by the Nernst relation at overpotentials less than about 60 mV; then Eqn. 8.35 becomes Eqn. 8.36:

$$i_{(t)} = \frac{zFD(c_\infty - c_\infty \exp[z\eta f])}{r_{(t)el}} \tag{36}$$

Now we proceed to derive an expression for the current, arising from the propagation of these diffusion zones, as a function of time. Material balance requires that the diffusion-limited current must be equal to the amount of material being deposited which, it is assumed, takes the geometry of a hemisphere (which is generally the only geometry considered). The rate of arrival of material will thus be equal to the changing volume of the deposit, dV/dt (as Eqn. 8.2) where this latter must be normalized to the changing surface area of these hemispherical grains or $2\pi r_{(t)}^2$ since the diffusion current is thus, i.e.:

$$\frac{zFDc}{r_{(t)}} = i_{(t)} = \frac{\rho}{M}\frac{zF2\pi r_{(t)}^2}{2\pi r_{(t)}^2}\frac{dr}{dt} \tag{37}$$

Cancelling common terms and rearranging then gives Eqn. 8.38:

$$\frac{cDM}{\rho}dt = r_{(t)}dr \tag{38}$$

which, upon integration and solving for $r_{(t)}$, gives the time-dependent radius of a growing hemisphere:

$$\sqrt{\frac{2cDMt}{\rho}} = r_{(t)} \tag{39}$$

The time-dependent current resulting from growth of this hemisphere is obtained by substituting $r_{(t)}$, Eqn. 8.39, into the expression for the current of a growing hemisphere, i.e. the first two terms of Eqn. 8.2. Common terms may be cancelled and t separated giving:

$$I_{(t)} = \frac{2}{3}zF\frac{\rho}{M}\pi\left(\frac{2cDMt}{\rho}\right)^{3/2}\frac{1}{dt} = \frac{2}{3}zF\left(\frac{M}{\rho}\right)^{1/2}\pi(2cD)^{3/2}\frac{t^{3/2}}{dt} \tag{40}$$

Differentiation with respect to t gives an expression for the growth rate of a single grain limited by diffusion, Eqn. 8.41:

$$I_{(t)} = zF\left(\frac{M}{\rho}\right)^{1/2}\pi(2cD)^{3/2}t^{1/2} \tag{41}$$

This hemispherical growth expression may be combined with either of the nucleation distributions. For instantaneous nucleation, $N_\infty$ grains per unit area are all nucleated at $t = 0$, then grow according to their hemispherical geometry; thus the growth relation for a single grain, Eqn. 8.41, is simply multiplied by $N_\infty$, giving Eqn. 8.42:

$$i_{(t)\text{-}3D\text{-}inst} = \pi zFN_\infty\left(\frac{M}{\rho}\right)^{1/2}(2cD)^{3/2}t^{1/2} \tag{42}$$

The growth rate is now measured as a current-density since the nucleation distribution is normalized to unit electrode area.

For the case where the nucleation distribution is time-dependent, i.e. it is progressive, the growing grains have varying moments ($t \geq 0$) of birth and this gives a distribution of sizes at any given time and hence a distribution of contributions from these to the overall current. This problem is solved via the convolution integral, Eqn. 8.18, the procedure being to differentiate the simplified nucleation law for progressive nucleation, $WN_\infty t$, with respect to time, and to combine this with the hemispherical growth law, Eqn. 8.41, and then to integrate over all lifetimes; this procedure gives:

$$i_{(t)\text{-}3D\text{-}prog} = \frac{2}{3}\pi zFWN_\infty\left(\frac{M}{\rho}\right)^{1/2}(2cD)^{3/2}t^{3/2} \tag{43}$$

### 8.4.2. Overlap of Growing Nuclei Controlled by Diffusion

Spherical diffusion and hence Eqns. 8.42 and 8.43 will describe the early stages of experimental current-transients, but the independent diffusion fields will eventually start to overlap leading to the consumption of all the solution species adjacent to the electrode surface. As a higher fraction of the interphase becomes occupied with diffusion fields the only source of depositable material will be that arriving from the bulk of solution and this will necessarily be via linear diffusion.

The overlap of the diffusion zones, and hence the transition from hemispherical to

linear diffusion, is modelled again by using the Avrami theorem (Eqn. 8.20). The problem has been approached by considering the *surface area* of the electrode occupied by the diffusion fields, $A_{grow}$, ignoring that part that extends into solution, since nucleation is, of course, in the plane of the electrode while the resulting diffusion zones grow both along the surface of the electrode *and* into solution. This reduces the problem to two-dimensions. The transition from hemispherical to linear diffusion is accomplished [170] by using the expression for semi-infinite linear diffusion (i.e. the Cottrell equation) and including therein the actual fractional area, $F_\theta$, of the diffusion zones.

$$I_{(t)} = \frac{zFD^{1/2}c(AF_\theta)}{(\pi t)^{1/2}} \tag{44}$$

The question then is what is the time-dependence of the area and hence $F_\theta$ of these diffusion zones? It is the areas and hence radii of these in the plane of the electrode that are of interest here. The time-dependent radius of the diffusion zones, $r_{(t)d}$, is given by Eqn. 8.45, an expression similar to that for the time-dependence of diffusion layer-thickness:

$$r_{(t)d} = (UDt)^{1/2} \tag{45}$$

It is related to the rate of diffusion of depositable material in solution and hence to a diffusion coefficient, D. $U$ is a unitless numerical constant that will be determined later. The electrode area covered by diffusion zones, $A_{grow}$, propagating from the sum of all growing grains (assuming the zones do not overlap) is described by Eqn. 8.46:

$$A_{grow} = \sum^{i} \pi r_{(t)i}^2 = \sum^{i} \pi UDt_i \tag{46}$$

In reality, once the growing diffusion zones start to intersect and Eqn. 8.46 begins to overestimate the actual area covered by diffusion zones, the Avrami theorem must be employed to determine the actual area relative to this overestimated or *extended* area, which requires the areas be converted to fractional areas, i.e. $F_{ex} = A_{grow}/A$.

For the case of instantaneous nucleation all the diffusion fields are the same size and the fractional area, $F_{ex}$, that $N_\infty$ of them occupy as a function of time would be:

$$F_{ex} = U_i N_\infty \pi Dt \tag{47}$$

which is dimensionless since $N_\infty$ is area normalized and $U_i$ is the unitless constant for this, instantaneous, case. This result may be substituted into the Avrami theorem to give the actual fractional area, $F_\theta$, of the diffusion zones:

$$F_\theta = 1 - \exp[-U_i N_\infty \pi D t] \tag{48}$$

This may be substituted for $F_\theta$ in the Cottrell equation as below:

$$I_{(t)} = \frac{zFD^{1/2}c(AF_\theta)}{(\pi t)^{1/2}} = \frac{zFD^{1/2}cA}{(\pi t)^{1/2}}(1 - \exp[-U_i N_\infty \pi D t]) \tag{49}$$

The constant $U_i$ is evaluated by recognizing that at short times before overlap, this expression (Eqn. 8.49) must reduce to an expression deacribing the growth of $N_\infty$ independent grains, i.e. Eqn 8.42. Thus Eqns. 8.42 and 8.48 are equated and the exponential in the latter linearized (since the time will be small when this equality is valid); the resulting relation can then be solved for $U_i$ which gives $U_i = (8\pi cM/\rho)^{1/2}$. Substituting this back into Eqn. 8.49 and normalizing both sides to electrode area, A, gives the expression for the current-density transient for the instantaneously-nucleated, diffusion-controlled growth of hemispheres in Eqn. 8.50:

$$i_{(t)\text{-3D-inst-dif}} = \frac{zFD^{1/2}c}{(\pi t)^{1/2}}\left(1 - \exp\left[-\left(\frac{8\pi cM}{\rho}\right)^{1/2} N_\infty \pi D t\right]\right) \tag{50}$$

In the case of progressive nucleation the area of a given diffusion fields depends on its moment of birth relative to those of all the other individual fields. The distribution of these fields for progressive nucleation is given by Eqn. 8.13, i.e. $N_{(t)} \approx WN_\infty t$, which may be combined with the time-dependent area of a single diffusion zone (Eqn. 8.46) by way of the convolution integral, Eqn. 8.18. Thus the distribution, $N_{(t)}$, is differentiated and the result multiplied by Eqn. 8.46. The resulting integral is evaluated in Eqn. 8.51:

$$F_{\infty} = \int_0^t U_p WN_\infty \cdot \pi D t dt = \frac{1}{2} U_p WN_\infty \pi D t^2 \tag{51}$$

where $U_p$ is the unitless constant for the progressive nucleation case. The use of $N_\infty$ has again normalized the expression and is thus equal to a *fractional area*, $F_\infty$, and this may

be introduced into the Avrami theorem to give the actual fractional area, $F_\theta$. This $F_\theta$ may be substituted into the Cottrell equation, the expression normalized and $U_p$ evaluated by equating the early-time linear-diffusion relation to the growth relation for progressive nucleation (Eqn. 8.43) which gives $U_p = 4/3(8\pi cM/\rho)^{1/2}$. Thus the current-time relation for the growth of *progressively nucleated hemispheres controlled by diffusion* is:

$$i_{(t)\text{-}3D\text{-}prog\text{-}diff} = \frac{zFD^{1/2}c}{(\pi t)^{1/2}}\left(1 - \exp\left[-\frac{2}{3}\left(\frac{8\pi cM}{\rho}\right)^{1/2} WN_\infty \pi D t^2\right]\right) \qquad (52)$$

The current-transients corresponding to Eqns. 8.50 and 8.52 are plotted in Figs. 8.5a and 8.5b for $M/\rho$ and D values consistent with the Al electrodeposition reaction in organic solvents. The series of curves in each of the figures corresponds to varying magnitudes of $N_\infty$ for the transients nucleated instantaneously and $WN_\infty$ for those nucleated progressively. Both types of transient show a growth regime which gives way to a maximum, ultimately passing into a diffusion decay. Of note is that the progressive transients come to behave, for large $WN_\infty$ values, analogously to the instantaneous cases. Large W's, of course, essentially correspond to instantaneous conditions (cf. Fig. 8.5*a* and *b*).

### 8.4.3. Saturation Number-Density

When the rate of nucleation is slow with respect to the diffusion coefficient of the depositing species it becomes impossible to nucleate all $N_\infty$ available sites. This is due to the fact that the diffusion zones propagating from extant grains, depleting depositing species in their immediate vicinity, effectively block any as-yet-unnucleated sites that happen to be within these zones, since nucleation requires a supersaturation of depositing species in the immediate vicinity. Once the entire surface is covered with diffusion zones, the nucleation process on the substrate is halted and an instantaneous-like situation prevails. In this case the saturation nucleation site-density, $N_{sat}$, is a more practically important quantity than $N_\infty$.

$N_{sat}$ is determined by recognizing that nucleation is occurring on a continuously decreasing fraction of the substrate area as diffusion zones come to occupy an increasingly large fraction of the electrode surface and hence block otherwise available nucle-

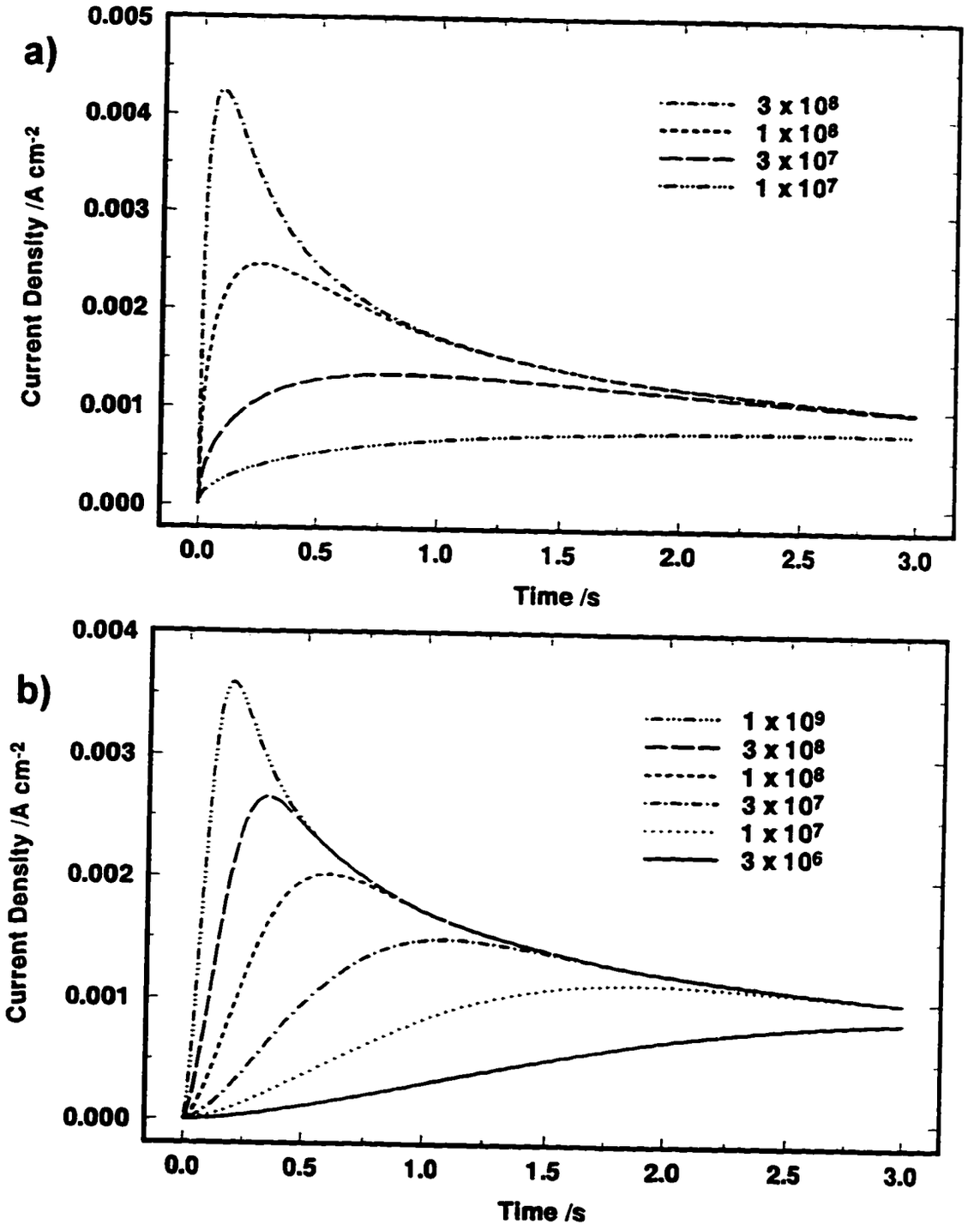


**Fig. 8.5.** A series of theoretical current transients for three-dimensional growth controlled by *diffusion* and nucleated **a)** instantaneously as per Eqn. 8.50; and **b)** progressively as per Eqn. 8.52. Both equations are evaluated for constants appropriate to Al electrodeposition from inorganic solvents. The series demonstrates the effect of varying $N_\infty$ in the former and $WN_\infty$ in the latter (values included as a legend).

ation sites. Recall that when limited by progressive nucleation, the number of nuclei, $N_{(t)}$, at any time t, is defined by the temporal progressive-nucleation function, Eqn. 8.13, but now the $N_\infty$ is modified by the decreasing surface area *not* covered by diffusion zones, i.e. $(1-F_\theta)$, cf. Fig. 8.2:

$$N_{(t)} = \int_0^t WN_\infty(1-F_\theta)dt \tag{53}$$

$1-F_\theta$ is obtained via the Avrami theorem (Eqn. 8.20) on the basis of Eqn. 8.51 as:

$$1 - F_\theta = \int_0^t \exp\left[-\frac{4}{3}\left(\frac{8\pi cM}{\rho}\right)^{1/2} WN_\infty \pi D t dt\right] \tag{54}$$

Inclusion of the expression for $1-F_\theta$, Eqn. 8.54 into that for $N_{(t)}$, Eqn. 8.53 gives:

$$\begin{aligned} N_{(t)} &= \int_0^t WN_\infty \exp\left[\int_0^\tau -\frac{4}{3}\left(\frac{8\pi cM}{\rho}\right)^{1/2} WN_\infty \pi D t dt\right] d\tau \\ &= WN_\infty \int_0^t \exp\left[-\frac{2}{3}\left(\frac{8\pi cM}{\rho}\right)^{1/2} WN_\infty \pi D \tau^2\right] d\tau \end{aligned} \tag{55}$$

$N_{sat}$, the saturation number-density, corresponds to the situation when $t \to \infty$. The solution to this definite integral can be found in published tables (for instance [1:p.A61]):

$$\int_0^\infty \exp[-a^2x^2]dx = \frac{1}{2a}\sqrt{\pi}\ ; \qquad \textit{for } a>0. \tag{56}$$

and thus the solution is:

$$N_{sat} = \frac{1}{2}WN_\infty \sqrt{\frac{\pi}{\frac{2}{3}\left(\frac{8\pi cM}{\rho}\right)^{1/2} WN_\infty \pi D}} = \sqrt{\frac{WN_\infty}{\frac{8}{3}\left(\frac{8\pi cM}{\rho}\right)^{1/2} D}} \tag{57}$$

### 8.4.4. Dimensionless Data Representation

Up to this point we have developed the current-density versus time relations for nucleation laws and deposit geometries most common to the initial stages of deposition of metallic phases onto foreign, inert substrates. In practice, however, it can happen that

the initial region of a deposition transient can be obscured due to charging of the ever-present electrical double-layer, ion adsorption phenomena or nucleation; hence comparison of experimental transients with the developed theoretical relations can prove troublesome. It has thus been found convenient, and is now common to present experimental data for systems under diffusion control in *dimensionless form* [154] by dividing each current and time value by those corresponding to the *current maximum*. This allows examination of whole transient curves and does not restrict analysis to time regimes that may be obscured by other processes. Additionally, this treatment offers some simplifications that enables isolation of some unknowns.

The dimensionless relations are developed here to illustrate the origins of the quantities that will be derived from experiment and discussed with respect to the electrodeposition of Al, subsequently. The current-density, $i_{max}$, and time, $t_{max}$, corresponding to the transient's maximum can be evaluated theoretical by equating the derivatives of Eqns. 8.50 and 8.52 to zero for instantaneous and progressive nucleation, respectively. The derivative for instantaneous nucleation is:

$$\frac{di_{(t)}}{dt} = \frac{d}{dt}\left(\frac{zFD^{1/2}c}{(\pi t)^{1/2}}\left(1 - \exp\left[-\left(\frac{8\pi cM}{\rho}\right)^{1/2} N_{\infty}\pi D t\right]\right)\right) = \frac{d}{dt}\left(\frac{U}{t^{1/2}}(1 - \exp[-Yt])\right) = 0 \qquad (58)$$

The presentation is simplified by substituting dummy variables $U$ for $zFc(D/\pi)^{1/2}$ and $Y$ for $N_{\infty}\pi D \cdot (8\pi cM/\rho)^{1/2}$. Carrying out the differentiation with these parameters gives:

$$-\frac{1}{2}Ut_{max}^{-3/2} + \frac{1}{2}Ut_{max}^{-3/2}\exp[-Yt_{max}] + UYt_{max}^{-1/2}\exp[-Yt_{max}] = 0 \qquad (59)$$

Dividing through by the first term and rearranging gives Eqn. 8.60:

$$1 = \exp[-Yt_{max}](1 + 2Yt_{max}) \qquad (60)$$

An algebraic solution for $t_{max}$ is not known for this transcendental equation, but approximate methods have been used [154] which give as solutions:

$$t_{max\text{-}inst} = \left(\frac{1.2564\rho^{1/2}}{N_{-}\pi D(8\pi cM)^{1/2}}\right) \tag{61}$$

and

$$i_{max\text{-}inst} = 0.6382zFDc\left(N_{-}\left(\frac{8\pi cM}{\rho}\right)^{1/2}\right)^{1/2} \tag{62}$$

Similarly, for progressive nucleation, we have:

$$t_{max\text{-}prog} = \left(\frac{3}{4}\cdot\frac{4.6733}{WN_{-}\pi D}\left(\frac{\rho}{8\pi cM}\right)^{1/2}\right)^{1/2} \tag{63}$$

and

$$i_{max\text{-}prog} = 0.4615zFD^{3/4}c\left(\frac{4}{3}WN_{-}\left(\frac{8\pi cM}{\rho}\right)^{1/2}\right)^{1/4} \tag{64}$$

A considerable simplification of the above expressions for instantaneous and progressive cases is realized when the maxima parameters are combined as $i_{max}^2 \cdot t_{max}$, the results being Eqns. 8.65 and 8.66:

$$\left(i_{max}^2 t_{max}\right)_{inst} = 0.1629(zFc)^2 D \tag{65}$$

and

$$\left(i_{max}^2 t_{max}\right)_{prog} = 0.2598(zFc)^2 D \tag{66}$$

Hence a measure of the diffusion coefficient of the species involved may be easily obtained from examination of the transients' maxima.

Beyond this, the whole transient curves may be compared to the dimensionless $(i_{\infty}/i_{max})^2$ vs. $t/t_{max}$ relations for instantaneous and progressive nucleation. That for the instantaneous case is obtained by dividing Eqns. 8.50 by 8.62, i.e. $i_{\infty}$ by $i_{max}$:

$$\left(\frac{i}{i_m}\right)^2_{inst} = \left(\frac{\dfrac{zFD^{1/2}c}{(\pi t)^{1/2}}\left(1 - \exp\left[-\left(\dfrac{8\pi cM}{\rho}\right)^{1/2} N_{-}\pi Dt\right]\right)}{0.6382zFDc\left(N_{-}\left(\dfrac{8\pi cM}{\rho}\right)^{1/2}\right)^{1/2}}\right)^2 \tag{67}$$

If Eqn. 8.61 is rearranged in terms of $N_\infty$, this expression may be substituted into Eqn. 8.67 which then simplifies to Eqn. 8.68:

$$\left(\frac{i}{i_m}\right)^2_{inst} = \frac{1.9542}{\left(\frac{t}{t_m}\right)}\left(1 - \exp\left[-1.2564\left(\frac{t}{t_m}\right)\right]\right)^2 \qquad (68)$$

Similarly for progressive nucleation Eqn. 8.52 is divided by Eqn. 8.64, which when $N_\infty$ is substituted from a rearranged Eqn. 8.63 gives:

$$\left(\frac{i}{i_m}\right)^2_{prog} = \frac{1.2254}{\left(\frac{t}{t_m}\right)}\left(1 - \exp\left[-2.3367\left(\frac{t}{t_m}\right)^2\right]\right)^2 \qquad (69)$$

These relations, Eqns. 8.68 and 8.69, are independent of the nature of the particular deposit for a diffusion-controlled deposition transient. They are plotted in Fig. 8.6 and show the difference between the two types of nucleation in diffusion-controlled electrocrystallization. The slower, exponential increase in the dashed curve corresponds to continuing nucleation consistent with progressive nucleation.

## 8.5. Experimental Details of the Nucleation Studies

Electrode areas had apparent surface areas of 0.0012 - 0.005 $cm^2$ in the cases of gold and platinum and 0.08 $cm^2$ for all GC electrodes. Electrodes for SEM examination were rinsed with thf inside the glove box in which experiments were conducted, and again with water outside, then dried in air. The deposits thus prepared were sometimes partially resistive which caused problems with sample imaging in the SEM. Imaging requires electrically conductive samples and good electrical contact with the instrument and thus depends on deposit conductivity and its good contact with the underlying substrate electrode.

Current-transients were recorded through the PAR376 current module without signal filtering nor *IR* compensation and stored on a digital oscilloscope. 60 Hz line-noise would often be significant so the data were carefully analyzed when transient features were of a similar magnitude and time-scale as the noise and smoothed by

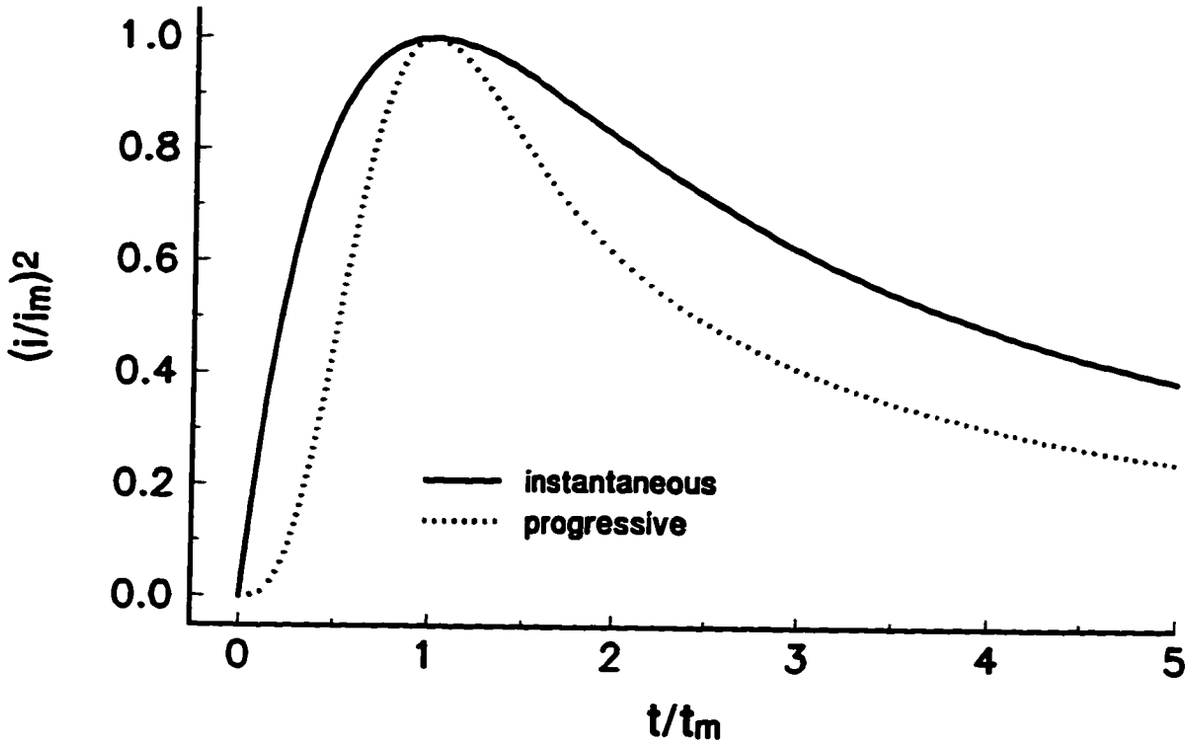


**Fig. 8.6.** Theoretical dimensionless current transients [$(i_{(t)} / i_{max})^2$ vs. $t / t_{max}$] for three-dimensional growth controlled by diffusion nucleated instantaneously (solid line) as per Eqn. 8.68 and progressively (dotted line) as per Eqn. 8.69.

floating-point averaging if this did not alter or skew the results.

The nucleation study protocol was to conduct potential steps on initially clean inert substrate electrodes from a potential region where no deposition occurred (typically about +300 mV vs. the Al pseudo-reference) to varying potentials at which the analyte metal was depositable. Potential steps would be repeated in some cases in order to assure reproducibility and the working electrode was stripped of previously deposited Al between experiments and cleaned by cycling at between 20 and 50 $mVs^{-1}$ in the range from 100 to 500 mV. At the respective extremes of this range, it was ensured that the current did not go cathodic and that the anodic background reaction, significant in some cases, was not appreciable. After cycling in this way until the current response was reproducible (at least 2 minutes), the sweep was stopped and the anodic current allowed to become steady before a subsequent step was initiated. This inter-experiment cleaning protocol was optimized (scan rate, limit or equilibration time) for any given bath in order to ensure reproducibility.

Control experiments were performed to verify the correct functioning of the experimental setup. The deposit morphology and initial current-transients for the deposition of Zn onto GC and of Pb onto GC from nitrate electrolytes were compared, in these control experiments, with results reported in the literature for these systems. The deposition process for the former is known [171] to be kinetically-controlled, with instantaneous nucleation, while that for the latter has been reported [172] to be diffusion-controlled and nucleated progressively. The results obtained from these "control" current-transient experiments and SEM examination corresponded to these previously published results on Zn and Pb deposition.

## 8.6. Foreword to the Results and Discussion Section

The initial stages of electrocrystallization of aluminum onto initially clean, aluminum-free, inert substrate electrodes were examined by conducting potential steps into the voltage range where plating processes became significant. Substrate electrodes examined were Au, Pt and GC. The current-voltage response in cyclic voltammetric experiments on hydride-baths of all compositions (examined in §6.4) on clean inert substrate elec-

trodes always showed a cathodic onset overpotential for the initiation of the plating reaction which is consistent with the nucleation and subsequent growth of the Al phase.

In order to distinguish and examine the current associated with grain growth, the time scale of all transients had to be corrected, as explained below. Grain growth will usually commence only after the initial nucleation and double-layer charging spike has decayed (except, of course, when it is superimposed upon this aforementioned decay, as may happen at higher step potentials); thus the moment corresponding to the current minimum following this spike is taken as time zero and the time scale is corrected accordingly (as $t - t_o$) for each transient.

The shapes of recorded current-transients were complex, varied and in many cases depended in an unpredictable fashion upon the history of the bath and the electrode on which experiments were being conducted. Reproducibility between separate experimental data-sets, on different hydride-bath solutions, for instance, was not good, but from the examination of results from many experiments on different solutions, two general types of behaviour emerged: 1) where the kinetics of incorporation into the growing lattice of hemispherical grains was rate-limiting, as was the case for experiments at GC electrodes; and 2) where diffusion was limiting as was the case for deposition from all solution compositions studied at Au and Pt.

## 8.7. Nucleation at GC

Fig. 8.7 shows current-transients typical of the initial nucleation and growth of an aluminum phase on GC from the hydride-bath. Fig. 8.7a shows a series of transients for an r = 1:3, $[Al]_{total} = 0.4$ M bath for potential steps from +200 to between -80 and -450 mV (vs Al) and Fig. 8.7b shows a corresponding series from +200 to between -100 and -450 mV for an r = 2:1, $[Al]_{total} = 1.0$ M bath.

The initial growth section of all transients was found to be very nearly linear with respect to the *square* of time which, when compared to the theoretical relations which have been reproduced in Table 8.1, would seem to indicate that the current was controlled by the *kinetics of growth of hemispherical grains nucleated instantaneously*. Progressively nucleated, kinetically-controlled, two-dimensional growth, which is also

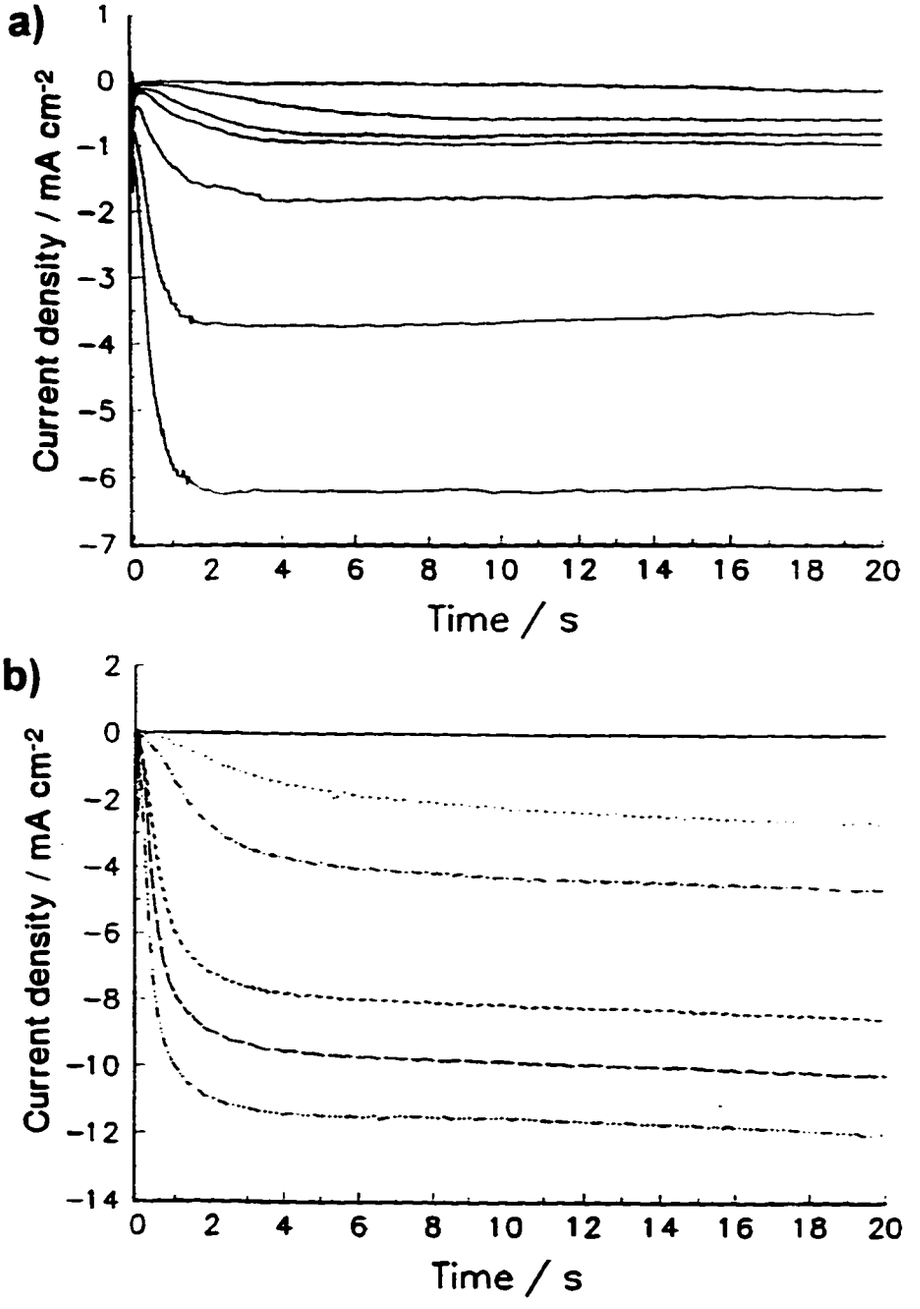


**Fig. 8.7.** Experimental current transients for electrodeposition of Al onto clean GC from a) an r = 1:3, $[Al]_{total}$ = 0.4 M hydride-bath for potential steps from +200 to: -80, -110, -140, -170, -250, -350, -450 mV; and from b) an r = 2.2:1, $[Al]_{total}$ = 1.0 M hydride-bath for potential steps from +200 to: -100, -200, -250, -350, -400 and -450 mV (vs. Al).

modelled by a time squared relation was discarded as a possibility due to the observable appearance of isolated hemispherical (i.e. *not* two-dimensional) nuclei in SEM micrographs (e.g. see Fig. 8.9) and the absence of other characteristics of this type of nucleation and growth in the current-transients, i.e. the slight oscillatory behaviour expected to accompany multi-layer growth (see e.g. Fig. 8.3 and §8.3.4). The length of time of the independent growth was short in duration (restricted to the first few seconds at intermediate step potentials), giving at longer times a current plateau. This behaviour was observed in all step experiments and there was no evidence of diffusion-control in the current-transients. Of note in the transients generated from higher step potentials is the appreciable overlap between the charging and growth features of the transients. This makes uncertain the time-zero, and the exact form of the initial growth relation becomes increasingly difficult to analyze as may be seen in Fig. 8.7 at early times and for larger step potentials.

Two individual current-transients along with their associated charges are examined in detail in Figs. 8.8a and 8.8b for the $H^-$-rich and $Cl^-$-rich baths, respectively, and the entire experimental transients are shown in the insets. *A*, *B* and *C* in Fig. 8.8b indicate the growth, transition and plateau regions, respectively. In Fig. 8.8a the charge passed up to the point where the plateau is reached was found to be about 4 $mC\,cm^{-2}$ for the r = 1:3 bath. This charge was roughly the same for all applied step potentials for this bath and corresponds, in this particular experiment, to *ca.* 5 monolayers of deposited aluminum, taking the theoretical charge for a complete (3 electron) Al (111) monolayer as 870 $\mu C\,cm^{-2}$. For the r = 2:1 bath (Fig. 8.8b) the charge up to the plateau was about 18 $mC\,cm^{-2}$ or 20 equivalent monolayers and was again the same for all step potentials applied in the particular bath. The plateau currents in these transients usually were not constant, as expected from the theory, but usually showed some additional growth feature. Closer inspection of the plateaux in the two examples in the insets of Fig. 8.8 shows evidence of a much slower growth on top of the plateau for the $H^-$-rich bath in the inset of Fig. 8.8*a* and a smooth, possibly linear, increasing plateau current for the $Cl^-$-rich bath in Fig. 8.8*b*. These different behaviours were not specific to any particular bath composition.

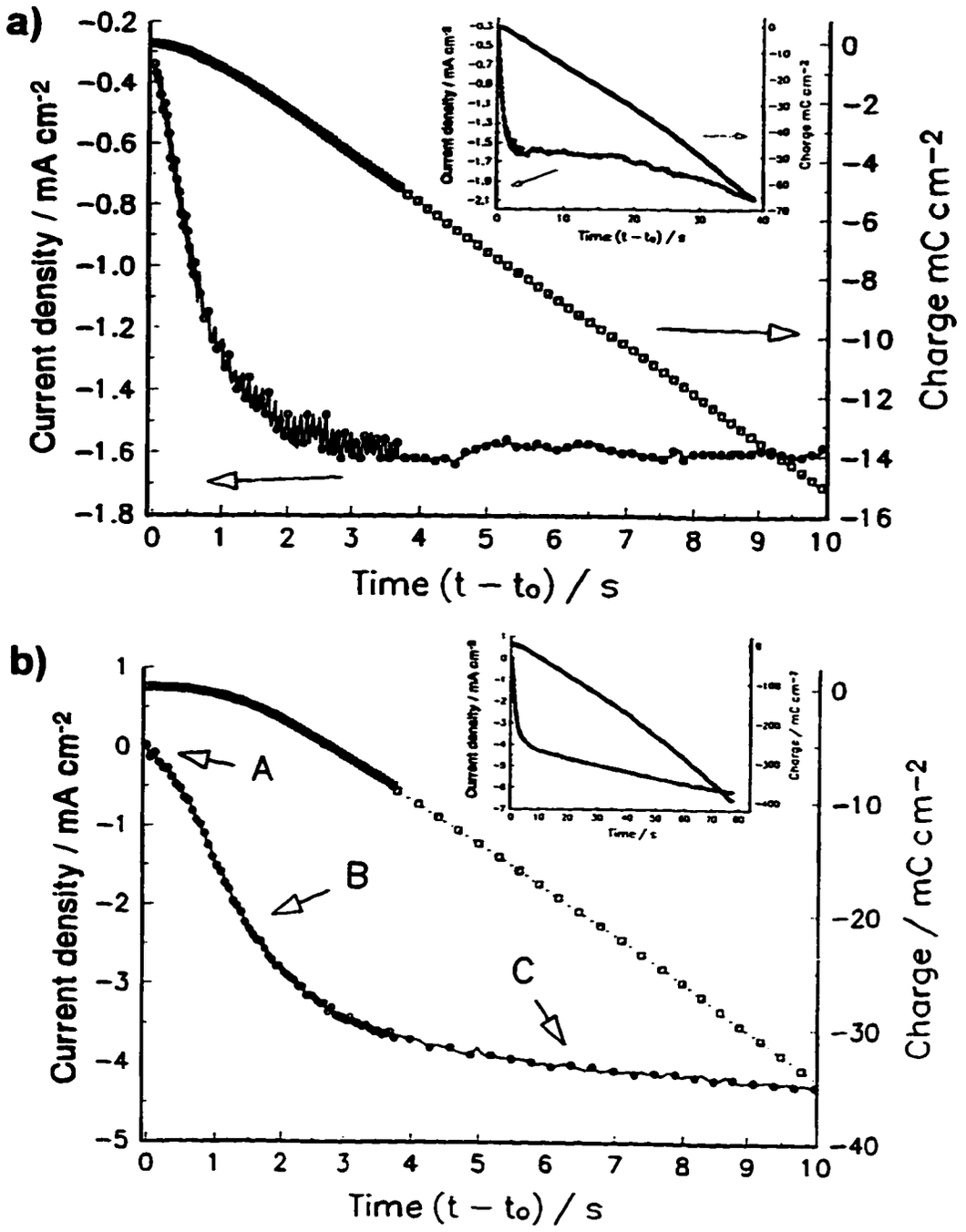


**Fig. 8.8.** Expanded views of two of the experimental current transients from Fig. 8.7. **a)** for the r = 1:3, $[Al]_{total}$ = 0.4 M hydride-bath (+200 to -250 mV) along with its corresponding charge (on the right axis) up to the end of the growth region. The inset is the entire transient. **b)** Similarly for the r = 2.2:1, $[Al]_{total}$ = 1.0 M bath (+200 to -250 mV).

Table 8.1. Current-Density Versus Time Relations For Phase Growth

| Initial transient | Whole transient |
|---|---|
| **Kinetic-control** | |
| *2-D* **Instantaneous** (Eqn. 8.14) $\frac{2\pi zFMhN_{\infty}k^2}{\rho}t$ | (Eqn. 8.29) $\frac{2\pi zFMhN_{\infty}k^2t}{\rho}\cdot\exp\left[-\frac{\pi N_{\infty}M^2k^2}{\rho^2}t^2\right]$ |
| *2-D* **Progressive** (Eqn. 8.19) $\frac{\pi zFMhWN_{\infty}k^2}{\rho}t^2$ | (Eqn. 8.30) $\frac{\pi zFMhWN_{\infty}k^2t^2}{\rho}\cdot\exp\left[-\frac{\pi WN_{\infty}M^2k^2}{3\rho^2}t^3\right]$ |
| *3-D* **Instantaneous** (Eqn. 8.15) $\frac{2\pi zFM^2N_{\infty}k^3}{\rho^2}t^2$ | |
| *3-D* **Progressive** (Eqn. 8.20) $\frac{2\pi zFM^2WN_{\infty}k^3}{3\rho^2}t^3$ | |
| **Diffusion-control** | |
| *3-D* **Instantaneous** (Eqn. 8.42) $\pi zFN_{\infty}\left(\frac{M}{\rho}\right)^{1/2}(2cD)^{3/2}t^{1/2}$ | (Eqn. 8.50) $\frac{zFD^{1/2}c}{(\pi t)^{1/2}}\left(1-\exp\left[-\left(\frac{8\pi cM}{\rho}\right)^{1/2}N_{\infty}\pi Dt\right]\right)$ |
| *3-D* **Progressive** (Eqn. 8.43) $\frac{2}{3}\pi zFWN_{\infty}\left(\frac{M}{\rho}\right)^{1/2}(2cD)^{3/2}t^{3/2}$ | (Eqn. 8.52) $\frac{zFD^{1/2}c}{(\pi t)^{1/2}}\left(1-\exp\left[-\frac{2}{3}\left(\frac{8\pi cM}{\rho}\right)^{1/2}WN_{\infty}\pi D\,t^2\right]\right)$ |

The theory of kinetically-controlled nucleation and growth, assumed to be operative here, would explain the onset of the limiting current plateau as the result of the conclusion of the overlapping of the initially independent hemispherical grains, leading to their complete coalescence into a single continuous phase, and hence a constant current since the deposit's area is supposed no longer to change. In the case here, however, it seems unlikely on geometrical grounds, that the passage of the equivalent of 5 or even 20 monolayers growing three-dimensionally as hemispheres in the two $Cl^-$-rich and $H^-$-rich baths could completely cover the substrate surface. This point was confirmed from the direct observation of the morphology of the deposit.

SEM micrographs of Al deposits grown on GC to charges equivalent to many times (tens or hundreds) that of the start of the plateau mentioned above are shown in Fig. 8.9. They show individual nuclei of various sizes on a smooth GC substrate which is inconsistent with the expected image of a continuous phase produced by intersecting hemispheres, e.g. as was illustrated in Fig. 8.4. The fact that the grains were observed to be of various sizes also does *not* correspond to the growth of an *instantaneously* nucleated deposit as deduced from the best-fit power-of-time within the growth region of the transients. In general, the distribution of Al nuclei on GC was not uniform; for example clumping of nuclei was significant and not restricted to obvious high current-density regions of the substrate surface, e.g. electrode edges and scratches.

Careful examination of the micrographs reveals that the grains do not possess the geometry of perfect hemispheres. The magnification of the deposit given in Fig. 8.9b shows clearly the facetted surfaces of the grains as well as the fact that they seem to actually resemble *spheres* more closely than hemispheres. The reason for this may be a disfavoured interaction between the depositing Al atoms and the growing Al lattice at the base of the grains adjacent to the GC substrate. Such a poor interaction with the substrate would give weak attachment between grain and substrate and therefore poorly adherent deposits as was in fact noted for nearly all deposits of Al on GC substrates. An unfavourable Al-GC interaction might also promote subsequent grain nucleation and growth preferentially on preexisting Al grains; this could offer an explanation for the tendency for aggregation amongst the deposits.

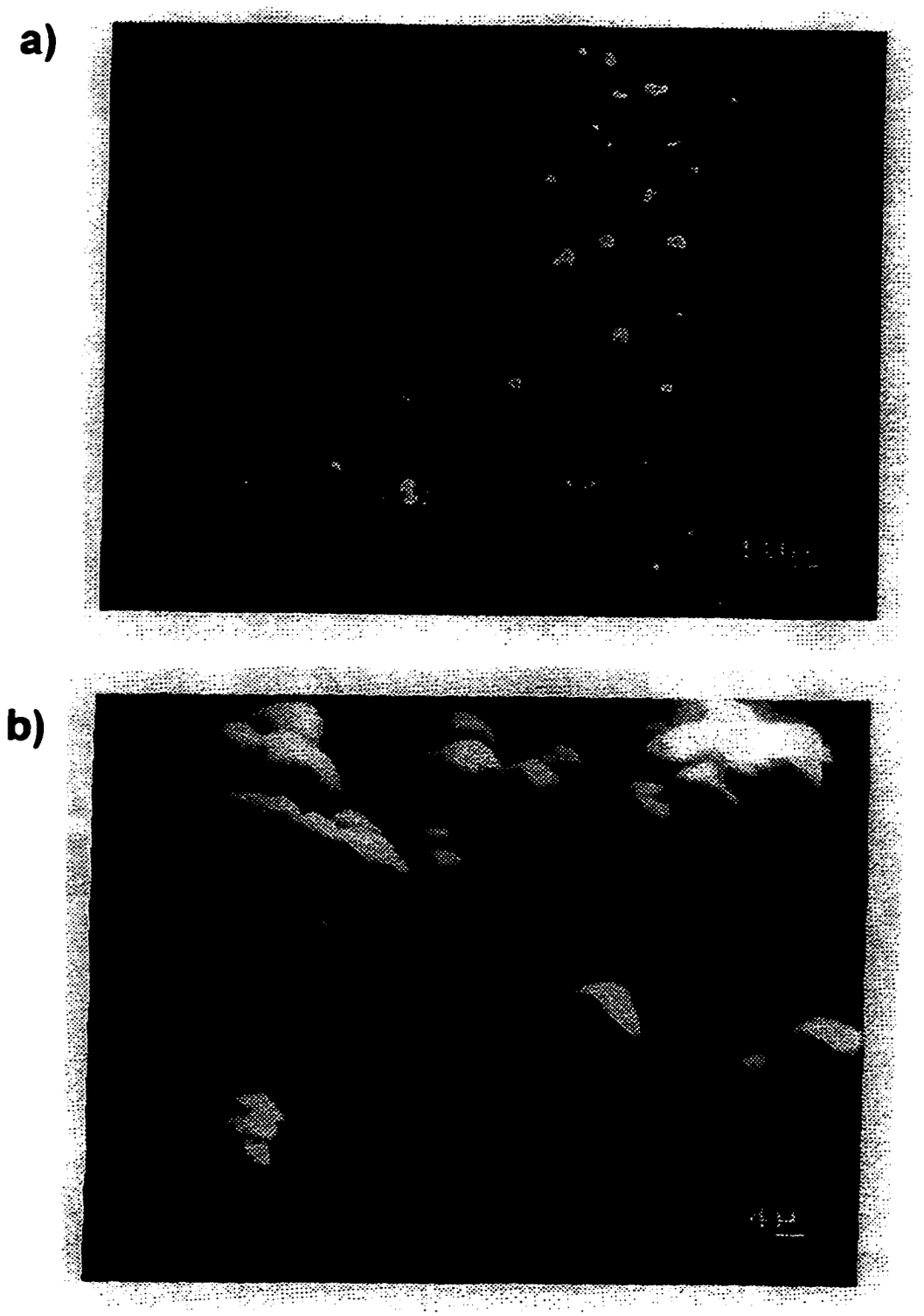


**Fig. 8.9.** Two SEM micrographs typical of Al deposits on GC. In this particular case Al was deposited galvanostatically at 10 $mA\,cm^{-2}$ for 100 s on a 0.08 $cm^2$ GC substrate.

The poor kinetics of nucleation on GC is probably a substrate effect. The glassy carbon electrode material is a network of thin, tangled, crosslinked ribbons of graphite-like sheets [173]. It is highly conductive, but essentially amorphous; thus a crystallographic mismatch between the depositing Al and the GC substrate may explain the kinetic limitation present here. In fact, this unfavourable Al-GC interaction was indicated in cyclic voltammograms recorded at GC, one of which was shown previously in Fig. 6.5 where a surprizingly large potential was necessary for the onset of phase growth on this substrate as compared to that for the Pt and Au substrates studied.

### 8.7.1. The Role of *IR*-Drop in the Potential Step Experiments

*In situ* IR compensation was not used in any of the step experiments for reasons mentioned earlier (§8.6.1). There is the possibility, however, that solution IR drop could have had a significant effect on the form of the experimental transients for this particular substrate, GC. This is due to the fact that the surface areas of the GC substrates were at least an order of magnitude larger than those of the other substrate electrodes, there being a limited selection of small-diameter GC rods available. The use of small-area electrodes will obviously give small absolute currents and therefore minimize IR "losses" even in fairly resistive media.

Solution resistances were appreciable in the hydride-baths; conductances varied between 0.5 - 20 mS $cm^{-1}$ so that the effect of an uncompensated solution resistance during the course of a nucleation and growth experiment would be that instead of a constant driving force for the deposition reaction, the *actual* deposition overpotential would decrease continuously as the current associated with the growing phase increased. This arises because, as the Faradaic current increases, a greater fraction of the applied potential will be dropped through the solution (i.e. $\Delta V = IR$).

In Fig. 8.10 is shown how the *actual* overpotential at the substrate electrode varies over the course of typical current-transients on GC as a percentage of the *applied* potential. The losses at the lower potential, -80 mV, Fig. 8.10a, were small through all of the growth region, i.e. up to *ca.* 2 s, giving a maximum error of 2% or 1.6 mV for the

transient. Losses for the step to -450 mV, Fig. 8.10b, were, however, much larger, from 7 to 10% or 31 to 45 mV over the whole growth region (*ca.* 0.2 s). As the transient progresses the driving force for deposition therefore decreases as the transient current becomes increased, leading to an underestimation of the power-of-time characterizing the growth regime. The error is thence smaller for smaller step potentials; thus only the smaller current-transients should be used to analyze the kinetics of growth of the phase and these with some caution.

This variation of the driving force can significantly alter the electrodeposition reaction; this is because there is potential-dependence of the number of available nucleation sites ($N_\infty$) and of the rate constants both for conversion of nucleation sites into actual grains and for the electron-transfer associated with the deposition process (§2.4).

### 8.7.2. Summary Concerning Behaviour at GC

GC is not a particularly interesting substrate on which to electroplate Al. The rather poor adhesion to, and relative difficulty to nucleate Al on GC does, however, serve to emphasize the role of the underlying substrate in the deposition of Al. The observed Al deposition transients appeared to correspond to growth of instantaneously-nucleated hemispheres, but micrographs of typical deposits were, in fact, only sparsely covered with individual nuclei of distributed sizes, inconsistent with the prediction of this sort of nucleation and growth model. The behaviour of Al on GC is thus complex, deviating significantly from expectations based on established theory.

## 8.8. Nucleation on Gold

### 8.8.1. Current-Transients

Unlike that on GC, the initial nucleation and growth of an Al phase on Au was found to be diffusion-controlled. The behaviour at Pt was similar to that at Au and will therefore not be discussed in detail here. Figs. 8.11a and 8.11b show current-transients at Au corresponding to depositions from the $Cl^-$-rich and $H^-$-rich baths respectively. Currents were larger in the $Cl^-$-rich bath. For all transients a double-layer and nucleation spike was observed initially after stepping, followed by a growth which quickly slowed,

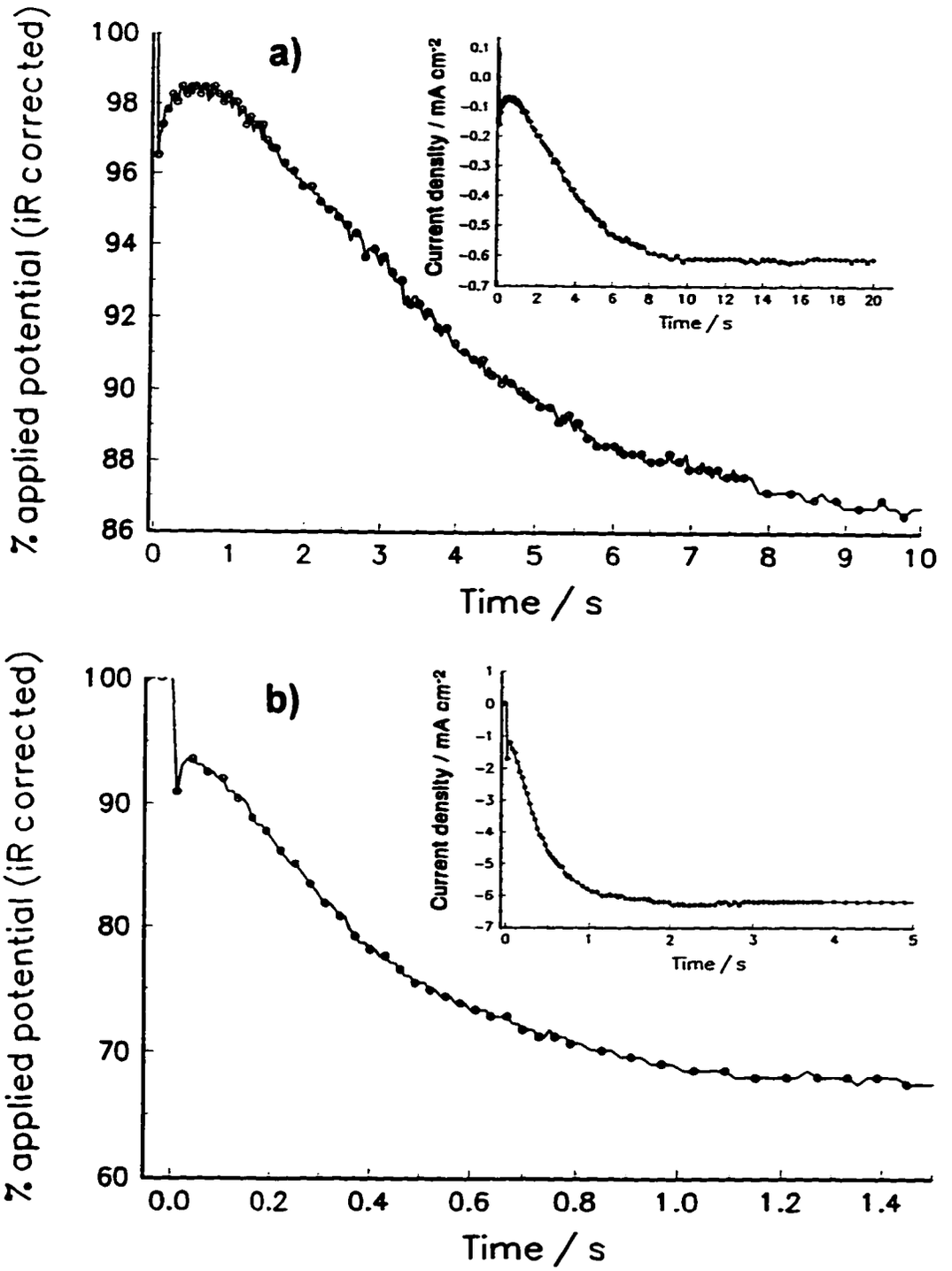


**Fig. 8.10.** Plots of the overpotential, expressed as a percentage of that initially applied, over the course of two transients experiments for the $H^-$-rich bath: **a)** +200 to -80 mV; and **b)** +200 to -450 mV. Insets show the actual current transient.

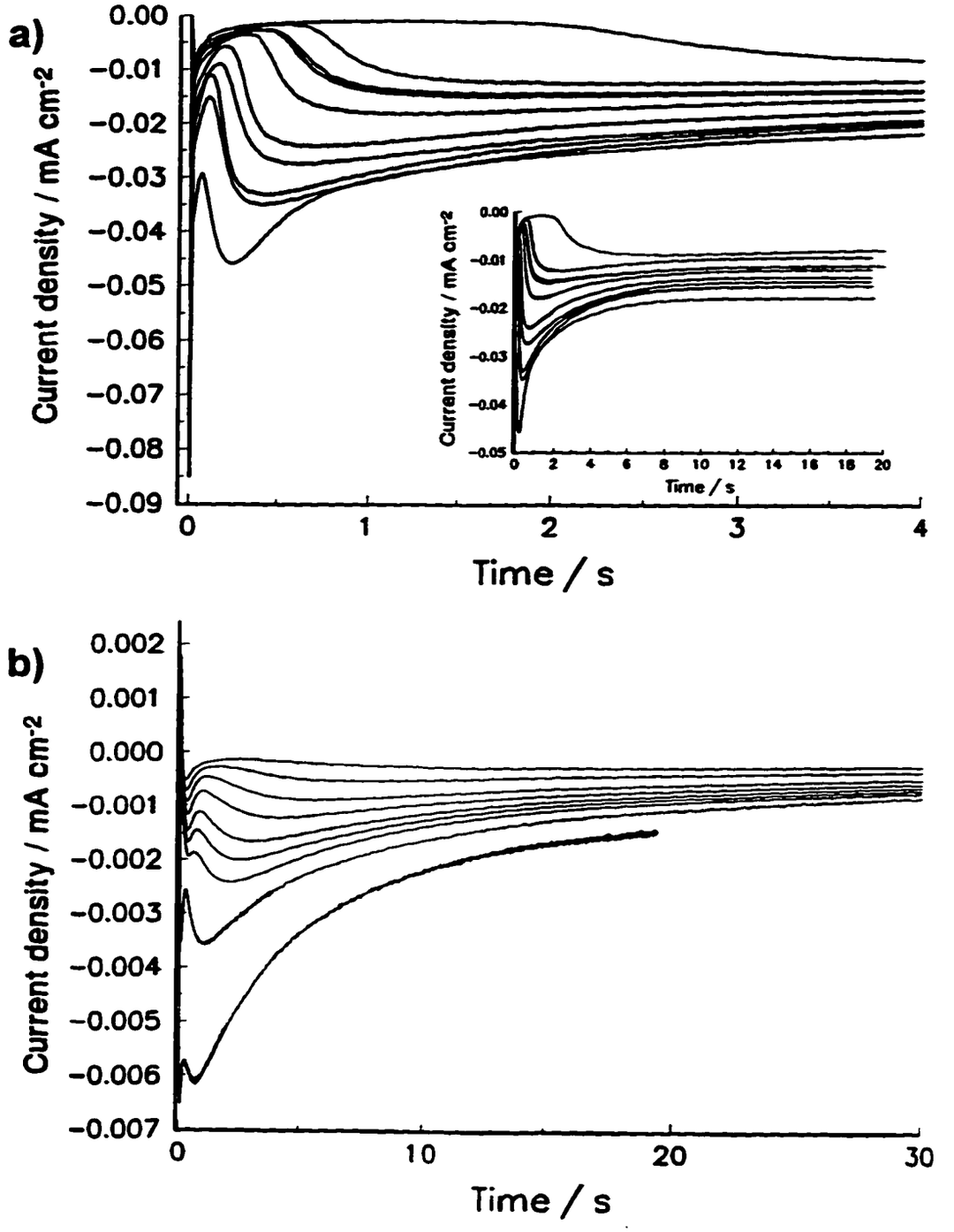


**Fig. 8.11.** Experimental current-transients for electrodeposition of Al onto clean Au **a)** for an r = 2:1, $[Al]_{total}$ = 0.8 M hydride-bath for potential steps from +200 to: -100, -120, -150 (3x), -170, -220, -270, -300, -350, -500 mV (the inset shows the same transients to longer times); and **b)** for an r = 1:3.3, $[Al]_{total}$ = 0.4 M hydride-bath for potential steps from +200 to: -320, -340, -360, -380, -400, -430, -460, -490 and -600

passed through a peak current and then gave a decay proportional to $t^{-1/2}$. The growth, peak and decay are modelled by the overlap of independent diffusion zones, and the type of nucleation (instantaneous or progressive) can be established from the most linear power-of-time plot for the initial growth region (with reference to Table 8.1).

This power-of-time comparison is illustrated most clearly by plotting a *single* transient for different powers of time, i.e. 1/2, 1, 3/2 and 2 which has been done for two separate transients in Figs. 8.12*a* and *b*. The drawn linear-regression lines (all calculated from a corrected time "zero") give a visual indication of the goodness of fit of the plots in different powers of time. They are included only for those curves that are close to being linear; for instance, in Fig. 8.12a the line for the $t^1$ is omitted due to the obvious curving relation for the data plot. The inset of this figure shows the actual transient, i.e. in $t^1$, over a longer time interval, to just beyond the current maximum and this illustrates the actual duration of the growth region (with respect to the entire transient) from which slope, and hence the applicable nucleation and growth law, were determined. In order to properly compare the best-fit power-of-time relation in Fig. 8.12, it must be emphasized that the actual data representation (solid curve) is the only curve for which data are uniformly distributed along the x-axis and thus the best-fit curve is identified as that which maintains linearity the furthest *down* the y-axis on the basis of a comparison of an equal number of data points. Limits had to be chosen guardedly and greater weighting given to shorter time points so as to avoid confusion between a transition region, due to overlap, with the actual growth region.

The transients were clearly not linear in either $t^{1/2}$ or $t^1$, but were more difinitely linear in either $t^{3/2}$ or $t^2$. The difference between these latter was, however, often quite subtle and in fact many transients were found to be best-fitted to $t^2$ for the very short time data points of the transients, which, recall, corresponds to kinetically-controlled growth (cf. Table 8.1). However, a $t^{3/2}$ relation would often give a longer linear region, but would not provide satisfactory fitting to the very first few points. This general trend is observable by comparing the $t^{3/2}$ and $t^2$ curves in Fig. 8.12 for very early times. The peak current, followed by decay, would clearly indicate the role of diffusion in the process contradicting a kinetic control, but the better fit for the very short-time data

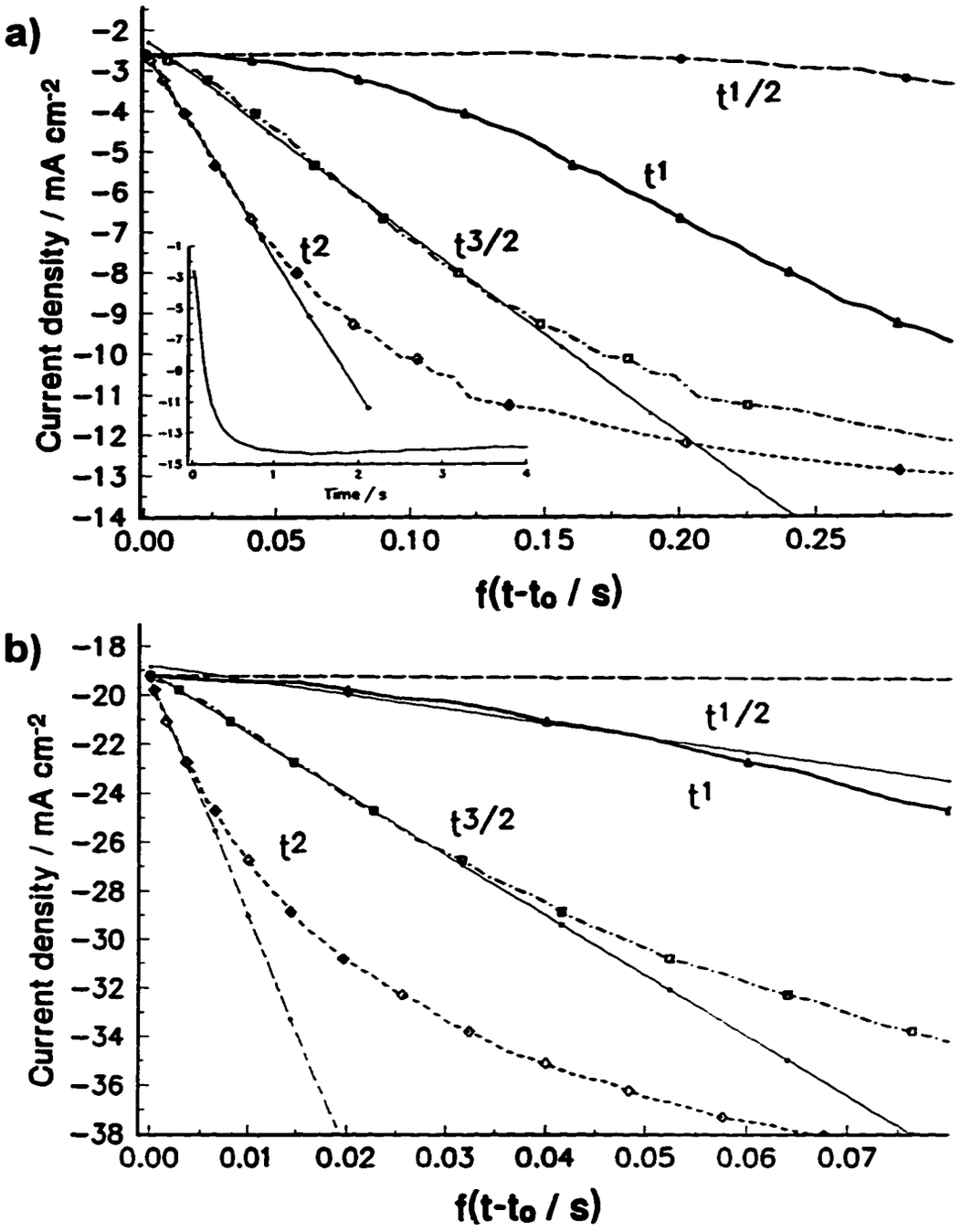


**Fig. 8.12.** Current-transients from **a)** +200 to -150 mV; and **b)** +200 to -400 mV plotted versus time to the powers 1/2, 1, 3/2 and 2 for a Au substrate in an r = 2:1, $[Al]_{total}$ = 0.8 M hydride-bath. The inset in **a** shows the same transient to just beyond the current maximum, thus demonstrating the growth region with respect to the whole

points for $t^2$ was consistently observed and is therefore a significant observation considering that the theoretical nucleation and growth relations (Table 8.1) should be expected to apply especially at the very beginning of deposit growth.

### 8.8.2. Dimensionless Analysis

Current-transients corresponding to the onset of diffusion-limited electrodeposition have been effectively analyzed in dimensionless form [154,170] as was indicated in §8.4.4; thus the current-transients of Fig. 8.11a ($Cl^-$-rich) have been plotted as $(i_{(t)}/i_m)^2$ vs $(t/t_m)$, in Fig. 8.13 and those for Fig. 8.11b ($H^-$-rich) in Fig. 8.14. These plots are expected to be independent of the characteristics of a given plating species, e.g. its diffusion coefficient, concentration, molecular weight, etc., depending only on the type of nucleation involved (see §8.4.4). The two theoretical dimensionless plots (Eqns. 8.68 and 8.70) are included with the plotted data in Figs. 8.13 and 8.14 for the cases of instantaneous (solid line) and progressive (dashed lines) nucleation.

The data for the hydride-bath did not correspond particularly closely to either of the two ideal, "whole-transient" curves, although it is known [170] that many systems indeed do. Most whole experimental curves for the hydride-bath appeared to more closely parallel the theoretical curve for *instantaneous* nucleation (see Figs. 8.13a and 8.14a), even though earlier analysis (§8.9.1) of the power-of-*t* relation for the original transients (as in Fig. 8.12) indicated that the deposit was nucleated *progressively*. Although the experimental dimensionless transients corresponded more closely to the case of instantaneous nucleation, a more critical examination of an expansion of the prepeak region in Figs. 8.13b and 8.14b, revealed that the initial growth was "*progressive*" in character. At larger step potentials the decay of the initial charging spike increasingly overlaps and obscures the growth-transient and this accounts for the larger deviations from ideal curves at time zero for higher step potentials.

For the $Cl^-$-rich bath (Fig. 8.13), the current response after the maxima was larger than either of the ideal dimensionless models, while that for the $H^-$-rich bath (Fig. 8.14) seemed to correspond more closely to the instantaneous nucleation model, even though

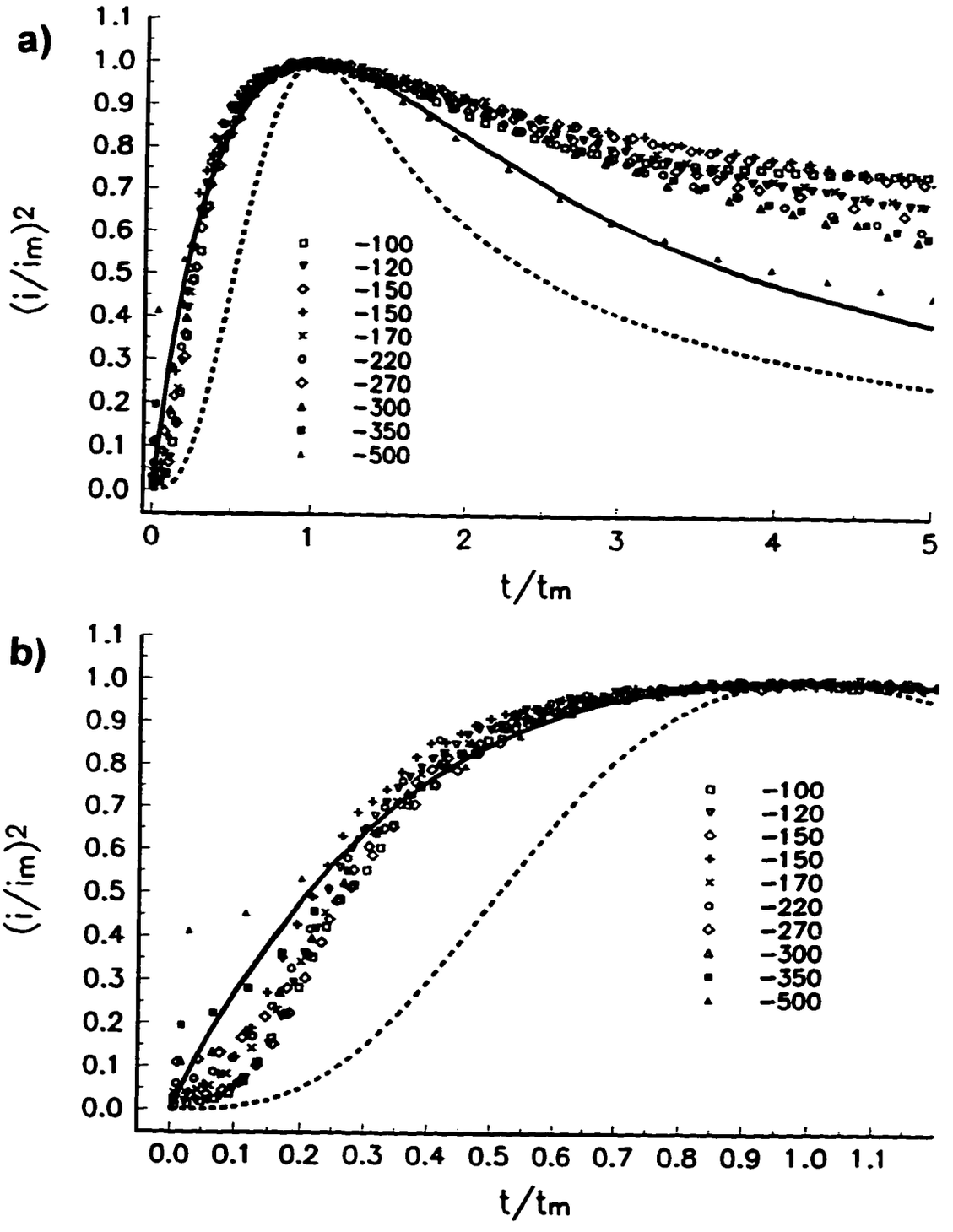


**Fig. 8.13. a) & b)** Dimensionless representation ($(i/i_m)^2$ vs $t/t_m$) of current-transients for data of Fig. 8.11a for step overpotentials indicated in the figure. **b)** Same data as in a, redrawn to expand the initial portion of the curves. The theoretical curves for instantaneous (solid) and progressive (dashed) are included.

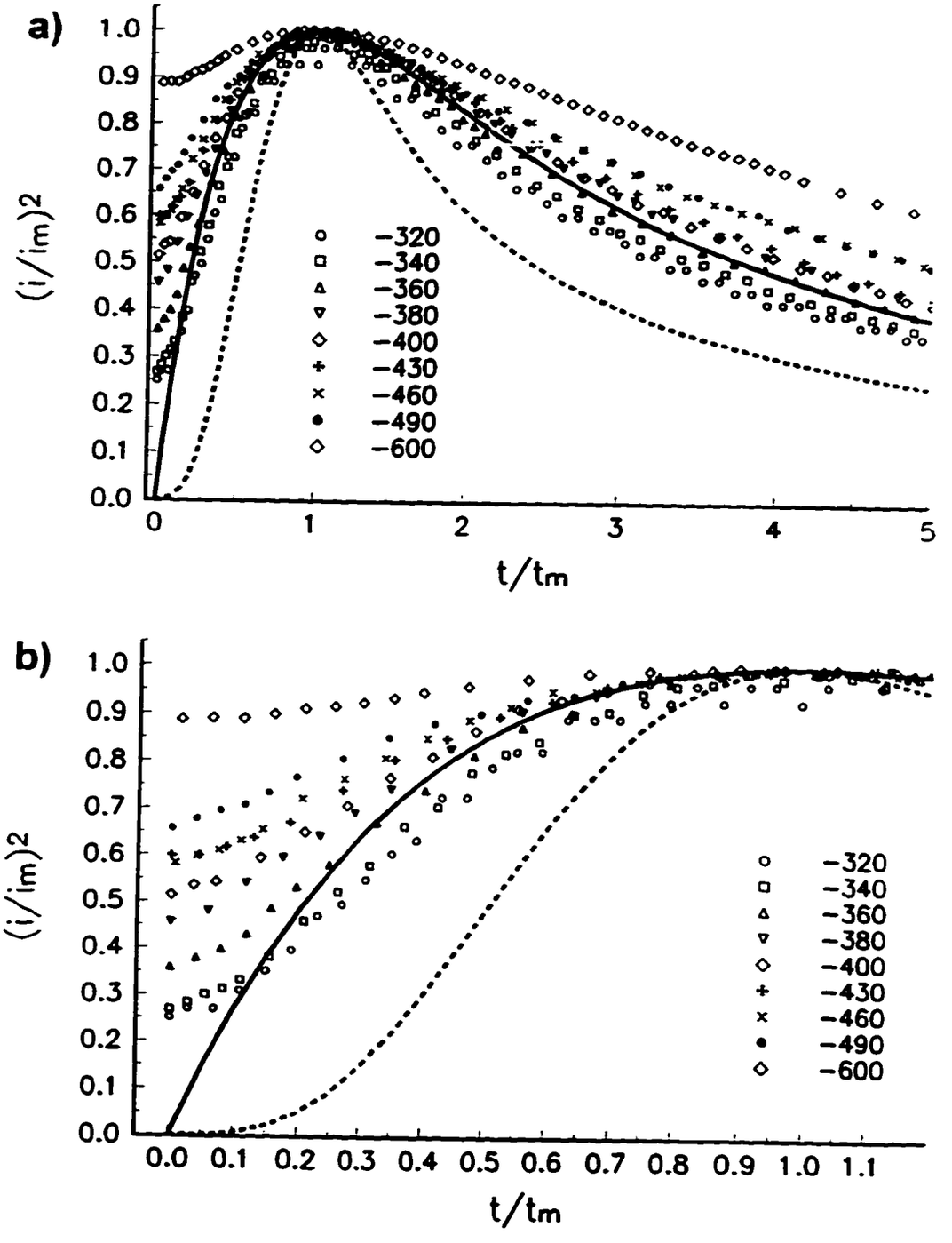


**Fig. 8.14.** **a) & b)** Dimensionless representation $((i/i_m)^2$ vs $t/t_m)$ of current-transients for data of Fig. 8.11*b* for step overpotentials indicated in the figure. **b)** Same data as in **a**, redrawn to expand the initial portion of the curves. The theoretical curves for instantaneous (solid) and progressive (dashed) are included.

the shape of the initial stages of all current-transients qualitatively indicated progressive nucleation. The larger than ideal currents after the maxima indicate subsequent nucleation and such a scenario is consistent with the observed macroscopic morphology of Al deposits from the hydride plating baths (examined in §8.9.6).

### 8.8.3. Diffusion Coefficients

#### 8.8.3.1 Current Maximum

The $(i^2 t)_{max}$ product of the maximum of each transient has been shown to reduce to a simple expression (see Eqn. 8.65 or 8.66) involving only c and D, the concentration and diffusion coefficient of the depositing species, respectively, and the product should be a constant for a given plating reaction for all step potentials if *c* and *D* are likewise constant. The $(i^2 t)_{max}$ products and the derived diffusion coefficients, $D_{max}$'s for the results obtained in hydride-baths of r = 2:1 and 1:3, the current-transients for which were shown in Fig. 8.11, are included in Tables 8.2 and 8.3, respectively. $D_{cottr}$ values, i.e. diffusion coefficients derived from the decaying portion of the current-transients proportional to $t^{-1/2}$, following the current maximum (see Fig. 8.11), are also included in these tables, and will be examined in the next section.

Table 8.2. Current-Transient Analysis for an r = 2:1, $[Al]_{total}$ = 0.8 M Bath

| $\eta$ mV | $i_{max}$ mA cm$^{-2}$ | $t_{max}$ s | $(i^2 t)_{max}$ A$^2$ s cm$^{-4}$ x10$^{-4}$ | $WN_\infty / cm^{-2} s^{-1}$ max x10$^{+7}$ | slope x10$^{+8}$ | $N_{sat}$ cm$^{-2}$ x10$^{+7}$ | $D_{Max}$ cm$^2$ s$^{-1}$ x10$^{-8}$ | $D_{Cottr}$ cm$^2$ s$^{-1}$ 10$^{-8}$ |
|---|---|---|---|---|---|---|---|---|
| -100 | 9.1 | 6.34 | 5.25 | 0.2 | 0.05 | 0.60 | 3.77 | 0.47 |
| -120 | 12.5 | 1.57 | 2.45 | 5.8 | 0.12 | 5.25 | 1.76 | 0.43 |
| -150 | 14.9 | 1.23 | 2.72 | 8.5 | 0.54 | 6.03 | 1.95 | 0.36 |
| -150 | 14.7 | 1.22 | 2.63 | 8.9 | 1.56 | 6.30 | 1.88 | 0.39 |
| -170 | 18.3 | 0.83 | 2.78 | 18.1 | 3.67 | 8.71 | 2.00 | 0.76 |
| -220 | 24.3 | 0.51 | 3.01 | 44.3 | 3.49 | 13.09 | 2.16 | 1.44 |
| -270 | 27.5 | 0.48 | 3.59 | 42.8 | 4.90 | 11.78 | 2.58 | 2.05 |
| -300 | 33.3 | 0.33 | 3.60 | 91.1 | 11.90 | 17.16 | 2.59 | 2.27 |
| -350 | 34.8 | 0.29 | 3.45 | 123.6 | 9.78 | 20.43 | 2.48 | 2.68 |
| -500 | 46.0 | 0.17 | 3.49 | 364.7 | 17.80 | 34.89 | 2.51 | 1.54 |

Table 8.3. Current-Transient Analysis for an r = 1:3, $[Al]_{total}$ = 0.4 M Bath

| $\eta$ mV | $i_{max}$ mA cm$^{-2}$ | $t_{max}$ s | $(i^2t)_{max}$ A$^2$ s cm$^{-4}$ x10$^{-5}$ | $WN_\infty$ / cm$^{-2}$ s$^{-1}$ max x10$^{+7}$ | slope x10$^{+8}$ | $N_{sat}$ cm$^{-2}$ x10$^{+8}$ | $D_{Max}$ cm$^2$ s$^{-1}$ x10$^{-9}$ | $D_{Cottr}$ cm$^2$ s$^{-1}$ x10$^{-9}$ |
|---|---|---|---|---|---|---|---|---|
| -300 | 0.27 | 10.58 | 0.08 | 15.0 | - | 9.20 | 0.21 | - |
| -320 | 0.53 | 5.98 | 0.17 | 21.7 | 1.48 | 7.54 | 0.44 | 0.54 |
| -340 | 0.89 | 4.42 | 0.35 | 19.5 | 1.29 | 5.00 | 0.90 | 1.17 |
| -360 | 1.23 | 3.10 | 0.47 | 29.5 | 1.71 | 5.30 | 1.21 | 1.76 |
| -380 | 1.66 | 2.08 | 0.57 | 53.0 | 2.63 | 6.39 | 1.50 | 2.69 |
| -400 | 2.01 | 1.73 | 0.70 | 63.0 | 1.82 | 6.32 | 1.82 | 3.61 |
| -430 | 2.43 | 1.42 | 0.84 | 77.8 | 1.85 | 6.41 | 2.19 | 4.25 |
| -430 | 4.40 | 0.98 | 1.90 | 72.4 | 3.58 | 4.11 | 4.94 | 6.59 |
| -460 | 4.08 | 0.90 | 1.49 | 110.8 | 4.18 | 5.75 | 3.87 | 6.91 |
| -490 | 4.38 | 0.79 | 1.51 | 139.7 | 3.57 | 6.40 | 3.94 | 7.94 |
| -600 | 6.15 | 0.42 | 1.59 | 470.8 | 24.90 | 11.46 | 4.14 | 13.37 |

For the $H^-$-rich bath (r = 1:3) the $(i^2t)_{max}$ data (column 4, Table 8.3), instead of being constant as expected, varied by nearly an order of magnitude between 0.17 to 1.59 x $10^{-5}$ $A^2cm^{-4}s$, increasing with step potential, while in the $Cl^-$-rich bath the range of these values was more limited between 2.45 and 5.25 x $10^{-4}$ $A^2cm^{-4}s$; it also varied less with potential than was the case for the $H^-$-rich bath. The potential-dependence of the $(i^2t)_{max}$ products for the $H^-$-rich and $Cl^-$-rich baths translated into similar trends for the calculated diffusion coefficients and this will be discussed below (§8.9.3.3).

### 8.8.3.2. "Cottrell-ian" Current Decay

Diffusion coefficients for species in the hydride-bath can be calculated from the current maxima of growth-transients, but they can also be derived from the current decay following the maximum where this is proportional to $t^{-1/2}$. This $t^{-1/2}$ relationship is diagnostic of the decay of a diffusion-limited process. If the step potential for a given experiment is sufficiently large, ensuring that the surface concentration of the depositing species is reduced to zero so that simple boundary conditions obtain for solution of the semi-infinite linear diffusion problem, then the slope of the current decay can be substituted into the Cottrell equation (Eqn. 8.44), rearranged as:

$$D_{Cottr} = \left(\frac{di_{(t)}}{dt^{-1/2}} \cdot \frac{\pi^{1/2}}{zFc}\right)^2 \quad (70)$$

to yield a diffusion coefficient for species involved in the electrode reaction. $D_{Cottr}$ values, calculated from transients in Fig. 8.11 for the two hydride-baths are included in Tables 8.2 and 8.3 (see $D_{Cottr}$ column) and were observed to vary by a factor of 20 and 5 between the step potential extremes in the $H^-$ and $Cl^-$ rich baths, respectively.

Ideally, the decays for all step potentials should converge (as demonstrated in the simulated transients in Fig. 8.5) to a single, limiting, current decay that is defined by the diffusive relaxation process. However, instead of converging as time progresses, all the experimental curves in Fig. 8.11 seemed to attain their own limiting-current values, these tending to be greater for larger step potentials. This feature is probably due to subsequent growth processes that become more prominent with increasing potential.

### 8.8.3.3. Diffusion Coefficients of the Aluminates

Diffusion coefficients are essentially rate constants for the movement or *flux*, $J_{(x,t)}$, of species across a concentration gradient, $\partial c_{(x,t)} / \partial x$ (where x is position and t time), according to Fick's first law of diffusion:

$$-J_{(x,t)} = D\frac{\partial c_{(x,t)}}{\partial x} \quad (71)$$

and are measures of the transport properties of species through a particular medium. Generally, diffusion coefficients of solutes, both ionic and uncharged, in water range from $10^{-6}$ - $10^{-5}$ $cm^2 s^{-1}$ [103:p.77]. Those calculated for species in the $H^-$-rich bath (Table 8.3) were less than $0.5 \times 10^{-8}$ $cm^2 s^{-1}$ and markedly potential-dependent, while those in the $Cl^-$-rich bath were *ca.* $2.5 \times 10^{-8}$ $cm^2 s^{-1}$, but independent of potential. These values are surprisingly low considering that the viscosity of thf is about half that of water (see Table 1.3) which should have resulted in larger relative values for the derived diffusion coefficients. These anomalously low values are likely the result of experimental limitations due to performing experiments in such poorly conductive media (as explained below).

It was not possible to employ a large concentration of an inert supporting electro-

lyte in these investigations due to solubility limitations and ion-pairing in thf. A supporting electrolyte increases solution conductivity and serves to "swamp-out" electrostatic attraction between the charges of electroactive species and that of the electrode (this latter being variable with applied potential), which, in the study of diffusion, removes the influence of analyte migration and thus isolates the diffusion behaviour of electroactive solutes. Thf has a low dielectric constant and in it common inert electrolytes have low solubilities. Tetramethylammonium-tetrafluoroborate, the electrolyte that exhibited the greatest solubility in the hydride-bath system, was used in several experiments, but was found to adversely affect the longevity of the baths and generally did little to improve bath conductivity, which means that the electrolyte ions probably remained associated in this solvent. An additional concern was the unknown effect that ancillary species might have had on the complicated ligand-exchange equilibria that control the aluminate distribution (characterized in Chapter 5) and hence the chemical and electrochemical reactivity of the hydride-baths. For these reasons supporting electrolytes were generally not employed and as a result, electrolytic *migration* could have been a significant interferant in the diffusion experiments, particularly in the $H^-$-rich baths where nearly all the depositable species are *anions*. Anions would be repelled by the negative charge on the working electrode required to electrodeposit Al.

For the $H^-$-rich bath data in Table 8.3 the apparent potential-dependence of the derived diffusion coefficients can be explained by considering bath composition, which has been shown in Chapter 5 to be a complicated mixture of uncharged, anionic and cationic aluminate complexes of varying ligand ($Cl^-$ and $H^-$) substitution and degree of solvation, and their distribution depends on a given bath's formal compositional ratio, $r$ (see §5.2 and Eqn. 5.6). These aluminate complexes, many of which can be electrochemically deposited, have been shown to possess varying chemical, and probably also electrochemical, reactivities (§5.6).

With this varying reactivity of the component species in mind, the apparent potential-dependence of the measured diffusion coefficients for the hydride-baths is best thought of as a systematic error in their calculation. The concentration used for the diffusion coefficient calculations was in all cases that of the *total* aluminum determined for

each bath, although generally some unknown proportion of the component aluminates will not deposit Al at all. This gives an overestimated concentration of depositing species. The distribution of reactivities of the depositable aluminates gives rise to a potential-dependence in that, at smaller step potentials, the less reactive aluminates will not participate in the electrode reaction or, alternately, their concentrations might not be reduced to zero at the electrode surface (a required boundary condition for the solution of the diffusion equation laws).

Generally, $Cl^-$-rich baths are composed, in the cases of the aluminates known to be depositable, of $AlHCl_3^-$ and $AlHCl_2 \cdot 2thf$ (see $^{27}$Al-NMR §5.4.2 and Fig. 5.4a) where the anion was usually of low abundance. This means that there is only a single species that participates in the reduction reaction in this bath type. On the other hand, the $H^-$-rich baths possess a more even distribution of depositable species (i.e. $AlHCl_3^-$, $AlH_2Cl_2^-$, $AlH_3Cl^-$ [see Fig. 5.3a]) which, if these had different reactivities, would give a varying concentration of diffusing species with changing potential. At higher growth potentials larger fractions of the available aluminate complexes would become electrochemically accessible giving an increased concentration of diffusing species and ergo an apparent potential-dependence for the measured diffusion coefficient.

Another complicating factor is that aluminates of varying ligand-substitution and solvent-coordination are of different sizes, e.g. $Cl^-$ is more bulky than $H^-$, which means that all these aluminates would possess different diffusion coefficients, and thus a derived diffusion coefficient would be some weighted average of the values for all the aluminates plating at the particular experimental growth potential.

These trends in the measured D's are consistent with diffusion through *solution*. Diffusion of adatoms along the substrate surface or ligands, decomplexed during the electrochemical reaction, away from the substrate or through a growing Al phase would not have shown the same dependencies on composition and potential.

#### 8.8.3.4. Summary of Diffusion Behaviour in the Hydride-Bath

The diffusion coefficients calculated from either the current maxima or current decays after initiation of deposition onto a foreign substrate gave similar values and

trends. D's were about an order of magnitude larger in the $Cl^-$-rich than $H^-$-rich baths. Electrostatic repulsion could explain this difference where reducible species in the $H^-$-rich baths, which are mostly *anions*, would be repelled and hence slowed more than those in $Cl^-$-rich baths where most electrodepositable aluminate complexes are neutral. The negative potentials required to electrochemically deposit aluminum would repel the anionic species that dominate the $H^-$-rich baths. The magnitude of the D's were smaller, however, than would have been expected in thf, given its relatively low viscosity.

### 8.8.4. Active Site Density: $N_\infty$

On any substrate there is a distribution of possible sites for development of foreign nuclei and they arise mainly from heterogeneity of the substrate surface. Associated with such sites is a distribution of energies. As the step potential in a nucleation experiment becomes larger, more sites become accessible which makes $N_\infty$, the maximum number of nucleation sites, potential-dependent. $N_\infty$ determines the basic characteristics of a deposit's adhesion and ultimate morphology on a particular substrate. In the case of progressive nucleation (seemingly the case for Al electrodeposition on Au and Pt), $N_\infty$ is not practically separable from the rate constant for site-to-nucleus conversion, W, although it could be done by the tedious procedure of manually counting the nuclei on each substrate electrode by SEM examination or, using double-pulse experiments [174] and optical examination, for *each* experimental transient.

The product of the two terms, $WN_\infty$, is called the *steady-state nucleation rate*, $i_{nucl}$. It can be calculated from experimental current-transient data from either the current maximum ($t_{max\text{-}prog}$ or $i_{max\text{-}prog}$, i.e. Eqn. 8.63 or 8.64) or from the slope of the initial growth transient to the appropriate power-of-time (Eqn. 8.43 for progressive nucleation). Both quantities composing $i_{nucl}$ have unknown dependencies on potential, but together they can be related to the number of atoms in the so-called critical nucleus, $n_{cn}$, and the work for its formation, $W_{cn}$, in Eqn. 8.73. This expression is based on the so-called atomistic model of nucleation in metal electrodeposition ([175] and references therein).

$$i_{nucl} = K_1 \exp\left[\frac{-W_{cr}}{k_B T}\right] \exp\left[(n_{cr} + 1 - \alpha)\frac{ze_o\eta}{k_B T}\right] \quad (72)$$

In Eqn. 8.72 $e_o$ is the value of elemental charge, $k_B$ the Boltzmann constant, $\alpha$ the electrochemical transfer coefficient, $K_1$ is a preexponential factor, $z$ the number of electrons required to deposit the metal and $\eta$ the potential. Note that a critical nucleus is one that contains just enough atoms to grow into a grain, where all subcritical nuclei simply redissolve.

$WN_\infty$ values, calculated from the current maxima and initial slopes, are included in Tables 8.2 and 8.3 (columns 5 and 6) for the $Cl^-$-rich and $H^-$-rich baths. The natural logarithms of the values calculated from the current maxima, i.e. in column 5, are plotted vs. step potential in Fig. 8.15. Those values based on $i_{max}$ are probably superior to those based on initial slopes due to the considerable overlap of the growth transient with the capacitance/nucleation spike at higher step potentials.

The slope of a plot of $ln\, i_{nucl}$ versus $\eta$ will be proportional to the argument of the second exponential term in Eqn. 8.72 and ergo the number of atoms, $n_{cr}$, in the critical nucleus. It is not unusual for the slope of the relation in Fig. 8.15 to change discretely as the number of atoms required to form a critical nucleus decreases with increasing step potential [176]. Both $Cl^-$-rich and $H^-$-rich baths showed linear regions of similar slope at higher potentials which gave values for the critical nucleus of $n_{cr} = (0.09[\pm 0.02] - \alpha)$. If $\alpha = 1/2$, the critical nucleus size has a negative value in the present case which is meaningless according to the theory. The $Cl^-$-rich bath showed another region of linearity at lower step potentials that gave $n_{cr} = (0.44[\pm 0.15] - \alpha)$ which closely corresponds to a critical nucleus of *zero* atoms, which means that the active sites on the substrate are themselves the critical nuclei. It is not unusual to see low values for $n_{cr}$ (typical sizes of the critical nucleus can be less than five [176-178]).

The results at low step potential would seem to suggest that nucleation on Au is not a limitation to deposition. The apparent negative $n_{cr}$ value determined at higher potentials would seem to indicate that the theory, upon which the calculation is based, no

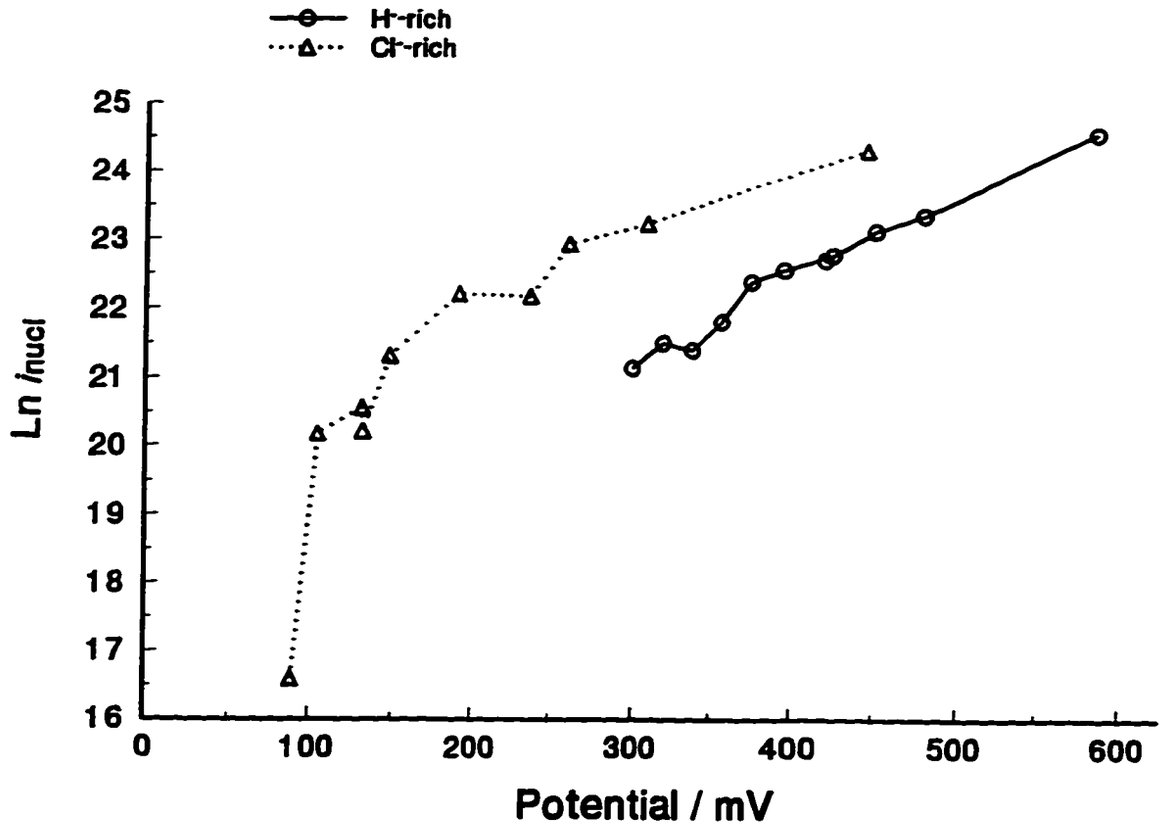


**Fig. 8.15.** Plot of the natural logarithm of $i_{nucl}$ ($N_\infty W$) from Tables. 8.2 and 8.3 calculated from initial growth transients for $H^+$-rich and $Cl^-$-rich versus step potential.

longer applies. Although the power-of-time for the initial slopes of growth-transients at Au were consistent with a *progressively-nucleated diffusion-controlled* deposition process and diffusion decays were observed for these, it turns out, as will be seen later when their macroscopic morphology is examined (§8.9.6), that the deposits did not actually grow according to the way expected for this theory. Diffusion-controlled growth would predict nucleation of a relatively small number of hemispherical grains whose propagating diffusion zones extinguish further nucleation. Actual deposits clearly showed subsequent nucleation on top of other growing grains. What does control the initial current response that is, in appearance, quite similar to diffusion-controlled nucleation and growth, is unclear.

### 8.8.5. Saturation Density: $N_{sat}$

As was concluded in §8.4.3, the $N_{\infty}$ sites are not *all* practically accessible as nucleation sites since many not-as-yet-nucleated sites can become covered by either adjacent growing grains (§8.3.4.1) or diffusion zones extending from them (§8.4.2), i.e. the Avrami effect. $N_{sat}$, which is calculated by Eqn. 8.57, has been included in Tables 8.2 and 8.3 in column 7. The value of $N_{sat}$ in the $H^-$-rich bath was *ca.* $5 \times 10^8$ sites $cm^{-2}$ and did not vary much with step potential (only by a factor of two and not in a potential-dependent manner), while in the $Cl^-$-rich bath $N_{sat}$ was about an order of magnitude smaller and varied considerably (potential-dependently and by *ca.* thirty times over a similar range of potential as that compared in the $H^-$-rich bath). The fact that $N_{sat}$ values were smaller and potential-dependent in the $Cl^-$-rich baths, but larger and potential-independent in the $H^-$-rich baths suggests that the $H^-$ ligand has an important role in the initial growth of the Al phase.

Such a conclusion was also drawn from the cyclic voltammetry of the baths, examined in §6.4.2, and the differences in morphology of deposits grown from either of the bath types. It was typical, in cyclic voltammetry conducted at a given sweep-rate, that larger onset potentials were required to initiate the electrodeposition process in the $Cl^-$-rich baths. Deposit grain size was usually finer when grown from $H^-$-rich baths. These facts are consistent with more facile nucleation in the $H^-$-rich baths.

### 8.8.6. Morphology

The macroscopic morphology of an electrodeposited phase is of ultimate importance to any practical application of an electrochemical deposition reaction. What macroscopic morphology a deposit attains can depend upon the type of interaction between the depositing phase and the underlying substrate and the energy of incorporation of adatoms at different crystallographic planes of the growing phase. In extreme cases this can give rise to epitaxial growth or, when also controlled by diffusion, unusual geometries, e.g. dendrites (trees) or whiskers (see [151]) that can be a serious problem to practical application (causing, e.g. electrical shorts). In less extreme cases, growth at certain preferred crystallographic orientations can give facetting in the growth phase. It is conceivable that at less preferred planes, nucleation of new crystallites would be preferred.

Al deposits from the hydride-baths were generally smooth, coherent and adherent. Deposits were usually textured and grain size was dependent on bath composition and was usually finer for deposits grown from $H^-$-rich baths, although, as with all other aspects of the work, these characteristics often varied in an unpredictable manner with bath and electrode history.

In Figs. 8.16 and 8.17 are shown a number of SEM photographs typical of Al electrochemically deposited from the hydride-bath under a variety of conditions. Figs. 8.16a and b show SEM photographs of deposits grown galvanostatically at 200 $\mu$A cm$^{-2}$ for 10,000 s and 25 mA cm$^{-2}$ for 100 s, respectively, onto *ca.* 1 cm$^2$ Au flag electrodes from an r = 5:1, $[Al]_{total}$ = 1.2 M bath. Only at very low deposition rates (Fig. 8.16a) was there any semblance of hemispherical growth, but in this particular case coverage was poor. It was more usual for the deposits to appear crystalline and facetted, as in Fig. 8.16b, with grain size being from the micron to the tens of microns scale. It should be mentioned that these macroscopic deposits are clearly not simply the result of continued growth of grains nucleated within the first few seconds of the transient. In the model of diffusion-controlled nucleation and growth, the time in which nucleation can take place is limited by the onset of diffusion-control, signalled in the transients of Fig. 8.11 by the current maxima. Clearly, from the morphologies of deposits from these baths, subsequent nucleation on the growing Al phase is not a problem.

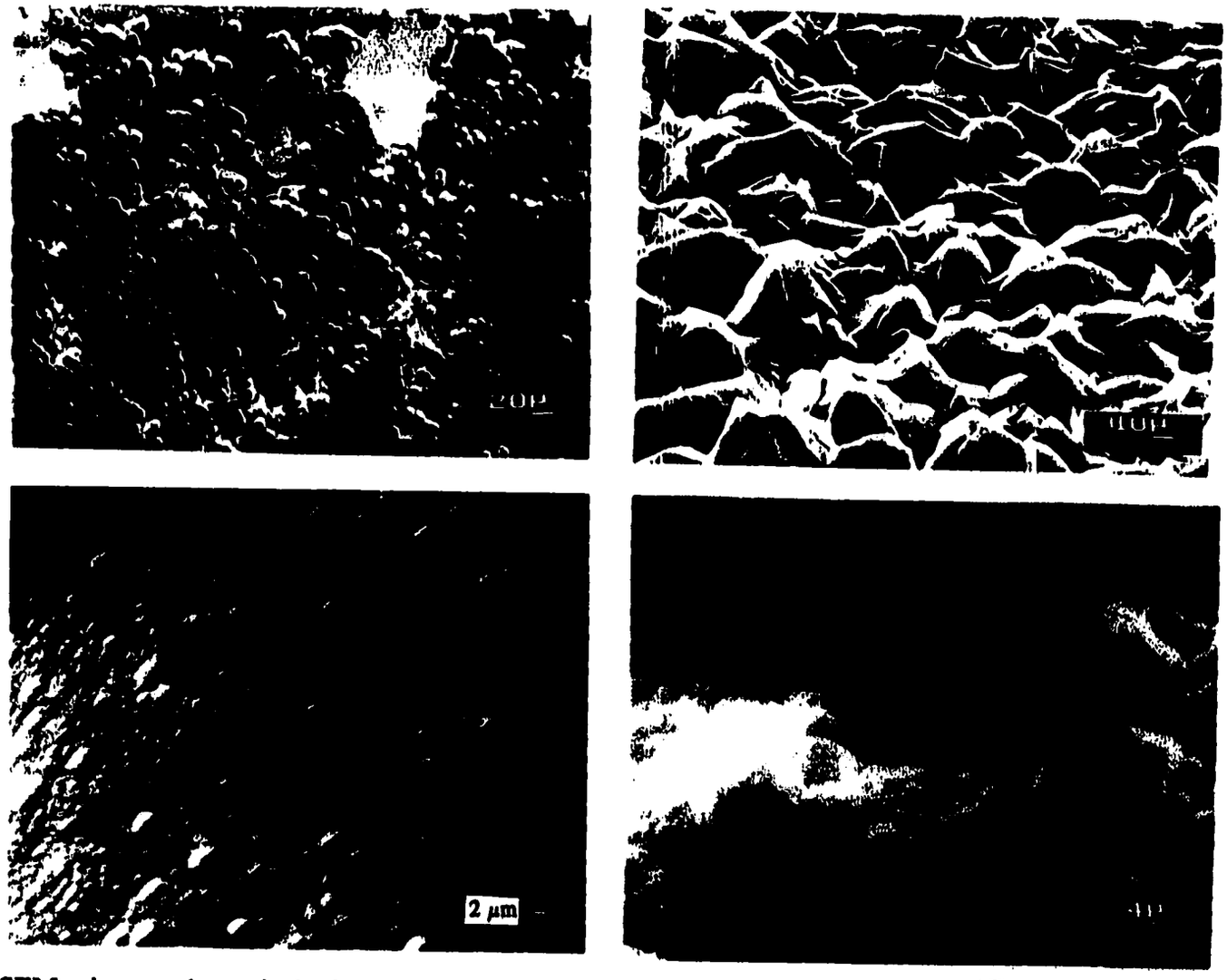


**Fig. 8.16.** SEM micrographs typical of Al deposits from (a,b) $Cl^-$-rich and (c,d) $H^-$-rich hydride-baths onto Au substrates. a) deposit grown galvanostatically at 200 $\mu A\,cm^{-2}$ for 8000 s (0 rpm) from an r = 5:1, $[Al]_{total}$ = 1.2 M bath; and b) 25 $mA\,cm^{-2}$ for 100 s from same bath. c) deposit grown galvanostatically at 20 $mA\,cm^{-2}$ for 200 s (0 rpm) from an r = 1:3, $[Al]_{total}$ = 0.42 M bath; and d) 100 $mA\,cm^{-2}$ for 100 s (500 rpm).

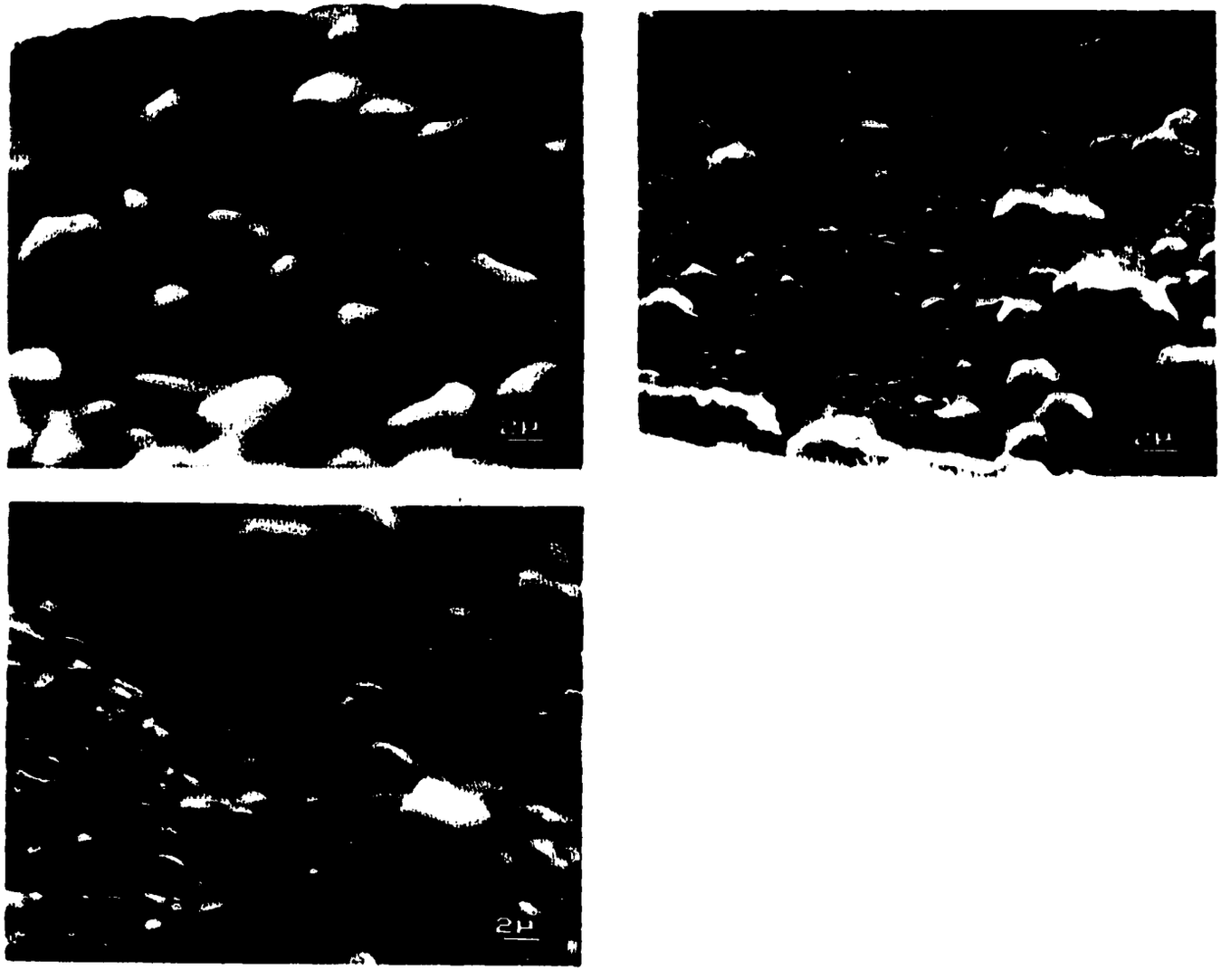


**Fig. 8.17.** SEM micrographs of Al deposits grown from an r = 2.2:1, $[Al]_{total}$ = 1.0 M bath onto an Au disc (0.002 $cm^2$) under the following conditions: a) 25 mA $cm^{-2}$ (0 rpm) for 200 s; b) 25 mA $cm^{-2}$ (500 rpm) for 200 s; c) 250 $\mu$A $cm^{-2}$ (0 rpm) for 2000 s.

SEM's in Figs. 8.16*c* and *d* show the morphology typical of deposits from the $H^-$-rich baths. Grain size was usually finer in the $H^-$-rich than in $Cl^-$-rich baths and under some conditions appeared "cauliflower"-like as in Fig. 8.16d.

Fig. 8.17 shows SEM photographs for deposits grown from an r = 2:1, $[Al]_{total}$ = 1 M bath under conditions of varying rate and electrode rotation. Note that the focus of these photographs was poor for reasons described in the Experimental section (§8.6), but a qualitative comparison is none-the-less possible. In Fig. 8.17a is a SEM of Al plated galvanostatically at 25 mA cm$^{-2}$ for 200 s on a 0.002 cm$^2$ Au disc electrode at rest. The deposit was of micron grain size and appeared crystalline. Variation of deposition conditions, with rotation (0 - 500 rpm) in *b* and plating rate (25 - 0.25 mA cm$^{-2}$) in *c*, did neither significantly nor consistently affect characteristics of the Al deposits.

### 8.8.7. Summary of Nucleation on Au

Although the current-transient response for the initiation of Al deposition onto Au corresponded closely to that for a *progressively nucleated diffusion-controlled* growth process, critical examination of the current-transients revealed characteristics that were inconsistent with the usual theory for such a mechanism (§8.4). The initial nucleation of Al does indeed exhibit a diffusion limitation, but significant deviations from expected behaviour were noted both before and after diffusion becomes dominant in the process, that is, both before and after the current maxima as e.g. in Fig. 8.11.

Before the current maximum, deviation from the power-of-time of 3/2 (the ideal for progressive nucleation under diffusion-control) was unmistakable for many transient experiments, as e.g. in Fig. 8.12. A more complicated electrocrystallization mechanism seems to be indicated. When the current-transients were analyzed in dimensionless form (in §8.9.2 and Figs. 8.13 and 8.14) significant deviations were observed in these data at both short and long times.

Diffusion coefficients calculated here were smaller than would have been expected for solution species in thf. Values had a maximum of about $2 \times 10^{-8}$ cm$^2$ s$^{-1}$ and it was concluded that the D's corresponded to species diffusing through solution and not say, adatoms along the surface or ions through a porous solid phase.

The potential-dependence of the nucleation rate, $i_{nuc}$, examined in §8.9.4, gave an impossible, negative, value for the size of the critical nucleus at high step potentials in both $Cl^-$-rich and $H^-$-rich baths. At low overpotentials another distinctly linear region corresponding closely to $n_{cr} = 0$ was observed, in the $Cl^-$-rich bath. These facts clearly indicate that nucleation is not a limitation to initial phase formation for Al. This conclusion is, however, in disagreement with the conclusion of analysis of the cyclic voltammetry of the plating onset region on bare inert substrates (§6.4), which clearly showed a dependence of the potential at which plating started on composition and rotation. The rotation-dependence, giving a delayed deposition onset with rotation, is consistent with a disruption of regions of supersaturation necessary for nucleation.

The saturation number density of nucleation sites, $N_{sat}$, was always larger in the $H^-$-rich (than in $Cl^-$-rich) baths and this seemed to correlate with generally finer grained deposits grown from these. Deposits from $Cl^-$-rich baths were markedly facetted, thus the Al phase seems to preferentially propagate along particular lattice orientations.

These results show that not only the elementary steps in electrodeposition of Al from $H^-$-rich and $Cl^-$-rich baths differ (as examined in Chapter 6) but that the cooperative aspects of formation of nuclei and their growth following such elementary processes, depend on the type of baths.

## 8.9. Conclusions

It is the intention of such current-transient studies to provide a link between the characteristics of the underlying electrochemical reactions by which the metal is deposited and the macroscopic morphology of the deposit. We have conducted a critical analysis of the initial stages of the Al deposition process on GC and Au. For deposition onto GC, adhesion to the substrate was poor, giving deposits that looked very nearly hemispherical. Deposition onto Au gave initial current-transients that showed behaviour typical of a diffusion-controlled process, although the form of the initial current-transient had little bearing on the ultimate morphology of the deposits. The deposited phase was usually smooth, adherent and continuous, covering the Au substrate well.

Deposit morphology appeared to vary with composition of the hydride-baths, tend-

ing to finer grained deposits for $H^-$-rich baths than for $Cl^-$-rich ones. An explanation for this could be due to differences in the ligand distribution between the baths. Recall from reaction 6.43 that an electron-transfer/ligand-decomplexation step was identified as the rds for the steady-state reaction. Final reduction of Al occurs in a disproportionation step involving three partially reduced aluminate species ($AlH_xCl_{2-x}^{\cdot}$ in reaction 6.43). Since there is a distribution of possible aluminates that give rise to plating, they are also likely to be of varying stabilities and this, for instance, could give a surface species $AlCl_2^{\cdot}$ having a longer lifetime than $AlHCl^{\cdot}$. That such a difference would affect deposit morphology would suggest that the reaction intermediates diffuse along the substrate surface and that disporportionation occurs at the growth sites. If this were not the case no differences in morphology would have been expected.

The $H^-$-rich baths would seem to have the most favourable characteristics for the plating of Al, showing high rates given the generally smaller total Al concentrations possible compared to the $Cl^-$-rich baths, facile nucleation, and fine grained, adherent deposits. The use of these baths is limited by the facts that the reactivity of the higher $H^-$-content species makes them more susceptible to reaction with the solvent as was shown in §5.9.2, and that Li codeposition, which has been observed from baths of high $H^-$-content, could be an interferant.

# Chapter 9 Conclusions and Claims to Original Research

Aluminum can be electroplated only from non-aqueous, aprotic media, for instance, molten salts or organic solvents. One such bath, the so-called *hydride-bath*, based on mixtures of $AlCl_3$ and $LiAlH_4$ in thf, has been found to be effective for electroplating aluminum. Baths of nearly all proportions give good quality Al electrodeposits at high rates. In the research described in this thesis all aspects of the kinetics and mechanism of the reaction have been thoroughly examined.

The success of the hydride-bath has been found to lie in the ligand mixing, catalyzed by $H^-$, which gives a distribution of aluminate complexes in solution. Additionally, the $H^-$ species has a role in improving bath conductivity. The extreme reactivity of the $H^-$ demands use of stringent conditions, since it is only stable in the very lowest polarity solvents which means that solution conductivity in thf is low and is usually not improved with addition of an inert supporting electrolyte. This species is not entirely responsible for enabling Al deposition since, interestingly, thf baths containing only $LiAlH_4$ did not plate Al.

Notwithstanding its limitations, the performance of the hydride-bath is superior to others for the same purpose that require elevated temperatures (e.g. > 150° for MCl-$AlCl_3$ melts [60]; > 80° [76]), or are limited by the transport of bulky species through solution (e.g. $Al_2X_7^-$ in aromatic hydrocarbons [45,46] and room-temperature molten salts [67,73]).

The hydride-bath has been the subject of numerous technical investigations (see §1.6) and several mechanistic studies, the conclusions of which have been examined in this thesis (see Chapter 3). Al electrodeposition, that necessarily involves the transfer of three electrons, is an example of a multi-step, electron-transfer reaction that has provided the opportunity to examine in close detail (Chapter 2) the means by which mechanism can be determined from electrochemical measurements. This development highlighted a number of limitations to the theory that seemed to have been forgotten or ignored in the works evaluated in Chapter 3. In the present author's opinion, the apparent confusion as to how experimental transfer coefficients are linked to reaction mechanism is a more

general problem in the electrochemical field and therefore Chapter 2, with particular emphasis on that part in which is developed the mechanistic situation involving a rds having a *stoichiometric number* greater than one, will be submitted as a chapter to an electrochemical review series.

Exchange current-densities for the deposition reaction were found to be as high as $1 \times 10^{-3}$ A cm$^{-2}$ and depended on concentration and compositional proportions. The kinetic parameters for Al deposition from the hydride-bath varied with the compositional ratio of the baths. It was concluded as part of the analysis presented that the symmetry factor, $\beta$, which describes the transition-state that limits the overall reaction rate, changes with the proportion of $Cl^-$ to $H^-$ ligands composing the bath. In an effort to explain the variation, the speciation of the plating bath, which was found to contain up to nine different aluminate complexes, was characterized by $^{27}$Al-NMR over a wide range of bath composition. A comparative examination of relative chemical shifts, linewidths and concentration dependencies has illuminated the reactivity of the individual chloro-hydrido-aluminates.

The plate quality of deposited Al was generally very good, but a substrate-dependence was observed (in the case of glassy carbon). The morphology of deposits from the hydride-bath was characterized and the mechanism of initial phase formation examined in terms of using nucleation and growth theories.

Claims to original research include the following:

1) A thorough critique of published literature on the mechanism and kinetics of Al deposition from the hydride-bath and the unequivocal assignment of a mechanism that applies to all compositions of the bath is given.
2) The experimental mechanistic studies enabled it to be concluded that Al deposition from the hydride bath proceeds by a thrice occurring single electron-transfer couple with a following disporportionation step involving complexed $Al^{2+}$ species, producing deposited Al metal.
3) In this regard, it was established that the symmetry factor, $\beta$, of the reaction varied between compositional extremes of the bath.

4) Development of ideas that grew out of work on (1) on the influence that the stoichiometric number, $\nu$, of the rds can have on observed Tafel slopes parameters. Analysis is given which enables identification of the only mechanism possibilities that can give rise to a $\nu$ value greater than one, i.e. a previous (reductive) dissociation or a following (reductive) combination. A restriction to possible values that non-rds reaction steps can make to the transfer coefficient values was demonstrated.

5) The speciation of hydride-baths of varying composition was carried out by $^{27}$Al-NMR over a wide range of composition and analyzed with respect to possible ligand-exchange equilibria. It was found that baths were extremely reactive and that significant decomposition (from auto-decomposition and reaction with moisture) arose, even during the stage of preparation of the bath.

6) NMR data, including relative chemical shifts, linewidths and concentration dependencies were used to characterize the reactivity of the various aluminate complexes in solution. It was shown that aluminate species of increasing $H^-$ ligand proportion gave an increasing trend in reactivity; in terms of the participation of these species in the electrode processes, but unfortunately also in terms of their susceptibility to chemical decomposition pathways.

7) A link was drawn between the reactivity of the aluminate species, characterized by NMR, and the changing electrochemical behaviour (i.e. $\beta$) of the baths with composition. A transition-state involving bridging Cl ligands was proposed.

8) Results of experiments on initiation of phase growth as well as examination of deposit morphology demonstrated that the $H^-$ ligand plays an important role in electrocrystallization. This suggests that partially reduced intermediates can easily diffuse along the substrate surface and that the chemical disproportionation step in the Al deposition reaction probably occurs directly at growth sites.

The electroplating of aluminum represents a significant technical challenge. Only under rigourous conditions are plating baths for this purpose useful. The hydride-bath

offers a unique ability to change, if not entirely controllably, the mean reactivity of depositable species via the ligand mixing of the Schlesinger reaction; the effect of this was clearly observed in the fundamental electrochemical reduction and oxidation steps, as well as the macroscopic morphology.

## References


[1] *CRC Handbook of Chemistry and Physics*; Weast, R.C., Lide, D.R., Eds.; CRC Press: Boca Raton, Florida, **1990**.

[2] Wade, K., Banister, A.J., In *Comprehensive Inorganic Chemistry*; Bailar, J.C., Emeleus, H.J., Nyholm, R., Trotman-Kickenson, A.F., Eds.; Pergamon: Oxford, **1973**; p.1973.

[3] Williams, T.I., *Endeavour, New Series*, **1993**, *17(2)*, 89.

[4] Lagowski, J.J., *Modern Inorganic Chemistry*; Dekker: New York, **1973**; p.285.

[5] Statistics from Aluminum Review available from http://www.usbm.gov/mi/stat/alum/tbl1.txt

[6] Rao, B.M.L., et al., In *Electrochemistry in Transition*; Murphy, O.J., Srinivasan, S., Conway, B.E., Eds.; Plenum: New York, **1992**; p.629.

[7] Hamlen, R.P., In *Handbook of Batteries*; Linden, D., Ed.; Magraw-Hill: New York, **1995**; *2nd Ed.*, Chp.38.

[8] Gutmann, V., *Coordination Chemistry in Nonaqueous Solutions*; Springer-Verlag: New York, **1968**.

[9] Linden, D., In *Handbook of Batteries*; Linden, D., Ed.; Magraw-Hill: New York, **1995**; *2nd Ed.*, Chp.1.

[10] Despic, A., Parkhutik, V.P., In *Modern Aspects of Electrochemistry*; Bockris, J.O'M., White, R., Conway, B.E., Eds.; Plenum: New York, **1989**; *Vol.20*.

[11] Kabanov, B.N., Astakhov, I.I., Kiseleva, I.G., *Electrochim. Acta*, **1979**, *24*, 167.

[12] Despic, A.R., Drazic, D.M., Purenovic, M.M., Cikovic, N., *J. Appl. Electrochem.*, **1976**, *6*, 526.

[13] Bai, L., Conway, B.E., *J. Electrochem. Soc.*, **1990**, *137(12)*, 3737.

[14] Burstein, G.T., Liu, C., *Electrochim. Acta*, **1994**, *39(7)*, 873.

[15] Malachesky, P.A., In *Encyclopedia of Electrochemistry of the Elements*; Bard, A.J., Ed.; Dekker: New York, **1973**; *Vol.6*, p.64.

[16] Galova, M., Lux, I., *Chem Zvesti*, **1975**, *29(3)*, 279.

[17] Gutmann, V., *Coord. Chem. Rev.*, **1976**, *18*, 225.

[18] Lux, L., *Chem Zvesti*, **1983**, *37(5)*, 623.

[19] Galova, M., *Electrochim. Acta*, **1984**, *29*, 323.

[20] Bai, L., Conway, B.E., *J. Appl. Electrochem.*, **1992**, *22*, 131.

[21] Gontmakher, N.M., Nechaeva, O.N., Grigor'ev, V.P., Nekrasov, L.N., *Elektrokhimiya*, **1977**, *13*, 1748.

[22] Faure-Geors, A., Dalard, F., Rais, A.B., *J. Appl. Electrochem.*, **1989**, *19*, 203.

[23] Dudley, J.T., et al., *J. Power Sources*, **1991**, *35*, 59.

[24] Venkatasetty, H.V., In *Lithium Battery Technology*; Venkatasetty, H.V., Ed.; Wiley: New York, **1984**; p.1.

[25] Couch, D.E., Brenner, A., *J. Electrochem. Soc.*, **1951**, *99*, 234.

[26] Schmidt, F.J., Hess, I.J., *Plating*, **1966**, *53*, 229.

[27] Beach, J.G., Faust, C.L., *J. Electrochem. Soc.*, **1959**, *106*, 659.

[28] Beach, J.G., McGraw, L.D., Faust, C.L., *Plating*, **1968**, *55* 936.

[29] Daenen, T., van der Berg, J., van Dijk, G., *Ann. Tech. Conf., Inst. Met. Finish.*, **1985**; p.3.

[30] Hurley, F.H., Wier, T.P., *J. Electrochem. Soc.*, **1951**, *99*, 207.

[31] Clay, F.A., Harding, W.B., Stimetz, C.J., *Plating*, **1969**, *56*, 1027.

[32] Mazin, V.A., Kazakov, V.A., Titova, V.N., *Elektrokhimiya*, **1991**, *27(3)*, 417. *Soviet Echem*, **1991**, 382.

[33] Galova, M., *Surf. Tech.*, **1980**, *11*, 357.

[34] Yoshio, M., Ishibashi, N., *J. Appl. Electrochem.*, **1973**, *3*, 321.

[35] Ishibashi, N., Yoshio, M., *Electrochim. Acta*, **1972**, *17*, 1343.

[36] Ishibashi, N., Hanamura, Y., Yoshio, M., Seiyama, T., *Denki Kagaku*, **1969**, *37*, 73.

[37] Badawy, W.A., Sabrah, B.A., Hilal, N.H.Y., *J. Appl. Electrochem.*, **1986**, *16*, 707.

[38] Badawy, W.A., Sabrah, B.A., Hilal, N.H.Y., *J. Appl. Electrochem.*, **1987**, *17*, 357.

[39] Galova, M., Kladeskova, D., Lux, I., *Surf. Tech.*, **1981**, *13*, 315.

[40] Eckert, J., Galova, M., *Electrochim. Acta*, **1981**, *26(8)*, 1169.

[41] Graef, M.W.M., *J. Electrochem. Soc.*, **1985**, *132(5)*, 1038.

[42] Peled, E., Gileadi, E., *Plating and Surf. Finish.*, **1975**, *62*, 342.

[43] Peled, E., Elam, M., Gileadi, E., *J. Appl. Electrochem.*, **1981**, *11*, 463.

[44] Peled, E., Gileadi, E., *J. Electrochem. Soc.*, **1976**, *123*, 15.

[45] Elam, M., Gileadi, E., *J. Electrochem. Soc.*, **1979**, *126(9)*, 1474.

[46] Capuano, G.A., Davenport, W.G., *J. Electrochem. Soc.*, **1971**, *118(10)*, 1688.

[47] Capuano, G.A., Davenport, W.G., *Plating*, **1973**, *60*, 253.

[48] Ladouceur, M., Capuano, G.A., *Can. Met. Q.*, **1990**, *29*, 87.

[49] Capuano, G.A., Davenport, W.G., *J. Electrochem. Soc.*, **1984**, *131*, 2595.

[50] Ziegler, K., Lehmkuhl, H., *Z. Anorg. Allg. Chem.*, **1956**, *293*, 414.

[51] Kautek, W., Birkle, S., *Electrochim. Acta*, **1989**, *34(8)*, 1213.

[52] Landau, I.U., *Ann. Tech. Conf.: Inst. of Met. Finish.*, **1986**, *1*, p 57.

[53] Hussey, C.L., Xu, X., *J. Electrochem. Soc.*, **1991**, *138(7)*, 1886.

[54] Barnard, P.A., Hussey, C.L., *J. Electrochem. Soc.*, **1990**, *137(3)*, 913.

[55] Robinson, J., Osteryoung, R.A., *J. Am. Chem. Soc.*, **1979**, *101(2)*, 323.

[56] Lin, F.-M., Hussey, C.L., *J. Electrochem. Soc.*, **1993**, *140(11)*, 3093.

[57] Hussey, C.L., King, L.A., Carpio, R.A., *J. Electrochem. Soc.*, **1979**, *126(6)*, 1029.

[58] Gau, W.J., Sun, I.W., *J. Electrochem. Soc.*, **1996**, *143(1)*, 170.

[59] Zhang, Y.J., et al., *J. Electroanal. Chem.*, **1986**, *210*, 127.

[60] Qingfeng, L., Hjuler, H.A., Berg, R.W., Bjerrum, N.J., *J. Electrochem. Soc.*, **1990**, *137(2)*, 593.

[61] Jovic, V.D., Jovicevic, J.N., *J. Appl. Electrochem.*, **1989**, *19(2)*, 275.

[62] Lantelme, F., Cherrat, E., Chryssoulakis, Y., Kalogeropoulou, S., *J. Appl. Electrochem.*, **1989**, *19(2)*, 203.

[63] Carlin, R.T., Osteryoung, R.A., *J. Electrochem. Soc.*, **1989**, *136(5)*, 1409.

[64] Takami, N., Koura, B., *J. Electrochem. Soc.*, **1989**, *136(3)*, 730.

[65] Chryssoulakis, Y., Poignet, J.-C., Manoli, G., *J. Appl. Electrochem.*, **1987**, *17*, 857.

[66] Takahashi, S., Ida, K., Mori, S., *Proc. 7th Int'l. Symp. Molten Salts*, **1990**, p 661.

[67] Lai, P.K., Skyllas-Kazacos, M., *Electrochim. Acta*, **1987**, *32(10)*, 1443.

[68] Robinson, J., Osteryoung, R.A., *J. Electrochem. Soc.*, **1980**, *127(1)*, 122.

[69] Manoli, G., Chryssoulakis, Y., Poignet, J-C,, *Plat. Surf. Finish.*, **1991**, *35(3-4)*, 321.

[70] Wilkes, J.S., Levisky, J.A., Wilson, R.A., Hussey, C.L., *Inorg. Chem.*, **1982**, *21*, 1263.

[71] Auborn, J.J., Barberio, Y.L., *J. Electrochem. Soc.*, **1985**, *132(3)*, 598.

[72] Carlin, R.T., Crawford, W., Bersch, M., *J. Electrochem. Soc.*, **1992**, *139(10)*, 2721.

[73] Lai, P.K., Skyllas-Kazacos, M., *J. Electroanal. Chem.*, **1988**, *248*, 431.

[74] Papageorgiou, N., Emmenegger, F.-P., *Electrochim. Acta*, **1993**, *38(2-3)*, 245.

[75] Jones, S.D., Blomgren, G.E., *Extended Abs. of Electrochem. Soc. (Spring)*, **1990**, p.857.

[76] Legrand, L., Tranchant, A., Messina, R., *J. Electrochem. Soc.*, **1994**, *141(2)*, 378.

[77] Legrand, L., Heintz, M., Tranchant, A., Messina, R., *Electrochim. Acta*, **1995**, *40(11)*, 1711.

[78] Legrand, L.L., Tranchant, A., Messina, R., *Electrochim. Acta*, **1994**, *39(10)*, 1427.

[79] Hisano, T., Terazawa, T., Matsui, H., *Chem. Lett.*, **1973**, 219.

[80] Hisano, T., Terazawa, T., Takeuchi, I., Inohara, S., Ikeda, H., *Bull. Chem. Soc. Jap.*, **1971**, *44*, 599.

[81] Chryssoulakis, Y., Kalogeropoulou, S., et al., *J. Appl. Electrochem.*, **1986**, *16*, 196.

[82] Gutmann, V., *The Donor-Acceptor Approach to Molecular Interactions*; Plenum: New York, **1978**.

[83] Unpublished results

[84] Lefebvre, M.C., to be submitted "*Modern Aspects of Electrochemistry*".

[85] Lefebvre, M.C., Conway, B.E., accepted for publication by *J. Electroanal. Chem.*, Jan. **1997**.

[86] Bockris, J.O'M., Reddy, A.K.N.; *Modern Electrochemistry*; Plenum: New York, **1977**, *6th Ed.*.

[87] Laidler, K.J., *Chemical Kinetics*; Harper Row: New York, **1987**; p.89.

[88] Eyring, H., Polanyi, M., In *Selected Readings in Chemical Kinetics*; Back, M.H., Laidler, K.J., Eds.; Pergamon: Oxford, **1967**.

[89] Conway, B.E., *Theory and Principles of Electrode Processes*; Ronald Press: New York, **1965**.

[90] Marcus, R.A., *Can. J. Chem.*, **1959**, *37*, 155.

[91] Bard, A.J., Faulkner, L.R., *Electrochemical Methods: Fundamentals and Applications*; Wiley: New York, **1980**.

[92] Parsons, R., *Pure Appl. Chem.* **1979**, *52*, 233.

[93] Horiuti, J., Polanyi, M., *Acta Physicochim.*, **1935**, *2*, 505.

[94] Butler, J.A.V., *Trans. Farad. Soc.*, **1924**, *19*, 729 & 734.

[95] Erdey-Gruz, T., Volmer, M., *Z. Physik. Chem.*, **1930**, *150A*, 203.

[96] Krishtalik, L.I., In *Comprehensive Treatise of Electrochemistry*; Conway, B.E., Bockris, J.O'M., Yeager, E., Khan, S.U.M., White, R.E., Eds.; Plenum: New York, **1983**; p 131.

[97] Makrides, A.C., *J. Electrochem. Soc.*, **1964**, *111(4)*, 392.

[98] Makrides, A.C., *J. Electrochem. Soc.*, **1964**, *111(4)*, 400.

[99] Meyer, R.E., *J. Electrochem. Soc.*, **1960**, *107*, 847.

[100] Horiuti, J., *J. Res. Inst. Catal., Hokkaido*, **1948**, *1*, 8.

[101] Horiuti, J., Ikusima, M., *Proc. Imper. Acad. Tokyo*, **1939**, *15*, 39.

[102] Lefebvre, M.C., Conway, B.E., to be submitted, **1997**).

[103] Sawyer, D.T., Roberts, Jr.J.L., *Experimental Electrochemistry for Chemists*; Wiley: New York, **1974**; p.53.

[104] Vogel, A.I., *Quantitative Inorganic Analysis*; Longman: London, **1962**; p.426.

[105] Harris, D.C., *Quantitative Chemical Analysis*; WH Freeman: New York, **1982**; p.287.

[106] Martell, A.E., Smith, R.M., *Critical Stability Constants*; Plenum: New York, **1974**; *Vol.1*, pp.204-211.

[107] Skoog, D.A., West, D.M., *Fundamentals of Analytical Chemistry*; Holt Rinehart & Winston: New York, **1976**; *3rd Ed.*, pp.179 & 726.

[108] Howarth, O., In *Multinuclear NMR*; Mason, J., Ed.; Plenum: New York, **1987**; Chp.5.

[109] Hinton, J.F., Briggs, R.W., In *NMR and the Periodic Table*; Harris, R.K., Mann, B.E., Eds.; Academic Press: New York, **1978**; p.279.

[110] Brevard, C., Granger, P., *Handbook of High Resolution Multinuclear NMR*; Wiley Intersci.: NY, **1981**.

[111] Delpuech, J.J., In *NMR of Newly Accessible Nuclei*; Laszlo, P., Ed.; Academic: New York, **1983**; *Vol.2*, p.153.

[112] Finholt, A.E., Bond, A.C., Schlesinger, H.I., *J. Am. Chem. Soc.*, **1947**, *69*, 1199.

[113] Shirk, A.E., Shriver, D.F., *J. Am. Chem. Soc.*, **1973**, *95(18)*, 5904.

[114] Derouault, J., Granger, P., Forel, M.T., *Inorg. Chem.*, **1977**, *16(12)*, 3214.

[115] Noth, H., Rurlander, R., Wolfgardt, P., *Z. Naturforschung*, **1982**, *B37*, 29.

[116] Huet, J., Durand, J., Infarnet, Y., *Org. Magn. Res.*, **1976**, *8*, 382.

[117] van Dijk, G.A.R., Smoorenburg, H.C.A.M., *J. Electrochem. Soc.*, **1984**, *131(2)*, 345.

[118] Gutmann, V., *Electrochim. Acta*, **1976**, *21*, 661.

[119] Vladiniroff, T., Malinowski, E.R., *J. Chem. Phys.*, **1967**, *46*, 1830.

[120] "Spartan SGI V.4.0.4GL", Wavefunction Inc. molecular modelling software on Silicon Graphics workstation, University of Ottawa.

[121] Pearson, R.G., In *Survey of Progress in Chemistry*; Scott, A.F., Ed.; Academic: New York, **1969**; *Vol.5*, p.1.

[122] Pearson, R.G., *J. Chem. Edu.* **1968**, *45*, 584 & 643.

[123] Kidd, R.G., In *The Multinuclear Approach to NMR Spectroscopy*; Lambert, J.B., Riddell, F.G., Eds.; D. Reidel Publishing: Dordrecht (Holland), **1983**; p.329.

[124] Detellier, C., In *Modern NMR Techniques and Their Application in Chemistry*; Popov, A.I., Hallenga, K., Eds.; Dekker: New York, **1991**; p.521.

[125] Breitmaier, E., Haas, G., Voelter, W., *Atlas of C-13 NMR Data*; Heyden & Son: London, **1975**.

[126] Lambert, J.B., Shurvell, H.F., Lightner, D., Cooks, R.G., *Introduction to Organic Spectroscopy*; Macmillan: New York, **1987**; p.117.

[127] Bailey, W.J., Marktscheffel, F., *J. Org. Chem.*, **1960**, *25*, 1797.

[128] Fletcher, S., et al., *J. Electroanal. Chem.*, **1983**, *159*, 267.

[129] Allen, P.L., Hickling, A., *Trans. Farad. Soc.*, **1957**, *53*, 1626.

[130] Mendenhall, W., Sincich, T., *Statistics for Engineering and Sciences*; Dellen Publishing Co: San Francisco, **1992**; *3rd Ed.*.

[131] Deslouis, C., Epelboin, I., Keddam, M., Lestrade, J.C., *Electroanal. Chem.*, **1970**, *28*, 57.

[132] Armstrong, R.D., Dickinson, T., Reid, M., *Electrochim. Acta*, **1976**, *21*, 935.

[133] Barral, G., Diard, J.P., Le Gorrec, B., Lu Dac Tri, Montella, C., *J. Appl. Electrochem.*, **1985**, *15*, 913.

[134] Bai, L., *J. Electroanal. Chem.*, **1993**, *355(1-2)*, 37.

[135] Devanathan, M.A.V., Bockris, J.O'M., Muller, K., *Proc. Roy. Soc. London*, **1963**, *A274*, 55.

[136] Grahame, D.C., *Chem. Rev.*, **1947**, *47*, 441.

[137] Payne, R., In "*Physical Chemistry of Organic Solvent Systems*; Covington, A.K., Dickinson, T., Eds.; Plenum: New York, **1973**; p.733.

[138] Payne, R., In *Adv. in Electrochem. and Electrochem. Eng.*; Delahay, P., Tobias, C.W., Eds.; Wiley: New York, **1970**; p.1.

[139] Puippe, J.-C., In *Theory and Practice of Pulse Plating*; Puippe, J.-C., Leaman, F., Eds.; Amer. Electroplaters Surf. Finish. Soc.: Orlando (Florida), **1986**; p.1.

[140] Tilak, B.V., Conway, B.E., *Electrochim. Acta*, **1976**, *21*, 745.

[141] Harrington, D.A., Conway, B.E., *J. Electroanal. Chem.*, **1987**, *221*, 1.

[142] Bauer, H.H., *J. Electroanal. Chem.*, **1968**, *16*, 419.

[143] Bell, R.P., *Acid-Base Catalysis*; Oxford: London, **1949**, Chp.2.

[144] Krishtalik LI, *Charge Transfer Reactions in Electrochemical and Chemical Processes*; Consultants Bureau (Plenum): New York, **1986**; p.4.

[145] Bockris, J.O'M., Khan, S.U.M., *Surface Electrochemistry*; Plenum: New York, **1993**.

[146] Fawcett, W.R., Foss, Jr.C.A., *J. Electroanal. Chem.*, **1988**, *250*, 225.

[147] Jordan, R.B., *Reaction Mechanisms of Inorganic and Organometallic Systems*; Oxford Press: New York, **1991**; p.183.

[148] Conway, B.E., Bockris, J.'OM., *Electrochim. Acta*, **1961**, *3(4)*, 340.

[149] Avrami, M., *J. Chem. Phys.*, **1940**, *8*, 212.

[150] Bosco, E., Rangarajan, S.K., *J. Electroanal. Chem.*, **1982**, *134*, 225.

[151] Fleischmann, M., Thirsk, H.R., In *Adv. in Electrochem. and Electrochem. Eng.*; Delahay, P., Tobais, C.W., Eds.; Interscience: New York, **1963**; *Vol.3*, p.123.

[152] Scharifker, B., Hills, G., *J. Electroanal. Chem.*, **1981**, *130*, 81.

[153] Hills, G., Pour, A.K., Scharifker, B., *Electrochim. Acta*, **1983**, *28(7)*, 891.

[154] Gunawardena, G., Hills, G., Montenegro, I., Scharifker, B., *J. Electroanal. Chem.*, **1982**, *138*, 225.

[155] Fulks, W., *Advanced Calculus*; Wiley: New York, **1978**; *3rd Ed.*, p.451.

[156] Harrison, J.A., Thirsk, H.R., In *Electroanal. Chem.*; Bard, A.J., Ed.; Marcel Dekker: New York, **1971**; *Vol.5*, p.67.

[157] Hoel, P.G., Port, S.C., Stone, C.J., *Introduction to Probability Theory*; Houghton Mifflin: Boston, **1971**; pp.145-7.

[158] Avrami, M., *J. Chem. Phys.*, **1939**, *7*, 1103.

[159] Avrami, M., *J. Chem. Phys.*, **1940**, *8*, 212.

[160] Avrami, M., *J. Chem. Phys.*, **1941**, *9*, 177.

[161] Abyaneh, M.Y., *Electrochim. Acta*, **1982**, *27(9)*, 1329.

[162] Abyaneh, M.Y., Fleischmann, M., *J. Electroanal. Chem.*, **1981**, *119*, 187.

[163] Abyaneh, M.Y., Fleischmann, M., *J. Electroanal. Chem.*, **1981**, *119*, 197.

[164] Fletcher, S., Matthews, D.B., *J. Appl. Electrochem.*, **1981**, *11*, 1.

[165] Bosco, E., Rangarajan, S.K., *J. Electroanal. Chem.*, **1982**, *134*, 213.

[166] Sonneveld, P.J., Visscher, W., Barendrecht, E., *Electrochim. Acta*, **1992**, *37(7)*, 1199.

[167] Hills, G.J., Schiffrin, D.J., Thompson, J., *Electrochim. Acta*, **1974**, *19(11)*, 657.

[168] Hills, G.J., Schiffrin, D.J., Thompson, J., *Electrochim. Acta*, **1974**, *19*, 671.

[169] Marchiano, S.L., Arvia, A.J., In *Comprehensive Treatise of Electrochemistry*; Yeager, E., Bockris, J.O'M., Conway, B.E., Sarangapani, S., Eds.; Plenum: NY, **1983**; *Vol.6*, p.91.

[170] Scharifker, B., Hills, G., *Electrochim. Acta*, **1983**, *28(7)*, 879.

[171] Beshore, A.C., et al., *J. Appl. Electrochem.*, **1987**, *17*, 765.

[172] Hills, G.H., Montenegro, I., Scharifker, B.R., *J. Appl. Electrochem.*, **1980**, *10*, 807.

[173] Kissinger, P.T., Heineman, W.R., *Laboratory Techniques in Electroanalytical Chemistry*; Marcel Dekker: New York, **1984**; p.308.

[174] Kaischev, R., Scheludko, A., Bliznakov, G., *Bull. Acad. Bulgare Sci. (Phys.)*, **1950**, *3*, 137.

[175] Milchev, A., Vassileva, E., Kertov, V., *J. Electroanal. Chem.*, **1980**, *107*, 323.

[176] Rigano, P.M., Mayer, C., Chierchie, T., *J. Electroanal. Chem.*, **1988**, *248*, 219.

[177] Milchev, A., Stoyanov, S., *J. Electroanal. Chem.*, **1976**, *72*, 33.

[178] Gunawardena, G., Hills, G., Montenegro, I., *J. Electroanal. Chem.*, **1982**, *138*, 241.